Georgy Givirovskiy

IN SITU HYDROGEN PRODUCTION IN POWER-TO-FOOD APPLICATIONS

ACTA UNIVERSITATIS LAPPEENRANTAENSIS 1015

Georgy Givirovskiy

IN SITU HYDROGEN PRODUCTION IN POWER-TO-FOOD APPLICATIONS

Dissertation for the degree of Doctor of Science (Technology) to be presented with due permission for public examination and criticism in the Auditorium 1325 at Lappeenranta–Lahti University of Technology LUT, Lappeenranta, Finland on the 4th of February, 2022, at noon.

Acta Universitatis
Lappeenrantaensis 1015

Supervisors Professor Jero Ahola
LUT School of Energy Systems
Lappeenranta–Lahti University of Technology LUT
Finland

Dr. Vesa Ruuskanen
LUT School of Energy Systems
Lappeenranta–Lahti University of Technology LUT
Finland

Reviewers Assistant Professor Annukka Santasalo-Aarnio
Department of Mechanical Engineering
Aalto University
Finland

Dr. Silvio Matassa
Department of Civil and Mechanical Engineering
University of Cassino and Southern Lazio
Italy

Opponents Dr. Martin Müller
Electrolysis Process Engineering Department
Jülich Research Centre
Germany

Assistant Professor Annukka Santasalo-Aarnio
Department of Mechanical Engineering
Aalto University
Finland

ISBN 978-952-335-789-1
ISBN 978-952-335-790-7 (PDF)
ISSN-L 1456-4491
ISSN 1456-4491

Lappeenranta–Lahti University of Technology LUT
LUT University Press 2022

Abstract

Georgy Givirovskiy
In situ hydrogen production in power-to-food applications
Lappeenranta 2022
79 pages
Acta Universitatis Lappeenrantaensis 1015
Diss. Lappeenranta–Lahti University of Technology LUT
ISBN 978-952-335-789-1, ISBN 978-952-335-790-7 (PDF), ISSN-L 1456-4491,
ISSN 1456-4491

Technologies capable of coupling sustainable generation of energy and production of valuable products are required to shift the focus from a fossil economy to a renewable-based and circular economy and to confront environmental pollution. In this regard, hybrid biological–inorganic (HBI) systems, which combine the advantages of biological components with electrochemical methods, provide a platform for efficient and sustainable chemical synthesis. HBI technology can be used to synthesize a wide range of high-value compounds, including microbial proteins, alcohols, and polymers. The operating principle of HBI systems is based on the use of special autotrophic microorganisms in systems with in situ water electrolysis, which are interfaced to biocompatible electrodes. These biocompatible catalysts or electrodes are then employed to convert electrical energy into H_2 or energetic reducing equivalents, which are then used by microorganisms as an energy source for assimilation of CO_2 to create new carbonaceous molecules. In this context, HBI systems are anticipated to play a critical role in storing energy from intermittent energy sources, as well as offering a sustainable mechanism for fixing CO_2.

With HBI being a nascent technology, this doctoral dissertation aims to study and improve the energy efficiency of in situ water electrolysis and to prove the feasibility of CO_2 assimilation into protein-rich biomass on a pilot scale. To achieve these goals, the performance of different conventional electrodes and transition metal electrocatalysts is comparatively studied in specific electrolytes used in HBI processes. So far, as the practical implementation of HBI systems requires the development of robust and scalable electrobioreactors, this work reports a series of in situ water electrolyzer stack designs as part of an electrobioreactor system. In addition, this research presents a Neo-Carbon Food concept that demonstrates pilot-scale synthesis of microbial biomass using direct CO_2 capture from the air, autotrophic bacteria, and in situ water electrolysis. The data collected during the experiments could be employed to simulate, investigate, and improve electrobioreactors with in situ water electrolysis used in HBI processes. The results attained in this research represent a significant step for the industrial implementation of HBI systems.

Keywords: Power-to-food, carbon dioxide capture, hybrid biological-inorganic system, in situ water electrolysis, electrobioreactor, hydrogen-oxidizing bacteria, microbial protein

Acknowledgements

The research presented in this dissertation was conducted at the LUT School of Energy Systems at Lappeenranta–Lahti University of Technology LUT, Finland, between 2017 and 2021.

I am deeply grateful to my supervisors Professor Jero Ahola and Dr. Vesa Ruuskanen for their guidance, active support, and assistance in venturing into a new scientific field, electrochemistry. I am grateful to our colleagues from the VTT Technical Research Centre of Finland for their expertise in bioelectrochemistry and mechanical engineering. Furthermore, I would like to dedicate separate thanks to laboratory technician Toni Väkiparta for his help with the experimental measurements, Dr. Hanna Niemelä for revising the language of this doctoral dissertation, and Professor Eveliina Repo, who provided me funding at the end of my doctoral studies.

My sincere thanks are due to Assistant Professor Annukka Santasalo-Aarnio and Dr. Silvio Matassa, whom I am honored to have had as preliminary examiners of this dissertation. Their constructive criticism and comments have pointed out issues that improved the quality of this dissertation and helped to emphasize the importance of the current research. Warm thanks to Dr. Martin Müller and Assistant Professor Annukka Santasalo-Aarnio for consenting to act as opponents at the public defence.

I wish to acknowledge the Academy of Finland for funding ”MOPED - Microbial Oil and Proteins from Air by Electricity-Driven Microbes,” and the Technology Industries of Finland Centennial Foundation with Jane and Aatos Erkko Foundation for ”Feed and food from carbon dioxide and electricity - research and piloting of the future protein production.”

As an international community, LUT University has provided a brilliant opportunity to build a solid friendship with people from all around the world. I used this opportunity wisely, and I wish to thank all my colleagues and friends, with whom I have shared many memorable experiences and moments during my work and life in Lappeenranta.

Eventually, I wish to express my innermost gratitude to my family and beloved wife Daria. Without their support, it would have been impossible to go through this challenging path.

Georgy Givirovskiy
February 2022
Lappeenranta, Finland

This work is dedicated to my parents
Oxana Givirovskaia
Stanislav Givirovskiy

Contents

List of publications

The doctoral dissertation has been written as a summary of the following published peer-reviewed articles.

I. Givirovskiy, G., Ruuskanen, V., Ojala, L. S., Lienemann, M., Kokkonen, P., Ahola, J. (2019). Electrode material studies and cell voltage characteristics of the in situ water electrolysis performed in a pH-neutral electrolyte in bioelectrochemical systems. *Heliyon*, 5(5), pp. 1–10.

II. Givirovskiy, G., Ruuskanen, V., Ojala, L. S., Kokkonen, P., Ahola, J. (2019). In Situ Water Electrolyzer Stack for an Electrobioreactor. *Energies*, 12(10), pp. 1–13.

III. Givirovskiy, G., Ruuskanen, V., Väkiparta, T., Ahola, J. (2020). Electrocatalytic performance and cell voltage characteristics of 1st–row transition metal phosphate (TM-Pi) catalysts at neutral pH. *Materials Today Energy*, 17, pp. 1–11.

IV. Ruuskanen, V., Givirovskiy, G., Elfving, J., Kokkonen, P., Karvinen, A., Järvinen, L., Sillman, J., Vainikka, M., Ahola, J. (2020). Neo–Carbon Food concept: A pilot–scale hybrid biological–inorganic system with direct air capture of carbon dioxide. *Journal of Cleaner Production*, 278, pp. 1–11.

V. Givirovskiy, G., Ruuskanen, V., Kokkonen, P., Karvinen, A., Givirovskaia, D., Repo, E., Ahola, J. (2021). Pilot-scale in situ water electrolyzer with an improved fluid flow and modified electrodes for upscaling hybrid biological–inorganic systems. *Journal of Cleaner Production*, 314, pp. 1–9.

Author's contribution

Georgy Givirovskiy has been the main author in **Publications I–III, V** being responsible for the experimental procedure and postprocessing of the measured data. In **Publications I–II**, the biological cultivation data have been provided by project collaborators from the VTT Technical Research Centre of Finland. In **Publication IV**, Dr. Vesa Ruuskanen was the corresponding author while Georgy Givirovskiy assisted with the experimental measurements and writing of the manuscript. All experimental and analytical work was performed under the active guidance and help of the supervisors as well as the LUT University's staff members.

Additional work during the doctoral study but not included in this dissertation:

- Nieminen, H., Givirovskiy, G., Laari, A., Koiranen, T. (2018). Alcohol promoted methanol synthesis enhanced by adsorption of water and dual catalysts. *Journal of CO_2 Utilization*, 24, pp. 180–189.

Nomenclature

Roman letters

A_{cell}	effective cell area, cm^2
$E_{\text{Ag/AgCl}}$	reference electrode potential, V
E_{RHE}	reversible hydrogen electrode potential, V
E_{s}	specific energy consumption, $\mathrm{kWh/kg}$
E_0	half-reaction potential, V
F	Faraday constant, $\mathrm{C/mol}$
I_{cell}	cell current, A
i	stack current, A
i_{cell}	current density in an electrolytic cell, $\mathrm{A/cm}^2$
i_{o}	exchange current density on the electrode surfaces, $\mathrm{A/cm}^2$
$\dot{m}_{\text{H}_2}$	hydrogen gas mass flow rate, $\mathrm{kg/s}$
$\dot{n}_{\text{H}_2}$	hydrogen gas molar flow rate, $\mathrm{mol/s}$
N_{cell}	number of cells
U	stack voltage, V
U_{act}	activation overvoltage, V
U_{cell}	cell voltage, V
U_{con}	concentration overvoltage, V
U_{ohm}	overvoltage caused by Ohmic losses, V
U_{rev}	reversible open-circuit voltage, V
U_{tn}	thermoneutral voltage, V
z	number of moles of electrons transferred in a reaction

Greek letters

α	charge transfer coefficient
δ_{m}	distance between the electrodes, cm
η_{F}	Faraday efficiency
η_{U}	voltage efficiency
σ_{m}	conductivity of the electrolyte, $\mathrm{S/cm}$

Acronyms

AFOLU	agriculture, forestry, and other land use
CAPEX	capital expense
CCU	carbon capture and utilization
CCS	carbon capture and storage
CDW	cell dry weight
CE	counter electrode
CV	cyclic voltammetry
DAC	direct air capture
DME	dimethyl ether
DS	degree scenario
EDX	energy dispersive X-ray spectroscopy
GHG	greenhouse gas
HER	hydrogen evolution reaction
HBI	hybrid biological–inorganic
HHV	higher heating value
HOB	hydrogen-oxidizing bacteria
ICI	Imperial Chemical Industries
IEA	International Energy Agency
IPCC	Intergovernmental Panel on Climate Change
LCOE	levelized cost of electricity
LSV	linear sweep voltammetry
MP	microbial protein
NF	nickel foam
OER	oxygen evolution reaction
ORR	oxygen reduction reaction
PBS	phosphate buffer solution
PEM	proton exchange membrane
PtG	power-to-gas
PtP	power-to-protein
PV	photovoltaic

ROS	reactive oxygen species
SEM	scanning electron microscope
SCP	single-cell protein
SILAR	successive ionic layer deposition and reaction
SOE	solid oxide electrolysis
SS	stainless steel
TM-Pi	transition metal phosphate
WE	working electrode
XRD	X-ray diffraction

1 Introduction

A steady and reliable supply of food, water, energy, and chemicals, among other things, is essential for the prosperity and daily comfort of our society (Nocera and Nash, 2006; Dresselhaus and Thomas, 2001). To achieve high standards of welfare, humans have been exploiting our planet quite intensively, which has led to a rapid economic growth and a significant population increase reaching 7.9 billion people in 2021 (Worldometer, 2021). The current global economy is, to a great extent, dependent on the consumption of fossil fuel-based energy and raw materials (Fig.1.1). In 2019, the average energy consumption rate was close to 18.5 TW, and it is projected to reach 27 TW and 43 TW in 2050 and 2100, respectively, (Nocera and Nash, 2006). Evidently, the increasing energy consumption coupled with the scale of the human population and the current pace of its growth significantly accelerate the environmental load. Numerous lines of scientific evidence show that the Earth's climate and natural ecosystems are in a state of change because of the anthropogenic impact and the use of carbon-based energy (Mac Dowell et al., 2017; Crist et al., 2017). Such phenomena as the Earth's surface warming, a loss in biodiversity, acidification and change in the salinity of the oceans, melting of icebergs, and the rise of the mean sea level are widely observed and are the subject of serious concerns. It has already become clear that maintaining a similar standard of living endangers the long-term viability of the natural world. This might be considered an ultimate challenge of the 21st century. In order to address this challenge in a sustainable fashion, the development of new large-scale, cost-effective, carbon-neutral technologies based on renewable energy is required.

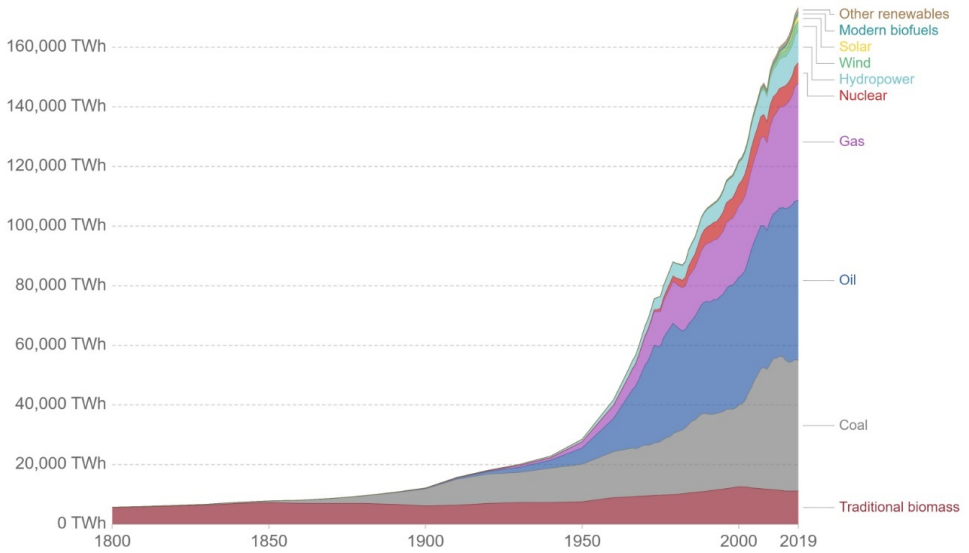

Figure 1.1: Global primary energy consumption by source (Ritchie, 2021).

1.1 Carbon dioxide emissions

The CO_2 and other greenhouse gas emissions have increased dramatically since the preindustrial period, mostly owing to the population growth and economic expansion, and are now higher than ever. The inexorable growth in CO_2 emissions has led to a drastic climatic change, which is likely a dominant cause of the observed global warming causing indubitable impacts on natural and human systems (IPCC, 2014). The lion share of CO_2 emissions originate from the combustion of fossil fuels in the energy, industrial, and transportation sectors; however, a considerable part of emissions is also associated with agriculture, forestry, and other land use (AFOLU) (IPCC, 2019). Despite the growing significance of renewable energy, fossil energy carriers will persist to be dominating for the primary energy supply in the foreseeable future. Based on some forecasts, the proportion of fossil fuel-based energy will likely account for more than 65% of the total energy mix in 2100 (Mac Dowell et al., 2017). Therefore, the likelihood that CO_2 emissions will continue to grow in the upcoming decades is very high.

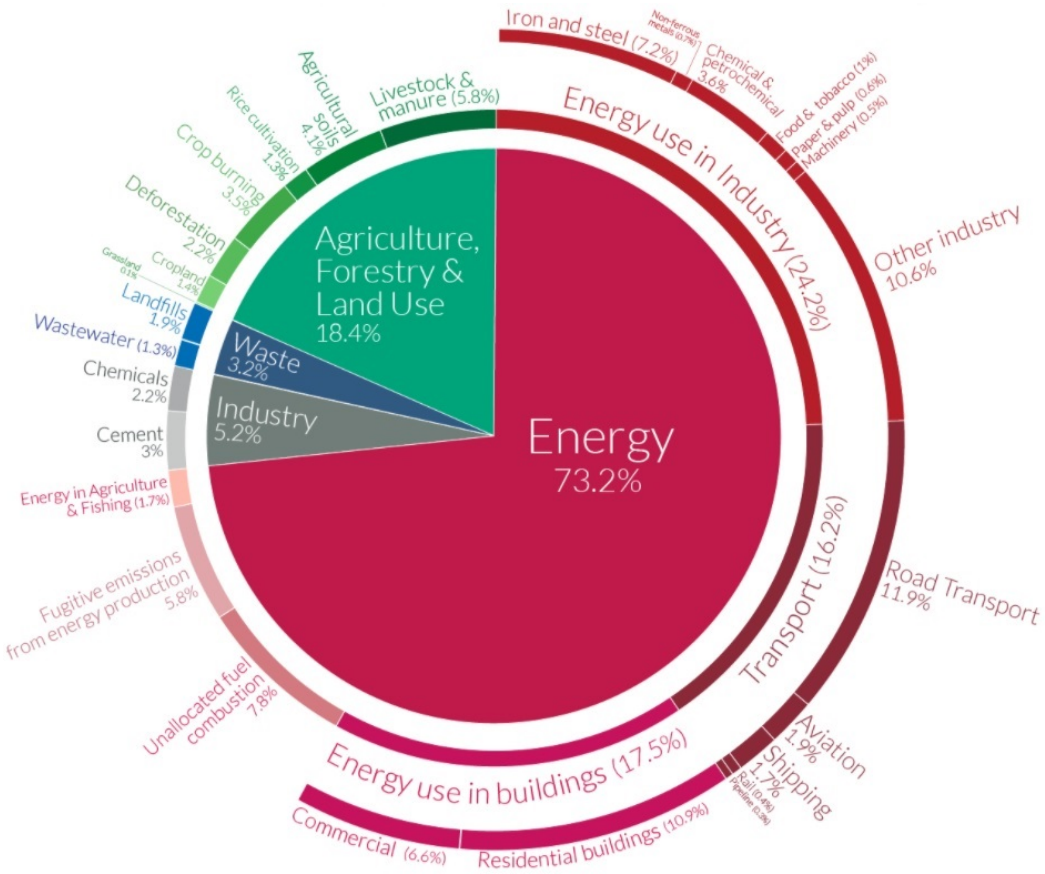

Figure 1.2: Global greenhouse gas emissions by sector in 2016 (Ritchie and Roser, 2021).

Future emissions scenarios are widely discussed by such reputable organizations as the International Energy Agency (IEA) or the Intergovernmental Panel on Climate Change (IPCC) (IEA, 2017; IPCC, 2014). One of such scenarios called the two-degree scenario (2DS) predicts that if anthropogenic emissions of CO_2 could be reduced to approximately 20 Gt per year, the world might await no more than $2\,^{\circ}\mathrm{C}$ of warming above preindustrial levels by 2050. On the contrary, the six-degree scenario (6DS) shows $6\,^{\circ}\mathrm{C}$ global warming by 2050 if CO_2 emissions increase to 60 Gt from the current 40 Gt per year. However, if anthropogenic emissions of CO_2 persist in conjunction with the recent growth trends, the rise in temperature may take place much faster than it has been described in the 6DS (Mac Dowell et al., 2017).

In order to prevent such a development, the Paris Agreement has been signed and entered into force in 2016 as a legally binding international treaty on climate change. In consonance with the Paris Agreement, countries commit to reach global peaking emissions of CO_2 and other greenhouse gases as soon as possible and reduce them thereafter (Haszeldine et al., 2018). By that means it will be possible to limit global warming to well below $2\,^{\circ}\mathrm{C}$, preferably to $1.5\,^{\circ}\mathrm{C}$, compared with preindustrial levels. Among all the proposed measures, carbon capture and storage (CCS) and carbon capture and utilization (CCU) have been strongly recommended as technologies to control global CO_2 emissions (Mac-Dowell et al., 2010; Majumdar and Deutch, 2018).

For the realization of 2DS, it is required to capture and store 120–160 Gt of CO_2 by CCS methods by 2050 (Mac Dowell et al., 2017). From a technological perspective, CCS has already proved its feasibility and is ready for widespread deployment; however, from the perspective of economical feasibility, the implementation is postponed. The financing issues are due to the fact that beyond climate change abatement, the CCS brings about no net profit, which makes it unattractive for potential investors. Furthermore, CCS leakage risks and possible impacts on the environment and human health should be studied in more detail as they might represent a serious concern (Majumdar and Deutch, 2018; Hepburn et al., 2019). Thus, in this context, CCU, as a metamorphosis of CCS, has received widespread attention among academic, industrial, and political stakeholders.

As an alternative for long-term storage of carbon dioxide, CCU offers a pathway to produce a wide range of value-added chemicals using CO_2 as a feedstock (Hepburn et al., 2019). Currently, the major CCU potential is represented by two processes: conversion of CO_2 to urea through a 2-step chemical process and to methanol by catalytic hydrogenation (Pikaar et al., 2018). However, the overall CCU potential in tackling the global CO_2 mitigation challenge is currently quite limited, and thus, new economically and technologically feasible technologies for CO_2 conversion are needed (Mac Dowell et al., 2017).

1.2 Role of water electrolysis and power-to-x technologies

In order to prevent further environmental destruction, a rapid and fundamental shift across all carbon-emitting sectors of the global economy is required. According to some bold estimates (Ram et al., 2019), a transition to a global 100% renewable energy system by 2050 is possible, and electrification is going to play a key role in such a system. Indeed, the cost of renewable energy harvesting has been steadily declining in recent years while several renewable electricity technologies, such as solar photovoltaics (PV) and wind turbines, are already among the most cost-competitive options for power generation. The following numbers for levelized cost of electricity (LCOE), namely the drop of solar LCOE by 89% and onshore wind LCOE by 70% during a ten-year period from 2009 to 2019, confirm that a significant increase in the share of renewables is expected (Roser, 2020).

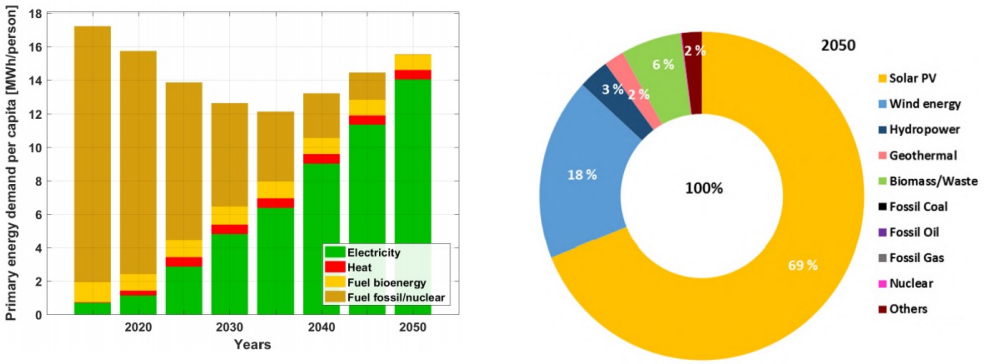

(a) (b)

Figure 1.3: Forecasts published in (Ram et al., 2019) based on LUT's state-of-the-art energy transition modeling simulation for (a) primary energy demand per capita and (b) shares of primary energy supply in 2050.

The shift from conventional electricity production to sustainable models with an increased share of renewables is associated with certain challenges. One of such challenges is connected with the alternating nature of renewable electricity generation and, as a consequence, an urgent need for storage technologies providing flexible demand response (de Vasconcelos and Lavoie, 2019). Some of the potential energy storage technologies include batteries, compressed air storage, pumped hydro, and flywheels, while other options propose chemical storage of renewable energy by power-to-x technologies. The overall principle of power-to-x technologies is based on electrical energy transformation into different carbon-neutral fuels and chemicals using CO_2 as a feedstock (de Vasconcelos and Lavoie, 2019; Daiyan et al., 2020).

A key step in the power-to-x concept is the production of hydrogen by water electrolysis. The water electrolysis process holds the potential to play an essential role in a forthcoming energy model based on electrification (Vidal et al., 2018; de Vasconcelos and Lavoie,

2019). Currently, main water electrolysis technologies include: (i) alkaline water electrolysis, which is the most established technology; (ii) proton exchange membrane (PEM) electrolysis enabling the production of high-purity H_2 and the ability to work under variable power feeding regimes; and (iii) solid oxide electrolysis (SOE) offering the highest energy efficiency among all electrolyzer devices but limited with the long-term stability of the electrolysis cells. Hydrogen produced by water electrolysis has been claimed to be one of the most prospective sustainable fuels for the following reasons: (i) a wide inflammability range both in the air (from 4 to 75 vol.%) and in oxygen (from 4 to 95 vol.%); (ii) the highest energy content per mass unit exceeding that of gasoline (the higher heating value (HHV) of H_2 gas is $39.4\,\mathrm{kW\,h/kg}$); and (iii) as a by-product, only water is formed during combustion of H_2, which has a minimal impact on GHG emissions (Ursúa et al., 2012). A power-to-x concept is always referred to as power-to-gas (PtG) if H_2 gas is the final product (Bailera et al., 2017). Notably, efficient and straightforward conversion of hydrogen back to electricity is also possible by using devices called fuel cells (Scott, 2006). However, because of the difficulties involved in storing and transporting H_2, its use in the manufacture of other value-added compounds is appealing.

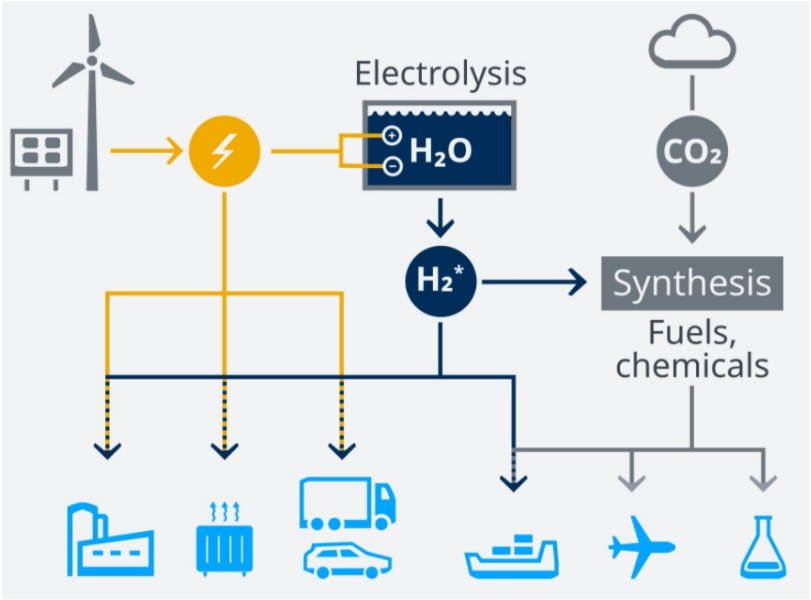

Figure 1.4: Overall idea of carbon-neutral fuels and chemicals production by the power-to-x concept (Gero Rueter, 2019).

If further processing is emphasized, CO_2 is an attractive feedstock for converting H_2 into other energy carriers or industrial products, which is typically the second step in the power-to-x concept. The well-established Fischer-Tropsch infrastructure provides a platform for CO_2 conversion into a variety of chemicals and fuels, such as methane, methanol, formic acid, diesel, DME, gasoline, and jet fuels (Daiyan et al., 2020; de Vasconcelos and Lavoie, 2019). A small-scale SOLETAIR plant demonstrating hydrocarbon production

directly from water, solar energy, and air is one of such successful implementations of the concept (Vidal et al., 2018). Furthermore, already nowadays there are companies such as Audi and Carbon Recycling International, who have successfully demonstrated power-to-x commercial plants. The main research in the field focuses now on the development of robust and efficient catalysts capable of withstanding the harsh conditions of CO_2 hydrogenation and being able to selectively produce target compounds (de Vasconcelos and Lavoie, 2019). Clearly, each of the above-mentioned compounds will find its niche in the future energy system with an increasing reliance on synthetic fuels. Currently, renewable energy utilization is mostly reducing the CO_2 footprint of the electricity sector, whereas decarbonization of the other sectors is going much slower (Daiyan et al., 2020). From this perspective, production of chemicals and fuels by power-to-x is not only a good option for renewable energy storage but also an opportunity to considerably contribute to the decarbonization challenge.

1.3 Food security and power-to-food concept

As can be observed in Fig.1.2, the AFOLU sector is the second largest emitter of CO_2 and other GHG, accounting for roughly 20% of the total GHG emissions (IPCC, 2019). Besides a considerable environmental footprint in terms of greenhouse GHG emissions, conventional agriculture and livestock production cause multiple undesired environmental impacts, such as a loss of biodiversity, eutrophication, salinization of groundwater, and overuse of pesticides (Food and Agriculture Organization of the United Nations (FAO), 2017). It is likely that as a result of the constantly growing population, the environmental pressures will be doubled by 2050 when compared with the 2010 levels (Crist et al., 2017; Poore and Nemecek, 2018). Moreover, according to the latest estimates, nearly half of habitable land is already used by agriculture (Fig.1.5). Increasing temperatures arising from the anthropogenic climate change are, in turn, anticipated to reduce agricultural yields of major crops (Zhao et al., 2017). This leads to a conclusion that conventional agriculture for the production of feed and food is running out of time, and reliable alternative solutions are needed to strengthen the future food security.

It is clear that a net-zero carbon emission society requires net CO_2-free production of food, which is less reliant, for instance, on weather conditions and arable land. One upcoming strategy that might substantially facilitate the dissociation of food production from the established agricultural production routes is the microbial assimilation of carbon. Miscellaneous microbes, such as yeast, algae, fungi, and bacteria have been well known for years for their capability of producing a microbial protein (MP), also known as a single-cell protein (SCP) (Pikaar et al., 2018). Amid diverse microorganisms, autotrophic hydrogen-oxidizing bacteria (HOB) have been recognized as one of the most powerful microbial actuators of the transition in the direction of sustainable food production. The distinctive and tremendously versatile metabolism of HOB allows to utilize the chemical energy embedded in H_2 gas to assimilate CO_2 and to produce new carbonaceous compounds and energy carriers (Yu, 2014). This peculiarity is useful as the efficiency of

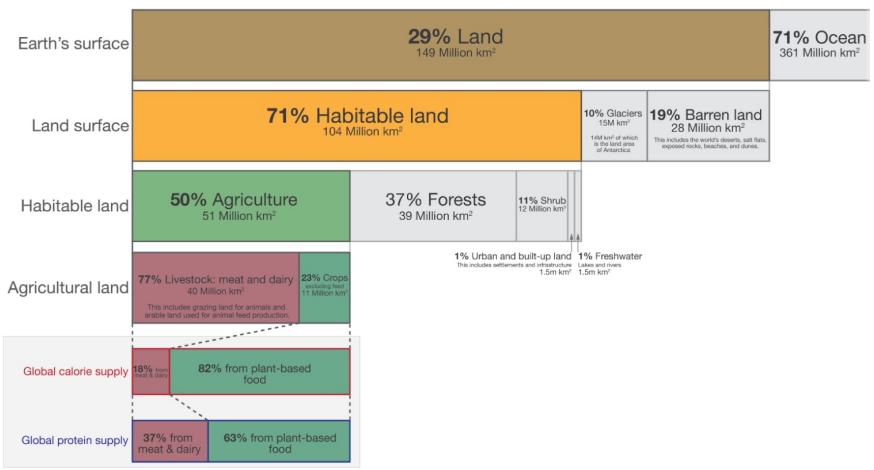

Figure 1.5: Global land use for food production (Ritchie, 2019).

the autotrophic growth of HOB is not obstructed by the use of costly plant-derived carbon sources, such as carbohydrates or sugars, necessary for heterotrophic growth (Nangle et al., 2017). HOB can easily shift between heterotrophic and autotrophic growth modes, using organic compounds or molecular H_2 as energy sources, both alternatively or concomitantly (Matassa et al., 2015). The natural premier product of CO_2 assimilation by HOB is biomass, which has high protein and valuable amino acid contents as well as availability for proteolytic enzymes. Therefore, the biomass synthesized by HOB can be considered a potential protein source and a meat substitute (Volova and Barashkov, 2010).

If both H_2 and O_2 are synthesized from renewable energy through water electrolysis and further used for the microbial assimilation of carbon, then the described biotechnology production platform is typically referred to as power-to-protein (PtP) (Mishra et al., 2020). An appealing characteristic of microbial-based systems is that the protein production can be carried out in fully controlled, automated, and enclosed fermentation bioreactors exhibiting a minimal environmental impact (Sillman et al., 2020). Reactor-based MP production is not reliant on the deployment of organic substrates, such as starch or cellulose, does not require the use of toxic pesticides to control weeds and pests, emits no phosphorus, and needs a minimal amount of freshwater inputs. Besides, the prime nutrient—ammonia, which is commonly produced by the Haber–Bosch method using fossil fuels, is fully utilized in the enclosed system (Pikaar et al., 2017). Taking into consideration that globally a substantial proportion of the arable land is currently reserved for agricultural production of food and feed, the shift to reactor-based protein production has the potential to considerably reduce the environmental pressure. As a result, net positive greenhouse gas emissions from agricultural land use can be significantly reduced, while simultaneously, issues associated with deforestation, biodiversity loss, and land-use change can be addressed.

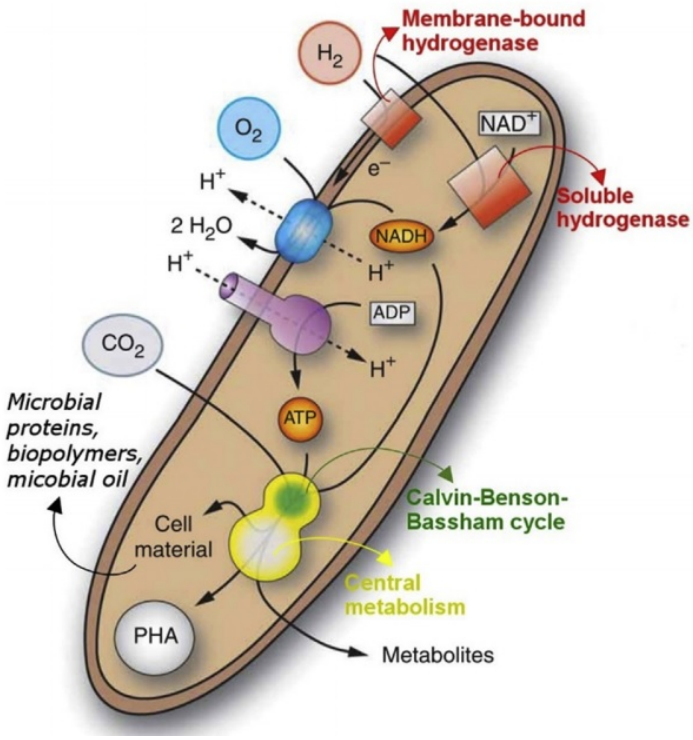

Figure 1.6: Schematic representation of metabolism and bioproduct formation in HOB (Matassa et al., 2015).

1.4 Status of power-to-food technologies

The idea of producing a vital protein for human and animal diet using microbes, anyplace where renewable energy is accessible, is spectacular. The opportunity of producing MP by using HOB attracted the curiosity of researchers already in the 1970s (Repaske and Mayer, 1976). The Soviet government strove to establish large-scale MP manufacture by using n-paraffin produced from oil as the carbon and energy source (Pikaar et al., 2018). However, the Imperial Chemical Industries (ICI) outpaced the USSR and was the first to bring to full-scale production and commercialization a MP product called Pruteen, which was produced from methanol oxidation by means of Methylophilus methylotrphus (Westlake, 1986). Despite the aforementioned significant international efforts, MP never reached the full market potential with most of the initiatives being terminated by the end of the 1980s (Pikaar et al., 2018).

The concept of CO_2 assimilation by HOB has already been successfully vindicated by various scientists on the lab scale. In particular, Matassa et al. (2016) estimated the potential of HOB to upgrade NH_3 and CO_2 under autotrophic conditions into biomass with a protein content of approximately 71%. The researchers were able to reach a maximum volumetric productivity of $0.41\ \mathrm{g}$ of cell dry weight per liter per hour (g CDW/L/h) under

the continuous fermentation process. Molitor et al. (2019) developed a two-stage bioprocess where anaerobic acetogenic bacteria were used to fix CO_2 in the 1st stage followed by growing fungi or yeasts in the 2nd stage under aerobic conditions with acetate as the intermediate metabolite. Molitor et al. (2019) managed to achieve a carbon yield of 25% as yeast biomass with a protein mass fraction of $40–50\,\%$. Hu et al. (2020) evaluated the potential for using N_2 gas as a direct nitrogen source for MP production by HOB and managed to synthesize biomass with a high protein content of up to 68%. The research of Yu et al. (2013) found out the trends exerting influence on the energy efficiency of CO_2 fixation in compliance with the limitation of essential gas substrates required for HOB growth. It was revealed that the efficiency of biomass production is, to a great extent, affected by the CO_2 concentration. The biomass was synthesized with a high energy efficiency of up to 50% with modest O_2 concentrations indicating a possible overall solar-to-biomass conversion efficiency of 5%. Under H_2 limitation, the CO_2 fixation efficiency decreased in the course of time. Evidently, the overall process efficiency of CO_2 fixation by HOB is substantially dependent on the mass transfer characteristics of the main reactant gases (CO_2, H_2, and O_2) to bacterial cells located in the cultivation medium (Yu, 2014). To the best of the authors' knowledge, the highest value of H_2 conversion efficiency of up to 80% in the continuous fermentation process is reported in (Matassa et al., 2016).

In order to achieve industrially relevant productivity of approximately 1–2 g CDW/l/h, considerable technical optimizations are necessary. Two key directions can be emphasized to increase the production rates: (i) the development of microbial culture that can be efficiently cultivated under aerobic conditions with enhanced CO_2 conversion rates and (ii) the development of an advanced bioreactor and process design. It is noteworthy that the scale-up of the MP-based production process requires paying attention to the critical aspects that are related to guarantee the stability of the growing culture, processing of cells to the final product, and assurance of the process safety and a high product quality (Pikaar et al., 2017; Linder, 2019). All the aforementioned requirements have already been successfully attained, and a number of commercial companies producing food and feed from microbial-based biomass operate in the market. Marlow Foods Ltd, UK is one such example producing a vegetarian meat substitute derived from the glucose-fed filamentous fungus strain under the brand name Quorn. Studies of the Marlow Foods product revealed that the Quorn protein quality is identical to high-quality protein sources such as egg and cow's milk while surpassing that of soy and beef (Linder, 2019). Another commercial success story in the field is Unibio Company, which produces methane-based MP called UniProtein in the U-Loop fermentor. The specific configuration of the bioreactor makes it possible to perform an optimal fermentation process with the reported production rate of 4 g CDW/l/h (UniProtein, 2019). The Finnish company Solar Foods makes use of chemoautotrophic HOB and CO_2 as a source of carbon for the production of a high-protein component branded Solein, which is going to be presented in the market in 2021 (Solein, 2019). One more interesting Finnish myco protein product, named PEKILO, was originally developed in the 1970s and provided an important novel domestic source of protein for the feed industry using side streams of the forest industry and microfungus for its synthesis (Pekilo, 2021). Other examples include products obtained from methanol

feedstock, such as KnipBio Meal, Provesta, and Pruteen or methane-based products, such as FeedKind (Linder, 2019).

Even though the industrial feasibility of MP production is already proven, there are still certain challenges that have to be surmounted to establish the emerging route of protein production as a major sector in the feed and food industry. The rate at which the MP production can be scaled up depends, to a great extent, on the public acceptance of the product as a suitable replacement of the conventional agriculture-based protein. Furthermore, considerable efforts must be taken to develop appropriate regulatory incentives and to compete with the existing conventional alternatives. From the perspective of public acceptance, in the nearest future, MP might be more accessible to the animal feed sector rather than as a meat substitute for human nutrition (Pikaar et al., 2017; Linder, 2019). A key direction that can be pointed out to enable the faster transition of MP to a human consumption market is creation of a product with the desired meat-like texture, enjoyable taste, appropriate nutritional value, and food safety. Without doubt, another dominant factor that will influence the transition rate is the MP cost to consumers, which is currently for example for the Quorn protein higher than for the agricultural-based protein. In order to increase the rate at which the global production of MP can be scaled up, the development of effective pricing of environmental pollution caused by agricultural production and alteration of the policy paradigm from the encouragement of the output-oriented agricultural production to sustainable and resource-efficient MP production may be required (Molitor et al., 2019; Pikaar et al., 2017; Linder, 2019).

1.5 Carbon dioxide fixation with hybrid biological–inorganic systems

As it has been mentioned before, the main constraint hindering the overall process efficiency of CO_2 fixation by HOB is the low solubility of the main reactant gases (CO_2, H_2, and O_2). In order to address this constraint, a scalable electricity-driven CO_2 fixation process in hybrid biological–inorganic (HBI) systems has been elaborated by Torella et al. (2015). Generally, HBI systems couple biocompatible catalysts for in situ H_2 production and specific microorganisms that use the obtained reducing equivalent as a source of energy for CO_2 fixation. Microbial CO_2 reduction in the context of HBI systems can be classified into two main categories: Type I, where electrons are directly transferred to immobilized acetogenic bacteria, and Type II, in which electrons are indirectly transferred to organisms through electrochemical H_2 evolution from water splitting followed by microbial H_2 oxidation that is coupled to CO_2 reduction (Nangle et al., 2017).

Coupling of in situ water electrolysis and CO_2 fixation by HOB in the HBI process could potentially overcome many of the challenges inherent to the traditional gas fermentation relying on the external input of the reactants. Apart from a better gas transfer to the liquid medium, the HBI process does not suffer from selectivity problems between organic compounds over a narrow thermodynamic range, it does not experience difficulties in performing multielectron reductions for C–C bond formation, and its efficiency is not dras-

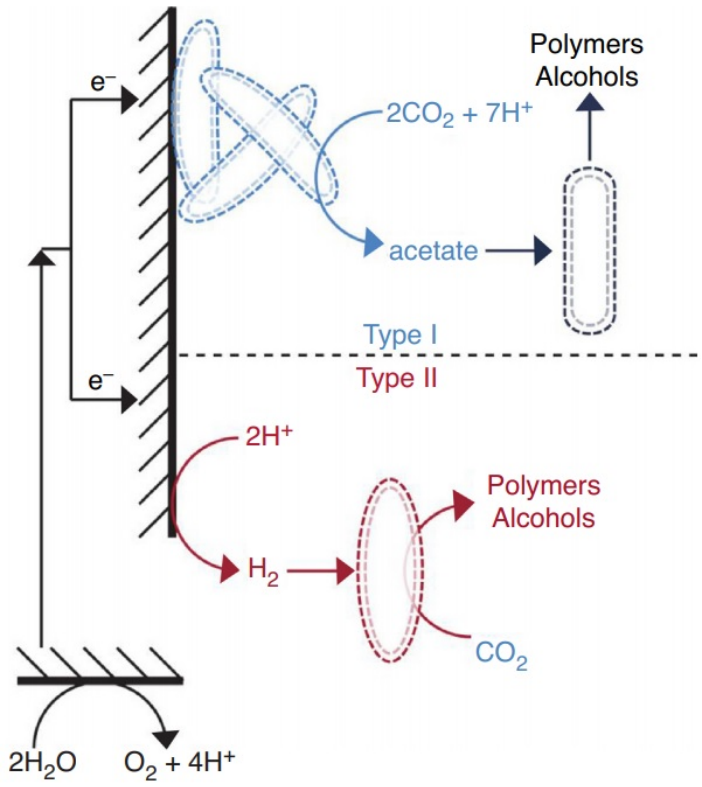

Figure 1.7: Schematic representation of the two main types of HBI systems with direct and indirect mechanisms of electron transfer (Nangle et al., 2017).

tically reduced when using air instead of a concentrated CO_2 source (Nangle et al., 2017; Liu et al., 2016). Furthermore, the HBI process is supposedly superior to gas fermentation as it allows to avoid the use of a separate electrolyzer unit and thus decreases the CAPEX. At the same time, the use of an in situ water electrolyzer does not raise safety concerns as explosive H_2 and O_2 mixture are utilized almost straight away during the bacterial growth.

The HBI process has been initially examined on a laboratory scale by Torella et al. (2015). Their research group reported the development of an integrated bioelectrochemical system in which earth-abundant biocompatible catalysts were applied for water splitting while simultaneously HOB were used to fix CO_2 into biomass and isopropanol with notable yields of 17.8% and 3.9% of the thermodynamic maximum over $24\,\mathrm{h}$, respectively. In later studies, Liu et al. (2016) were able to upgrade the HBI process and reached a CO_2 reduction efficiency of around 50% when producing biomass. It is noteworthy that the CO_2 reduction efficiency declined only by a factor of 2.7 and reached 20% when substituting pure CO_2 by air. Nevertheless, the use of concentrated CO_2 is likely to play a significant role in the overall HBI process efficiency as a smaller flow-rate is required, which leads, for instance, to a smaller effect on the temperature balance in the bioreactor than in a case

when air is used as the CO_2 source. Other chemicals, such as polyhydroxybutyrate (PHB) and isopropanol, were produced with the 24-hour maximum efficiencies of 42% and 39%, respectively. Finally, the calculated solar-to-chemical efficiencies were 9.7% for biomass, 7.6% for bioplastic, and 7.1% for fusel alcohols.

Following the HBI process proof-of-concept, the scientific focus has switched to the goals of increased energy efficiency, process robustness, product selectivity, and attempts to scale up (Nangle et al., 2017). Practical implementation and scaling up of the HBI technology is, to a considerable extent, contingent on the successful resolution of the challenges identified in the initial phase. In this respect, the main research directions include, but are not limited to, the following items: development of stable microbial cultures or microbiomes allowing fast CO_2 conversion rates under aerobic conditions, integration of innovative material structures, and successful implementation of advances in bioreactor and process designs.

1.6 Outline of the doctoral dissertation

In order to make the production of MP using systems with integrated water electrolysis a competitive technology, certain challenges should be overcome. First of all, the energy efficiency of in situ water electrolysis in neutral pH should be properly studied to provide a basis for future investigation. Thus, the dissertation aims to offer innovations and insight into the energy efficiency of in situ H_2 production, which is extensively studied and improved by the application of earth-abundant electrocatalysts. For the moment, the production of MP using in situ water electrolysis has been proven on a laboratory scale, and the research in the field has mostly concentrated on single electrocatalytic cells. Multiple cell stack structures required for upscaling of the process have not been reported yet. Hence, this doctoral dissertation aims to develop and study the performance of novel in situ water electrolyzer stacks for neutral pH. The final objective of the study is to develop and demonstrate an upscaled electrobioreactor system based on CO_2 capture and in situ water electrolysis for the production of MP.

The main highlights of the five original papers are discussed in the five following paragraphs.

Publication I reports the initial results of in situ electrolysis performed in a pH-neutral medium for HOB cultivation. Various combinations of traditional electrodes along with electrodes coated with earth-abundant nickel–iron and cobalt were tested to measure the water splitting performance. A water electrolysis model was developed and implemented to characterize the current-voltage relations of the HBI system prototype. Furthermore, HOB cultivation using in situ water electrolysis was performed in a small-scale electrobioreactor in order to support the experimental results. The developed model and the data gathered were used as an initial insight for the further development and improvement of in situ water electrolysis devices presented in the following publications.

Publication II presents a simplified stack structure for in situ water electrolysis in HBI systems, which is intended to boost up hydrogen production in comparison with reactor tank-immersed electrodes. The energy efficiency and hydrogen production rate of the prototype were experimentally examined in a pH-neutral medium for HOB cultivation. The investigation established that with a water electrolysis energy efficiency (HHV) of 50%, the current density can be up to a range of $5\,\mathrm{mA/cm^2}$ if special coatings are applied to electrodes. The results of the scientific article were supplemented with HOB cultivation experiments. The experimental work highlights the improvements required for the further development of in situ water electrolyzer stacks.

Publication III concentrates on performance evaluation studies of amorphous transition-metal phosphate (TM-Pi) electrocatalysts, which have recently attracted ample attention because of their exceptional electrocatalytic properties. In this scientific article, the oxygen evolution reaction (OER) performance of a series of amorphous first-row TM-Pi catalysts, in particular Co – Pi, NiFe – Pi, and Fe – Pi, prepared with various deposition strategies onto different substrates, was comparatively examined in a neutral phosphate buffer solution (PBS). Furthermore, a simplified cell model was applied to analyze the current–voltage characteristics and quantitatively evaluate and compare the reversible, ohmic, and activation overvoltage components of the studied TM-Pi. The investigation revealed that TM-Pi catalysts deposited onto a highly ordered nickel foam (NF) substrate can compete with commercial precious Pt and IrO_2 electrocatalysts in respect of OER activity and long-term stability.

Publication IV introduces the Neo-Carbon Food concept that is the first in the world pilot-scale HBI process suitable for the production of microbial biomass. The concept includes integrated hydrogen production by water electrolysis. For that purpose, a second version of the in situ water electrolyzer stack was developed. Moreover, direct air capture (DAC) of carbon dioxide and its subsequent assimilation by autotrophic HOB were presented. The specific energy consumption of in situ water electrolysis and direct air capture of CO_2 were reported. The hydrogen production with in situ electrolysis achieved a specific energy consumption just below $100\,\mathrm{kWh/kg_{H_2}}$, which indicated a gap for further improvement. The specific energy consumption of DAC was around $20\,\mathrm{kWh/kg_{CO_2}}$. The study revealed the importance of an accurate sterilization procedure, which was not carefully designed and performed during the operation of the pilot, and as a consequence, led to the contamination of the final product.

Publication V reports an in situ water electrolyzer stack design as part of an electro-bioreactor system required for the pilot-scale operation of the HBI process. The former trials revealed issues that were taken into consideration in the proposed design. The electrolyzer was designed with the help of fluid dynamics simulation tools in order to model the electrolyte flow and to avoid stagnated flows. The design takes into account the problem of leakage currents, identified in earlier versions, which was addressed by applying an electrically insulating coating. Different electrode surface modification methods, for

example coating with electrocatalysts and etching, were applied for additional improvement of the performance and energy efficiency of the electrolyzer prototype. Neutral phosphate buffer solution (PBS) was again used to examine the performance of the electrolyzer stack. In comparison with the previous experimental work, the performance of the in situ water electrolyzer was substantially enhanced. The designed in situ water electrolyzer demonstrated a high Faraday efficiency of about 90% and a reasonable specific energy consumption below $90\,\mathrm{kWh/kg_{H_2}}$.

The motivation for the research topic and its practical importance are addressed briefly in Chapter 1. Chapter 2 elucidates the fundamentals of in situ water electrolysis. Chapter 3 focuses on electrode materials and electrocatalytic coatings used to enhance the sluggish kinetics of oxygen evolution reaction (OER) in pH-neutral conditions. Chapter 4 provides an insight into the development of in situ water lectrolyzer stacks for an electrobioreactor system. Chapter 5 gives an overview of the developed Neo-Carbon Food pilot process suitable for the production of MP from CO_2 and renewable H_2. The chapter is complemented with HOB cultivation results in a small-scale electrobioreactor with in situ water electrolysis. Chapter 6 summarizes the research topic discussed in the doctoral dissertation and provides suggestions for future work.

1.7 Scientific contributions

The scientific contributions of the publications comprising this doctoral dissertation are summarized as follows:

- Performance of different conventional electrode materials is analyzed for in situ water electrolysis with the aid of a simplified mathematical model.
- Different transition metal coatings are tested as potential substitutes for noble metals, and their water splitting performance is evaluated in the pH-neutral conditions.
- A series of in situ water electrolyzer stacks are developed using modern fluid dynamics tools, and their energy efficiency is analyzed. An improvement in performance is achieved by the application of insulating and electrocatalytic coatings.
- A microbial process based on the in situ water electrolysis and CO_2 assimilation by HOB is demonstrated on a laboratory scale.
- A Neo-Carbon Food pilot plant, suitable for the production of MP from electricity, water, air, and nutrients, is constructed and demonstrated.

2 In situ water electrolysis characteristics

2.1 Water electrolysis reactions in neutral pH

The water electrolysis process has provided the scientific basis for a range of energy storage and conversion devices, with electrolyzers (Zeng and Zhang, 2010; Marini et al., 2012), fuel cells (Carrette et al., 2001), and metal-air batteries (Li and Lu, 2017) being the most efficient and well-researched ones. Bioelectrochemical systems (BES) (Kumar et al., 2017) and hybrid biological-inorganic (HBI) systems (Nangle et al., 2017) introduce a burgeoning research field and are promising illustrations of coupling water electrolysis and biological fixation of CO_2 into multicarbon organic compounds. Notwithstanding that the module design of the aforementioned systems differs, their common feature is that they are all two-electrode systems involving the hydrogen evolution reaction (HER) at the cathode and the oxygen evolution reaction (OER) at the anode (Nian-Tzu et al., 2017).

The water electrolysis in neutral pH conditions is defined by the electrochemical reactions represented below (Cheng and Ping, 2015). Half-cell potentials are given in the convention of reduction potentials. Subsequently in the dissertation, the modular values of the given potentials will be used for clarity in the descriptions.

The oxidation half-reaction at the anode–oxygen evolution reaction (OER):

$$2\,H_2O \longrightarrow O_2 + 4\,H^+ + 4\,e^-, E_0 = 0.817\,V \tag{2.1}$$

The reduction half-reaction at the cathode–hydrogen evolution reaction (HER):

$$4\,H_2O + 4\,e^- \longrightarrow 2\,H_2 + 4\,OH^-, E_0 = -0.413\,V \tag{2.2}$$

The overall reaction in the electrolytic cell:

$$2\,H_2O + \text{electrical energy} \longrightarrow O_2 + 2\,H_2, E_0 = -1.23\,V \tag{2.3}$$

2.2 Overvoltages

A complex pathway involving the extraction of four electrons and four protons is used in the OER to form molecular oxygen. On the contrary, the HER is based on a two-electron transfer reaction mechanism and, hence, requires a considerably smaller amount of energy (overpotential) to overcome the kinetics of the reaction (Nian-Tzu et al., 2017; Tahir et al., 2017). The OER is highly pH-dependent. In alkaline conditions, four OH^- are oxidized into two molecules of H_2O and one O_2 molecule, while in acidic and neutral conditions, two H_2O molecules are oxidized to be transformed into four H^+ and one O_2 molecule (Tahir et al., 2017). The high stability of water makes electrochemical water splitting difficult, requiring $237\,kJ/mol$ of the Gibbs free energy change for the entire reaction (Cheng and Ping, 2015). According to thermodynamics, the equilibrium or reversible cell

voltage, which is the lowest potential necessary for electrolysis to occur at $25\,^{\circ}\mathrm{C}$ and 1 atm, corresponds to $1.23\,\mathrm{V}$. In practice, however, commercial water electrolyzers usually operate in the region of 1.8–2.1 V, signifying that electrolysis of water proceeds far from its equilibrium potential (Ursúa et al., 2012). Considerable energy losses resulting from the high overpotentials required to perform water dissociation at adequately fast rates are mainly the consequence of the sluggish OER kinetics (Nian-Tzu et al., 2017; Tahir et al., 2017; Irshad and Munichandraiah, 2015). De facto, to initiate the water splitting process, higher voltages exceeding $1.23\,\mathrm{V}$ are required, which leads to a considerable energy loss. The additional overvoltages are described in the following equation (Ursúa et al., 2012):

$$U_{\text{cell}} = U_{\text{rev}} + U_{\text{ohm}} + U_{\text{act}} + U_{\text{con}}, \tag{2.4}$$

where U_{cell} is the cell voltage, U_{rev} is the reversible open circuit voltage, U_{ohm} is the overvoltage caused by ohmic losses in the cell elements, U_{act} is the activation overvoltage caused by electrode kinetics, and U_{con} is the concentration overvoltage caused by mass transport processes (usually, U_{con} is substantially lower than U_{ohm} and U_{act}, and it can thus be neglected).

2.3 Energy efficiency characteristics

There are several important parameters characterizing the electrochemical water splitting. Cell voltages are typically well above the thermoneutral voltage $1.48\,\mathrm{V}$, at which H_2 and O_2 are produced with 100% thermal efficiency. Voltage efficiency can be defined by the stack voltage and the thermoneutral voltage:

$$\eta_{\mathrm{U}} = \frac{U_{\mathrm{tn}}\, N_{\text{cell}}}{U}, \tag{2.5}$$

where U_{tn} is the thermoneutral voltage, N_{cell} is the number of cells in series, and U is the stack voltage.

The hydrogen production rate $(\mathrm{mol/s})$ of an electrolyzer stack is linearly proportional to the stack current:

$$\dot{n}_{\mathrm{H_2}} = \eta_{\mathrm{F}} N_{\text{cell}}\, \frac{i}{z\, F}, \tag{2.6}$$

where z is the number of moles of electrons transferred in the reaction (for hydrogen, z = 2), F is the Faraday constant ($9.6485 \times 10^4\,\mathrm{C/mol}$), i is the stack current (A), and η_{F} is the Faraday efficiency, also known as the current efficiency, and N_{cell} is the number of electrolytic cells in series.

The specific energy consumption E_{s} of an electrolysis process can be obtained based on the stack voltage, current, and hydrogen production rate:

$$E_\mathrm{s} = \frac{\int_0^T i(t)\,u(t)\,\mathrm{d}t}{\int_0^T \dot{m}_{\mathrm{H_2}}\,\mathrm{d}t}, \tag{2.7}$$

where T is the time interval under study. The higher heating value (HHV) is the minimum energy required to produce hydrogen gas with a thermoneutral process. The per mass unit HHV of hydrogen gas is $39.4\,\mathrm{kW\,h/kg}$, which can be assumed to represent the energy consumption of the process with a 100% energy efficiency.

The energy efficiency of a water electrolysis process can be calculated from

$$\eta_\mathrm{e} = \frac{\mathrm{HHV}_{\mathrm{H_2}}}{E_\mathrm{s}}. \tag{2.8}$$

2.4 Reaction mechanism of OER in neutral pH

Extensive description of kinetic equations under diverse reaction conditions can be found for instance in (Bockris, 1956), while the mechanistic schemes are covered in (Nian-Tzu et al., 2017). Generally, the OER mechanism in alkaline and neutral conditions can be characterized by the following equations (Irshad and Munichandraiah, 2015):

$$\mathrm{S} + \mathrm{OH^-} \rightleftharpoons \mathrm{S{-}OH} + \mathrm{e^-} \tag{2.9}$$

$$\mathrm{S{-}OH} + \mathrm{OH^-} \rightleftharpoons \mathrm{S{-}O} + \mathrm{H_2O} + \mathrm{e^-} \tag{2.10}$$

$$2\,\mathrm{S{-}O} \rightleftharpoons 2\,\mathrm{S} + \mathrm{O_2} \tag{2.11}$$

where S represents active sites on the catalyst, and S–OH and S–O stand for adsorbed intermediates.

If the Tafel slope is near to 120 mV/dec, the reaction described by Equation (2.9) depicts a rate-determining step. However, if the Tafel slope is close to 60 mV/dec, the rate-determining step differs. The reaction described by Equation (2.9) is separated into the following steps described by Equation (2.12) and Equation (2.13). The reaction described by Equation (2.13) is then considered the rate-determining step for Tafel slope close to 60 mV/dec.

$$\mathrm{S} + \mathrm{OH^-} \rightleftharpoons \mathrm{S{-}OH^*} + \mathrm{e^-} \tag{2.12}$$

$$\mathrm{S{-}OH^*} \longrightarrow \mathrm{S{-}OH} \tag{2.13}$$

where S–OH* and S–OH stand for adsorbed intermediates with the same chemical structure, but different energy states.

2.5 Electrocatalysts for in situ water electrolysis

Electrocatalysts with a high OER efficiency are required to decrease the energy barrier and increase the overall efficiency of the water electrolysis. Presently, benchmark electrocatalysts made from noble iridium (Ir) and ruthenium (Ru) and particularly oxides of the aforementioned metals show a superior performance toward OER. An inherent drawback of these electrocatalysts is unsuitability for large-scale H_2 production because of their exorbitant price and scarcity. Moreover, in both alkaline and acidic conditions, RuO_2 and IrO_2 encounter stability problems at high anodic potentials as a consequence of their oxidation into IrO_3 and RuO_4, respectively, and subsequent dissolution in the electrolyte (Nian-Tzu et al., 2017). For that reason, substantial efforts have been dedicated to developing stable, efficient, cheap, and earth-abundant catalysts able to operate at different pHs at low overpotentials as alternatives to precious metal electrocatalysts (Nian-Tzu et al., 2017; Tahir et al., 2017).

Various transition metal (TM) oxides (Liu et al., 2018; Zaffran and Toroker, 2017; Huang et al., 2018), hydroxides (Morales-guio et al., 2016), sulfides (Long et al., 2015; Ma et al., 2017), nitrides (Wang et al., 2016; Xu et al., 2015), borides (Chen et al., 2019; Masa et al., 2016), carbides (Liao et al., 2014; Lin et al., 2016), selenides (Tang et al., 2015), and phosphides (Tian et al., 2014; Wang et al., 2016; Huang et al., 2017; Zhang et al., 2017a,b) have been broadly studied as effective electrocatalysts for the water dissociation process. Among others, transition metal phosphates (TM-Pi) have attracted ubiquitous scientific attention when Matthew W. Kanan and Daniel G. Nocera developed a cobalt phosphate (Co – Pi) catalyst in 2008 (Kanan and Nocera, 2008). In the succeeding studies, a host of other TM-Pi catalysts have been explored, and their electrocatalytic activity toward OER and HER has been proven. As an example, Fig. 2.1 represents the surface morphology of the NiFe-Pi electrocatalyst prepared for **Publication III** of this doctoral dissertation.

An inherent peculiarity of all TM-Pi catalysts is the doping of phosphate groups into a crystal lattice of transition metals, such as Ir (Irshad and Munichandraiah, 2015; Wang et al., 2019), Fe (Babar et al., 2018; Zhong et al., 2017), Co (Kanan and Nocera, 2008; Wang et al., 2019), Ni (Zhang et al., 2018; Xing et al., 2016; Liang et al., 2018; Li and Zhao, 2016), and Mn (Jin et al., 2014) by various techniques including for instance hydrothermal synthesis, electrodeposition, and precipitation. Phosphate groups facilitate the oxidation of metal atoms during the proton-coupled electron transfer process and distort the native atomic geometry favoring adsorption and oxidation of water molecules (Guo et al., 2018). By virtue of this unique feature, several reported TM-Pi catalysts, such as Ir – Pi (Irshad and Munichandraiah, 2015) and IrCo – Pi (Wang et al., 2019), show an excellent performance surpassing that of the benchmark IrO_2. Nevertheless, although the content of Ir in IrCo – Pi is lowered by 50%, there is still a substantial capacity for opti-

mization, particularly in decreasing the use of expensive Ir.

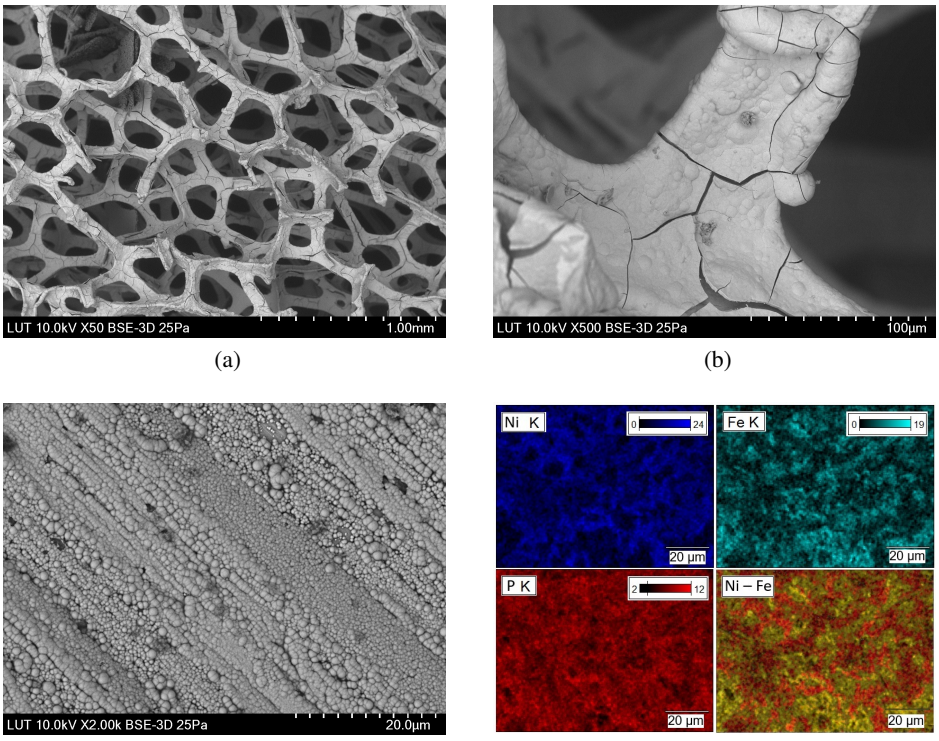

Figure 2.1: Example of the surface morphology of the NiFe-Pi electrocatalyst prepared for **Publication III** of this doctoral dissertation. (a-c) NiFe-Pi on NF at different magnifications and (d) the corresponding EDS elemental mappings.

2.6 Constraints of in situ water electrolysis

The side reactions of reactive oxygen species (ROS) formation at the cathode, in particular hydroxyl radicals or hydrogen peroxide (H_2O_2), was pointed out as a conspicuous constraint of the HBI processes. It was found that the formation of ROS is thermodynamically more favorable than the formation of H_2 at and below the potentials of HER. The high toxicity of ROS to HOB cells was mentioned as one of the key aspects hindering biological growth and affecting the energy efficiency of the HBI process. Great efforts have been devoted to tackle this problem and to develop and apply electrocatalysts selective for H_2 production instead of ROS production (Nangle et al., 2017). One of the successful examples is the study of Liu et al. (2016), who managed to achieve a substantial increase in performance compared with the previous research of Torella et al. (2015) when using

cobalt-phosphorous (Co-P) as a HER catalyst for the HBI synthesis of biomass and alcohols. As it has been mentioned before, the sluggish kinetics of the OER in neutral pH represents another serious constraint for HBI processes. To overcome this issue, Kanan and Nocera (2008) developed a cobalt–phosphate (Co–Pi) catalyst, which was successfully used as a coating for the anode to drive HOB cultivation and to improve the OER performance in the experimental work of (Torella et al., 2015; Liu et al., 2016).

3 Electrode materials for in situ water electrolysis

As it has been stated before, owing to the deprotonated molecules available for OER and HER, water electrolysis is kinetically challenging in pH-neutral conditions and more favorable in basic and acidic conditions (Cheng and Ping, 2015). Nevertheless, pH-neutral conditions are much less corrosive to electrochemical devices and are critical for fast-developing biological processes involving integrated water electrolysis. For alkaline water electrolyzers, the impacts of different OER catalysts have been widely documented in the literature, but there have been few investigations of electrolyzer cell performance in pH-neutral bioreactors. Thus, one of the major tasks of this research was to evaluate the performance of different electrode materials in a specific pH-neutral electrolyte. This chapter is a brief summary of the research performed in **Publication I** and **III**.

3.1 Materials and methods

3.1.1 Experimental setup

All electrochemical experiments for **Publication I** and **III** were performed in the experimental setup depicted in Fig. 3.1. The setup represents a three-electrode electrolyzer cell, which is controlled by a WaveNow potentiostat. The electrolyte is continuously circulated with the aid of a constant flow pump while a constant temperature is maintained by a Lauda thermostat. A more detailed description of the device is presented in the aforementioned publications.

3.1.2 Electrolytes

For **Publication I**, a mineral medium, the composition of which was slightly modified form the original recipe (DSMZ GmbH, 2011) and is given in Table 3.1, was used as an electrolyte for the tests. According to measurements, the pH of the medium is 7, and the conductivity is $12\,\mathrm{mS/cm}$.

For **Publication III**, a phosphate buffer solution (PBS), which was prepared by mixing 0.1 M KH_2PO_4 and 0.1 M K_2HPO_4, was selected as the electrolyte for the water electrolysis tests. The PBS has a pH of 7 and a conductivity of $22.5\,\mathrm{mS/cm}$.

3.1.3 Conventional electrodes

In **Publication I**, various electrode material combinations, such as SS, Ni, graphite, Pt, and IrO_2, were examined. The following grounds were used to justify the selection of these materials. Because of its low cost and good corrosion resistance in most environments, SS is a frequently used material. Ni-based metals are often employed in alkaline

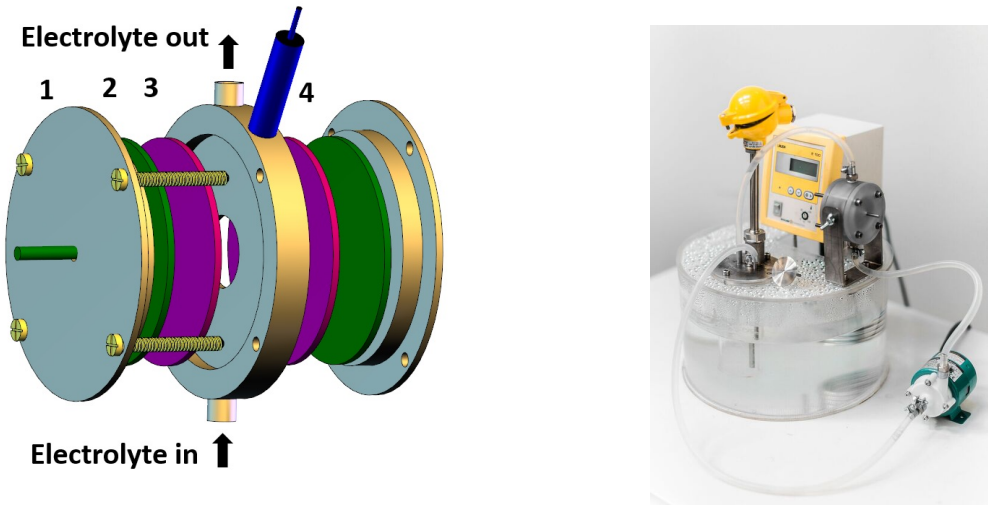

(a) (b)

Figure 3.1: For the electrolysis experiments, an experimental setup was employed. (a) Electrolyzer cell 3D model and (b) photograph of the test setup.

Table 3.1: Composition of the cultivation medium

Compound	Amount
KH_2PO_4	2.3 g/l
Na_2HPO_4*$2H_2O$	2.9 g/l
Na_2SO_4	5.45 g/l
$(NH_4)_2SO_4$	1.19 g/l
$MgSO_4$*$7H_2O$	0.5 g/l
$CaSO_4$*$2H_2O$	11.7 mg/l
$MnSO_4$*H_2O	4.4 mg/l
$NaVO_3$	5 mg/l
$NaHCO_3$	0.5 mg/l
$C_6H_8FeNO_7$	5 mg/l
$ZnSO_4$*$7H_2O$	0.5 mg/l
H_3BO_3	1.5 mg/l
$CoCl_2$*$6H_2O$	1 mg/l
$CuCl_2$*$2H_2O$	0.05 mg/l
$NiCl_2$*$6H_2O$	0.1 mg/l
Na_2MoO_4*$2H_2O$	0.15 mg/l

water electrolyzers, and thus, Ni is used as a benchmark for the other materials (Schalenbach et al., 2018). In (Nevin et al., 2010), graphite was employed as an electrode for the first bioelectrochemical cultivation experiments of an acetogenic microbe. The catalytic activity of noble metals and their oxides, such as Pt and IrO_2, is well recognized.

3.1.4 Electrocatalysts

The performance of the electrodeposited Co and a Fe – Ni alloy was initially evaluated in **Publication I** in order to get an impression of whether these transition metals can compete with the noble electrocatalysts. Subsequently, in **Publication III**, a series of first-row transition metal phosphates (TM-Pi), in particular Co – Pi, Fe – Pi, and NiFe – Pi, were prepared and tested. The Co – Pi catalyst of the TM-Pi family was chosen as a benchmark catalyst because it was specifically designed to conduct water splitting in artificial photosynthesis systems at neutral pH under ambient conditions (Kanan and Nocera, 2008). Owing to its abundance and low cost, Fe – Pi was chosen as a candidate for analysis as it can be produced using a simple successive ionic layer deposition and reaction (SILAR) technique (Babar et al., 2018; Zhong et al., 2017). According to a literature review, Ni – Fe catalysts represent a promising substitute to precious metal catalysts. It should be noted that Ni – Fe catalysts are substantially more active toward OER than pure Fe or Ni (Xing et al., 2016; Li and Zhao, 2016). Hence, bimetallic NiFe – Pi (Xing et al., 2016) was chosen to measure the synergistic impact of iron in NiFe-based structures. The procedure of the electrocatalyst preparation is described in more detail in **Publication I** and **III**.

3.1.5 Material characterization

The surface morphologies and compositional distribution of the elements of the synthesized catalysts were analyzed using a Hitachi S-3400N scanning electron microscope (SEM) equipped with energy dispersive X-ray spectroscopy (EDX) measurement. A Bruker D8 Advance X-ray diffractometer was used for the X-ray diffraction (XRD) analysis of the crystal structure of the TM-Pi catalysts.

3.1.6 Electrochemical measurements

In the two-electrode and three-electrode configurations of the system, all electrochemical measurements were performed with a WaveNow Potentiostat purchased from Pine Research Instrumentation, USA. In **Publication I**, various combinations of electrode materials were tested as working electrodes (WE) and counter electrodes (CE). In **Publication III**, as-deposited onto graphite or NF TM-Pi catalysts were utilized as the WE, Pt was used as the CE, and Ag/AgCl,Cl^-(3M) was employed as the reference electrode (RE). Linear sweep voltammetry (LSV) with a scan rate of $5\,\mathrm{mV/s}$ was used to produce polarization curves. The chronopotentiometry mode was used to conduct 36 h durability testing. The following equation was used to calibrate all of the potentials measured in **Publication III** to a reversible hydrogen electrode (RHE):

$$E_{\mathrm{RHE}} = E_{\mathrm{Ag/AgCl}} + 0.1976\,\mathrm{V} + 0.059pH \tag{3.1}$$

3.1.7 Cell model

In order to have an instrument for the evaluation of different electrode and electrocatalyst performance, a cell model was proposed. The simplified cell model in the equation below enables quantitative assessment and comparison of reversible, ohmic, and activation overvoltages of various electrode configurations:

$$U_{\text{cell}} = U_{\text{rev}} + \frac{\delta_{\text{m}} i_{\text{cell}}}{\sigma_{\text{m}}} + \alpha \left(\frac{i_{\text{cell}}}{2 i_0} \right), \tag{3.2}$$

where δ_{m} is the distance between the electrodes (cm), i_{cell} is the current density (A/cm^2), σ_{m} is the conductivity of the electrolyte (S/cm), α is the charge transfer coefficient, and i_{o} is the exchange current density on the electrode surfaces. U_{rev}, σ_{m}, α, and i_0 are the parameters to be fitted by the experimental data.

3.2 Results and discussion

3.2.1 Verification of the simplified cell model

To verify the cell model described in Section 3.1.7, variable distance experiments were performed using SS for both the anode and the cathode. Because the only condition that changes is the distance between the electrodes, and resistive conduction losses are defined by the electrolyte conductivity, all of the model parameters were intended to match in every case. The distance of $3\,\text{mm}$ was selected as the minimum while the maximum distance applied was $16\,\text{mm}$. The parameters U_{rev}, σ_{m}, α, and i_0 in Eq. (3.2) for variable distance experiments were determined using experimental voltage and current data and the method of nonlinear least square regression, and presented in Table 3.2. Based on the results presented in the table, it can be concluded that the model was verified successfully.

Table 3.2: Parameters of the simplified cell model (Eq. (3.2)) in experiments with a variable distance and SS electrodes presented in **Publication I**

δ_{m} (mm)	U_{rev} (V)	σ_{m} (S/cm)	α (-)	i_0 (A/cm)
3	1.905	0.012	0.393	0.0010
6	2.058	0.012	0.425	0.0021
9	2.132	0.012	0.530	0.0036
16	1.92	0.012	0.278	0.0007

It was found that in neutral pH the distance between the electrodes has a considerable influence on voltage because of the substantial ohmic losses produced by the poor conductivity of the electrolyte (Fig.3.2a). In a case where the electrolysis voltage efficiency is intended to be more than 50%, considering the thermoneutral voltage of $1.48\,\text{V}$, the current density should be more than $10\,\text{mA}/\text{cm}^2$ at a distance between the electrodes of $3\,\text{mm}$. The allowed current density would be even lower at larger distances between the

electrodes. Notably, commercial alkaline electrolyzers operate at current densities of up to $500\,\mathrm{mA/cm^2}$ at similar voltage values (Decourt et al., 2014) that can be explained due to the significantly higher conductivity of the alkaline electrolyte. Therefore, in order to achieve a high efficiency and a compact structure of in situ water electrolysis applications, the space between the electrodes should be as low as possible.

3.2.2 Comparison of conventional anode materials

After the initial tests, the distance between the electrodes was set to $3\,\mathrm{mm}$ for all further experiments. In Fig. 3.2b, the cell voltages of various anode materials are shown as a function of current density. Based on the obtained data, it is clear that the anode material has a considerable influence on the cell voltage, in particular at higher current densities. With the highest cell voltage, graphite obviously exhibits the lowest performance, whereas Ni and Pt anodes show voltages that are very close to each other. Of the materials investigated in **Publication I**, the IrO_2 anode is clearly the most attractive material exhibiting a current density of $15\,\mathrm{mA/cm^2}$ at the 50% voltage efficiency.

Table 3.3: Parameters of the simplified cell model (Eq. (3.2)) in experiments with various anode materials published in **Publication I**

Anode	U_{rev} (V)	σ_{m} (S/cm)	α (-)	i_0 (A/cm)
C	2	0.012	0.455	0.0010
Ni	2	0.012	0.338	0.0007
Pt	1.975	0.012	0.332	0.0007
IrO_2	1.766	0.012	0.351	0.0013

In **Publication I** and **III**, the reversible voltage, ohmic voltage, and activation voltage terms as a function of current density were analyzed and plotted for all the studied cases. In this dissertation, an example of this analysis is presented later for the experiments with different TM-Pi/NF in Figs. 3.7b–d published in **Publication III**. Table 3.3 provides the model parameters for the case being discussed here, in which it can be seen that the reversible and activation voltages are both significantly affected by the material choice. In comparison with the other materials, IrO_2 shows a somewhat lower reversible voltage. The activation overpotential of the graphite anode is the highest, whereas the activation overpotentials of the other materials are in the same range. The low-conductivity electrolyte medium is clearly the primary source of resistive voltage loss, and thus, the anode material selection has a minor effect on it.

3.2.3 Initial tests with coatings

Fig. 3.2c and Table 3.4 show the current-voltage relations and fitted model parameters for the initial tests with coatings, respectively. From Fig. 3.2c it can be noticed that coated

electrodes could be regarded as an appealing substitute for precious metal catalysts. Co and Ni-Fe alloy electrodeposition allows modification of the substrate surface structure by increasing the electrochemically active surface area. The produced highly ordered CoPi coatings outperformed the Pt anode, whereas the performance of the Ni-Fe film was close to that of the IrO_2 anode. When deploying SS coated with the Ni-Fe, a current density of about $14\,\mathrm{mA/cm^2}$ was reached with a voltage efficiency of 50%. At this stage of the experimental work, it was first found that the electrochemical performance of the electrode was influenced by the substrate material selection. The CoPi coating on the graphite substrate performed somewhat worse than the identical coating electrodeposited on SS substrates.

Table 3.4: Parameters of the simplified cell model (Eq. (3.2)) in the initial experiments with coatings published in **Publication I**

Anode	U_{rev} (V)	σ_{m} (S/cm)	α (-)	i_0 (A/cm)
C(CoPi-sol.1)	1.790	0.012	0.443	0.0014
SS(CoPi-sol.1)	1.630	0.012	0.359	0.0006
SS(CoPi-sol.2)	1.695	0.012	0.370	0.0009
SS(NiFe)	1.449	0.012	0.338	0.0004

3.2.4 Noble anodes and cathodes

Eventually, to determine whether the performance could be enhanced further, the most promising anode materials were employed as the cathode material in **Publication I**. Similarly to the material presented before, Fig. 3.2d and Table 3.5 summarize the results of this experiment. Current densities of 25, 15, and $10\,\mathrm{mA/cm^2}$ were reached at the 50% voltage efficiency, and correspondingly when IrO_2, Pt, and SS were used for both the anode and the cathode. Despite the fact that IrO_2 performs best as an anode and cathode material, the SS performance is still satisfactory when taking into account the high production cost of precious metal catalysts. Furthermore, SS might be regarded as a promising low-cost substrate material for coating deposition. It may be inferred that the cathode material has a considerable impact on the water electrolysis performance in pH=7 conditions. The reversible voltage is substantially lower with Pt- and IrO_2 cathodes than with SS cathodes. Furthermore, compared with Pt, the IrO_2 cathode has a smaller activation overpotential.

Table 3.5: Parameters of the simplified cell model (Eq. (3.2)) in experiments with the best-performing electrode materials published in **Publication I**

An./Cath.	U_{rev} (V)	σ_{m} (S/cm)	α (-)	i_0 (A/cm)
Pt-Pt	1.4	0.012	0.255	0.0002
IrO_2-IrO_2	1.366	0.012	0.227	0.0004

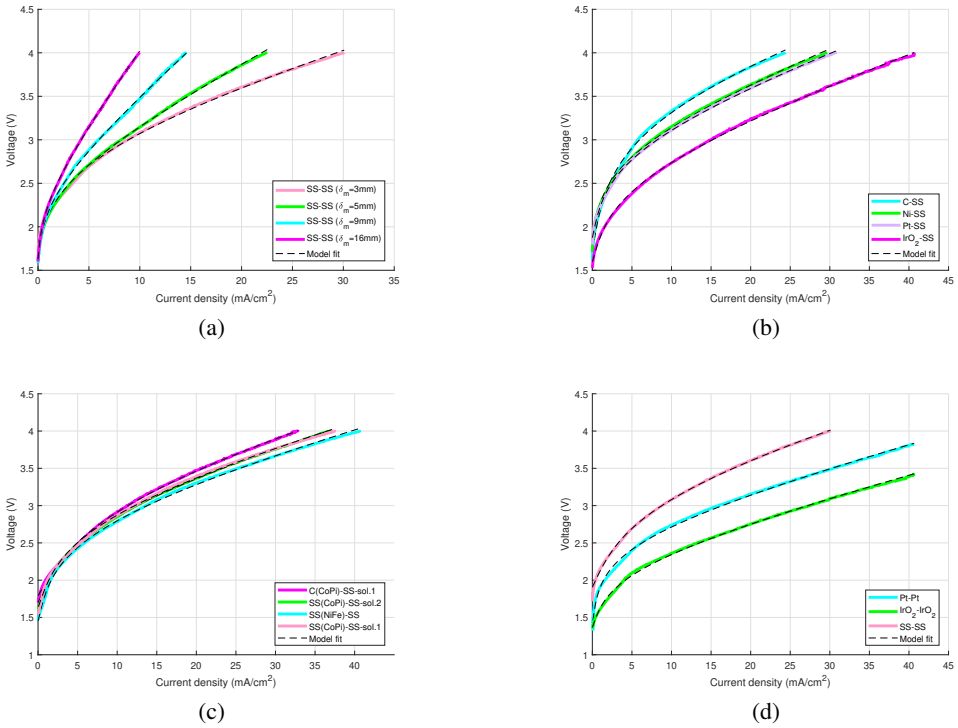

Figure 3.2: Experimentally determined cell voltages as a function of current density, published in **Publication I**: (a) in the variable distance experiments with SS electrodes, (b) in the experiments with various anode materials, (c) in the initial tests with Co- and NiFe-based coatings, and (d) in the experiments with best-performing combinations of the electrode materials.

3.2.5 Synthesis of TM-Pi electrocatalysts

The detailed procedure for the electrocatalyst synthesis is presented in **Publication III**. As it can be seen from Fig. 3.3, the central region of the NF was uniformly coated with a black coating after deposition of NiFe – Pi and Co – Pi, whereas the coating changed color to silver when depositing NiFe – Pi onto graphite. After the SILAR deposition of Fe – Pi, the substrates tested in **Publication III** were coated with flocculent precipitate (Zhong et al., 2017) that could be seen with the naked eye all over the surface.

The XRD analysis revealed the amorphous nature of all the synthesized TM-Pi electrocatalysts. Results of SEM analysis, published in **Publication III**, are presented in Fig. 4.11 and Fig. 2.1. In all cases, the SEM analysis indicated that the NF surface was fully and evenly coated with TM-Pi electrocatalysts. As an example, the elemental mapping of Ni, Fe, and P compounds and their homogeneous distribution onto the surface of the NF substrate is shown in Fig. 2.1d. This observation held true also for the other TM-Pi cat-

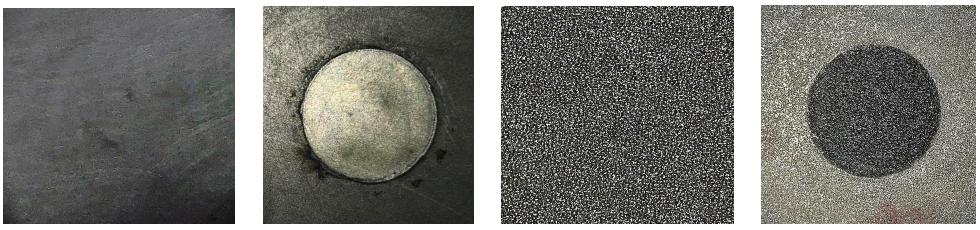

(a) (b) (c) (d)

Figure 3.3: Electrode images: (a) graphite, (b) NiFe-Pi deposited onto graphite, (c) NF, and (d) Co-Pi deposited onto NF.

alysts. Based on the high magnification images, all the TM-Pi catalysts exhibit distinct surface structures. For example, the Fe-Pi coating shows a highly rippled flake structure with many agglomerates, which is in good agreement with the previous research (Babar et al., 2018; Zhong et al., 2017). The Co-Pi coating is created with plenty of 3D-porous micrometre-sized particles on top of the film (Kanan and Nocera, 2008). The hierarchical NiFe-Pi mainly consists of nanobubbles (Xing et al., 2016). The cracks observed in all of the TM-Pi catalysts are most likely the consequence of water loss during sample drying in ambient air. The occurrence of the desired Ni, Fe, Co, and P was confirmed by EDXA, as evidenced by the matching peaks in the EDXA diagrams.

3.2.6 Performance of TM-Pi electrocatalysts

During the experimental work, NiFe-Pi catalyst was deposited onto the graphite substrate using a varying Ni/Fe composition. According to the findings, the electrodes containing 25 wt.% Ni and 75 wt.% Fe had the lowest electrochemical activity and the largest overpotential. The OER performance of the electrodes containing 50 wt.% Ni and 50 wt.% Fe was moderately better than in the case with 75 wt.% Ni and 25 wt.% Fe. Hence, at this stage, a 50/50 wt.% composition was selected as optimal for future experiments in **Publication III**.

One of the goals of the research was to further study how the substrate material affects the TM-Pi performance. Figs. 3.5a and b show the electrolysis tests results of all the studied TM-Pi electrocatalysts deposited onto graphite and NF, respectively. The electrocatalytic properties were compared with the benchmark Pt and IrO_2 also used in **Publication I** of this doctoral dissertation. Once again it was shown that, while the catalyst composition is the most critical factor in determining OER activity, the type of the substrate on which the catalyst is placed also has a considerable effect. According to the obtained results, Pt and IrO_2 overtook TM-Pi deposited onto graphite. After $1.5\,\mathrm{V}$, the current at noble Pt and IrO_2 began to climb sharply reaching $1\,\mathrm{mA/cm^2}$ at overpotentials of $450\,\mathrm{mV}$ and $430\,\mathrm{mV}$, respectively. In the case of Co−Pi deposited onto graphite, after $1.5\,\mathrm{V}$, the current rise was less abrupt, reaching $1\,\mathrm{mA/cm^2}$ at a considerably higher overpotential of

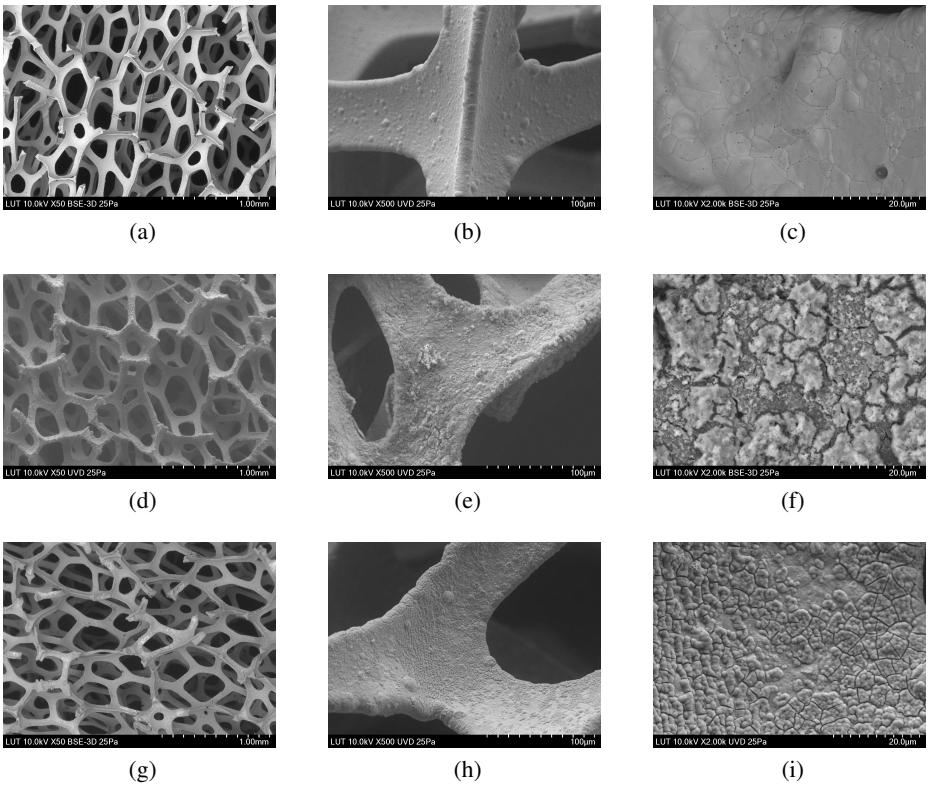

Figure 3.4: SEM images of (a–c) NF, (d–f) Fe-Pi deposited onto NF, and (g–i) Co-Pi deposited onto NF, published in **Publication III**.

$510\,\mathrm{mV}$. The Fe – Pi and NiFe – Pi catalysts deposited onto graphite were approximately similar in performance, having the onset potential at $1.6\,\mathrm{V}$ and reaching current densities of $0.6\,\mathrm{mA/cm^2}$ and $0.88\,\mathrm{mA/cm^2}$ at $1.8\,\mathrm{V}$, respectively.

As it can be seen in Figs. 3.5b, when TM-Pi catalysts were deposited onto NF, the electrocatalytic activity was considerably increased and the onset overpotentials were comparable with the benchmark Pt and IrO_2. The Co-Pi/NF outperformed the noble electrodes during the whole water splitting process, achieving $1\,\mathrm{mA/cm^2}$ at the $420\,\mathrm{mV}$ overpotential. The remarkable Co-Pi OER performance is due to its large active surface area (Fig. 4.11 g–i) as well as its high intrinsic catalytic activity. The NiFe-Pi/NF and Fe-Pi/NF exhibited comparable OER activities reaching $1\,\mathrm{mA/cm^2}$ at $495\,\mathrm{mV}$, and $534\,\mathrm{mV}$ overpotentials, respectively. However, at 1.7 V, the activity of NiFe-Pi started to rise steeply and $4.45\,\mathrm{mA/cm^2}$ was reached at 1.8 V, which was higher than the corresponding current densities shown by Pt and IrO_2. At potentials higher than 1.7 V, the Fe-Pi/NF performance was comparable with the bare NF.

In the subsequent experiments published in **Publication III**, TM-Pi/NF catalysts were

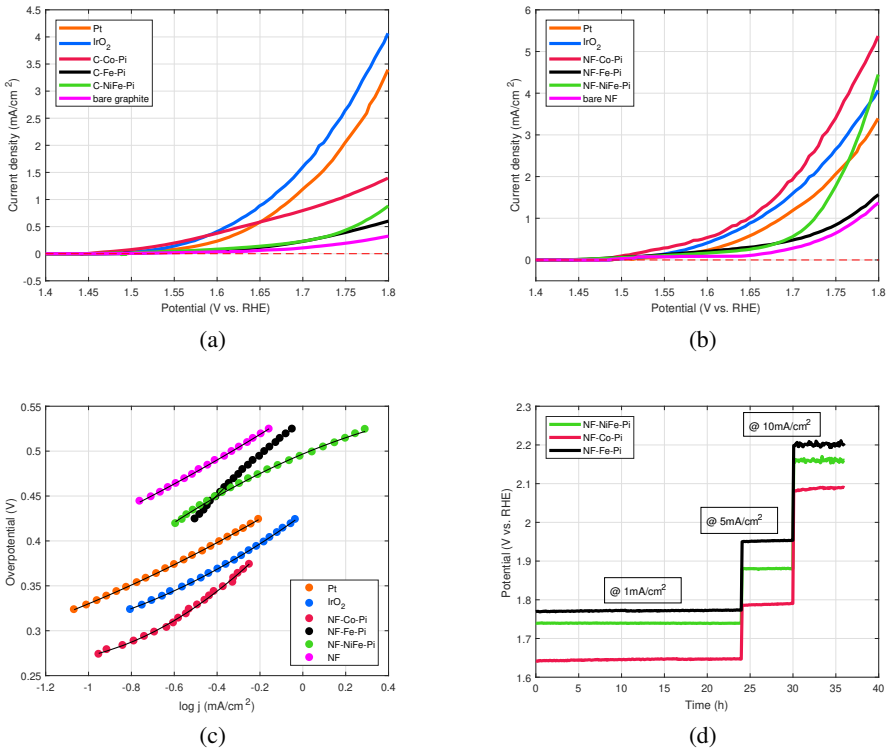

Figure 3.5: Electrocatalytic properties of: (a) different TM-Pi deposited onto graphite versus noble catalysts, (b) different TM-Pi deposited onto NF versus noble catalysts, (c) corresponding Tafel plots, and (d) 36-hour durability tests, published in **Publication III**.

selected for further analysis because of their superior OER activity. For evaluating OER kinetics, the Tafel slope is a crucial representative parameter. The data in Fig. 3.5c were used to calculate the TM-Pi/NF Tafel slopes. It was found that the Tafel slopes of IrO_2 and Co-Pi were virtually identical at 60 mV/dec, which corresponds to a chemical rate-determining step with fast OER kinetics. Other examined catalysts had Tafel slopes near to or above 120 mV/dec, which corresponds to a slow OER (Reier et al., 2012).

In practical applications, stability is a critical criterion for evaluating catalyst performance. In **Publication III** of this doctoral thesis, TM-Pi/NF stability was analyzed for 36 h at 1, 5, and $10\,\mathrm{mA/cm^2}$ (Fig. 3.5d). The SEM images of TM-Pi/NF electrocatalysts after the test are shown in Fig. 3.6, from which it can be seen that the catalyst layer is partly peeled off from the NF. Despite peeling off, the catalysts maintained a steady potential and activity during the water electrolysis, which suggests that a sufficient TM-Pi layer stays on the NF surface. The slight rise in the overpotential over time can be explained by the development of bubbles on the electrode surfaces and partial detachment of TM-Pi catalysts.

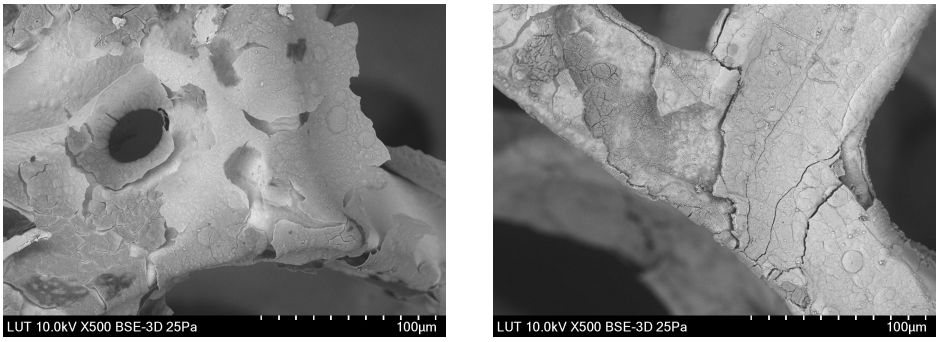

(a) (b)

Figure 3.6: Example of the SEM analysis of the TM-Pi electrocatalysts after the 36 h durability tests, published in **Publication III**.

In **Publication III**, a simplified cell model was once again used to describe the cell voltage components of the TM-Pi/NF electrocatalysts in a two-electrode configuration, and the test results are shown in Fig. 3.7 and Table 3.6. Co-Pi/NF exhibited the lowest U_{rev} (Table 3.6) and outperformed NiFe-Pi/NF and Fe-Pi/NF. All of the tested TM-Pi catalysts had a comparable ohmic overpotential (σ_{m}), which is mostly generated by the voltage drop across the PBS electrolyte. Table 3.7 summarizes the reversible voltage, ohmic, and activation overvoltages for different TM-Pi/NF at $10\,\text{mA}/\text{cm}^2$.

Table 3.6: Parameters of the simplified cell model in experiments with various TM-Pi catalysts, published in **Publication III**

Anode material	U_{rev} (V)	σ_{m} (S/cm)	α (-)	i_0 (A/cm^2)
NF-NiFe-Pi	1.5799	0.0220	0.1801	0.0001
NF-Co-Pi	1.5166	0.0223	0.1708	0.0001
NF-Fe-Pi	1.5627	0.0222	0.2180	0.0001

Table 3.7: Overvoltage analysis results for various TM-Pi/NF at $10\,\text{mA}/\text{m}^2$, published in **Publication III**

Anode material	U_{rev} (V)	U_{ohm} (V)	U_{act} (V)	U_{cell} (V)
NF-NiFe-Pi	1.5799	0.2500	0.8294	2.6593
NF-Co-Pi	1.5166	0.2466	0.7866	2.5498
NF-Fe-Pi	1.5627	0.2477	1.0039	2.8143

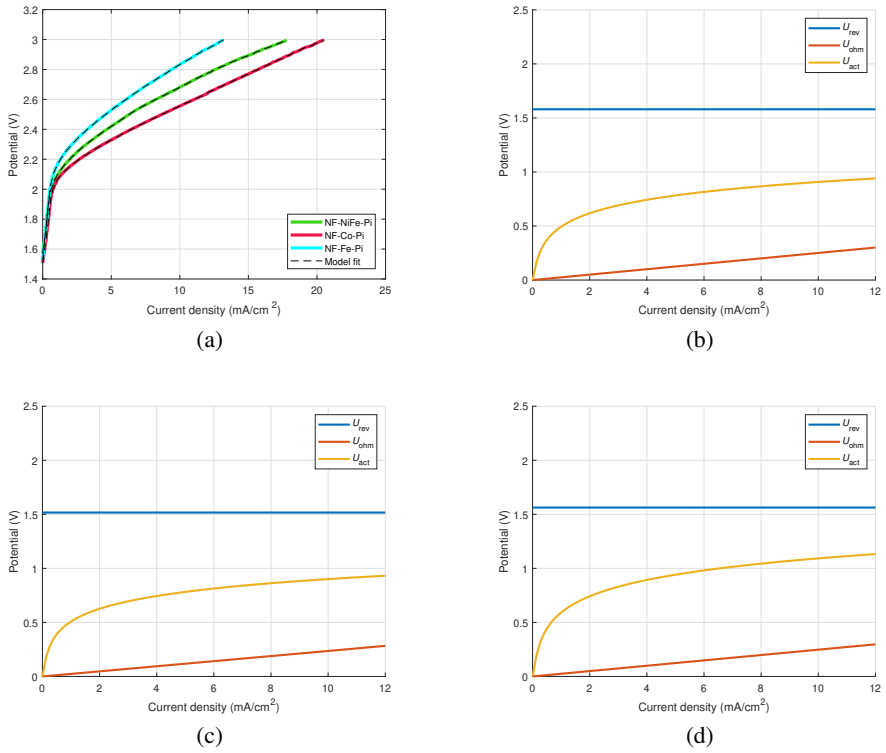

Figure 3.7: (a) Experimentally determined cell voltages as a function of current density of different TM-Pi/NF and the corresponding overvoltages analysis of (b) NiFe-Pi/NF, (c) Co-Pi/NF, and (d) Fe-Pi/NF, published in **Publication III**.

4 Development of in situ water electrolyzer stacks

The upscaling of an HBI system is closely associated with the development of a robust, efficient, and ergonomic reactor design with the in-situ electrolysis of the cultivation medium (Krieg et al., 2014). Stackable reactor structures, which are extensively employed in industrial electrolysis and dialysis applications, are a feasible technical alternative for this purpose, because they can achieve the desired capacities simply by increasing the number of stacked units. Moreover, using a stacked reactor for in situ electrolysis has a number of advantages, including improved power output and current generation, mitigation of ohmic losses and edge effects, homogeneous current distribution over the reaction volume, and ease of characterization of the overall performance by analyzing individual cell performance. Many of the existing problems associated with HBI systems, such as the low conductivity of the cultivation medium, increased ohmic losses, current density limitations imposed by microorganisms, and the need for a design with an acceptable electrode surface-to-volume ratio, could presumably be mitigated by this technology. Furthermore, employing electrode surface coatings that also address biocompatibility concerns might result in a significant boost in performance (Liu et al., 2016). This chapter presents a brief summary of the research dedicated to the development of the in situ water electrolyzer stacks published in **Publications II, IV**, and **V**.

4.1 Materials and methods

4.1.1 In situ water electrolyzer stack v1

An initial design of the in situ water electrolyzer stack was published in **Publication II**, where its scheme (Figure 4.1) can be found. The stack is made up of bipolar SS(316L) electrodes, which are connected in series (10 cells with a $10\,\mathrm{mm}$ distance in between), tubular PVC spacers, and SS endplates serving as current collectors and pressure plates. Each circular electrode has an effective electrode area of $86.6\,\mathrm{cm}^2$ and a diameter of $10.5\,\mathrm{cm}$. The current is supplied to the connection bolt welded to the end plates, whereas the insulated tightening rods are assembled via the corner holes to compress the stack structure. In order to make a parallel electrolyte flow through the electrolyzer, $6\,\mathrm{mm}$ PVC tubes were used. The mineral medium described in **Publication I** was used as an electrolyte for the tests. Keithley 2701 Data acquisition system was applied to measure the cell voltages.

4.1.2 In situ water electrolyzer stack v2

For the research published in **Publication IV**, an in situ water electrolyzer stack shown in Fig. 4.2 was developed. In this prototype, a zig-zag flow of the electrolyte (described in **Publication I**) through slit orifices in electrode plates was performed. OpenFOAM was used to model the optimal location of the slit orifices to provide a uniform flow distribution between the electrodes. Modest turbulence of the electrolyte was set as a design goal to

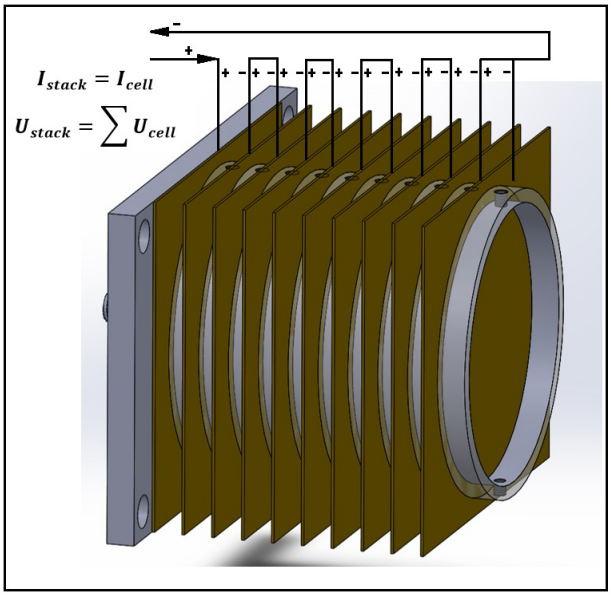

Figure 4.1: First version of the in situ water electrolyzer stack published in **Publication II**.

prevent the attachment of the biomass to the electrode surfaces and provide the local mixing enhancing mass transfer of the gases to HOB. There were 10 series-connected cells with an active electrode area of $380\,\mathrm{cm}^2$ and a distance minimized to $2.8\,\mathrm{mm}$ between them. Special electrical connections were installed on the electrode plates to monitor the individual cell voltage during experimental work. The distance between the electrodes was set with the aid of machined spacer rings made of polyacetal (POM) plastic functioning also as electrical insulation and providing the preload of the stack assembly. Planar elastomer seal rings kept the electrodes sealed. AISI 316L SS endplates served as pressure plates while eight M8 bolts were used to compress the stack. Sorensen DLM (40V/15A) and Aim-TTi QPX1200SP (60V/50A) laboratory power sources were used to supply the stack current in series and parallel modes, respectively, while Keithley 2701 was used for cell voltage measurements.

4.1.3 In situ water electrolyzer stack v3

Based on the results of the test runs with previous prototypes published in **Publications II** and **IV**, an improved electrolyzer stack was developed and presented in **Publication V**. The electrolyzer device, depicted in Fig. 4.3, is made up of a stack of electrode plates separated by spacers that function as flow guides. Similar to previous prototypes, the pressure load is carried by the SS endplates and the stack is compressed with M8 bolts. Duplex stainless steel 1.4462 was selected as the material for the stack to adress the corrosion problems revealed in previous prototypes. The zig-zag flow arrangement was changed back to the parallel flow arrangement and electrical insulation provided by a $100\,\mu\mathrm{m}$

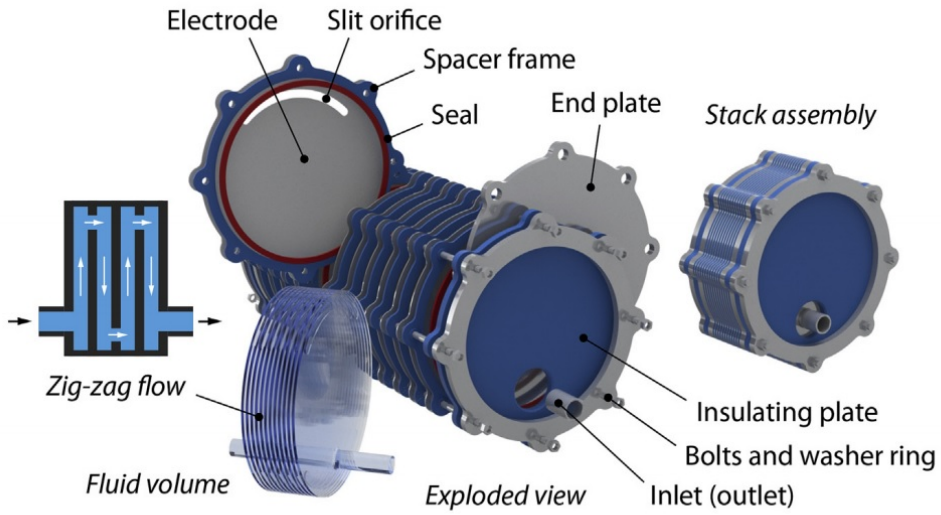

Figure 4.2: Second version of the in situ water electrolyzer stack published in **Publication IV**.

Teflon coating was used to decrease leakage currents that reduce the Faraday efficiency of the electrolyzer stack. Only the active areas, indicated by orange in Fig. 4.3, were left uncoated with Teflon, but afterward, TM-Pi electrocatalysts were deposited on it. The distance between the electrode plates was further reduced to 2 mm in order to improve the electrochemical process efficiency by reducing ohmic losses. A GAMRY reference 3000 potentiostat and a Reference 30k Booster were used to supply and measure the electrolyzer stack current. The measurements were verified using a Hioki PW6001 power analyzer and a Hioki CT6862-05 current probe. A more detailed description of the design features of all the studied electrolyzers is provided in **Publications II, IV**, and **V**.

4.2 Results and discussion

4.2.1 Initial results of electrolyzer energy efficiency

On the basis of the gathered current-voltage relationships (Fig. 4.4), the key parameters of the first version of the electrolyzer stack efficiency were determined. Table 4.1 summarizes the values of the aforementioned parameters. Based on the collected data points for the electrolyzer with a $10\,\mathrm{mm}$ distance between the electrodes and using the model presented in Eq. (3.2), the electrolyzer stack efficiency was recalculated for the $3\,\mathrm{mm}$ distance. The computed hydrogen production rate and power as a function of stack current density, as well as the SEC for the electrolyzer stack with a $3\,\mathrm{mm}$ spacing between the electrodes, are shown in Fig. 4.4.

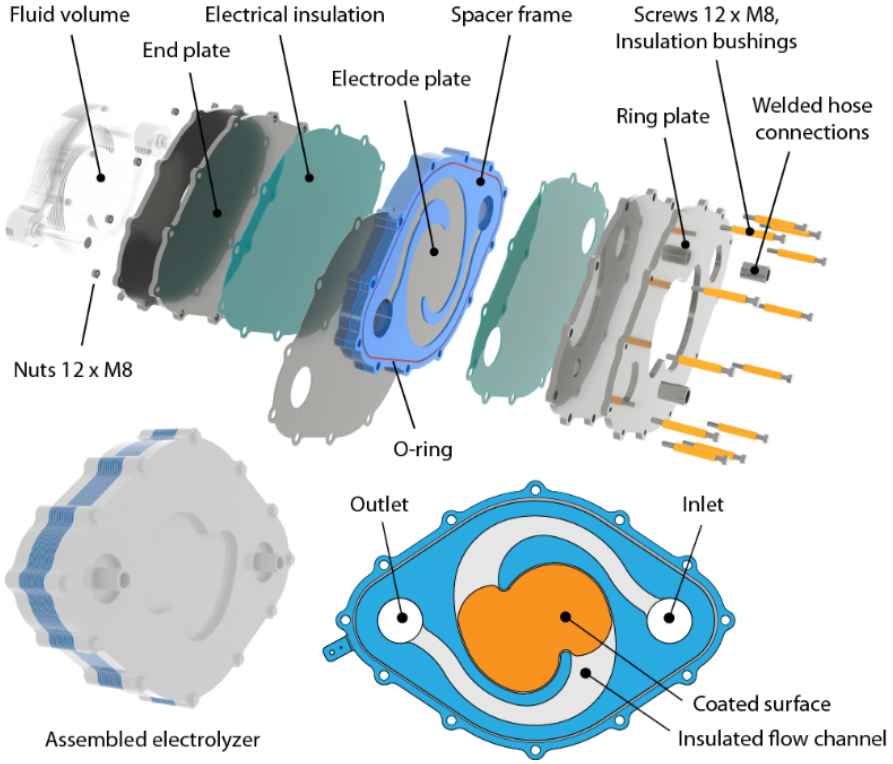

Figure 4.3: Third version of the in situ water electrolyzer stack published in **Publication V**.

Table 4.1: Energy efficiency parameters of the first electrolyzer stack prototype published in **Publication II**.

U_{stack} [V]	I_{stack} [A]	f_{H_2} [N l/h]	E_{s} [kW h/(N m^3)]	$\eta_{\text{E,HHV}}$ [%]
30	0.20	0.82	7.18	49.33
31	0.26	1.07	7.42	47.74
32	0.30	1.25	7.65	46.25
33	0.34	1.42	7.89	44.85
34	0.39	1.64	8.13	43.53
35	0.46	1.92	8.37	42.29
36	0.53	2.23	8.61	41.11
37	0.62	2.57	8.85	40.00
38	0.70	2.94	9.09	38.95
39	0.81	3.37	9.33	37.95

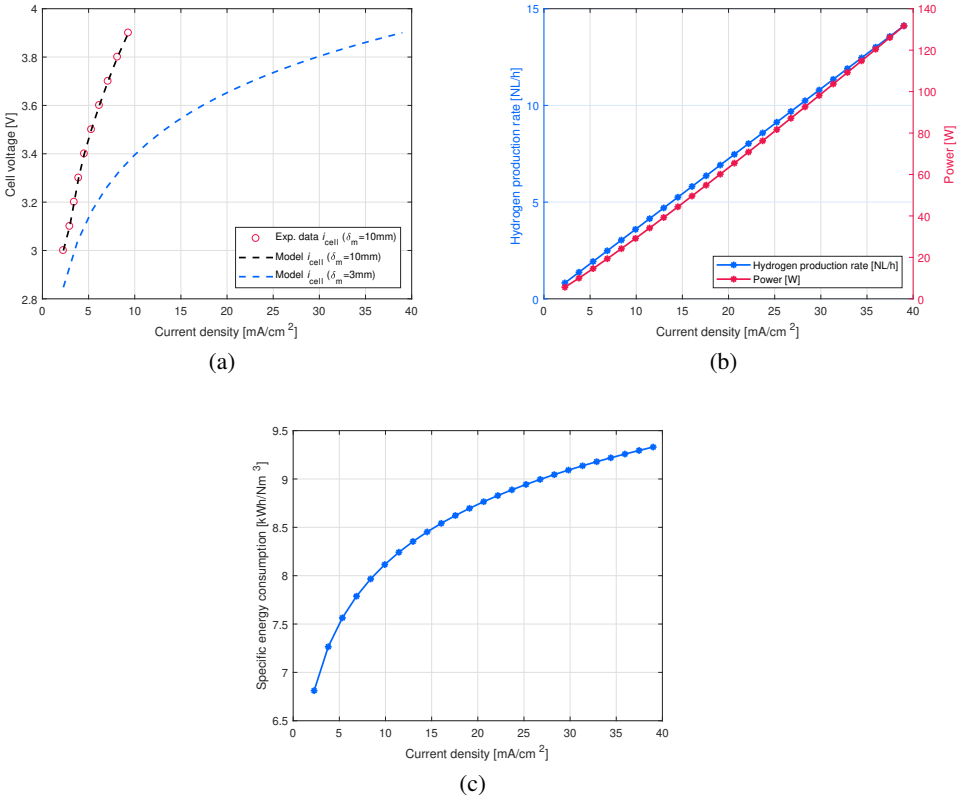

Figure 4.4: Computed energy efficiency parameters of the first electrolyzer stack prototype with a decreased distance between the electrodes, published in **Publication II**.

4.2.2 Hydrogen production in neutral pH

The performance of the in situ electrolysis without H_2-consuming biomass was evaluated in **Publication IV** by measuring the exhaust gas H_2 concentration using a thermal conductivity detector (TCD) under constant air flush. The test was carried out with the electrolyzer stack cells connected in series and parallel to compare the performance and, in particular, to determine the amount of stray currents. Fig. 4.5 shows measured stack voltages as a function of current. It can be seen that the typical cell voltages are substantially over the thermoneutral voltage of $1.48\,\mathrm{V}$. Interestingly, when the cells were connected in parallel, they all had almost the same voltage, but when they were connected in series, the outermost cells had a considerably higher voltage than the other cells. This leads to a conclusion that high leakage currents are present in the system in the case of series connection.

The calculated Faraday efficiency for the second electrolyzer prototype is presented in Fig. 4.6. In the case of series connections, the Faraday efficiency was poor throughout the

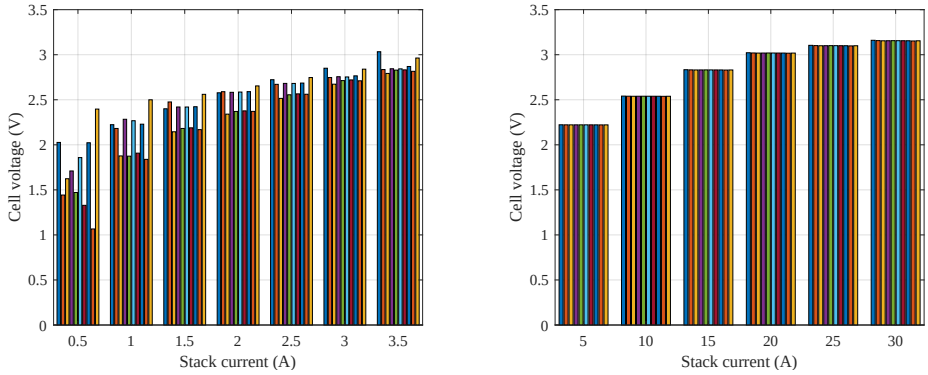

(a) (b)

Figure 4.5: Individual cell voltages vs. current of the second electrolyzer prototype in the case of (a) series and (b) parallel connection, published in **Publication IV**.

whole current range, once again signifying the problem of leakage currents in the flow channels. At currents above $15\,\mathrm{A}$, the Faraday efficiency increased to approximately 80% when using a parallel connection. The poor efficiency at the lower currents has yet to be explained, although the H_2 and O_2 recombination, other potential side reactions, and measurement error are the most likely explanations of the observed phenomena.

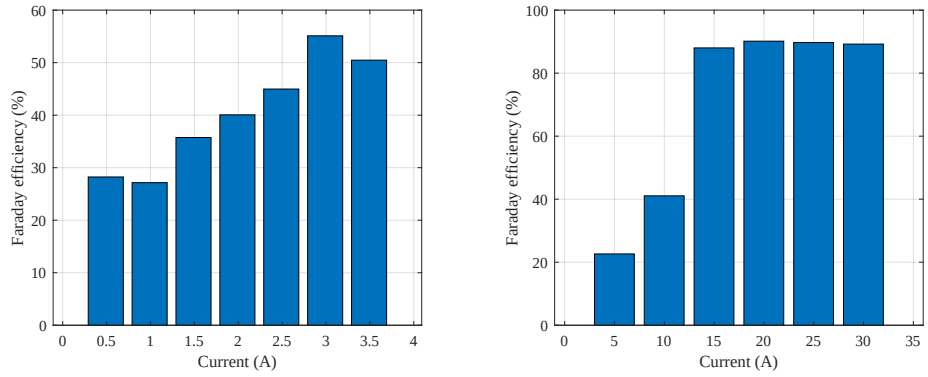

(a) (b)

Figure 4.6: Values of the Faraday efficiency of the second electrolyzer prototype in the case of (a) series and (b) Parallel connection, published in **Publication IV**.

The SEC of the in situ electrolyzer is shown in Fig. 4.7. The SEC is much higher compared with the standard alkaline or PEM electrolyzers, which usually reach values of $50\,\mathrm{kWh/kg_{H_2}}$. The low conductivity of the pH-neutral electrolyte and the lack of catalyst coating are the major reasons for the high SEC even with Faraday efficiencies above 80%.

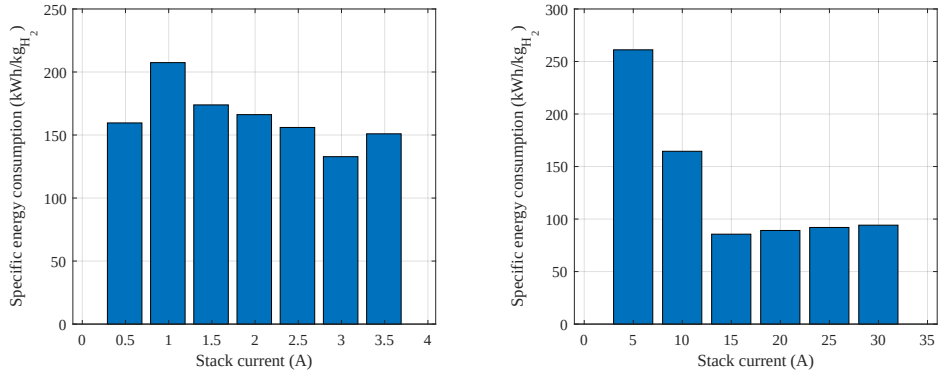

(a) (b)

Figure 4.7: Values of the SEC of the second electrolyzer prototype in the case of (a) series and (b) parallel connection, published in **Publication IV**.

4.2.3 Effect of insulating coating on leakage currents

The problem of leakage currents was successfully addressed in the later version of the third version of the electrolyzer stack prototype, published in **Publication V**, by coating the electrolyzer stack plates with an insulating Teflon coating except for the active electrode region in the middle. On the basis of the collected current–voltage relationships and the observed H_2 generation, the SEC and Faraday efficiency of the stack were computed and displayed in Fig. 4.8. Uniformly distributed cell voltages for both parallel and series connections indicated successful application of the insulation. At the cell currents of 1.5–$2.5\,\mathrm{A}$, the Faraday efficiency was near to 90% while the typical value of the H_2 production rate was close to $3.7\,\mathrm{N\,l/h}$ at $2\,\mathrm{A}$ and $2.9\,\mathrm{V}$ per electrolyzer cell in both cases. Moreover, the SEC was substantially lower than in the previous study. The specific energy consumption for the current range of 1.5–$2.5\,\mathrm{A}$ per cell did not surpass $90\,\mathrm{kWh/kg_{H_2}}$, indicating once again that the electrolyzer stack was successfully redesigned with proper insulation.

4.2.4 Effect of electrocatalytic coatings on stack performance

For the third electrolyzer prototype, published in **Publication V**, several surface modification methods were applied in order to further improve the performance. In the first place, stack electrodes were coated in situ with the benchmark Co–Pi, which resulted in uniform black coating throughout the surface of the anode-acting electrode plates (Fig. 4.9). Linear sweep voltammetry was used to evaluate the performance of the parallel-connected electrolyzer prior and after coating with Co–Pi. As can be observed in Fig. 4.10, there was no current flow in the electrolyzer stack before coating until $2.15\,\mathrm{V}$, and afterward, the current gradually increased. Overpotentials of $1.14\,\mathrm{V}$ and $1.6\,\mathrm{V}$ per cell were required to reach $1\,\mathrm{mA/cm^2}$ and $5\,\mathrm{mA/cm^2}$, respectively. The electrolyzer stack performance was significantly improved when the anode plates were coated with Co–Pi as already after $1.85\,\mathrm{V}$ the current began to increase rapidly, while the aforementioned current densities

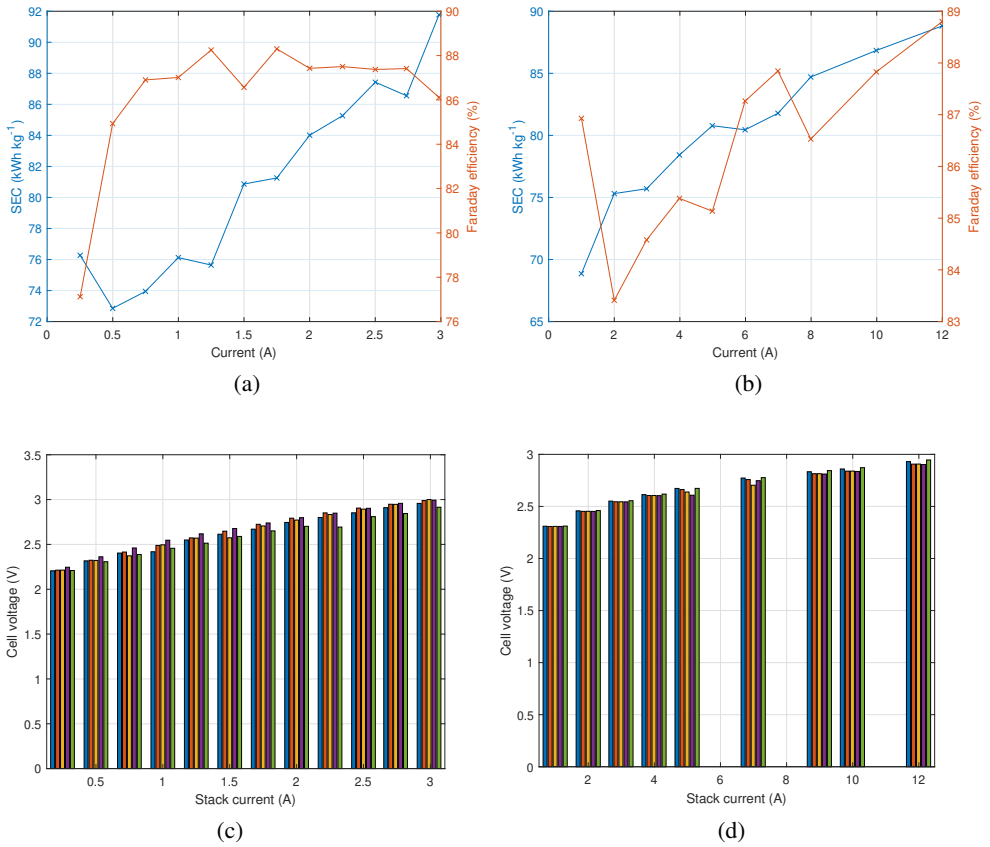

Figure 4.8: Values of the SEC and Faraday efficiency of the third electrolyzer prototype for (a) series and (b) parallel connection, and (c–d) corresponding cell voltage distribution, published in **Publication V**.

were reached at $0.9\,\mathrm{V}$ and $1.28\,\mathrm{V}$ overpotentials.

After that, the substrate surface was roughened and the stainless steel grains were bared by etching using a combination of H_2O_2 and HCl. The active area of the electrolyzer stack plates was considerably enlarged by this method, as can be seen in Fig. 4.11c. Linear sweep voltammetry was used to investigate the influence of etching on the electrolyzer stack performance, as shown in Fig. 4.10. In the etched electrolyzer, an overpotential of $1.28\,\mathrm{V}$ was required to reach $5\,\mathrm{mA/cm^2}$. Although the stack performance was somewhat lower before $2.5\,\mathrm{V}$ compared with the prior test with the Co–Pi coating, the current increase in the etched stack was faster after $2.5\,\mathrm{V}$, and $18\,\mathrm{A}$ was reached at $3\,\mathrm{V}$.

Subsequently, CoFe–P was applied to the etched electrode surfaces because of the reported OER activity (Li et al., 2019; Yoon et al., 2018). After the deposition process, the chosen plate was examined using the SEM equipped with EDX, which indicated a signif-

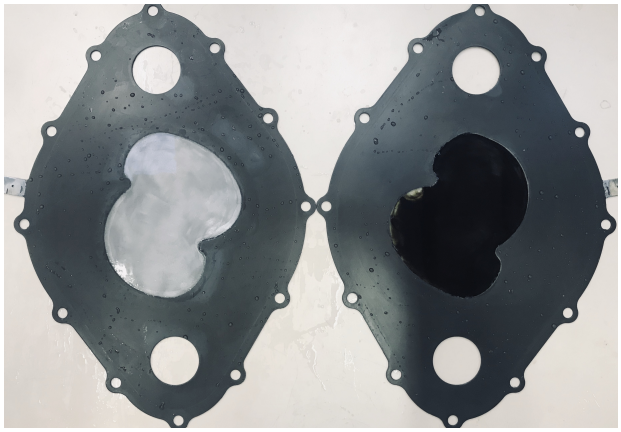

Figure 4.9: Images of the third electrolyzer prototype before and after deposition of Co-Pi, published in **Publication V**.

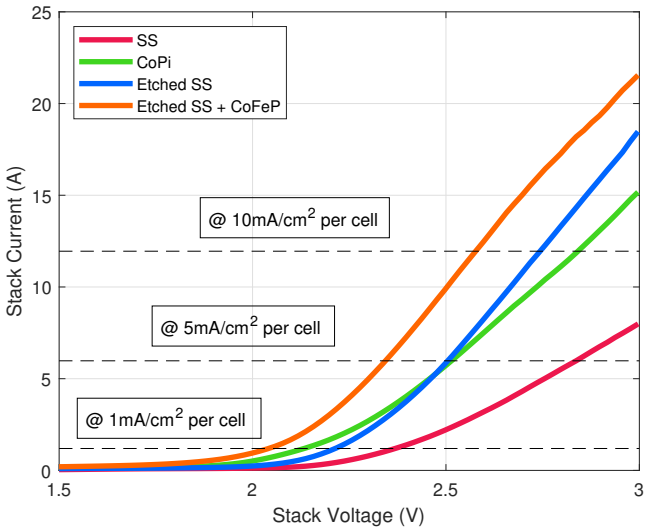

Figure 4.10: Polarization curves of the third electrolyzer prototype with different electrode surface modifications, published in **Publication V**.

icant change in the surface morphology (Fig. 4.11d) and the presence of nodular grains covered with nanoparticles typical of this coating. The onset overpotential appeared to be the lowest with the CoFe–P, and all the reference current densities were attained at lower overpotentials than with any of the previously evaluated alternatives. An overpotential of $1.07\,\mathrm{V}$ was required to reach $5\,\mathrm{mA/cm^2}$. The current in the etched and CoFe–P-coated electrolyzer at $3\,\mathrm{V}$ was approximately 2.7 times as high as with the initial tests with uncoated SS electrodes.

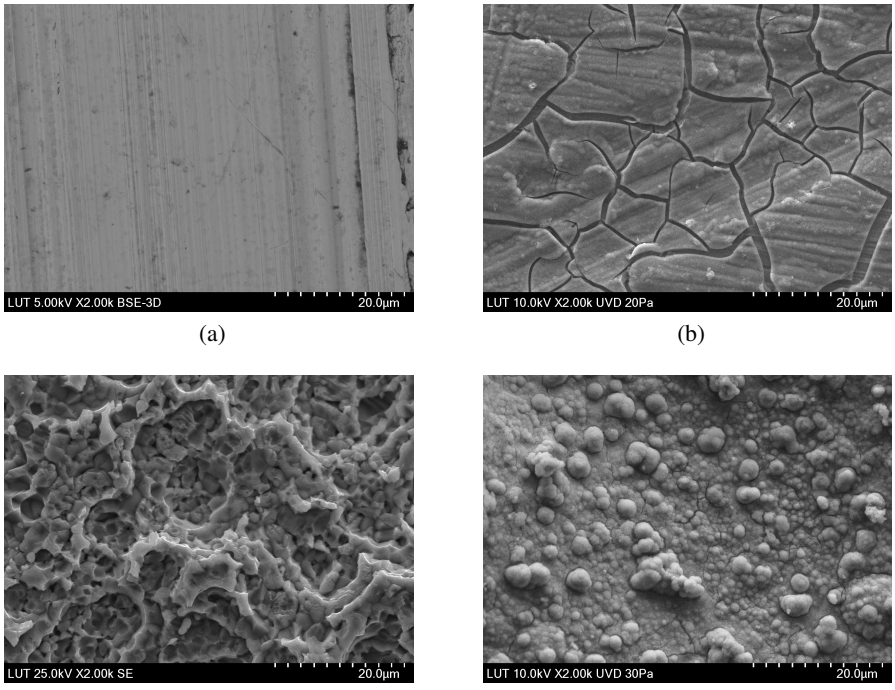

(a) (b)

(c) (d)

Figure 4.11: SEM images of (a) SS, (b) Co-Pi on SS, (c) etched SS, and (d) CoFe-P on the etched SS, published in **Publication V**.

5 Neo-Carbon Food proof-of-concept

Cultivation of HOB with in situ water electrolysis has been successfully performed and demonstrated in the present research work. This chapter includes research results published in **Publications I, II**, and **IV**. First, small-scale HOB cultivation results obtained at the VTT Technical Research Centre of Finland are presented. Following that, the Neo-Carbon Food concept is discussed, which is a pilot-scale HBI process for the generation of microbial biomass. The idea involves integrated H_2 generation by water electrolysis, O_2 DAC, and later HOB assimilation of captured carbon.

5.1 Materials and methods

5.1.1 Medium and HOB strains

The mineral medium, the composition of which is summarized in Table 3.1, was used for the electro-assisted cultivation of HOB in **Publications I, II**, and **IV**. In the first two publications, the HOB strain was Cupriavidus necator H16 (DSM 428) supplied by the Leibniz-Institut DSMZ. In **Publication IV**, Nocardioides nitrophenolicus VTT E-183562 was used as a strain for the experimental work. The inoculum for the HBI cultivation was grown in $20\,\mathrm{ml}$ liquid volume shake flasks under $12.5\,\%$ H_2, $13.1\,\%$ O_2, $25\,\%$ CO_2, and $49.4\,\%$ N_2 until late exponential phase.

5.1.2 Description of the small-scale HOB cultivation procedure

Scientists of the VTT Technical Research Centre of Finland were responsible for carrying out small-scale HOB cultivation. In **Publications I** and **II**, the contributions of the authors are clearly stated, while small-scale HOB cultivation results are included in this dissertation as an example of the research performed during the MOPED project. The growth was carried out in a small $60\,\mathrm{ml}$ electrobioreactor with an IrO_2 anode and an SS cathode as shown in Fig. 5.1. The electrodes were made using wires of the aforementioned materials, which were wrapped in coils to give each electrode a surface area of approximately $13\,\mathrm{cm}^2$. Before the actual cultivation, the electrobioreactor filled with sterile growth media was purged with CO_2 for 2 h in order to stabilize. During experiments, CO_2 gas was sparged from the bottom, a constant electrolysis current of $18\,\mathrm{mA}$ was supplied, and the temperature was maintained at $30\,^{\circ}\mathrm{C}$. The first data point was taken at the end of the preinoculation stabilization phase when a suitable volume of inoculum (typically $2\,\mathrm{ml}$) was added to get an initial optical density of 0.2 .

5.1.3 Optical density and cell dry weight measurements

In all the publications, the microbial growth was monitored by measuring the optical density of the medium at 600 nm (OD_{600}). Samples collected from the bioreactor were analyzed using a spectrophotometer after appropriate dilution. The OD_{600} was correlated

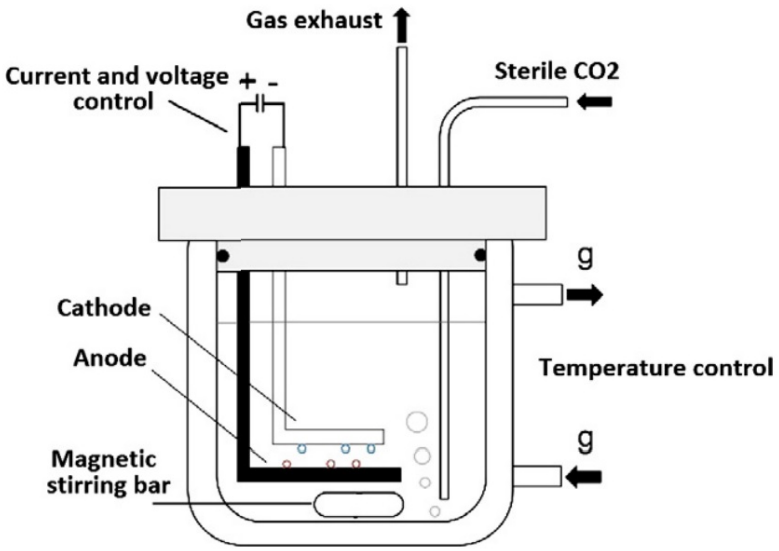

Figure 5.1: Small-scale electrobioreactor used for the HOB cultivation in **Publications I** and **II**.

with cell density by measuring the cell dry weight (CDW). For this purpose, a 500 ml sample was extracted, separated by centrifugation at 3000 g over 20 min, washed with pure water, and dried at $105\,^{\circ}\mathrm{C}$ overnight. The correlation between the OD_{600} and the CDW was presented separately in **Publications I, II**, and **IV**.

5.1.4 Description and operation of the Neo-Carbon Food pilot

The bioreactor tank, the CO_2 DAC unit, and the in situ water electrolyzer are the major components of the developed Neo-Carbon Food pilot, as illustrated in Fig. 5.2a. A second version of the in situ water electrolyzer, described in the previous chapter, was used in the Neo-Carbon Food pilot to generate H_2 and O_2. An SS bioreactor tank equipped with a 2-blade stirrer was used for biomass growth, accumulation, sampling, and process monitoring. The appropriate temperature for the HOB cultivation of $30\,^{\circ}\mathrm{C}$ was maintained using a water jacket and a Lauda RP855 thermostat. To provide consistent liquid circulation in the system, an EBARA model EVMSUL centrifugal vertical multistage pump with a maximum flow rate of $3\,\mathrm{m}^3/\mathrm{h}$ was employed, controlled by an ABB ACS355 frequency converter.

The system was flushed with ethanol to sterilize it at the start of the procedure. Following that, using the Flowrox dosing pump and the sterile filtration system, 20 l of fresh medium and enriched HOB culture were sequentially delivered to the bioreactor tank. The system was set up for semicontinuous operation by extracting a certain volume and feeding the

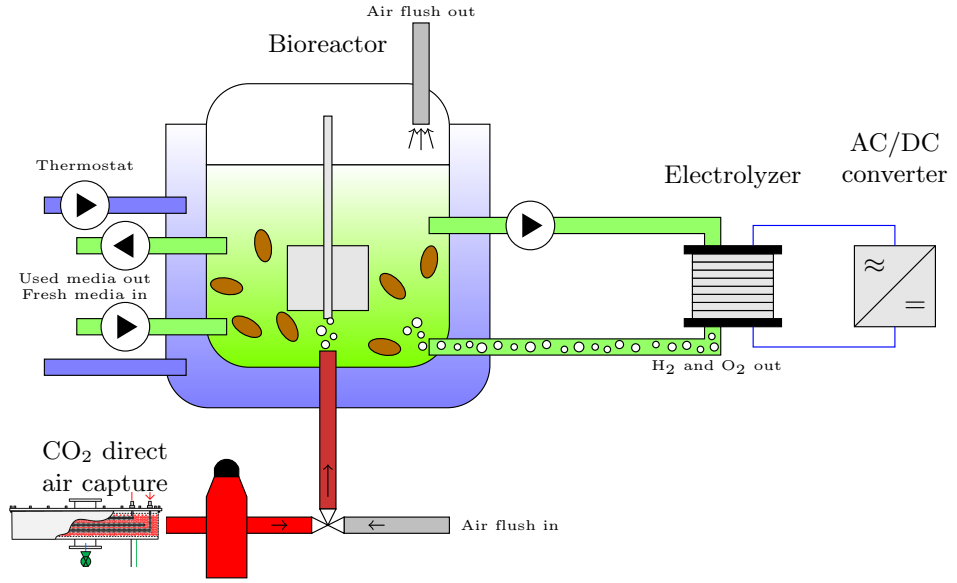

(a)

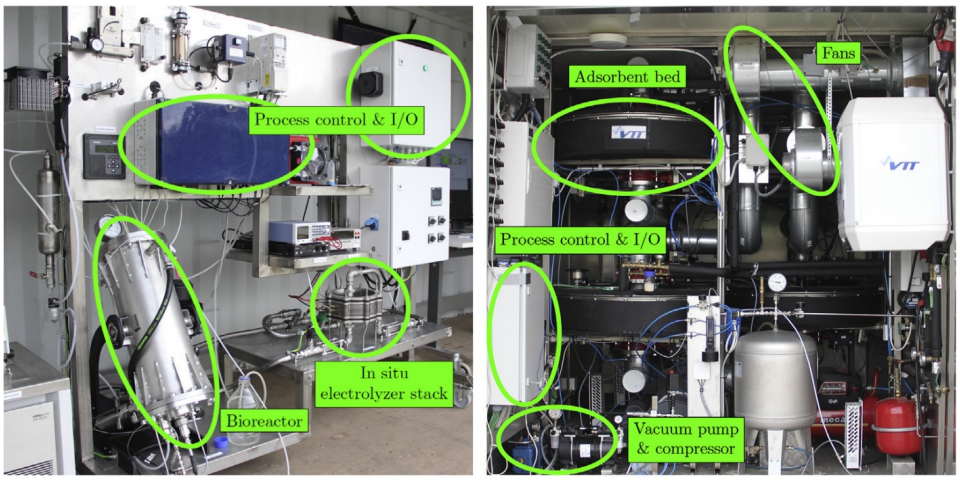

(b)

Figure 5.2: (a) Schematic diagram and (b) photo of the Neo-Carbon Food pilot, published in **Publication IV**.

same amount of new medium to the bioreactor at intervals determined by the observed optical density. The pH-neutral conditions were maintained during the procedure using 1M NH_4OH and 1M H_3PO_4 solutions. The flammability of H_2 raises concerns about the safety of any H_2-based procedure. Thus, air purging was implemented in the bioreactor to ensure that accumulation of an explosive gas mixture does not take place even when the H_2 production exceeds consumption.

5.1.5 Measurements of H_2 concentration

The concentration of H_2 in the exhaust gas was defined using a BCP-H_2 (BlueSens) thermal conductivity detector (TCD) with a two-stage drying solution consisting of a condensing dryer followed by a silica gel tank to prevent moisture ingress from the gas flow into the TCD. The current in the electrolyzer stack was varying in response to the data acquired on H_2 concentration in the exhaust. Throughout the pilot operation, the H_2 concentration was kept below the lower explosion limit of 4%. The ambient H_2 level was monitored with a Honeywell Sensepoint XCL gas detector.

5.1.6 CO_2 capture

In this study, CO_2 was captured from the air by using a DAC device based on temperature–vacuum swing adsorption. A proprietary aminoresin was used as the solid adsorbent in the DAC system. The operation of the DAC unit and the physicochemical properties of the adsorbent were previously described in (Bajamundi et al., 2019) and (Elfving et al., 2017a,b), respectively. Similar to the SOLETAIR project (Vidal et al., 2018), the unit was operated by adsorbing at night, and generating CO_2 in the daytime. The automated procedure published previously in (Bajamundi et al., 2019) was used for the desorption step. Typically, a $60\,\mathrm{min}$ CO_2 desorption time was used for each bed pair, which means the time when the bed pair is subjected to both heating at a maximum temperature of $80\,^{\circ}\mathrm{C}$ and a vacuum. The produced CO_2 gas was stored into an initially empty buffer with a volume of 650 l, consisting of one 50 l buffer tank and a 600 l bundle. CO_2 from the buffer was constantly fed into the bioreactor at a flow rate of $250\,\mathrm{ml/min}$ and sparged at the bottom of the bioreactor with an airflow of $1\,\mathrm{l/min}$.

5.2 Results and discussion

5.2.1 Small-scale HOB cultivation results

Initially, in a small scale electrobioreactor, the growth of HOB with in situ water electrolysis was successfully tested. In **Publication I** of this doctoral dissertation, the culture consisted of a mixed population of yet-to-be-identified species viable in the HBI environment. An average cell voltage of $2.31\,\mathrm{V}$ was used in the process. The cell mass increased in a linear fashion as the growth was limited by the availability of H_2. Assuming a water electrolysis Faradic efficiency of unity and full H_2 consumption, a $2.5\,\mathrm{g_{biomass}/mol_{H_2}}$ yield was calculated, which was comparable with the traditional gas fermentation results, but without the requirement to handle and store dangerous H_2 and O_2 gas mixtures.

In **Publication II**, the cultivation of Cupriavidus necator H16 was performed in the same bioreactor setup in similar conditions. A Pfeiffer Vacuum Omnistar GDS 301 Gas analysis system was used to measure the H_2 concentration in the reactor gas exhaust. The gas analysis system was calibrated before the cultivation against a known H_2 concentration

of 10% in a reference gas supplied by AGA. To determine the HOB biomass growth rate, the H_2 concentration at the bioreactor effluent was transformed into an H_2 utilization ratio:

$$\mathrm{H_2\ utilization} = \frac{\mathrm{c}_{\mathrm{H_2}}^{\mathrm{Out,Initial}} - \mathrm{c}_{\mathrm{H_2}}^{\mathrm{Out}}}{\mathrm{c}_{\mathrm{H_2}}^{\mathrm{Out,Initial}}} \tag{5.1}$$

where $\mathrm{c}_{\mathrm{H_2}}^{\mathrm{Out}}$ is the H_2 concentration at the reactor outlet, and $\mathrm{c}_{\mathrm{H_2}}^{\mathrm{Out,Initial}}$ is the concentration at the beginning of cultivation.

The use of H_2 was assumed to increase at the same rate with the biomass growth. A generic exponential function was fitted to the increasing range (between 0.5–$12\,\mathrm{h}$) of the H_2 utilization data:

$$\mathrm{H_2\ utilization} = Ae^{\mu t} \tag{5.2}$$

where A is a preexponential constant, and μ is a rate constant.

The best fit was achieved with $A = 0.1675$ and $\mu = 0.1422\,\mathrm{h}^{-1}$. The rate constant can be regarded as an estimate of the biomass growth rate, because the biomass growth is dependent on H_2 consumption. Fig. 5.3 shows the results of small-scale HOB cultivation.

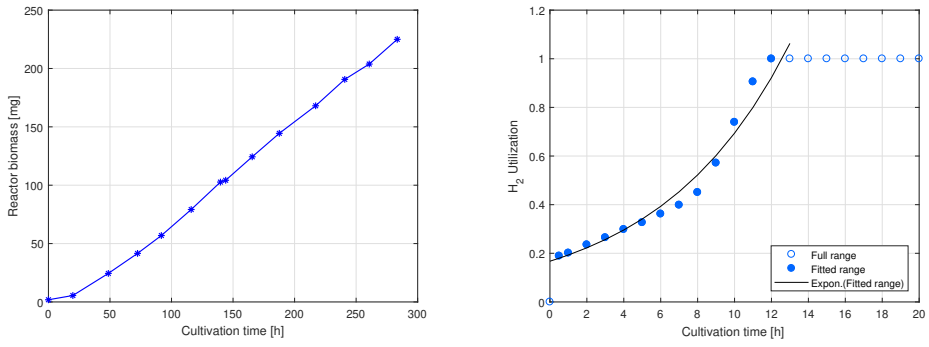

(a) (b)

Figure 5.3: Small-scale HOB cultivation with in situ water electrolysis: (a) biomass increase of a mixed culture and (b) development of the H_2 utilization in the small-scale electrobioreactor and exponential curve fitting to the part of the data range associated with the exponential biomass growth, published in **Publications I** and **II**.

5.2.2 Carbon dioxide production

The DAC unit's CO_2 output of 2–3 kg per day (Bajamundi et al., 2019) was much higher than the bioreactor's CO_2 requirement of $0.49\,\mathrm{kg}$ per day. As a result, the DAC unit was not used every day following the initial filling of the CO_2 buffer. The SEC of the DAC was estimated throughout the course of six typical days of operation, as illustrated in Fig. 5.4. Higher generated CO_2 amounts typically resulted in a reduced SEC, as can be observed in Fig. 5.4. It is also clear that the desorption phase contributes significantly more to the overall SEC than the adsorption phase, ranging from 62% up to 73% of the total SEC.

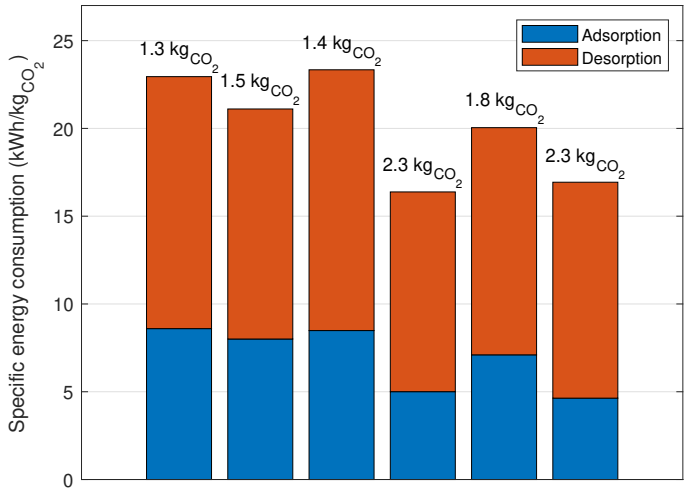

Figure 5.4: SEC and daily produced CO_2 of the DAC unit of six different experiments, published in **Publication IV**.

5.2.3 Pilot-scale biomass production

For the proof of the Neo-Carbon Food concept, a bench-scale pilot was operated over three test campaigns from summer 2019 to winter 2020, but the results of the last and most successful campaign are emphasized here. The pilot was operated in a semicontinuous mode throughout the third test campaign, with periodic extraction of the biomass-rich medium and simultaneous input of the same amount of approximately 4 l of fresh growth medium to the system. The CO_2 captured from air was continuously sparged from the bottom of the bioreactor through the mineral medium with an experimentally defined flow of $1\,\mathrm{l/min}$ while in the top section of the bioreactor air purging was performed with the flow rate of $250\,\mathrm{ml/min}$. In order to saturate the culture with H_2 and O_2, the medium and cells were pumped through the in situ electrolyzer stack with a constant flow rate of approximately $1\,\mathrm{m^3/min}$. The hydrogen production rate was controlled manually to keep the exhaust hydrogen rate as low as possible and below the lower explosion limit of 4%. Circulation of the medium with a high flow rate enabled to avoid biofilm formation on

the electrode surfaces and provided an additional mixing required for the intensification of the dissolution of the main reactant gases.

Biomass concentration, stack current, and hydrogen content in the exhaust line during the third test campaign are shown in Fig. 5.5. The graph shows that the HBI process was separated into several phases. At the beginning, a clear lag phase with practically no biomass growth was observed, which was followed by a steep increase in biomass concentration in the reactor volume. When the biomass concentration reached approximately 2.5 g CDW/l, the dilution process was launched and the aforementioned concentration was successfully maintained in the bioreactor for 900 h (37 days). Notably in Fig. 5.5, there was no clear correlation between the stack current indicating hydrogen production rate and the microbial growth. Presumably, the use of hydrogen by the HOB was not consistent and varied during the whole experimental process. However, there was a clear trend indicating that the absence of hydrogen in the exhaust gas was every time interconnected with the start of the increase in biomass concentration. This trend observed at approximately 100 h, 190 h, 300 h, and 970 h of the experimental procedure could be explained as a phase of intensification of the oxidation of hydrogen coupled with the assimilation of CO_2 by the HOB culture into cell biomass. After the last intensification phase, the HBI pilot system was operated in a batch mode for $700\,\mathrm{h}$ in order to achieve a stable growth phase. The maximum biomass concentration reached during the stable growth phase was $15\,\mathrm{g\,l^{-1}}$, while average biomass production rates in the two batches were $0.038\,\mathrm{g\,l^{-1}\,h^{-1}}$ and $0.032\,\mathrm{g\,l^{-1}\,h^{-1}}$, respectively.

The start of the stable and intensive growth of cell culture observed at 970 h occurred when the stack current was increased to 30 A with the corresponding cell voltage of slightly above 3V. This observation could be explained by the fact that high cell potentials favor the use of cathodic current for the hydrogen evolution reaction (HER) instead of the reactive oxygen species (ROS) formation at lower potentials, leading to toxicity and cell viability issues (Torella et al., 2015; Liu et al., 2016). It is worth noting that Torella et al. (2015) reported an operational window of 2.3 V $>$ Ecell $>$ 4 V at which the biological viability of HOB was not hindered by the ROS toxicity. Subsequent studies of Liu et al. (2016) clearly showed that the application of selective catalysts kinetically favoring OER at the anode and especially HER at the cathode proved to facilitate an increase in the production rate at a much higher energy efficiency. In the present study, selective catalysts were not applied, and SS electrode plates were used both for the HER and the OER. However, the use of the developed stack structure for the electrolyzer prototype was assumed to reduce the leakage currents to some extent, and as a consequence, the possibility of emerging undesired side reactions.

The achieved value of production rate is close to the productivity reached by using a two-stage bioprocess reported by Molitor et al. (2019), and to the values of volumetric productivity achieved in sequence batch reactor conditions by Matassa et al. (2016). Because the exhaust H_2 concentration is significantly lower in the test without microorganisms with the same current, most of the generated H_2 is consumed in the process. Even though

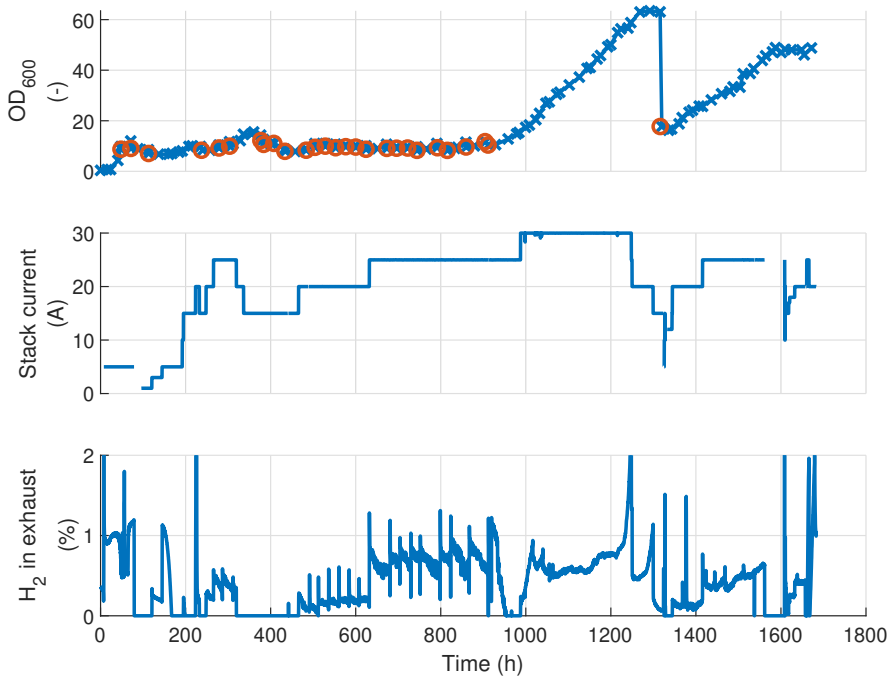

Figure 5.5: Cell dry weight concentration, stack current, and H_2 content in the exhaust line as a function of time. Adding fresh medium, which decreases the optical density, is indicated by circles on the optical density curve. Because of contamination, the results were excluded from **Publication IV**.

for the bulk of the time there was a minor surplus of hydrogen ranging from 0.5% to 2%, which was not consumed by HOB microbes, it is evident that the hydrogen utilization efficiency of the HBI system is far higher than in the processes with the external production of the main reactant gases used in traditional gas fermentation designs (Matassa et al., 2016).

However, it is necessary to point out that significant contamination was detected in the biomass analysis, and thus, it cannot be stated that all the biomass consists of the desired MP. The most likely cause of contamination is the failure to sterilize the system despite sanitation with 2% NaOH and flushing with 70% ethanol at a temperature of $55\,^{\circ}\mathrm{C}$ before the autoclaved growth medium was introduced through a sterile filter. Hence, it is difficult to perform any analysis of the specific energy consumption of the MP production because of contamination.

5.2.4 Influence of HOB cultivation on stack electrodes

Fig. 5.6 shows the electrode plate after long-lasting HBI cultivation and the CFD velocity distribution analysis. The amount of deposited biomass on the surface of the electrode plate and the flow velocity distribution measured by the CFD indicate a strong correla-

tion. A thick layer of biomass was attached at areas with a low flow velocity (locations A and D), while almost clean surfaces can be seen at a higher velocity (location C).

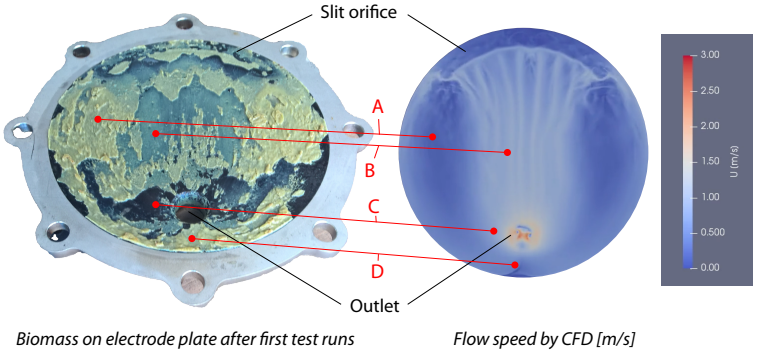

Figure 5.6: Images of (a) electrode plate after long-lasting HBI cultivation and (b) computed by CFD velocity distribution on the similar electrode plate, published in **Publication IV**.

The surfaces of the SS electrodes were thoroughly coated after the first run, as can be seen in Fig. 5.7. According to the EDX, most of the compounds deposited onto the electrode surface were metals from the cultivation medium and carbon referring to the biomass. Periodic switching of the polarity solved the problem of metal deposition, while more powerful mixing was applied to decrease the attachment of the biomass. Corrosion of the electrode plates along the edges of the slit orifices was another problem that was observed. The corrosion may have resulted from the cavitation-induced erosion in combination with the presence of O_2 in the process, and thus, more corrosion-resistant SS for the electrode plates would be required.

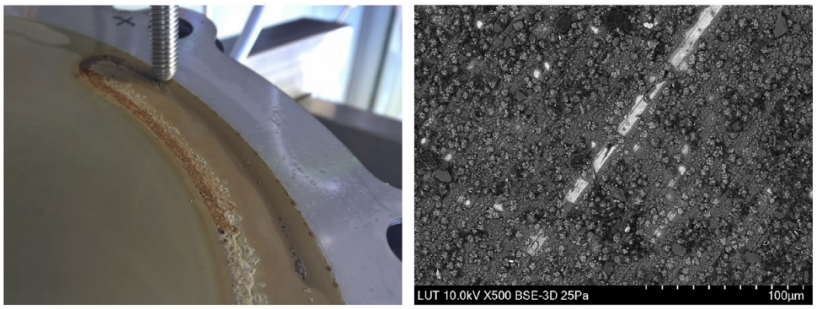

Figure 5.7: Changes in the in situ water electrolyzer stack electrodes after the HOB cultivation experiments: corrosion and SEM images showing electrodeposited metals from the medium solution.

6 Conclusion and suggestions for future work

It is evident that the supply of sufficient food, energy, and water represents a huge global challenge at present. Indeed, there is no universal solution for tackling this challenge. Instead, what will be needed are situation-oriented tailored solutions based on creative and cross-sectoral thinking. The power-to-food concept could become one of such creative solutions capable of helping to feed the increasing population of the world while mitigating the negative environmental impacts of conventional agriculture. From this perspective, HBI systems provide a sustainable, efficient, and versatile synthesis platform suitable for the production of high-quality proteins by microbial assimilation of CO_2 and in situ water electrolysis.

In this work, the energy efficiency of in situ water electrolysis performed in neutral pH was extensively studied, and attempts to improve the efficiency were made. Furthermore, the feasibility of CO_2 conversion into protein-rich biomass using HOB was proven on a laboratory and pilot scale. The main conclusions obtained are summarized as follows:

- Because of the substantial ohmic losses induced by the poor conductivity of the electrolyte, the distance between the electrodes has a considerable influence on voltage in electrobioreactors. To achieve a high energy efficiency and a compact design structure, the space between the electrodes should be kept as low as possible. For instance, if in the case of plain SS the electrodes are located at a $3\,\mathrm{mm}$ distance and the voltage efficiency of the electrolysis is required to be higher than 50%, the current density would be in the range of $10\,\mathrm{mA/cm^2}$.

- Because the anode half-reaction has a greater potential than the cathode half-reaction, the anode material has a considerable impact on the cell voltage, especially at higher current densities. Among the conventional electrocatalysts, precious IrO_2 exhibited the best OER performance, showing a current density of $15\,\mathrm{mA/cm^2}$ with a voltage efficiency of 50% at a $3\,\mathrm{mm}$ distance. If IrO_2 is also used as a cathode material, a current density of up to $25\,\mathrm{mA/cm^2}$ could be reached at a similar voltage efficiency.

- In terms of OER activity, TM-Pi catalysts placed onto a highly ordered NF substrate are competitive with commercial Pt and IrO_2 catalysts for short experiments. In a neutral PBS, the intrinsic OER activity of the investigated catalysts declined in the sequence of Co-Pi $>$ NiFe-Pi $>$ Fe-Pi. The reference current density of $1\,\mathrm{mA/cm^2}$ was reached at relatively small overpotentials of $420\,\mathrm{mV}$, $495\,\mathrm{mV}$, and $534\,\mathrm{mV}$ for Co-Pi, NiFe-Pi, and Fe-Pi, respectively.

- A series of in situ water electrolyzer stack prototypes for HBI systems were designed and tested. With the initial version of the stack it was possible to achieve only $2.3\,\mathrm{mA/cm^2}$ of current density at the 50% efficiency. In the latest version, the performance was considerably enhanced by application of insulating coatings preventing leakage currents and electrocatalytic TM-Pi coatings. It was possible to reach a

current density of approximately $10\,\mathrm{mA/cm^2}$ at 2.5 V per electrolyzer cell by using a less conductive electrolyte solution. The in situ water electrolyzer showed a high Faraday efficiency close to 90% and an acceptable SEC below $90\,\mathrm{kWh/kg_{H_2}}$.

- The cultivation of HOB with in situ water electrolysis was successfully tested in a small-scale electrobioreactor. The cell mass increases in a linear fashion as the growth is limited by the availability of H_2. In one case, the apparent biomass yield from hydrogen was calculated to be $2.5\,\mathrm{g_{biomass}/mol_{H_2}}$, which is comparable with the typical yields of gaseous H_2 feed cultivation.

- The Neo-Carbon Food concept, which is a pilot-scale HBI process suitable for the production of microbial biomass, was introduced. According to the concept, the plant operation is based on integrated H_2 production by water electrolysis, the DAC of CO_2, and its subsequent assimilation by autotrophic HOB. The SEC of the DAC was around $20\,\mathrm{kWh/kg_{CO_2}}$. The pilot plant achieved a total operating time of approximately $1650\,\mathrm{h}$ and a maximum bacterial biomass production rate of $0.038\,\mathrm{g\,l^{-1}\,h^{-1}}$. Unfortunately, the biomass analysis revealed heavy contamination despite sterilization of the system by sanitation with 2% NaOH and flushing with 70% EtOH at a temperature of $55\,^{\circ}\mathrm{C}$ before HOB cultivation. Therefore, the SEC of the MP production was not calculated in this study.

Because HBI systems are still in their infancy, further research is required from the viewpoint of fundamental and applied research. The value obtained for biomass productivity indicates that further technical optimization is required to achieve industrially relevant production rates. Further, the contamination of biomass requires more attention to the sterilization process. In situ electrolysis has the benefit of high H_2 utilization, but the efficiency of H_2 generation is limited, and in situ electrolysis also increases system complexity, making sterilization more difficult than with external electrolysis. Furthermore, the best SEC values obtained for in situ water electrolysis in this study are nearly 1.8 times as high as those obtained for traditional alkaline and PEM electrolyzers, which are typically around $50\,\mathrm{kWh/kg_{H_2}}$ at 47%–82% efficiency (Ursúa et al., 2012). The lower conductivity of the cultivation medium compared with, for example, KOH used in alkaline water electrolysis, could be pointed out as a major factor contributing to the greater SEC even at the 90% Faraday efficiency. Despite the fact that the pH-neutral in situ water electrolysis and the conventional water electrolysis have certain similarities, the applications of both technologies differ substantially. Therefore, making unfavorable judgments about the feasibility of the investigated process only on the basis of the Faraday efficiency and SEC differences is not fair (Rieth and Nocera, 2020).

The key directions of future research will be focused on:

- Development of microbial culture capable of increasing the rate of CO_2 conversion into bacterial biomass.

- Optimization of the electrolyzer stack design in order to further increase the energy efficiency of in situ water electrolysis, reaching values comparable with alkaline and PEM electrolyzers.
- Application of biocompatible earth-abundant electrode coatings and high-surface materials to improve the electrocatalytic efficiency of water splitting and avoid leaching of compounds toxic for bacterial growth on the pilot scale.
- Assessing whether tailoring the DAC process for microbial cultivation can reduce the SEC of the produced CO_2, and to support this objective;
- Studying which are the optimal CO_2 concentration levels for the maximum growth of the microbial biomass, and
- Studying which are the maximum current densities that HOB can tolerate.
- Comprehensive environmental assessment together with an extensive economic and life cycle analysis is essential to evaluate the industrial viability of the HBI production of protein.

Nevertheless, even now it is possible to conclude that the HBI processes with in situ water electrolysis represent a groundbreaking technology that could potentially revolutionize the food and feed production industries, drastically changing their effect on the planet's environment.

References

Babar, P.T., Lokhande, A.C., Shim, H.J., Gang, M.G., Pawar, B.S., Pawar, S.M., and Hyeok, J. (2018). SILAR deposited iron phosphate as a bifunctional electrocatalyst for efficient water splitting. *J. Colloid Interface Sci.*, 534, pp. 350–356. doi: 10.1016/j.jcis.2018.09.015.

Bailera, M., Lisbona, P., Romeo, L.M., and Espatolero, S. (2017). Power to Gas projects review: Lab, pilot and demo plants for storing renewable energy and CO_2. *Renew. Sustain. Energy Rev.*, 69, pp. 292–312. doi: 10.1016/j.rser.2016.11.130.

Bajamundi, C.J.E., Koponen, J., Ruuskanen, V., Elfving, J., Kosonen, A., Kauppinen, J., and Ahola, J. (2019). Capturing CO_2 from Air : Technical Performance and Process Control Improvement. *J. CO_2 Util.*, 30, pp. 232–239. doi: 10.1016/j.jcou.2019.02.002.

Bockris, J.O. (1956). Kinetics of activation controlled consecutive electrochemical reactions: Anodic evolution of oxygen. *J. Chem. Phys.*, 24(4), pp. 817–827. doi: 10.1063/1.1742616.

Carrette, L., Friedrich, K.A., and Stimming, U. (2001). Fuel Cells - Fundamentals and Applications. (1), pp. 5–39. doi: https://doi.org/10.1002/1615-6854(200105)1:1⟨5::AID-FUCE5⟩3.0.CO;2-G.

Chen, X., Yu, Z., Wei, L., Zhou, Z., Zhai, S., and Chen, J. (2019). Ultrathin nickel boride nanosheets anchored on functionalized carbon nanotubes as bifunctional electrocatalysts for overall water splitting. *J. Mater. Chem. A*, 7, pp. 764–774. doi: 10.1039/c8ta09130g.

Cheng, Y. and Ping, S. (2015). Advances in electrocatalysts for oxygen evolution reaction of water electrolysis-from metal oxides to carbon nanotubes. *Prog. Nat. Sci.*, 25, pp. 545–553. doi: 10.1016/j.pnsc.2015.11.008.

Crist, E., Mora, C., and Engelman, R. (2017). The interaction of human population, food production, and biodiversity protection. *Sci.*, 356(6335), pp. 260–264. doi: 10.1126/science.aal2011.

Daiyan, R., Macgill, I., and Amal, R. (2020). Opportunities and Challenges for Renewable Power-to-X. *ACS Energy Lett.*, 5(12), pp. 3843–3847. doi: 10.1021/acsenergylett.0c02249.

Decourt, B., Lajoie, B., Debarre, R., and Soupa, O. (2014). *The hydrogen-based energy conversion FactBook*. The SBC Energy Institute.

Dresselhaus, M.S. and Thomas, I.L. (2001). Alternative energy technologies. *Nature*, 414, pp. 332–337. doi: 10.1038/35104599.

DSMZ GmbH (2011). *81. Mineral Medium For Chemolithotrophic Growth (H - 3)*. URL https://www.dsmz.de/microorganisms/medium/pdf/DSMZ{_}Medium81.pdf.

Elfving, J., Bajamundi, C., and Kauppinen, J. (2017a). Characterization and performance of direct air capture sorbent. *Energy Proc.*, 114, pp. 6087–6101. doi: 10.1016/j.egypro.2017.03.1746.

Elfving, J., Bajamundi, C., Kauppinen, J., and Sainio, T. (2017b). Modelling of equilibrium working capacity of PSA , TSA and TVSA processes for CO_2 adsorption under direct air capture conditions. *J. CO_2 Util.*, 22, pp. 270–277. doi: 10.1016/j.jcou.2017.10.010.

Food and Agriculture Organization of the United Nations (FAO) (2017). *The future of food and agriculture: Trends and challenges*. Rome, Italy. ISBN 978-92-5-109551-5.

Gero Rueter (2019). *Power-to-X: The secret to a 100% renewable energy system?* URL https://www.dw.com/en/power-to-x-the-secret-to-a-100-renewable-energy-system/a-51662014.

Guo, R., Lai, X., Huang, J., Du, X., Yan, Y., Sun, Y., Zou, G., and Xiong, J. (2018). Phosphate-based electrocatalysts for water splitting: a review on recent progress. *ChemElectroChem*, 5, pp. 3822–3834. doi: 10.1002/celc.201800996.

Haszeldine, R.S., Flude, S., Johnson, G., and Scott, V. (2018). Negative emissions technologies and carbon capture and storage to achieve the Paris Agreement commitments. *Phil.Trans.R.Soc.A*, 376, p. 20160447. doi: 10.1098/rsta.2016.0447.

Hepburn, C., Adlen, E., Beddington, J., Carter, E.A., Fuss, S., Mac Dowell, N., Minx, J.C., Smith, P., and Williams, C.K. (2019). The technological and economic prospects for CO_2 utilization and removal. *Nature*, 575(7781), pp. 87–97. doi: 10.1038/s41586-019-1681-6.

Hu, X., Kerckhof, F.M., Ghesquière, J., Bernaerts, K., Boeckx, P., Clauwaert, P., and Boon, N. (2020). Microbial Protein out of Thin Air: Fixation of Nitrogen Gas by an Autotrophic Hydrogen-Oxidizing Bacterial Enrichment. *Environ. Sci. Technol.*, 54(6), pp. 3609–3617. doi: 10.1021/acs.est.9b06755.

Huang, J., Li, Y., Xia, Y., Zhu, J., Yi, Q., Wang, H., and Xiong, J. (2017). Flexible cobalt phosphide network electrocatalyst for hydrogen evolution at all pH values. *Nano Res.*, 10, pp. 1010–1020. doi: 10.1007/s12274-016-1360-y.

Huang, J., Su, Y., Zhang, Y., Wu, W., Wu, C., Sun, Y., Li, Y., and Jie, X. (2018). FeOx/FeP Hybrid Nanorods Neutral Hydrogen Evolution Electrocatalysis: Insight into Interface. *J. Mater. Chem. A*, 6, pp. 9467–9472. doi: 10.1039/C8TA02204F.

IEA (2017). *World Energy Outlook*. Paris, France.

IPCC (2014). *Climate Change 2014: Synthesis Report. Contribution of Working Groups I, II and III to the Fifth Assessment Report of the Intergovernmental Panel on Climate Change [Core Writing Team, R.K. Pachauri and L.A. Meyer (eds.)]*. Geneva, Switzerland.

IPCC (2019). *Special Report on Climate Change and Land*. Geneva, Switzerland.

Irshad, A. and Munichandraiah, N. (2015). High Catalytic Activity of Amorphous Ir-Pi for Oxygen Evolution Reaction. *ACS Appl. Mater. Interfaces*, 7, pp. 15765–15776. doi: 10.1021/acsami.5b02601.

Jin, K., Park, J., Lee, J., Yang, K.D., Pradhan, G.K., Kim, S.H., Han, S., and Nam, K.T. (2014). Hydrated Manganese(II) Phosphate ($Mn_3(PO_4)_2 \cdot 3H_2O$) as a Water Oxidation Catalyst. *J. Am. Chem. Soc.*, 136, pp. 7435–7443. doi: https://doi.org/10.1021/ja5026529.

Kanan, M.W. and Nocera, D.G. (2008). In situ formation of an oxygen-evolving catalyst in neutral water containing phosphate and Co^{2+}. *Sci.*, 321(5892), pp. 1072–1075. doi: 10.1126/science.1162018.

Krieg, T., Sydow, A., Schro, U., Schrader, J., and Holtmann, D. (2014). Reactor concepts for bioelectrochemical syntheses and energy conversion. *Trends Biotechnol.*, 32(12), pp. 645–655. doi: 10.1016/j.tibtech.2014.10.004.

Kumar, G., Saratale, R.G., Kadier, A., Sivagurunathan, P., Zhen, G., Kim, S.H., and Saratale, G.D. (2017). A review on bio-electrochemical systems (BESs) for the syngas and value added biochemicals production. *Chemosphere*, 177, pp. 84–92. doi: 10.1016/j.chemosphere.2017.02.135.

Li, K., Li, Y., Peng, W., Zhang, G., Zhang, F., and Fan, X. (2019). Bimetallic Iron-Cobalt catalysts and their applications in energy-related electrochemical reactions. *Catalysts*, 9(9). doi: 10.3390/catal9090762.

Li, Y. and Lu, J. (2017). Metal-Air Batteries : Will They Be the Future Electrochemical Energy Storage Device of Choice? *ACS Energy Lett.*, (2), pp. 1370–1377. doi: 10.1021/acsenergylett.7b00119.

Li, Y. and Zhao, C. (2016). Iron-Doped Nickel Phosphate as Synergistic Electrocatalyst for Water Oxidation. *Chem. Mater*, 28, pp. 5659–5666. doi: 10.1021/acs.chemmater.6b01522.

Liang, Q., Zhong, L., Du, C., Luo, Y., Zheng, Y., and Li, S. (2018). Achieving highly efficient electrocatalytic oxygen evolution with ultrathin 2D Fe-doped nickel thiophosphate nanosheets. *Nano Energy*, 47, pp. 257–265. doi: 10.1016/j.nanoen.2018.02.048.

Liao, L., Wang, S., Xiao, J., Bian, X., and Zhang, Y. (2014). A nanoporous molybdenum carbide nanowire as an electrocatalyst for hydrogen evolution reaction. *Energy Environ. Sci.*, 7, pp. 387–392. doi: 10.1039/c3ee42441c.

Lin, H., Shi, Z., He, S., Yu, X., Wang, S., Gao, Q., and Tang, Y. (2016). Heteronanowires of MoC-Mo_2C as Efficient Electrocatalysts for Hydrogen Evolution Reaction. *Chem. Sci.*, 7, pp. 3399–3405. doi: 10.1039/C6SC00077K.

Linder, T. (2019). Making the case for edible microorganisms as an integral part of a more sustainable and resilient food production system. *Food Secur.*, 11(2), pp. 265–278. doi: https://doi.org/10.1007/s12571-019-00912-3.

Liu, C., Colón, B.E., Silver, P.A., and Nocera, D.G. (2018). Solar-powered CO_2 reduction by a hybrid biological | inorganic system. *J. Photochem. and Photobiol. A: Chem.*, 358, pp. 411–415. doi: 10.1016/j.jphotochem.2017.10.001.

Liu, C., Colón, B.C., Ziesack, M., Silver, P.A., and Nocera, D.G. (2016). Water splitting–biosynthetic system with CO_2 reduction efficiencies exceeding photosynthesis. *Sci.*, 352(6290), pp. 1210–1213. doi: 10.1126/science.aaf5039.

Long, X., Li, G., Wang, Z., Zhu, H., Zhang, T., Xiao, S., Guo, W., Yang, S., Long, X., Li, G., Wang, Z., Zhu, H., Zhang, T., Xiao, S., and Guo, W. (2015). Metallic Iron-Nickel Sulfide Ultrathin Nanosheets As a Highly Active Electrocatalyst for Hydrogen Evolution Reaction in Acidic Media Metallic Iron-Nickel Sulfide Ultrathin Nanosheets As a Highly Active Electrocatalyst for Hydrogen Evolution Reaction in Ac. *J. Am. Chem. Soc.*, 137, pp. 11900–11903. doi: 10.1021/jacs.5b07728.

Ma, Z., Meng, H., Wang, M., Tang, B., and Li, J. (2017). Porous Ni-Mo-S Nanowire Network Film Electrode as High- efficiency Bifunctional Electrocatalyst for Overall Water Splitting. *ChemElectroChem*, 5, pp. 335–342. doi: 10.1002/celc.201700965.

Mac Dowell, N., Fennell, P.S., Shah, N., and Maitland, G.C. (2017). The role of CO_2 capture and utilization in mitigating climate change. *Nat Clim Chang*, 7(4), pp. 243–249. doi: 10.1038/nclimate3231.

MacDowell, N., Florin, N., Buchard, A., Hallett, J., Galindo, A., Jackson, G., Adjiman, C.S., Williams, C.K., Shah, N., and Fennell, P. (2010). An overview of CO_2 capture technologies. *Energy Environ. Sci.*, 3(11), pp. 1645–1669. doi: 10.1039/c004106h.

Majumdar, A. and Deutch, J. (2018). Research Opportunities for CO_2 Utilization and Negative Emissions at the Gigatonne Scale. *Joule*, 2(5), pp. 805–809. doi: 10.1016/j.joule.2018.04.018.

Marini, S., Salvi, P., Nelli, P., Pesenti, R., Villa, M., Berrettoni, M., Zangari, G., and Kiros, Y. (2012). Advanced alkaline water electrolysis. *Electrochim. Acta*, 82, pp. 384–391. doi: 10.1016/j.electacta.2012.05.011.

Masa, J., Weide, P., Peeters, D., Sinev, I., Xia, W., Sun, Z., Somsen, C., Muhler, M., and Schuhmann, W. (2016). Amorphous Cobalt Boride (Co_2B) as a Highly Efficient Nonprecious Catalyst for Electrochemical Water Splitting : Oxygen and Hydrogen Evolution. *Adv. Energy Mater.*, 6, p. 1502313. doi: 10.1002/aenm.201502313.

Matassa, S., Boon, N., and Verstraete, W. (2015). Resource recovery from used water: The manufacturing abilities of hydrogen-oxidizing bacteria. *Water Res.*, 68, pp. 467–478. doi: 10.1016/j.watres.2014.10.028.

Matassa, S., Verstraete, W., Pikaar, I., and Boon, N. (2016). Autotrophic nitrogen assimilation and carbon capture for microbial protein production by a novel enrichment of hydrogen-oxidizing bacteria. *Water Res.*, 101, pp. 137–146. doi: 10.1016/j.watres.2016.05.077.

Mishra, A., Ntihuga, J.N., Molitor, B., and Angenent, L.T. (2020). Power-to-Protein: Carbon Fixation with Renewable Electric Power to Feed the World. *Joule*, 4(6), pp. 1142–1147. doi: 10.1016/j.joule.2020.04.008.

Molitor, B., Mishra, A., and Angenent, L.T. (2019). Power-to-protein : converting renewable electric power and carbon dioxide into single cell protein with a two-stage bioprocess. *Energy Environ. Sci.*, (12), pp. 3515–3521. doi: 10.1039/C9EE02381J.

Morales-guio, C.G., Liardet, L., and Hu, X. (2016). Oxidatively Electrodeposited Thin-Film Transition Metal (Oxy)hydroxides as Oxygen Evolution Catalysts. *J. Am. Chem. Soc.*, 138, pp. 8946–8957. doi: 10.1021/jacs.6b05196.

Nangle, S.N., Sakimoto, K.K., Silver, P.A., and Nocera, D.G. (2017). Biological-inorganic hybrid systems as a generalized platform for chemical production. *Curr. Opin. Chem. Biol.*, 41, pp. 107–113. doi: 10.1016/j.cbpa.2017.10.023.

Nevin, K.P., Woodard, T.L., Franks, A.E., Summers, Z.M., and Lovley, D.R. (2010). Microbial Electrosynthesis: Feeding Microbes Electricity To Convert Carbon Dioxide and Water to Multicarbon Extracellular Organic Compounds. *mBio*, 1(2). doi: 10.1128/mBio.00103-10.

Nian-Tzu, S., Sung-Fu, H., Quan, Q., Nan, Z., Yi-Jun, X., and Hao Ming, C. (2017). Electrocatalysis for the oxygen evolution reaction : recent development and future perspectives. *Chem. Soc. Rev.*, 46, pp. 337–365. doi: 10.1039/C6CS00328A.

Nocera, D.G. and Nash, M.P. (2006). Powering the planet: Chemical challenges in solar energy utilization. *PNAS*, 103(43), pp. 15729–15735. doi: 10.1073/pnas.0603395103.

Pekilo (2021). *EniferBIO*. URL `www.eniferbio.fi`.

Pikaar, I., Matassa, S., Rabaey, K., Bodirsky, B.L., Popp, A., Herrero, M., and Verstraete, W. (2017). Microbes and the Next Nitrogen Revolution. *Environ. Sci. Technol.*, 51(13), pp. 7297–7303. doi: 10.1021/acs.est.7b00916.

Pikaar, I., Vrieze, J.D., Rabaey, K., Herrero, M., Smith, P., and Verstraete, W. (2018). Carbon emission avoidance and capture by producing in-reactor microbial biomass based food , feed and slow release fertilizer : Potentials and limitations. *Sci. Total Environ.*, 644, pp. 1525–1530. doi: 10.1016/j.scitotenv.2018.07.089.

Poore, J. and Nemecek, T. (2018). Reducing food's environmental impacts through producers and consumers. *Sci.*, 360(6392), pp. 987–992. doi: 10.1126/science.aaq0216.

Ram, M., Bogdanov, D., Aghahosseini, A., Oyewo, S.A., Child, M., Caldera, U., Sadovskaia, K., Farfan, J., Barbosa, L.S., Fasihi, M., Khalili, S., Dalheimer, B., Gruber, G., Traber, T., Caluwe, F.D., Fell, H.J., and Breyer, C. (2019). Global Energy system based on 100% renewable energy — Power, heat, transport, and desalination sectors. In: *Study by Lappeenranta University of Technology and Energy Watch Group*. Lappeenranta, Berlin.

Reier, T., Oezaslan, M., and Strasser, P. (2012). Electrocatalytic Oxygen Evolution Reaction (OER) on Ru , Ir , and Pt Catalysts : A Comparative Study of Nanoparticles and Bulk Materials. *ACS Catal.*, 2, pp. 1765–1772. doi: https://doi.org/10.1021/cs3003098.

Repaske, R. and Mayer, R. (1976). Dense Autotrophic Cultures of Alcaligenes eutrophus. *Appl Environ Microbiol.*, 32(4), pp. 592–597.

Rieth, A.J. and Nocera, D.G. (2020). Hybrid Inorganic-Biological Systems: Faradaic and Quantum Efficiency, Necessary but Not Sufficient. *Joule*, 4(10), pp. 2051–2055. doi: 10.1016/j.joule.2020.08.012.

Ritchie (2019). *Half of the world's habitable land is used for agriculture.* URL `https://ourworldindata.org/global-land-for-agriculture`.

Ritchie (2021). *Energy Production and Consumption*. URL `https://ourworldindata.org/energy-production-consumption`.

Ritchie and Roser (2021). *Emissions by sector*. URL `https://ourworldindata.org/emissions-by-sector`.

Roser (2020). *Why did renewables become so cheap so fast? And what can we do to use this global opportunity for green growth?* URL `https://ourworldindata.org/cheap-renewables-growth`.

Schalenbach, M., Zeradjanin, A.R., Kasian, O., and Cherevko, S. (2018). A Perspective on Low-Temperature Water Electrolysis-Challenges in Alkaline and Acidic Technology. *Int. J. Electrochem. Sci.*, 13, pp. 1173–1226. doi: 10.20964/2018.02.26.

Scott, J.H. (2006). The development of fuel cell technology for electric power generation: From NASA's manned space program to the "hydrogen economy". *Proc. IEEE*, 94(10), pp. 1815–1825. doi: 10.1109/JPROC.2006.883702.

Sillman, J., Uusitalo, V., Ruuskanen, V., Ojala, L., Kahiluoto, H., Soukka, R., and Ahola, J. (2020). A life cycle environmental sustainability analysis of microbial protein production via power-to-food approaches. *Int. J. Life Cycle Assessm.*, 25, pp. 2190–2203.

Solein (2019). *Solar Foods*. URL `www.solarfoods.fi`.

Tahir, M., Pan, L., Idrees, F., Zhang, X., Wang, L., Zou, J.J., and Wang, Z.L. (2017). Electrocatalytic oxygen evolution reaction for energy conversion and storage: A comprehensive review. *Nano Energy*, 37, pp. 136–157. doi: 10.1016/j.nanoen.2017.05.022.

Tang, C., Cheng, N., Pu, Z., Xing, W., and Sun, X. (2015). NiSe Nanowire Film Supported on Nickel Foam : An Efficient and Stable 3D Bifunctional Electrode for Full Water Splitting. *Angew. Chem. Int. Ed.*, 54, pp. 9351–9355. doi: 10.1002/anie.201503407.

Tian, J., Liu, Q., Cheng, N., Asiri, A.M., and Sun, X. (2014). Self-Supported Cu_2P Nanowire Arrays as an Integrated High-Performance Three-Dimensional Cathode for Generating Hydrogen from Water. *Angew.Chem.Int. Ed.*, 53, pp. 9577–9581. doi: 10.1002/anie.201403842.

Torella, J.P., Gagliardi, C.J., Chen, J.S., Bediako, D.K., Colón, B., Way, J.C., Silver, P.A., and Nocera, D.G. (2015). Efficient solar-to-fuels production from a hybrid microbial-water-splitting catalyst system. *Proc. Nat. Acad. Sci.*, 112(8), pp. 2337–2342. doi: 10.1073/pnas.1424872112.

UniProtein (2019). *Unibio*. URL `www.unibio.dk`.

Ursúa, A., Gandía, L., and Sanchis, P. (2012). Hydrogen Production From Water Electrolysis: Current Status and Future Trends. *Proc. IEEE*, 100(2), pp. 410 –426. doi: 10.1109/JPROC.2011.2156750.

de Vasconcelos, B.R. and Lavoie, J.M. (2019). Recent advances in power-to-X technology for the production of fuels and chemicals. *Front. Chem.*, 7, pp. 1–24. doi: 10.3389/fchem.2019.00392.

Vidal, F., Koponen, J., Ruuskanen, V., Bajamundi, C., Kosonen, A., Simell, P., Ahola, J., Frilund, C., Elfving, J., Reinikainen, M., Heikkinen, N., Kauppinen, J., and Piermartini, P. (2018). Power-to-X technology using renewable electricity and carbon dioxide from ambient air : SOLETAIR proof-of-concept and improved process concept. *J. CO_2 Util.*, 28, pp. 235–246. doi: 10.1016/j.jcou.2018.09.026.

Volova, T.G. and Barashkov, V.A. (2010). Characteristics of proteins synthesized by hydrogen-oxidizing microorganisms. *Appl. Biochem. Microbiol.*, 46(6), pp. 574–579. doi: 10.1134/S0003683810060037.

Wang, X., Li, W., Xiong, D., Petrovykh, D.Y., and Liu, L. (2016). Bifunctional Nickel Phosphide Nanocatalysts Supported on Carbon Fiber Paper for Highly Efficient and Stable Overall Water Splitting. *Adv. Funct. Mater.*, 26, pp. 4067–4077. doi: 10.1002/adfm.201505509.

Wang, Z., Lin, Z., and Diao, P. (2019). Hybrids of iridium-cobalt phosphates as a highly efficient electrocatalyst for the oxygen evolution reaction in neutral solution. *ChemComm*, 55, pp. 3000–3003. doi: 10.1039/C8CC10278C.

Westlake, R. (1986). Large-scale continuous production of single cell protein. *Chemie Ing. Tech.*, 58(12), pp. 934–937.

Worldometer (2021). *Current World Population*. URL `https://www.worldometers.info/world-population/`.

Xing, J., Li, H., Cheng, M.M.c., Geyer, S.M., and Ng, K.Y.S. (2016). Electro-synthesis of 3D porous hierarchical Ni-Fe phosphate film / Ni foam as a high-efficiency bifunctional electrocatalyst for overall water splitting. *J. Mater. Chem. A*, 4, pp. 13866–13873. doi: 10.1039/c6ta05952j.

Xu, K., Chen, P., Li, X., Tong, Y., Ding, H., Wu, X., Xu, K., Chen, P., Li, X., Tong, Y., Ding, H., Wu, X., and Chu, W. (2015). Metallic Nickel Nitride Nanosheets Realizing Enhanced Electrochemical Water Oxidation. *J. Am. Chem. Soc.*, 137, pp. 4119–4125. doi: 10.1021/ja5119495.

Yoon, S., Kim, J., Lim, J.H., and Yoo, B. (2018). Cobalt Iron-Phosphorus Synthesized by Electrodeposition as Highly Active and Stable Bifunctional Catalyst for Full Water Splitting. *J. Electrochem. Soc*, 165(5), pp. H271–H276. doi: 10.1149/2.1221805jes.

Yu, J. (2014). Bio-based products from solar energy and carbon dioxide. *Trends Biotechnol.*, 32(1), pp. 5–10. doi: 10.1016/j.tibtech.2013.11.001.

Yu, J., Dow, A., and Pingali, S. (2013). The energy efficiency of carbon dioxide fixation by a hydrogen-oxidizing bacterium. *Int. J. Hydrogen Energy*, 38(21), pp. 8683–8690. doi: 10.1016/j.ijhydene.2013.04.153.

Zaffran, J. and Toroker, M.C. (2017). A deep understanding of oxygen evolution reaction on two- dimensional NiO_2 catalyst. *ChemElectroChem*, 4, pp. 2764–2770. doi: 10.1002/celc.201700445.

Zeng, K. and Zhang, D. (2010). Recent progress in alkaline water electrolysis for hydrogen production and applications. *Prog. Energ. Combust.*, 36(3), pp. 307–326. doi: 10.1016/j.pecs.2009.11.002.

Zhang, B., Lui, Y.H., Ni, H., and Hu, S. (2017a). Bimetallic $(Fe_xNi_1 - x)_2P$ nanoarrays as exceptionally efficient electrocatalysts for oxygen evolution in alkaline and neutral media. *Nano Energy*, 38, pp. 553–560. doi: 10.1016/j.nanoen.2017.06.032.

Zhang, B., Lui, Y.H., Zhou, L., Tang, X., and Hu, S. (2017b). An alkaline electro-activated Fe-Ni phosphide nanoparticle-stack array for high-performance oxygen evolution under alkaline and neutral conditions. *J. Mater. Chem. A*, 5(26), pp. 13329–13335. doi: 10.1039/c7ta03163g.

Zhang, Q., Li, T., Liang, J., Wang, N., Kong, X., Wang, J., Qian, H., Zhou, Y., Liu, F., Wei, C., Zhao, Y., and Zhang, X. (2018). High Wettable and Metallic NiFe-Phosphate/Phosphide Catalyst Synthesized by Plasma for High Efficient Oxygen Evolution Reaction. *J. Mater. Chem. A*, 6, pp. 7509–7516. doi: 10.1039/C8TA01334A.

Zhao, C., Liu, B., Piao, S., Wang, X., Lobell, D.B., Huang, Y., Huang, M., Yao, Y., Bassu, S., Ciais, P., Durand, J.L., Elliott, J., Ewert, F., Janssens, I.A., Li, T., Lin, E., Liu, Q., Martre, P., Müller, C., Peng, S., Peñuelas, J., Ruane, A.C., Wallach, D., Wang, T., Wu, D., Liu, Z., Zhu, Y., Zhu, Z., and Asseng, S. (2017). Temperature increase reduces global yields of major crops in four independent estimates. *Proc. Nat. Acad. Sci.*, 114(35), pp. 9326–9331. doi: 10.1073/pnas.1701762114.

Zhong, D., Liu, L., Li, D., Wei, C., Wang, Q., Hao, G., Zhao, Q., and Li, J. (2017). Facile and fast fabrication of iron-phosphate supported on nickel foam as a highly efficient and stable oxygen evolution catalyst. *J. Mater. Chem. A*, 5, pp. 18627–18633. doi: 10.1039/C7TA05580C.

Publication I

Givirovskiy, G., Ruuskanen, V., Ojala, L. S., Lienemann, M., Kokkonen, P., and Ahola, J.

Electrode material studies and cell voltage characteristics of the in situ water electrolysis performed in a pH-neutral electrolyte in bioelectrochemical systems

Heliyon,
vol. 5, no. 5, May. 2019

Heliyon 5 (2019) e01690

Contents lists available at ScienceDirect

Heliyon

www.elsevier.com/locate/heliyon

Electrode material studies and cell voltage characteristics of the in situ water electrolysis performed in a pH-neutral electrolyte in bioelectrochemical systems

Georgy Givirovskiy [a,*], Vesa Ruuskanen [a], Leo S. Ojala [b], Michael Lienemann [b], Petteri Kokkonen [b], Jero Ahola [a]

[a] LUT University, P.O. Box 20, FI-53851, Lappeenranta, Finland
[b] VTT Technical Research Centre of Finland Ltd., P.O. Box 1000, 02044 VTT, Finland

ARTICLE INFO

Keywords:
Bioengineering
Electrochemistry
Materials chemistry

ABSTRACT

Hydrogen-oxidizing bacteria (HOB) have been shown to be promising micro-organisms for the reduction of carbon dioxide to a wide range of value-added products in bioelectrochemical systems with in situ water electrolysis of the cultivation medium, also known as a hybrid biological-inorganic systems (HBI). However, scaling up of this process requires overcoming the inherent constraints of the low energy efficiency partly associated with the pH-neutral electrolyte with low conductivity. Most of the research in the field is concentrated on the bacterial cultivation, whereas the analysis and evaluation of the electrode material performance have received little attention in the literature so far. Therefore, in the present work, in situ electrolysis of a pH-neutral medium for HOB cultivation was performed with different combinations of electrode materials. Besides conventional electrode types, electrodes with coatings made of earth-abundant cobalt and a nickel-iron alloy, known for their catalytic activity for the kinetically sluggish oxygen evolution reaction (OER), were prepared and tested as potential substitutes for catalysts made of precious metals. The cultivation of HOB with in situ water electrolysis has been successfully tested in a small scale electrobioreactor in order to support the experimental results. A simplified water electrolysis model was developed and applied to evaluate the current-voltage characteristics of an bioelectrochemical system prototype. Application of the developed model allows quantitative evaluation and comparison of reversible, ohmic, and activation overvoltages of different electrode sets. The modeling results were found to agree well with the experimental data. The developed model and the data gathered can be applied to further investigation, simulation, and optimization of HBI systems.

1. Introduction

The rapid economic growth and the increasing consumption of fossil-fuel-based energy have led to higher concentrations of pollutant gases in the atmosphere, depletion of natural resources, adverse climate impacts, and geopolitical tensions. The global shift from a fossil-fuel-based economy to a renewable-energy-based one has the potential to tackle the aforementioned problems [1, 2]. Electrical energy produced from abundant renewable energy sources, such as solar and wind power, is considered to be the cleanest form of energy. However, the fluctuating nature of these sources leads to technical challenges associated with the storage of the generated electricity [3]. Recently, hydrogen, which is the simplest and lightest element, has been shown to be a sustainable and promising energy carrier in the Hydrogen Economy Concept [4]. Even though the currently dominating technologies of hydrogen production are steam reforming, partial oxidation of hydrocarbons, and coal gasification, the development of advanced technologies for renewable-energy-based hydrogen production is given a high priority, and the topic is attracting scientific interest. One of the most mature technologies of renewable hydrogen production is electrolysis of water [5]. By this method, surplus peak electricity from renewable energy sources is applied to generate renewable hydrogen, which can be further used in Power-to-X processes to produce net carbon-neutral fuels and chemicals [6, 7].

One approach attracting scientific interest in this context is microbial electrosynthesis (MES), electricity-driven synthesis of chemicals

* Corresponding author.
E-mail address: georgy.givirovskiy@lut.fi (G. Givirovskiy).

https://doi.org/10.1016/j.heliyon.2019.e01690
Received 19 October 2018; Received in revised form 5 April 2019; Accepted 7 May 2019

and fuels. Microbial electrosynthesis (MES) is an emerging technology capable of using water electrolysis and various microorganisms directly for the reduction of carbon dioxide to value-added compounds in bioelectrochemical systems (BESs). The concept was first proven by Nevin et al. [8], who were able to reduce carbon dioxide to acetate and small amounts of 2-oxobutyrate by applying electric current to acetogenic microorganisms. The subsequent research revealed an opportunity of applying in situ water electrolysis and microbes for the efficient production of other value-added commodities. Information about chemicals that can be produced in bioelectrochemical systems can be found in [9] and [10]. Hydrogen-oxidizing bacteria (HOB), the metabolic growth of which is based on the use of hydrogen as an electron donor and oxygen as an electron acceptor, were shown to be promising microorganisms for the reduction of carbon dioxide to a wide range of value-added products [11]. Volova et al. [12] found that the biological value of proteins synthesized by different strains of hydrogen-oxidizing bacteria is sufficient to consider them as a potential protein source for human and animal nutrition. Moreover, research is currently carried out into HOB-based single cell protein production. For instance, Matassa et al. [13] used autotrophic hydrogen-oxidizing bacteria to recycle ammonia recovered by air stripping from a wastewater treatment plant and captured CO_2, together with hydrogen and oxygen produced by water electrolysis, to food and feed [13, 14]. Furthermore, a pilot plant has been constructed in Belgium within the framework of a Power-to-Protein project, which produces single cell protein with a targeted capacity of 1 kg–2 kg per day [15]. However, these processes require external supply of hydrogen and oxygen to the bioreactors where the HOB are being cultivated. The application of bioelectrochemical system with in situ water electrolysis could provide a solution for overcoming the mass transfer limitations of this process, and could thus be considered a prospective strategy for renewable electrical energy storage. Torella et al. [16] reported development of a scalable integrated bioelectrochemical system using HOB for carbon dioxide conversion into biomass and isopropyl alcohol with maximum bioelectrochemical efficiencies of 17.8% and 3.9%, respectively. A distinctive feature of this BES was the use of a cobalt phosphate (CoPi) anode, which is capable of performing oxygen evolution reaction (OER) at low overpotentials at a neutral pH. The same anode material was used in combination with a cobalt-phosphorus (Co-P) alloy cathode in the studies of Liu et al. [17] to establish an effective water splitting system for HOB conversion into biomass at an efficiency of approximately 55% within a period of six days at an applied potential of 2.0 V. In addition to biomass, polyhydroxybutyrate (PHB), which is considered an intermediate compound in microbial assimilation of carbon dioxide, was synthesized with a 36% energy efficiency. Furthermore, different fusel alcohols were produced with efficiencies ranging from approximately 15% to 30%. Hybrid biological-inorganic (HBI) systems, which couple microorganisms with chemical catalysts to derive value-added products, have also been applied, for example, to ammonia [18] and bacterial biomass production [19].

Nevertheless, upscaling of bioelectrochemical processes for HOB cultivation requires overcoming the inherent constraints of low energy efficiency. The target of the present study is to develop a scalable energy efficient system for cultivation of hydrogen-oxidizing bacteria. The effects of various oxygen evolution (OER) catalysts are extensively reported in the literature for alkaline water electrolyzers, but there are only a few studies of electrolyzer cell performance in bioreactors with pH-neutral conditions so far. Further, a simplified mathematical model is introduced, based on models developed for traditional water electrolyzers. The model parameters are tuned and the model is verified by experimental results. The model is applied to quantitatively evaluate and compare possible overvoltage sources in the system with various electrode materials.

This paper is organized as follows. The characteristics of the in situ water electrolysis, initial HOB cultivation results with in situ water electrolysis, the experimental setup used for electrode material tests, the procedure describing in situ formation of coatings, and the simplified electrolyzer cell voltage model are introduced in Section 2. The cell voltage model parameters are fitted by experimental results, and the model is applied to describe the performance of the selected electrode materials in Section 3. Finally, Section 4 concludes the paper.

2. Materials & methods

This section first defines the special characteristics of the in situ water electrolysis compared with traditional water electrolyzers. HOB cultivation results with in situ water electrolysis are shown. Further, the experimental setup and methods applied for electrolyzer cell studies in this paper, including the analytical model used to describe the operation characteristics of the electrolytic cell, are introduced.

2.1. In situ water electrolysis characteristics

One of the key issues of the gas-fermentation-based hydrogen-oxidizing bacteria production is the mass transfer of the hydrogen gas to the cultivation medium, even though a hydrogen gas conversion efficiency up to 81% has been reported [13]. The mass transfer problems can be effectively avoided by BES, where the in situ water electrolysis takes place directly in the cultivation medium. However, the in situ water electrolysis imposes some constraints on the system. Firstly, the temperatures and pressures must be in a favorable range for the HOB. Secondly, the current densities applied to the water electrolysis must be limited to levels not harming the HOB. Finally, numerous requirements are set on the electrolyte, which also acts as a cultivation medium, and the electrodes themselves. Contrary to the traditional alkaline water electrolysis, the cultivation medium must offer an almost pH-neutral environment for the bacteria. This constraint is connected to the kinetically sluggish oxygen evolution reaction (OER), which produces a high activation overvoltage. Further, the side reactions producing toxic compounds must be prevented. In practice, these limitations lead to a significantly lower conductivity of the electrolyte compared with the traditional alkaline electrolysis. Therefore, to achieve an acceptable energy efficiency of the water electrolysis, relatively low current densities have to be applied, which leads to large electrode areas, yet the distance between the electrodes is minimized. Because of the large electrode area, low-cost electrode materials are preferred. Finally, the electrode materials must be corrosion resistant not to release any toxic compounds to the cultivation medium.

2.2. HOB cultivation experiments with in situ water electrolysis

The cultivation of HOB with in situ water electrolysis has been successfully tested in a small scale electrobioreactor [20]. The research utilized a BES with internal liquid volume of 60 ml as shown in Fig. 1a. CO_2 gas was fed to the reactor, while hydrogen and oxygen for the microbial growth and CO_2 fixation were generated inside the reactor vessel at a stainless steel cathode and an iridium oxide coated titanium anode. The electrodes were manufactured from wires of aforementioned materials which were looped in coils so that the surface of each electrode was 13 cm^2.

In Fig. 1b, the biomass increase of a hydrogen enrichment culture is presented. The culture was a mixed population of yet unidentified species, which had evolved at least some resistance towards the BES environment. The bioreactor was fed with 0.13 $g\,h^{-1}$ gaseous CO_2, and supplied with electrolysis current of 18 mA, which roughly equals current density of 1 $mA\,cm^{-2}$ at the surface of the electrodes, with average cell voltage of 2.31 V.

The cell mass increases in linear fashion as the growth is limited by the availability of hydrogen. Assuming faradic efficiency of unity for the electrolysis of water and complete consumption of the hydrogen, the apparent biomass yield from hydrogen was calculated to be 2.5 $g_{biomass}/mol_{H_2}$. Matassa et al. have collected biomass to hydrogen

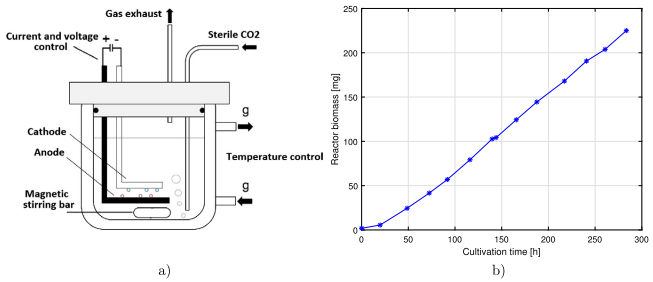

Fig. 1. Experimental setup used for the cultivation tests: (a) scheme of the small-scale in-situ electrolysis bioelectrochemical system, and (b) biomass increase of a mixed hydrogen enrichment culture.

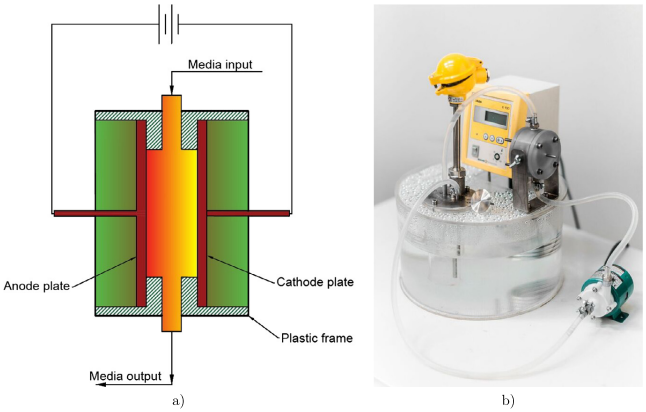

Fig. 2. Experimental setup used for the electrolysis tests: (a) cross section of the electrolyzer cell, (b) photo of the experimental setup.

yields for various HOB species cultivated with gaseous hydrogen feed [13].

The published values range between 1.12 $g_{biomass}/mol_{H_2}$–4.64 $g_{biomass}/mol_{H_2}$, therefore the HOB cultivation with in situ electrolysis gives biomass yield comparable to the gaseous H_2 feed cultivation, but without the need for handling and storage of flammable, and potentially explosive, hydrogen gas and hydrogen – oxygen gas mixtures.

The volumetric productivity of biomass during the cultivation test is below 15 $mg\,l^{-1}\,h^{-1}$ while the hydrogen production is the limiting factor for the growth. Therefore, the hydrogen production rate must be improved to enhance the volumetric productivity of the electrobioreactor. Therefore, the current density or electrode area must be increased to improve the productivity. In this article, the electrode materials are studied to enhance the current density without lowering the efficiency.

2.3. Experimental electrode material study setup

The experimental setup is presented in Fig. 2. The setup consists of the following elements: (i) an electrolyzer cell with a cross-sectional area of 2.6 cm^2 and an initial distance of 3 mm between the electrodes, (ii) a WaveNow potentiostat to conduct electrochemical measurements, (iii) a water bath with a submerged Lauda heater to keep the system optimal for the bacterial cultivation temperature of 33 °C, and (iv) a constant flow pump to circulate the medium through the external vessel equipped with the temperature measurement. Different combinations of electrode materials, such as stainless steel (SS), nickel (Ni), graphite (C), platinum (Pt), cobalt phosphate (CoPi), nickel-iron (NiFe), and iridium dioxide (IrO_2) deposited onto a titanium substrate, were tested. Stainless steel is widely used material because of the relatively low cost and high corrosion resistance in most environments. Applicability of SS 304 material for HOB cultivations was first studied by [16], while the effect of stainless steel or carbon surface modification by CoPi or CoP electrocatalysts was further investigated in the subsequent state of the art studies of the same research group [17, 18, 19]. However, HOB have showed to have effect on the corrosion of the low carbon steels [21]. Further, the selected 316L has been mentioned to be vulnerable to microbial corrosion, and some other steel should be selected if uncoated electrodes are used for longer periods of time [22]. Platinum is widely used as electrode material because of its stability despite the high cost. Nickel based metals are widely used in alkaline water electrolyzers, and therefore, used as a reference for the other materials [23]. Graphite is also stable, but not highly catalytic material. CoPi coatings are shown to be self healing and biocompatible in the literature [17]. IrO_2 coated anode is found to be a promising candidate in the HOB cultivation experiments described above. Linear sweep voltammetry (I–V) was applied to measure the cell voltage as a function of cell current. The sweep rate of the linear sweep voltammetry was selected to be 10 $mV\,s^{-1}$ to mitigate the effect of cell capacitances.

The mineral medium, used for the bioelectrochemical cultivation of hydrogen-oxidizing bacteria prepared according to the DSM-81-LO4 recipe at the VTT Technical Research Centre of Finland, was applied as an electrolyte in the study. One liter of the medium solution con-

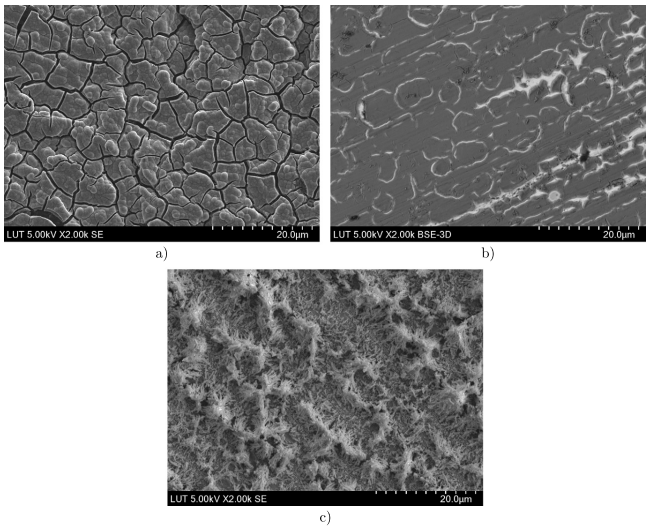

Fig. 3. Scanning electron microscope (SEM) images of the cobalt phosphate (CoPi) coating onto (a) graphite substrate, (b) stainless steel substrate, and (c) nickel-iron (NiFe) coating onto stainless steel substrate.

tained distilled water, 50 ml of phosphate buffer, 2.3 g (KH_2PO_4), 2.9 g (Na_2HPO_4), 2 ml (NH_4)(Fe)(citrate), 0.005 g of ferric ammonium citrate (16% Fe), 10 ml of ($NaHCO_3$) solution, 0.5 g ($NaHCO_3$), mineral salts, 5.45 g (Na_2SO_4), 1.19 g ($(NH_4)_2SO_4$), 0.5 g ($MgSO_4{\cdot}5H_2O$), 0.0117 g ($CaSO_4{\cdot}2H_2O$), 0.0044 g ($MnSO_4{\cdot}1H_2O$), 0.005 g ($NaVO_3$), and 5 ml of trace element solution. 500 ml of trace element stock solution was made from 0.05 g ($ZnSO_4{\cdot}7H_2O$), 0.15 g (H_3BO_3), 0.1 g ($CoCl_2{\cdot}6H_2O$), 0.005 g ($CuCl_2{\cdot}2H_2O$), 0.01 g ($NiCl_2{\cdot}6H_2O$), and 0.015 g (Na_2MoO_4). The phosphate buffer, the ammonium iron (III) citrate, the mineral salts, and the trace element solutions were autoclaved separately. The vitamin solution ($NaHCO_3$) was filter sterilized. The solutions were combined aseptically at room temperature. The pH and conductivity of the medium, measured before and after the electrolysis tests, were 7 and 12 mS cm^{-1}, respectively.

2.4. In situ catalyst formation

Electrodeposition of coatings based on earth-abundant first-row transition metals such as Co and Fe–Ni is considered an efficient method for the electrode surface structure modification and enhancement of the electrochemical activity. In the present study, in situ preparation of coatings was performed in the experimental setup described in the previous section based on the electrodeposition strategies adopted from [16] and [24]. Cobalt phosphate (CoPi) coating was electrodeposited onto graphite and stainless steel plates (substrates) in a solution containing 0.1 M KH_2PO_4 and 0.5 mM $Co(NO_3)_2{\cdot}6H_2O$ and 250 ml of distilled deionized water. Pretreatment of the electrode samples included polishing with sand paper and rinsing with acetone and deionized water. Electrolytic deposition was carried out by bulk electrolysis at 2 V for 5 h for the graphite substrate and for 3 h for the stainless steel substrate. Graphite and stainless steel were used as the auxiliary and reference electrode for the corresponding experiments in a two-electrode system. Solution with two times increased concentration of Co_{2+} was also deposited onto the stainless steel substrate to investigate the influence of the increased cobalt mass on the coating structure and the electrochemical performance of the synthesized catalyst.

In situ formation of nickel-iron (NiFe) coating was carried out by the bulk electrolysis method at 2.8 V for 15 min in the solution containing 0.1 M Na_2SO_4, 0.25 M $NiSO_4{\cdot}6H_2O$, 0.25 M $FeSO_4{\cdot}7H_2O$, and 250 ml of distilled deionized water. A small amount of H_2SO_4 was added to the solution to adjust the pH to 2. A stainless steel plate with the aforementioned pretreatment was used as a substrate for the electrolytic deposition of the nickel-iron (NiFe) film. Scanning electron microscope (SEM) images of the obtained cobalt phosphate (CoPi) and nickel-iron (NiFe) structures are presented in Fig. 3.

2.5. Cell model

In neutral conditions (pH=7), the water electrolysis is described by the following electrochemical reactions [7]. Oxidation half-reaction at the anode–oxygen evolution reaction (OER):

$$2H_2O \longrightarrow O_2 + 4H^+ + 4e^-,\ E_0 = 0.817\ \text{V} \tag{1}$$

Reduction half-reaction at the cathode–hydrogen evolution reaction (HER):

$$4H_2O + 4e^- \longrightarrow 2H_2 + 4OH^-,\ E_0 = -0.413\ \text{V} \tag{2}$$

The overall reaction in the electrolytic cell:

$$2H_2O + \text{electrical energy} \longrightarrow O_2 + 2H_2,\ E_0 = -1.23\ \text{V} \tag{3}$$

The above equations demonstrate that the equilibrium or reversible cell voltage, which is the lowest potential required for the electrolysis to take place at 25 °C and 1 atm, is equal to 1.23 V. However, in practice, higher voltages are required to dissociate water; this is due to the additional overvoltages presented in the following equation:

$$U_{\text{cell}} = U_{\text{rev}} + U_{\text{ohm}} + U_{\text{act}} + U_{\text{con}}, \tag{4}$$

where U_{cell} is the cell voltage, U_{rev} is the reversible open circuit voltage, U_{ohm} is the overvoltage caused by ohmic losses in the cell elements, U_{act} is the activation overvoltage caused by electrode kinetics, and U_{con} is the concentration overvoltage caused by mass transport processes [1].

In electrolysis, the production of hydrogen and oxygen is directly proportional to the mean value of the current flowing through the electrolyzer cell. Thus, the hydrogen and oxygen production rates (mol s^{-1}) of a single electrolytic cell can be expressed as:

$$f_{H_2} = \eta_F \frac{i_{cell} A_{cell}}{zF}, \quad (5)$$

where z (z = 2 and 4 for hydrogen and oxygen, respectively) is the number of moles of electrons transferred in the reaction, F is the Faraday constant (9.6485×10^4 C mol^{-1}), i_{cell} is the current density (A cm^{-2}), A_{cell} is the effective cell area (cm^2), and η_F is the Faraday efficiency, also known as the current efficiency. In this study, the Faraday efficiency can be assumed to be unity because there should be no leakage currents, and further, as the product gas is a mixture of hydrogen and oxygen, there is no leakage of hydrogen to the oxygen line as in traditional electrolyzers [25]. Therefore, the hydrogen production rate can be directly estimated based on current, and the voltage eventually describes the energy efficiency of the cell.

A simplified model to describe the electrolytic cell voltage behavior as a function of current is introduced. The open-circuit voltage can be described using the Nernst equation [26]

$$U_{rev} = U^0_{rev} + \frac{RT_{el}}{zF} \ln\left(\frac{p_{H_2} \cdot p_{O_2}^{1/2}}{p_{H_2O}}\right), \quad (6)$$

where U^0_{rev} is the reversible cell voltage, R is the universal gas constant (8.3144621 J mol^{-1} K^{-1}), and T_{el} is the temperature. Further, p_{H_2}, p_{O_2}, and p_{H_2O} are the hydrogen, oxygen, and water partial pressures.

The reversible cell voltage is defined as a function of temperature; for example, for a PEM electrolyzer cell in [27] and for an alkaline electrolyzer cell with the KOH electrolyte in [28]. However, in this simplified case, the open-circuit cell voltage under constant operating temperature and atmospheric pressure is considered as one parameter to be found by the curve fitting of the measured data.

The ohmic overpotential is mainly caused by the voltage across the cultivation medium with the conductivity in the range of 10 mS cm^{-1} as the conductivity of titanium or stainless steel electrodes is roughly 2.5 kS cm^{-1}. Therefore, the ohmic overpotential can be expressed as

$$U_{ohm} = \frac{\delta_m i_{cell}}{\sigma_m}, \quad (7)$$

where δ_m is the distance between the electrodes in (cm), and σ_m is the conductivity of the medium in (S cm^{-1}).

The activation overpotential is typically described by using the Butler–Volmer equation [29]

$$U_{act} = \frac{RT_{el}}{\alpha_{an} F} \operatorname{arcsinh}\left(\frac{i_{cell}}{2i_{o,an}}\right) + \frac{RT_{el}}{\alpha_{cat} F} \operatorname{arcsinh}\left(\frac{i_{cell}}{2i_{o,cat}}\right), \quad (8)$$

where α is the charge transfer coefficient for the anode and the cathode separately, and i_o is the exchange current density on the electrode surfaces. The charge transfer coefficients and the exchange current densities are experimentally defined as a function of temperature for example in [30].

Finally, the simplified model for the cell voltage as a function of current can be expressed as

$$U_{cell} = U_{rev} + \frac{\delta_m i_{cell}}{\sigma_m} + \alpha \operatorname{arcsinh}\left(\frac{i_{cell}}{2i_0}\right), \quad (9)$$

where U_{rev}, σ_m, α, and i_0 are the parameters to be fitted by the experimental data.

3. Results & discussion

Graphite was used as an electrode material for the first bioelectrochemical cultivation tests of an acetogenic microorganism in [8]. Nickel and stainless steel have traditionally been used with alkaline electrolyzers whereas noble metals and their oxides, such as platinum and iridium dioxide, are known for their high catalytic activity. Therefore, the performance of the aforementioned materials was studied for the electrolyte introduced in Section 2. The potential of coated electrodes prepared by electrodeposition of Co and a Fe–Ni alloy as a possible substitute for electrodes made of precious metals was also evaluated.

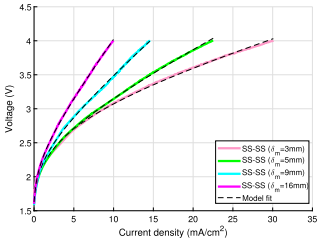

Fig. 4. Experimental results of water electrolysis with stainless steel (SS) electrodes, obtained with a variable distance, and the modeling results with Eq. (9).

Both hydrogen and oxygen are important in the cultivation of HOB, and thus, a membrane-free electrolyzer cell prototype was used for the electrolysis tests. The absence of a membrane makes it possible to decrease the distance between the electrodes and increase the electrical efficiency, which is especially important in pH-neutral conditions. However, the flow of biomass through the electrolyzer can become an issue at very low distances between the electrodes. Hence, the electrode materials were tested at distances varying from 3 mm to 16 mm to collect the voltage-current characteristics of the electrolyzer cell as a function of distance between the electrodes. In the present section, the linear sweep voltammetry results for various anode and cathode material sets of the in situ water electrolysis are presented and analyzed with the developed cell model.

3.1. Stainless steel electrodes

First, stainless steel electrodes were used as the anode and the cathode. The main solutes of the Sanmac 316L alloy per weight are: chromium 17.0%, nickel 10.1%, molybdenum 2.0%, and manganese 1.6%. The distance of the electrodes was varied to study the effect of distance on the cell voltage. Further, the results are used to verify the simplified cell model. As only the distance between the electrodes is changed and resistive conduction losses are described by the medium conductivity, all the model parameters should match each other in all cases. A minimum distance of 3 mm between the electrodes was selected to limit the flow resistance of the electrolyte. Further, it was assumed that distances exceeding 10 mm cannot be used because of the low conductivity of the electrolyte. The cell voltage as a function of current density is shown in Fig. 4.

The distance between the electrodes has a significant impact on voltage owing to the high ohmic losses caused by the low conductivity of the medium. If the voltage efficiency of the electrolysis is required to be higher than 50%, considering the thermoneutral voltage of 1.48 V, the current density cannot exceed the value of 10 mA cm^{-2} at the distance of 3 mm between the electrodes as the current densities in commercial alkaline electrolyzers are up to 500 mA cm^{-2} [31]. At greater distances the allowed current density would be even lower. Therefore, it can be concluded that the distance between the electrodes should be as short as possible to achieve a high efficiency and a compact structure. The parameters U_{rev}, σ_m, α, and i_0 in Eq. (9) were determined using experimental voltage and current data and the method of nonlinear least square regression, and presented in Table 1. Further, the reversible voltage, the ohmic voltage, and the activation voltage terms are presented separately in Fig. 5.

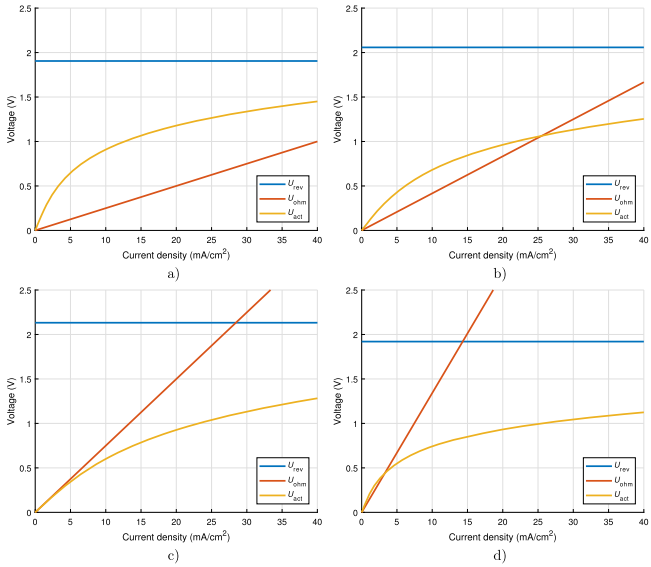

Fig. 5. Reversible voltage, ohmic overvoltage, and activation overvoltage as a function of current density for the water electrolysis experiments with a variable distance between the stainless steel electrodes: (a) $\delta_m = 3$ mm, (b) $\delta_m = 5$ mm, (c) $\delta_m = 9$ mm, and (d) $\delta_m = 16$ mm.

Table 1
Experimentally fitted parameters of the simplified cell model with stainless steel electrodes.

δ_m (mm)	U_{rev} (V)	σ_m (S cm^{-1})	α (-)	i_0 (A cm^{-1})
3	1.905	0.012	0.393	0.0010
6	2.058	0.012	0.425	0.0021
9	2.132	0.012	0.530	0.0036
16	1.92	0.012	0.278	0.0007

We can see that the ohmic overpotential becomes higher than the activation overpotential at relatively moderate current densities of 3 mA cm^{-1}–25 mA cm^{-1} depending on the distance between the electrodes. At great distances between the electrodes the ohmic overpotential even exceeds the reversible voltage. The reversible voltage and the activation overpotential are almost the same with all distances between the plates, as supposed, that supports the use of the simplified model.

3.2. Anode material comparison

According to Eq. (1), the potential of the anode half reaction is higher than the potential of the cathode half reaction. Therefore, all the studied materials were applied to the anode as the cathode is made of stainless steel. The cell voltages with different anode materials with the electrode distance of 3 mm are presented as a function of current density in Fig. 6.

As can be seen in Fig. 6, the anode material has a significant effect on the cell voltage, especially at higher current densities. Graphite clearly exhibits the worst performance with the highest cell voltage, and the nickel and platinum anodes have voltages relatively close to each other. The iridium-dioxide-coated anode is obviously the most favorable anode material of the studied materials. With the iridium dioxide, a current density of 15 mA cm^{-2} can be achieved with a voltage efficiency of 50%. The reversible voltage, the ohmic voltage, and the activation voltage terms as a function of current density with different anode materials are compared with each other in Fig. 7 and the model parameters are shown in Table 2.

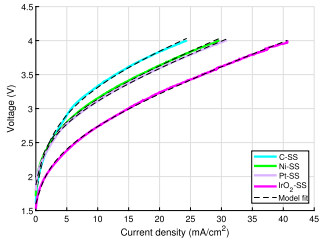

Fig. 6. Cell voltage as a function of current density with various anode materials and a stainless steel cathode. The solid lines indicate the measured data and the dashed lines represent the simplified model.

Table 2
Experimentally fitted parameters of the simplified cell model with various anode materials.

Anode	U_{rev} (V)	σ_m (S cm^{-1})	α (-)	i_0 (A cm^{-1})
C	2	0.012	0.455	0.0010
Ni	2	0.012	0.338	0.0007
Pt	1.975	0.012	0.332	0.0007
IrO_2	1.766	0.012	0.351	0.0013

The material selection significantly affects the reversible voltage and the activation voltage. The iridium oxide yields a slightly lower reversible voltage compared with the other materials. The activation overpotential is highest in the case of the graphite anode as the activation overpotentials with the other materials are in the same range with each other. Furthermore, the resistive voltage loss is mainly caused by

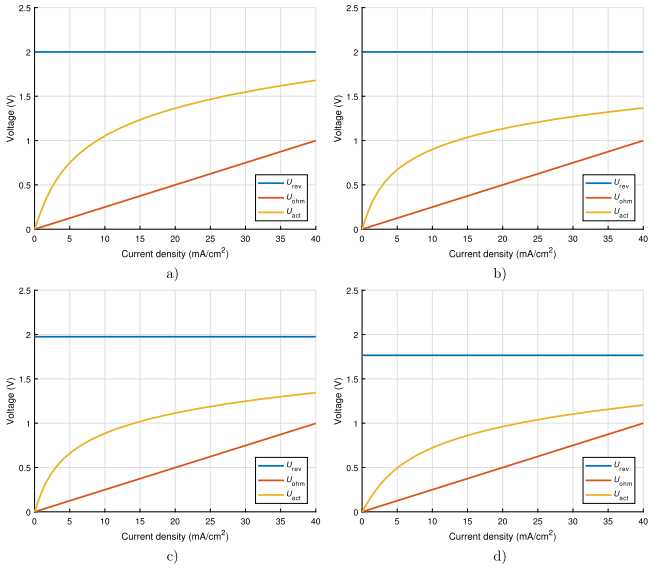

Fig. 7. Separated overvoltages for the water electrolysis experiments with different anode materials: (a) graphite (C), (b) nickel (Ni), (c) platinum (Pt), and (d) iridium dioxide (IrO_2).

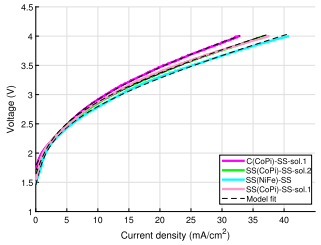

Fig. 8. Cell voltage as a function of current density with coated electrodes used as the anodes and stainless steel as the cathode.

the low-conductivity electrolyte medium, and thus, the electrode material has practically no impact on it.

3.3. Coated electrodes

Subsequently, coated electrodes were applied to the anode and stainless steel was used as the cathode. The cell voltages with different coated anode materials with the electrode distance of 3 mm are presented as a function of current density in Fig. 8.

It can be clearly seen from Fig. 8 that coated electrodes can be considered an attractive alternative for catalysts made of precious metals. Electrodeposition of Co and the Ni-Fe alloy enables substrate surface structure modification by enhancement of the electrochemically active surface area, which is well shown in Fig. 3. The obtained highly ordered CoPi coatings exhibited a better performance than the Pt anode, whereas the performance of the Ni-Fe film was comparable with the IrO_2 anode. A current density of approximately 14 mA cm^{-2} was achieved with a voltage efficiency of 50% when using stainless steel coated with the Ni-Fe alloy. It was also found that the substrate material had an effect on the electrochemical performance of the electrode. The performance of the CoPi coating on the graphite substrate was slightly lower than the performance of the same coating electrodeposited onto stainless steel substrates. The performances of the CoPi coatings electrodeposited onto the stainless steel substrate from solution 1 and solution 2 with 0.5 and 1 mM concentrations of Co_{2+}, respectively, were similar.

Table 3
Experimentally fitted parameters of the simplified cell model with various coated electrodes used as the anode materials.

Anode	U_{rev} (V)	σ_m (S cm^{-1})	α (-)	i_0 (A cm^{-1})
C(CoPi-sol.1)	1.790	0.012	0.443	0.0014
SS(CoPi-sol.1)	1.630	0.012	0.359	0.0006
SS(CoPi-sol.2)	1.695	0.012	0.370	0.0009
SS(NiFe)	1.449	0.012	0.338	0.0004

The reversible voltage, the ohmic voltage, and the activation voltage terms as a function of current density with different coated anodes are compared with each other in Fig. 9 and the model parameters are shown in Table 3.

3.4. Cathode material comparison

Finally, the most promising anode materials were also used as the cathode material to see if the performance can be further improved. The cell voltages with different anode and cathode material combinations are presented as a function of current density in Fig. 10, and the model parameters are summarized in Table 4.

Current densities of 25, 15, and 10 mA cm^{-2} were achieved with the voltage efficiency of 50% for IrO_2, Pt, and SS used for both the anode and the cathode. In the previous research [16], HOB managed to tolerate and grow at current densities up to approximately 4 mA cm^{-2} with 2.5 V cell potential. Further increase of the driving voltage up to 3 V resulted in the exponential increase of the cell densities and the

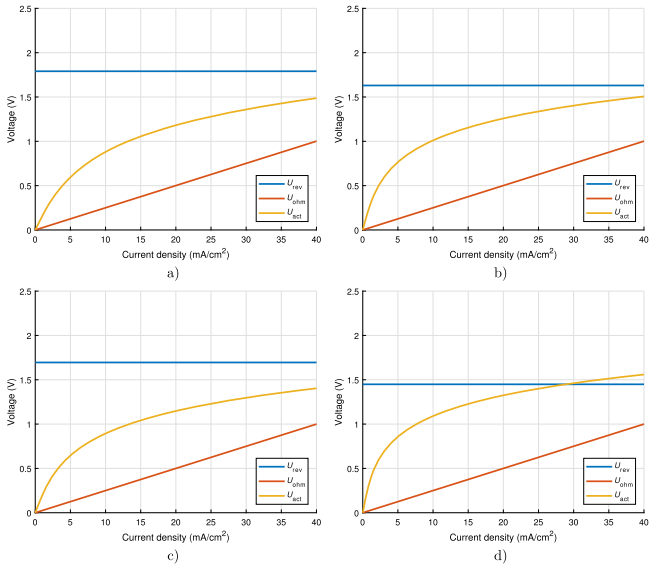

Fig. 9. Separated overvoltages for the water electrolysis experiments with different coated electrodes used as the anode materials: (a) graphite coated with CoPi using solution 1, (b) stainless steel coated with CoPi using solution 1, (c) stainless steel coated with CoPi using solution 2, and (d) stainless steel coated with NiFe.

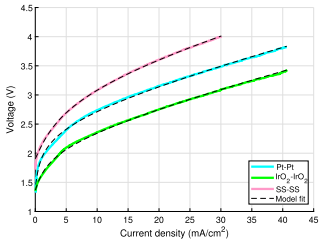

Fig. 10. Cell voltage as a function of current density with the best-performing anode and cathode materials.

Table 4
Experimentally fitted parameters of the simplified cell model with the best-performing electrode materials.

An./Cath.	U_{rev} (V)	σ_m (S cm^{-1})	α (-)	i_0 (A cm^{-1})
Pt-Pt	1.4	0.012	0.255	0.0002
IrO_2-IrO_2	1.366	0.012	0.227	0.0004

highest reported value for the current density, which bacteria managed to tolerate, was 11 mA cm^{-2}.

It is important to note, that there was no substantial increase in the performance when using CoPi and Ni-Fe coated catalysts for both electrodes in comparison with the experiments where SS was used as the cathode material. Thus, we can state that the aforementioned coatings are catalytically active for oxygen evolution reaction (OER) but do not exhibit high catalytic activity for hydrogen evolution reaction (HER). Even though IrO_2 shows the best performance as the anode and cathode material, the SS performance is still acceptable when considering the high manufacturing cost of catalysts made of precious metals. Furthermore, the SS can be considered a potential cost-effective substrate material for electrodeposition of coatings. It can be concluded that in a neutral environment the cathode material also has a significant effect on the water electrolysis performance. The cell overpotentials with different electrode material combinations are shown in Fig. 11.

The reversible voltage with both the platinum- and iridium-dioxide-coated cathodes is significantly lower than with the stainless steel cathode. Further, the iridium-dioxide-coated cathode exhibits a lower activation overpotential than platinum.

4. Conclusions

In the present paper, a simplified cell model was proposed to describe the cell voltage components as a function of current density. It is noteworthy that the chemical formulation of the electrolyte significantly affects the electrical resistance of the electrolysis cell and thereby the energy efficiency of the whole process. The developed model was implemented to analyze the applicability of numerous electrode materials for the in situ electrolysis of a pH-neutral medium for bioelectrochemical cultivation of hydrogen oxidizing bacteria. The model enables quantitive evaluation of the reversible voltage, ohmic overpotential, and activation overpotential for different sets of electrode materials.

The obtained highly ordered CoPi and Ni-Fe coatings exhibited an oxygen evolution reaction (OER) performance exceeding that of the Pt anode and being comparable with the IrO_2 anode. However, the aforementioned coatings did not show a substantial improvement in performance for the hydrogen evolution reaction (HER) compared with the stainless steel cathode. Based on this observation, we can conclude that additional research is required to find suitable coatings with high electrocatalytic performance for the HER.

The lowest cell voltage as a function of current density was reached with the IrO_2 coating both at the anode and the cathode. With the stainless steel electrodes, the same voltage level was achieved at roughly 50% lower current densities compared with the IrO_2-coated electrodes.

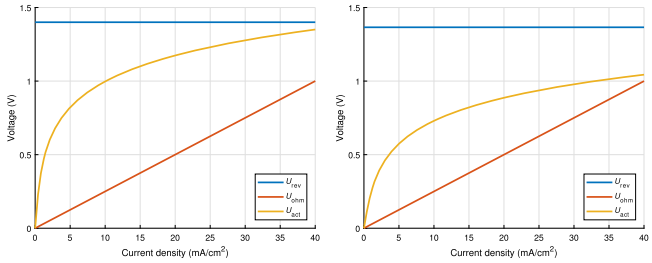

Fig. 11. Separated overvoltages for the water electrolysis experiments of the best electrode material combinations: (a) platinum-platinum (Pt–Pt), and (b) iridium-iridium (IrO_2–IrO_2).

Despite this, the stainless steel can be considered a potential cost-effective substrate material for preparation of coatings in electrobioreactors with in situ electrolysis of media.

A detailed energy efficiency analysis of the bioelectrochemical system and an analysis of the effects of the in situ water electrolysis on the microbial growth, e.g. maximum allowable current density, will be conducted in the further research into the topic.

Declarations

Author contribution statement

Georgy Givirovskiy, Vesa Ruuskanen, Jero Ahola, Leo Ojala, Michael Lienemann, Petteri Kokkonen: Conceived and designed the experiments; Performed the experiments; Analyzed and interpreted the data; Contributed reagents, materials, analysis tools or data; Wrote the paper.

Funding statement

This work was supported by Finnish Academy of Science for "MOPED – Microbial Oil and Proteins from Air by Electricity-Driven Microbes" project funding under number 295866.

Competing interest statement

The authors declare no conflict of interest.

Additional information

No additional information is available for this paper.

References

[1] A. Ursúa, L. Gandía, P. Sanchis, Hydrogen production from water electrolysis: current status and future trends, Proc. IEEE 100 (2) (2012) 410–426.
[2] I. Dincer, C. Acar, Review and evaluation of hydrogen production methods for better sustainability, Int. J. Hydrog. Energy 40 (34) (2014) 11094–11111.
[3] T. Kousksou, P. Bruel, A. Jamil, T. El Rhafiki, Y. Zeraouli, Energy storage: applications and challenges, Sol. Energy Mater. Sol. Cells 120 (PART A) (2014) 59–80.
[4] United Nations Environment Programme, The hydrogen economy: a non-technical review, https://www.unenvironment.org/resources/report/hydrogen-economy-non-technical-review, 2006.
[5] S.E. Hosseini, M.A. Wahid, Hydrogen production from renewable and sustainable energy resources: promising green energy carrier for clean development, Renew. Sustain. Energy Rev. 57 (2016) 850–866.
[6] M. Lehner, R. Tichler, H. Steinmüller, M. Koppe, Power-to-Gas: Technology and Business Models, Springer International Publishing, New York, 2014.
[7] Y. Cheng, S.P. Jiang, Advances in electrocatalysts for oxygen evolution reaction of water electrolysis-from metal oxides to carbon nanotubes, Prog. Nat. Sci. 25 (6) (2015) 545–553.
[8] K.P. Nevin, T.L. Woodard, A.E. Franks, Z.M. Summers, D.R. Lovley, Microbial electrosynthesis: feeding microbes electricity to convert carbon dioxide and water to multicarbon extracellular organic compounds, mBio 1 (2) (2010), http://mbio.asm.org/content/1/2/e00103-10.full.pdf.
[9] S. Bajracharya, M. Sharma, G. Mohanakrishna, X. Dominguez Benneton, D.P. Strik, P.M. Sarma, D. Pant, An overview on emerging bioelectrochemical systems (BESs): technology for sustainable electricity, waste remediation, resource recovery, chemical production and beyond, Renew. Energy 98 (2016) 153–170.
[10] G. Kumar, R.G. Saratale, A. Kadier, P. Sivagurunathan, G. Zhen, S.H. Kim, G.D. Saratale, A review on bio-electrochemical systems (BESs) for the syngas and value added biochemicals production, Chemosphere 177 (2017) 84–92.
[11] J. Yu, A. Dow, S. Pingali, The energy efficiency of carbon dioxide fixation by a hydrogen-oxidizing bacterium, Int. J. Hydrog. Energy 38 (21) (2013) 8683–8690.
[12] T.G. Volova, V.A. Barashkov, Characteristics of proteins synthesized by hydrogen-oxidizing microorganisms, Appl. Biochem. Microbiol. 46 (6) (2010) 574–579.
[13] S. Matassa, W. Verstraete, I. Pikaar, N. Boon, Autotrophic nitrogen assimilation and carbon capture for microbial protein production by a novel enrichment of hydrogen-oxidizing bacteria, Water Res. 101 (2016) 137–146.
[14] S. Matassa, N. Boon, I. Pikaar, W. Verstraete, Microbial protein: future sustainable food supply route with low environmental footprint, Microb. Biotechnol. 9 (5) (2016) 568–575.
[15] F. Oesterholt, S. Matassa, L. Palmen, K. Roest, W. Verstraete, Pilot scale production of single cell proteins using the power-to-protein concept future global challenges, in: 2nd International Resource Recovery Conference, 2018, pp. 1–16.
[16] J.P. Torella, C.J. Gagliardi, J.S. Chen, D.K. Bediako, B. Colón, J.C. Way, P.A. Silver, D.G. Nocera, Efficient solar-to-fuels production from a hybrid microbial–water-splitting catalyst system, Proc. Natl. Acad. Sci. 112 (8) (2015) 2337–2342.
[17] C. Liu, M. Ziesack, P.A. Silver, Water splitting – biosynthetic system with CO_2 reduction efficiencies exceeding photosynthesis, Science 352 (6290) (2016) 1210–1213.
[18] C. Liu, K.K. Sakimoto, B.C. Colón, P.A. Silver, D.G. Nocera, Ambient nitrogen reduction cycle using a hybrid inorganic–biological system, Proc. Natl. Acad. Sci. 114 (25) (2017) 6450–6455.
[19] C. Liu, B.E. Colón, P.A. Silver, D.G. Nocera, Solar-powered CO_2 reduction by a hybrid biological | inorganic system, J. Photochem. Photobiol. A, Chem. 358 (2018) 411–415.
[20] M. Wuokko, Chemolithoautotrophic Growth of Knallgas Bacteria in an Electrobioreactor Using in situ Water Electrolysis, Master's thesis, 2017, http://urn.fi/URN:NBN:fi:aalto-201705114594.
[21] R. Moreira, M.K. Schütz, M. Libert, B. Tribollet, V. Vivier, Fluence of hydrogen-oxidizing bacteria on the corrosion of low carbon steel: local electrochemical investigations, Bioelectrochemistry 97 (2014) 69–75.
[22] Sandvik, Microbiologically influenced corrosion (MIC), https://www.materials.sandvik/fi-fi/tietopankki/korroosiotietoja/wet-corrosion/microbiologically-influenced-corrosion-mic/, 2019. (Accessed 4 April 2019).
[23] M. Schalenbach, A.R. Zeradjanin, O. Kasian, S. Cherevko, A perspective on low-temperature water electrolysis – challenges in alkaline and acidic technology, Int. J. Electrochem. Sci. 13 (2018) 1173–1226.
[24] K.H. Kim, J.Y. Zheng, W. Shin, Y.S. Kang, Preparation of dendritic NiFe films by electrodeposition for oxygen evolution, RSC Adv. 2 (2012) 4759–4767.
[25] M. Schalenbach, M. Carmo, D. Fritz, J. Mergel, D. Stolten, Pressurized PEM water electrolysis: efficiency and gas crossover, Int. J. Hydrog. Energy 38 (35) (2013) 14921–14933.
[26] A. Awasthi, K. Scott, S. Basu, Dynamic modeling and simulation of a proton exchange membrane electrolyzer for hydrogen production, Int. J. Hydrog. Energy 36 (22) (2011) 14779–14786.
[27] K. Harrison, E. Hernández-Pacheco, M. Mann, H. Salehfar, Semiempirical model for determining PEM electrolyzer stack characteristics, J. Fuel Cell Sci. Technol. 3 (2) (2005) 220–223.
[28] R. LeRoy, C. Bowen, D. LeRoy, The thermodynamics of aqueous water electrolysis, J. Electrochem. Soc. 127 (9) (1980) 1954–1962.

[29] J. Larminie, A. Dicks, Fuel Cell Systems Explained, John Wiley & Sons Ltd., England, 2003.

[30] C. Biaku, N. Dale, M. Mann, H. Salehfar, A. Peters, T. Han, A semiempirical study of the temperature dependence of the anode charge transfer coefficient of a 6 kW PEM electrolyzer, Int. J. Hydrog. Energy 33 (16) (2008) 4247–4254.

[31] B. Decourt, B. Lajoie, R. Debarre, O. Soupa, The Hydrogen-Based Energy Conversion FactBook, The SBC Energy Institute, 2014.

Publication II

Givirovskiy, G., Ruuskanen, V., Ojala, L. S., Kokkonen, P., and Ahola, J.
In Situ Water Electrolyzer Stack for an Electrobioreactor

Energies,
vol. 12, no. 10, May. 2019

energies

MDPI

Article

In Situ Water Electrolyzer Stack for an Electrobioreactor

Georgy Givirovskiy [1,*], Vesa Ruuskanen [1], Leo S. Ojala [2] and Petteri Kokkonen [2] and Jero Ahola [1]

[1] School of Energy Systems, LUT University, P.O. Box 20, FI-53851 Lappeenranta, Finland; vesa.ruuskanen@lut.fi (V.R.); jero.ahola@lut.fi (J.A.)
[2] VTT Technical Research Centre of Finland Ltd., P.O. Box 1000, 02044 VTT, Espoo, Finland; leo.ojala@vtt.fi (L.S.O.); petteri.kokkonen@vtt.fi (P.K.)
* Correspondence: georgy.givirovskiy@lut.fi; Tel.: +358-50-470-6727

Received: 18 April 2019; Accepted: 15 May 2019; Published: 18 May 2019

Abstract: Hydrogen-oxidizing bacteria provide a sustainable solution for microbial protein production. Renewable electricity can be used for in situ water electrolysis in an electrobioreactor. The use of cultivation medium as the electrolyte enhances the hydrogen dissolution to the medium. This paper proposes a stack structure for in situ water electrolysis to improve the productivity of the electrobioreactor. The hydrogen production rate and the energy efficiency of the prototype stack are analyzed.

Keywords: in situ water electrolysis; microbial protein; hydrogen-oxidizing bacteria; electrobioreactor

1. Introduction

The intensive use of fossil fuels has resulted in the depletion of natural resources, increasing levels of greenhouse gas emissions, and undesired climate changes. The generation of electrical energy from abundant renewable energy sources, such as wind and solar energy, provides a sustainable and environmentally friendly alternative to fossil-fuel-based energy [1]. However, the intermittent nature of solar and wind energy sources requires the development of efficient and flexible methods for energy storage [2]. Moreover, in order to deal with the challenge of climate change, there is an urgent need for efficient technologies that are capable of capturing and using carbon. One emerging strategy that might significantly contribute to the transition towards a renewable energy-based economy is the microbial assimilation of carbon. This method enables the fixation of abundantly available atmospheric CO_2 and its further use as a source of carbon for carbonaceous products and energy carriers by means of microorganisms [3–5].

Considering various microorganisms, autotrophic aerobic hydrogen-oxidizing bacteria (HOB) have been found to be among the most prospective candidates to exploit the potential of renewable energy generation. The distinctive feature of HOB is that they can be grown in a mineral medium containing low amounts of citrate as a minor source of organic carbon, using atmospheric or point source CO_2 as the source of carbon along with H_2 and O_2, which act as the electron donor and the electron acceptor, respectively, for the production of new cellular materials [6]. The intrinsic premier product of CO_2 assimilation by HOB is biomass, the content of which can be tuned to be rich in carbohydrates, proteins, or fatty acids. Thus, HOB have the potential to play a significant role in future sustainable food production systems [7].

The obtained microbial biomass is frequently referred to as a single cell protein (SCP) also known as a microbial protein (MP) because of its high crude protein content of approximately 70–75% [8]. Volova et al. [9] found that the biological value of proteins synthesized by different strains of HOB

is sufficient for them to be considered as a potential protein source for human and animal nutrition. The feasibility of CO_2 assimilation by HOB has recently been proven on a pilot scale within the framework of the Power-to-Protein project in Belgium. A pilot plant produces an MP with a targeted capacity of 1–2 kg per day using HOB with H_2 and O_2 produced by water electrolysis and CO_2 and NH_3 recovered from a wastewater treatment plant [10]. Polyhydroxybutyrate (PHB) is another possible bio-based product, which can be derived from CO_2 assimilation by HOB [6,11]. Interestingly, PHB is a biopolymer and is considered a carbon and energy storage material in bacteria. A wide variety of important platform chemicals can be derived from PHB including thermoplastic, methyl-esterified 3-hydroxybutyrate oligomers, R-3-hydroxybutyric acid, 1,3-butandiol (BDO), crotonic acid, acetoacetic acid, and some others [12].

The low solubility of the main reactant gases H_2, O_2, and CO_2 in the aqueous solution where the HOB cells are being suspended drastically decreases the mass transfer and overall process efficiency [12]. The highest reported average H_2-to-biomass conversion efficiencies are up to 80% in continuous operation and up to 65% in the sequence batch reactor [11]. To overcome this constraint, there is increasing scientific interest in combining water electrolysis and CO_2 assimilation by HOB into a single vessel, which is called a hybrid biological-inorganic (HBI) system. This provides an advantage of improved gas transfer of H_2 and O_2 to the liquid phase over the conventional gas fermentation process with an external supply of main reactant gases. The concept was successfully proven on a laboratory scale by Pamela A. Silver and Daniel G. Nocera's research group. For instance, Torella et al. [13] reported a development of integrated bioelectrochemical systems in which HOB was used to convert CO_2 into biomass and fuel alcohols at high efficiencies using scalable earth-abundant catalysts. In subsequent studies, Liu et al. [14] developed a hybrid water splitting-biosynthetic system based on CO-based catalysts possessing unique self-healing properties, which made it possible to achieve a CO_2 reduction efficiency above 50% and a solar-to-chemical efficiency of almost 10% when coupled with the existing photovoltaic systems. A hybrid inorganic-biological system and the same biocompatible catalysts were used to fix CO_2 and N_2 into NH_3 and a biofertilizer in the studies of [15] and for biomass synthesis from CO_2 in the studies of [16].

After successful proof-of-concept of CO_2 assimilation by HOB using the HBI systems, the scientific focus shifted towards the objectives of enhanced energy efficiency, product selectivity, and scaling up [17]. The development of a robust, efficient, and ergonomic reactor system designed with in situ electrolysis of the cultivation medium for the HBI process is considered one of the key research directions in this field. The main requirements for such a design are the following: (i) the system has to be biocompatible; (ii) the system must have an acceptable electrode surface-to-volume ratio, and (iii) the system components must be low cost and have long-term stability [18]. Other main limitations of the HBI systems are the low conductivity of the cultivation medium, an increase in the ohmic losses, and the current density limitations set by the microorganisms. In the traditional alkaline and proton exchange membrane (PEM) electrolyzers, the electrolytic cells are series connected to form a stack structure with a high efficiency and a compact design [19]. Thus, the electrolyzer stack structure has not been reported to be applied to HBI systems.

The purpose of this study is to develop and present a conceptual design of an electrobioreactor to enable upscaling of the HBI process to an industrial scale and to discuss the main aspects affecting the energy efficiency of the system. To reach these targets, a novel in situ water electrolyzer stack structure for an electrobioreactor is introduced to enhance the hydrogen production rate and energy efficiency of HOB cultivation. The performance of the in situ electrolyzer stack is experimentally studied. Further, the achievable energy efficiency and the volumetric hydrogen production rate are discussed based on the cell model.

This paper is organized as follows: Section 2 describes the principles of HOB production with in situ water electrolysis. The in situ water electrolyzer stack prototype is introduced and the experimental results are discussed in Section 3 and in Section 4, respectively. Finally, Section 5 concludes the paper.

2. Theory and Concept Background

To date, all reported bioelectrochemical systems (BES) have been studied at volumes ranging from 100 mL to 1 L by applying simplified electrode configurations [5,13–16]. This leads to the conclusion that the BES design technology is currently in its infancy. This section aims to provide a possible conceptual design for a scaled-up prototype for the BES by first defining the special characteristics of in situ water electrolysis and the BES, then describing the design idea, and finally, proving and testing the concept on an experimental scale.

2.1. In Situ Water Electrolysis and Electrobioreactor Characteristics

While the technical performance and energy efficiency of the electrobioreactors are crucial aspects that have to be taken into consideration in the design stage, water electrolysis can be considered one of the major phenomena that affects those criteria. The minimum thermodynamic potential required for water electrolysis, called reversible voltage, is 1.23 V under standard ambient conditions. Without auxiliary heat, the required minimum voltage is higher and is dependent on the electrolysis conditions (e.g., 1.43 V under standard ambient conditions). From the perspective of energy efficiency, the voltage driving the electrolysis should thus be kept as low as possible. The actual voltage required to drive the electrolysis is higher because of overvoltages (i.e., voltage losses) caused by the impedance between the electrodes and the activation reactions. Hence, the overall cell voltage is the sum of different overvoltages (overpotentials), as presented in the following equation:

$$U_{\text{cell}} = U_{\text{rev}} + U_{\text{ohm}} + U_{\text{act}} + U_{\text{con}}, \tag{1}$$

where U_{cell} is the cell voltage, U_{rev} is the reversible open circuit voltage, U_{ohm} is the overvoltage caused by ohmic losses in the cell elements, U_{act} is the activation overvoltage caused by electrode kinetics, and U_{con} is the concentration overvoltage caused by the mass transport processes [20].

There are several crucial parameters that describe the water electrolysis process. First of all, the production of hydrogen can be estimated according to Faraday's laws of electrolysis. The hydrogen production rate (NL/h) is directly proportional to the electric charge transferred at the electrodes and can be expressed as

$$f_{\text{H}_2} = \eta_{\text{F}} \frac{N_{\text{cell}} i_{\text{cell}} A_{\text{cell}}}{zF} 22.41 \frac{\text{NL}}{\text{mol}} 3600 \frac{\text{s}}{\text{h}}, \tag{2}$$

where z is the number of moles of electrons transferred in the reaction (for hydrogen, z = 2), F is the Faraday constant (9.6485×10^4 C/mol), N_{cell} is the number of cells constituting the electrolyzer stack, i_{cell} is the current density (A/cm^2), A_{cell} is the effective cell area (cm^2), and η_F is the Faraday efficiency, also known as the current efficiency.

Secondly, the specific energy consumption E_{s} (kWh/Nm^3) of an electrolysis process, which relates the energy consumed to produce hydrogen, can be obtained from

$$E_{\text{s}} = \frac{\int_0^t N_{\text{cell}} i_{\text{cell}} A_{\text{cell}} U_{\text{cell}} \text{d}t}{\int_0^t f_{\text{H}_2} \text{d}t}, \tag{3}$$

where f_{H_2} is the hydrogen flow rate in Nm/h[3].

Finally, the electrolyzer stack efficiency can be calculated based on the higher heating value (HHV), which is the minimum energy required to produce hydrogen gas by a thermoneutral process. The per volume unit HHV of hydrogen gas is 3.54 kWh/Nm^3, which can be assumed to represent the energy consumption of the process with a 100% efficiency. Thus, the electrolyzer efficiency can be described by the following equation:

$$\eta_{\text{E}} = \frac{\text{HHV}_{\text{H}_2}}{E_{\text{s}}} 100\%. \tag{4}$$

On the other hand, the particularity of the process itself is definitely yet another dominating aspect in the design development of the HBI system. Due to the fact that both H_2 and O_2 are important for CO_2 fixation by HOB, a simplified design that does not require expensive separation of anode and cathode compartments is possible for this process. The application of an electrolyzer without a separator facilitates the operation and maintenance of the system while reducing the capital costs. Furthermore, a simplified construction eliminates the internal resistance and therefore the ohmic overpotential related to the separator. However, the main source of ohmic overpotential is the pH-neutral electrolyte with a relatively low conductivity which is typically used in HBI systems.

One notable constraint of the HBI process is the incidental formation of toxic reactive oxygen species (ROS) on the cathode side, represented by superoxide, hydrogen peroxide, and hydroxyl radicals, at and below potentials required for the H_2 evolution reaction [17]. This phenomenon can be mitigated by using biocompatible ROS-resistant catalysts. For instance, a cobalt-phosphorous (CoP) alloy cathode, which kinetically favors H_2 generation, was used in combination with a self-healing cobalt–phosphate anode to enhance the production rate and achieve high solar-to-fuel and solar-to-biomass energy efficiencies in the studies of [14]. Distinctive advantages of the aforementioned catalysts include (i) biocompatibility; (ii) low overpotentials required for water splitting; (iii) low cost as a result of the use of earth-abundant materials as raw materials, and (iv) ease of manufacture by electrodeposition into a variety of conventional substrate materials, such as stainless steel or nickel sheets.

2.2. Immersed Electrodes

So far, the bioelectrochemical systems for the above-mentioned microbial protein production have used simple rod or plate electrodes immersed inside the bioreactor tank. Figure 1 shows the progress of a typical BES cultivation with a small-scale (60 mL liquid volume) bioreactor with immersed rod electrodes (for the details of the cultivation, the reader is referred to Appendix A.1). The hydrogen concentration at the BES exhaust is also presented.

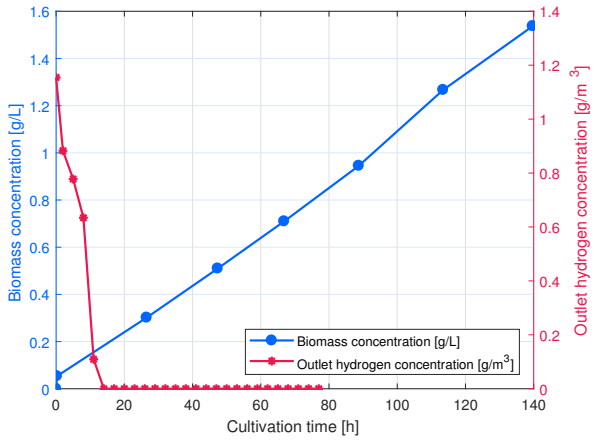

Figure 1. BES cultivation of *Cupriavidus necator* H16 with immersed electrodes, compared with the hydrogen concentration at the bioreactor gas outlet.

The first points in Figure 1 correspond to a situation before inoculation, i.e., a 0 g/L biomass and a 1.15 g/m^3 hydrogen concentration at the outlet. The hydrogen evolution rate before the inoculation was 5.3×10^{-7} kg/h. The theoretical hydrogen evolution rate based on the electrolysis current was 6.8×10^{-7} kg/h, and therefore, the current efficiency of the hydrogen generation was 78%. Very soon after the beginning of the cultivation, the H_2 concentration decreased below the detection limit, and the

biomass grew at a constant rate, as the growth was limited by the availability of the produced H_2. Therefore, the hydrogen utilization rate was close to 100%, which is considerably higher than the gaseous H_2 utilization rate of 80% cited by [11]. During the first 12 h of cultivation, before the hydrogen evolution rate started to limit the growth, the hydrogen utilization ratio increased at an exponential rate. This rate was assumed to be comparable with the biomass growth rate (see Appendix A.2). From the hydrogen data, the specific growth rate of the biomass was estimated to be 0.14 h^{-1}. Previously, for instance in the study by Yu and Munasinghe (2018) [21], similar specific growth rates have been reported for the autotrophic growth of *Cupriavidus necator*: 0.094–0.12 h^{-1} under different gaseous H_2 pressures.

The main issues related to the electrodes immersed in the reactor tank are as follows:

- The electrode area must be increased to maximize the hydrogen production.
- The coil-shaped electrodes inside each other lead to inhomogeneous current densities in the electrode surface and the electrolyte.
- The rod electrodes also force most of the current to travel along an unnecessarily long path through the low-conductivity electrolyte.
- The electrodes make the mixing of the reactor more difficult.
- The internal resistance of the electrode limits the length and thus the surface area of the electrode.
- The serial connection of the immersed electrodes is not allowed to avoid excessive leakage currents, although it would be necessary to scale the system voltage to a favorable level for the industrial-scale AC/DC converters

These aspects can be addressed by applying a stack structure for water electrolysis.

2.3. Conceptual Design of the Electrobioreactor System

The integration of electrodes inside the bioreactor, while keeping the structure compact and ergonomic, is a challenging engineering task. Despite the lack of information about possible BES designs, outstanding progress has been achieved in alkaline and PEM water electrolyzer stack designs. Mimicking stack structure designs and integrating them into the electrobioreactor could provide significant benefits for increasing the energy efficiency and overall technical performance of the system. For that reason, our research team proposes the following electrobioreactor design concept with an external in situ water electrolyzer stack (Figure 2).

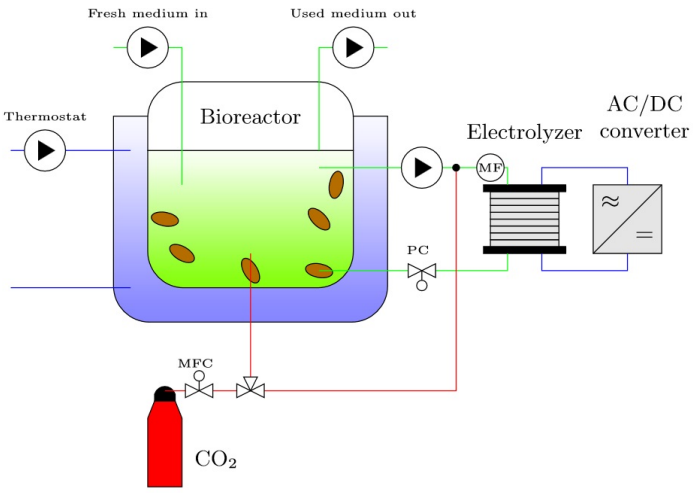

Figure 2. Proposed process diagram of the electrobioreactor with an external electrolyzer stack for the hybrid biological-inorganic (HBI) process.

It can be clearly seen from the process diagram that the electrode stack assembly is not immersed in the cultivation medium, but the cultivation medium is constantly circulating through the external stack where the water electrolysis takes place. The microbes are allowed to flow through the electrolyzer stack, thereby increasing the total volume used for the microbial growth. If the microbes were not allowed to enter the electrolyzer, for example, because of the current density being too high for the microbes, a porous separator could be used to prevent microbes from entering the electrolyzer part of the system. A Nafion 117 proton-exchange membrane was used to separate the anode and cathode compartments of the bioelectrochemical reactor in [5]. However, a careful design would be required to avoid the separator blocking up because of the microbes.

The electrodes in the stack operate in a bipolar mode acting as an anode from one side and as a cathode from the other side. Depending on the electrode function, each side can be coated with a suitable catalyst material by performing electrodeposition prior to CO_2 assimilation by the HOB. The medium flows between the electrodes in a flow channel formed by the nonconducting separator plates. No separator is needed to separate hydrogen and oxygen gases, contrary to the traditional alkaline electrolyzer stack, as both gases can be dissolved in the bioreactor cultivation medium [22]. Any type of conventional bioreactor can be used to perform stirring, the control of the main process parameters, such as a CO_2 supply, and for other important operations required for HOB cultivation. The proposed system design enables achievement of the following:

- A high electrode area per volume;
- A constant distance between electrodes, leading to constant current densities;
- Simple series connection of electrolytic cells;
- Low leakage currents, resulting in enhanced power densities;
- Stack voltage levels suitable for industrial AC/DC converters;
- A high energy efficiency.

3. Materials and Methods

3.1. Experimental Setup

Figure 3a illustrates the experimental setup used for the electrolysis tests, consisting of an external manifold with simple hosing to enable parallel electrolyte flow, a pump to provide constant circulation of the medium through the system, a vessel for the medium input and output, and an electrolyzer stack. The electrolyzer stack is schematically presented in Figure 3b. The stack consists of series-connected bipolar electrodes (uncoated 316 L stainless steel with a thickness of 1 mm) separated by tubular plastic (PVC) spacers and end plates made of stainless steel acting both as a current collector and a pressure plate. The effective electrode area of each circular electrode is 86.6 cm^2, with a diameter of 10.5 cm. The distance between the electrodes is 10 mm, and there are ten cells connected in series. The current is supplied using a standard cable shoe to the connector bolt welded to the end plate. The stack structure is compressed with insulated tightening rods assembled through the corner holes of the pressure plates. The hosing providing the parallel electrolyte flow of the cells is made from plastic (PVC) tube with a diameter of 6 mm. The measurement system control and data logging were implemented in a LabVIEW environment. Current was supplied and measured with a Sorensen DLM (40 V/15 A) laboratory power source with a current stability of 7.5 mA. The stack and cell voltages were measured with a Keithley 2701 data acquisition system with a voltage measurement accuracy of 0.015% for reading and 0.006% for the 100 V range. A Grundfos Alpha2 25–60 household hot water circulation pump with an integrated frequency converter was used to pump the electrolyte. Tests were performed at room temperature. The temperatures of the manifold inlet and outlet flows were measured with PT100 thermistors with an IPAQ-C201 mA-signal transmitter. The mA signal was further read with a NI-9208 C series current input module.

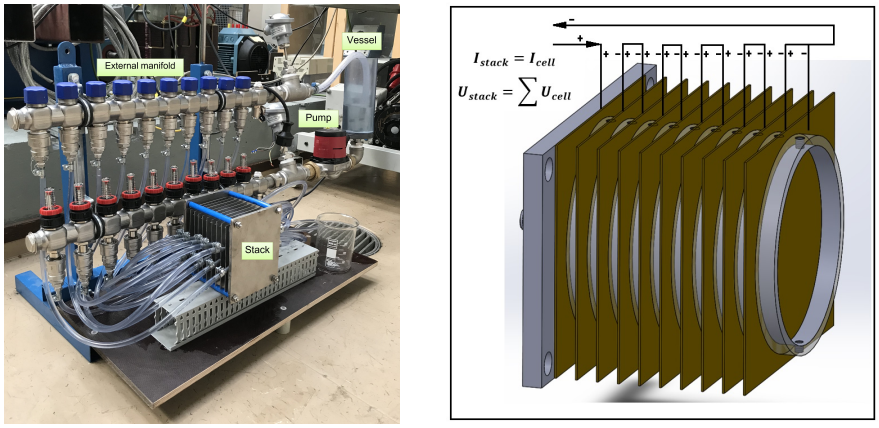

(**a**) Experimental setup (**b**) Electrolyzer stack

Figure 3. Experimental setup used for the electrolysis tests and a schematic of the electrolyzer stack. The ten cells are electrically connected in series, and the electrolyte flow is equally divided between the parallel cells by the manifolds.

3.2. Electrolyte

The mineral medium used for the cultivation of HOB is based on Leibniz-Institut DSMZ growth medium number 81 [23] with the following changes: (i) The major chloride compounds were replaced with the corresponding sulfates to minimize the production of chlorine gas by the electrolysis current. The trace element solution SL-6 of Pfennig [24] used in the medium preparation was left unchanged both for the sake of convenience and because some bacteria might require chloride as a micronutrient, especially at high salt concentrations [25]. (ii) The ferric ammonium citrate concentration was reduced to 5 mg/L from the 50 mg/L recommended by DSMZ to prevent iron precipitation from the medium during storage of even a few days. (iii) Na_2SO_4 was added to increase the electrical conductivity of the medium and reduce the required electrolysis voltage. The final mineral medium composition was 2.3 g/L KH_2PO_4, 2.9 g/L $Na_2HPO_4 \cdot 2\,H_2O$, 5.45 g/L Na_2SO_4, 1.19 g/L $(NH_4)_2SO_4$, 0.5 g/L $MgSO_4 \cdot 7\,H_2O$, 11.7 mg/L $CaSO_4 \cdot 2\,H_2O$, 4.4 mg/L $MnSO_4 \cdot H_2O$, 5 mg/L $NaVO_3$ (metavanadate), 0.5 g/L $NaHCO_3$, 5 mg/L ferric ammonium citrate (16% Fe), 0.5 mg/L $ZnSO_4 \cdot 7\,H_2O$, 1.5 mg/L H_3BO_3, 1 mg/L $CoCl_2 \cdot 6\,H_2O$, 0.05 mg/L $CuCl_2 \cdot 2\,H_2O$, 0.1 mg/L $NiCl_2 \cdot 6\,H_2O$, 0.15 mg/L $Na_2MoO_4 \cdot 2\,H_2O$. The medium had a pH of 7 and a conductivity of 12 mS/cm.

4. Results and Discussion

Figure 4a depicts the measured currents as a function of time with various voltages ranging from 30 V to 39 V during 1 h of experimental time. The stack voltage as a function of stack current is presented in Figure 4b, and the cell voltage as a function of current density is shown in Figure 4c.

The main parameters of the electrolyzer stack efficiency were calculated based on the collected current–voltage relationships. Figure 5a presents the hydrogen production rate and the electrical supply power as a function of the stack current density. Figure 5b,c shows the specific energy consumption and the electrolyzer efficiency as a function of the stack current density. The values of the aforementioned parameters are summarized in Table 1.

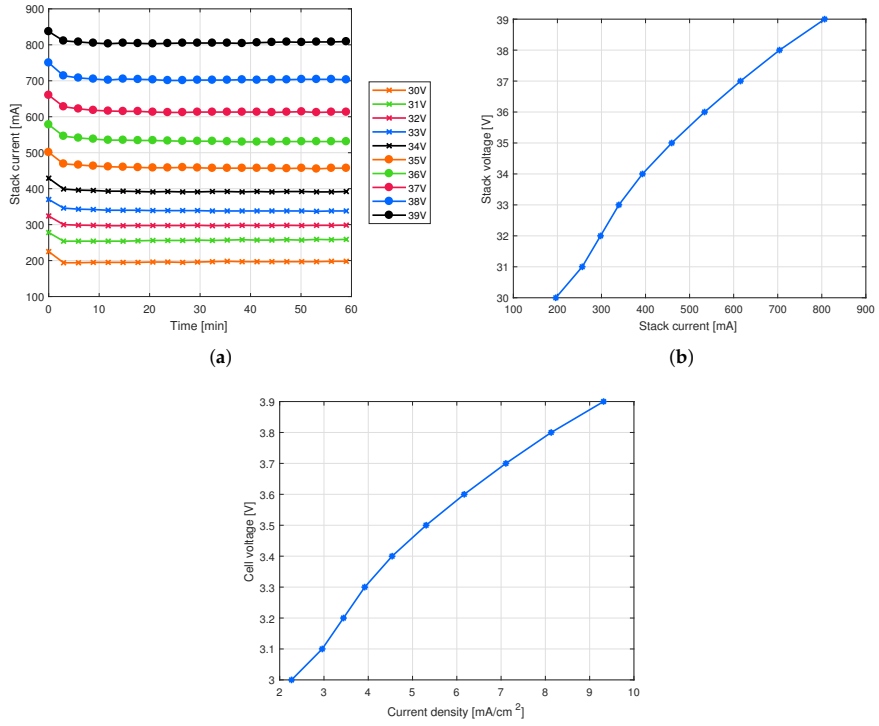

(**a**) (**b**)

(**c**)

Figure 4. Measured currents and current densities of the electrolyzer stack with various supply voltages. (**a**) Measured currents as a function of time with various voltages; (**b**) stack voltage as a function of stack current; (**c**) cell voltage as a function of current density.

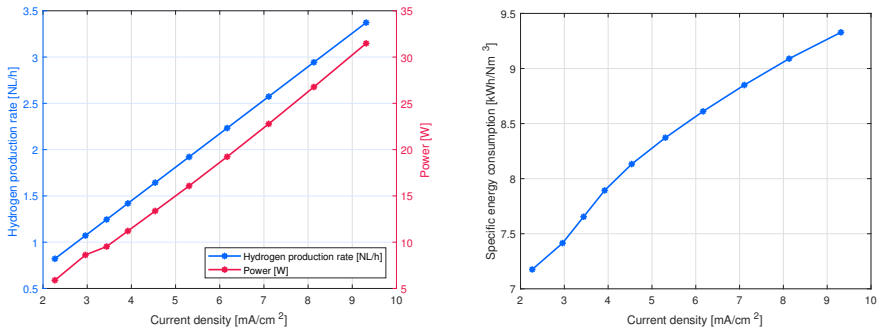

(**a**) Hydrogen production rate and power (**b**) Specific energy consumption

Figure 5. *Cont*.

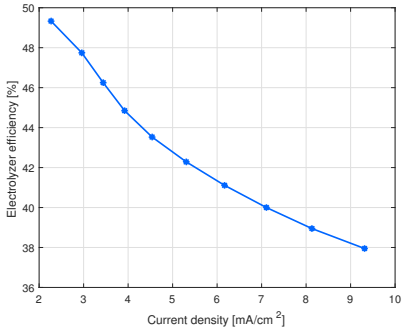

(**c**) Electrolyzer efficiency (higher heating value, HHV)

Figure 5. Main energy efficiency parameters of the electrolyzer stack.

Table 1. Main energy efficiency parameters of the electrolyzer stack calculated based on the measured stack voltage and current.

U_{stack} [V]	I_{stack} [A]	f_{H_2} [NL/h]	E_s [kWh/(N m^3)]	$\eta_{E,HHV}$ [%]
30	0.20	0.82	7.18	49.33
31	0.26	1.07	7.42	47.74
32	0.30	1.25	7.65	46.25
33	0.34	1.42	7.89	44.85
34	0.39	1.64	8.13	43.53
35	0.46	1.92	8.37	42.29
36	0.53	2.23	8.61	41.11
37	0.62	2.57	8.85	40.00
38	0.70	2.94	9.09	38.95
39	0.81	3.37	9.33	37.95

4.1. Effect of Electrode Distance on the Cell Performance

As was stated in Section 2, the efficiency of the HOB cultivation process can be enhanced by reducing the electric power consumption during the water electrolysis process. According to Equation (1), the overall cell potential is the sum of different overpotentials, one of which is the ohmic overpotential, representing the electrical resistance of the cell elements. We may state that the ohmic overpotential is mainly caused by the voltage loss across the cultivation medium with a low conductivity. Consequently, a reduction in space between the electrodes in the stack substantially decreases the electrical resistance and leads to elevated current densities at the same cell potentials. Having measured the current and voltage data of the electrobioreactor electrolyzer stack with a 10 mm distance between the electrodes, the corresponding data were calculated for the same stack with a 3 mm distance between the electrodes, according to the simplified cell voltage model published in [26] and presented by the following equation:

$$U_{cell} = U_{rev} + \frac{\delta_m i_{cell}}{\sigma_m} + \alpha \operatorname{arcsinh}\left(\frac{i_{cell}}{2i_0}\right), \quad (5)$$

where δ_m is the distance between the electrodes in (cm), σ_m is the conductivity of the medium in (S/cm), α is the charge transfer coefficient for the anode and the cathode separately, and i_o is the exchange current density on the electrode surfaces.

The modeling results of the stack current densities as a function of cell voltage with a 10 mm and 3 mm distance between the electrodes are illustrated in Figure 6a. Figure 6b shows the hydrogen production rate and the power as a function of stack current density. Figure 6c depicts the specific

energy consumption as a function of the stack current density for the electrolyzer stack with a 3 mm distance between the electrodes.

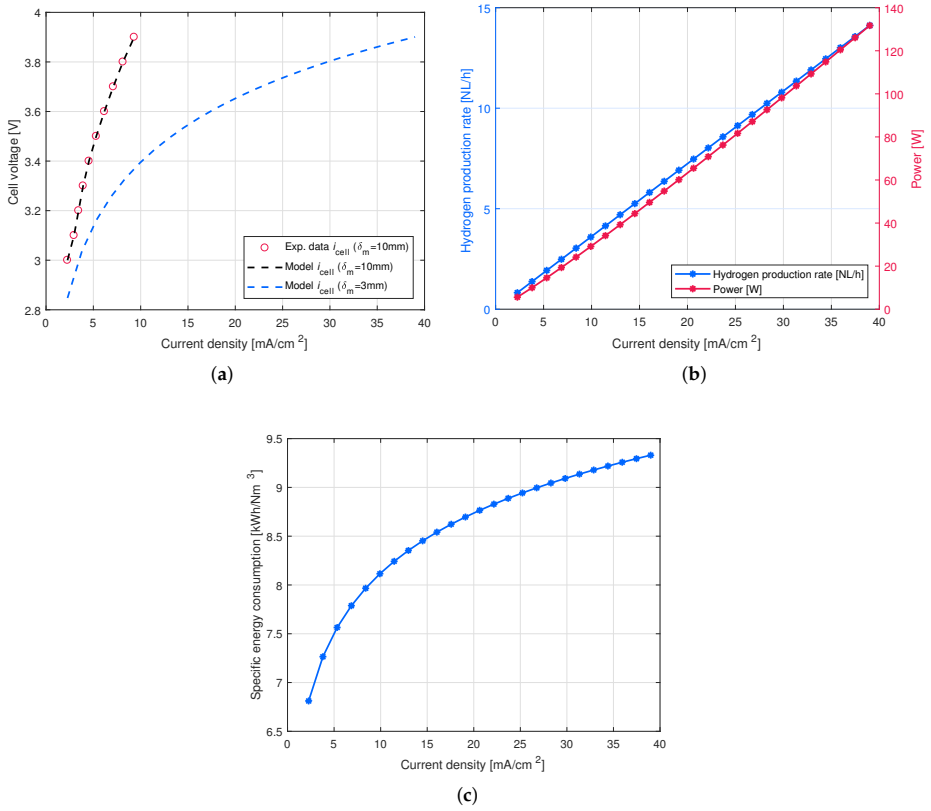

Figure 6. The main energy efficiency parameters of the electrolyzer stack with a decreased distance between the electrodes. (**a**) Cell voltage as a function of current density at variable electrode separations; (**b**) hydrogen production rate and supply power as a function of current density with a 3 mm distance between the electrodes; (**c**) specific energy consumption as a function of the current density with a 3 mm distance between the electrodes.

4.2. Volumetric Productivity

As an example, a bioreactor with a volume of 1000 L with a specific production rate of 0.2 g/(L h) would produce 200 g of biomass per hour. With the 2.5 g/mol biomass yield from hydrogen, the hydrogen consumption is 80 mol/h. If CoP-coated electrodes are used, a 50% HHV efficiency can be reached with current densities up to 5 mA/cm^2 [26]. According to (2), the required cell area is 85.8 m^2. By assuming that there are 100 circular cells in series and that the total axial length of the cell is 5 mm, the electrolyzer volume is 429 L. Thus, it can be stated that with coated electrodes, the electrolyzer volume is roughly half of the bioreactor volume, and in the case of noncoated stainless steel electrodes, the bioreactor and electrolyzer volumes are roughly the same. This leads to the fact that the actual bioreactor tank might not be needed at all, or, at least, the size could be significantly reduced, as the electrolyzer stack structure provides a significant proportion of the volume required for microbial growth.

5. Conclusions

Hydrogen production for HOB cultivation in an electrobioreactor with in situ water electrolysis was studied. A stack structure was introduced to enhance hydrogen production compared with reactor tank-immersed electrodes. The energy efficiency of the prototype stack was experimentally studied. It was found that with a water electrolysis energy efficiency (HHV) of 50%, the current density could be up to a range of 5 mA/cm^2 with coated electrodes. Thus, the volume of the in situ water electolyzer stack is approximately half of the total volume required for microbial cultivation. However, the results are based on the energy efficiency of the water electrolysis process, and the maximum allowed current density that does not harm microbial growth has not been studied yet.

Author Contributions: Conceptualization, G.G., V.R., L.S.O., P.K. and J.A.; methodology, G.G., V.R., L.S.O., and P.K.; software, G.G. and V.R.; formal analysis, G.G. and V.R.; investigation, G.G., L.S.O. and V.R.; writing—original draft preparation, G.G. and V.R.; writing—review and editing, L.S.O., P.K. and J.A.; project administration, V.R. and J.A.

Funding: Financial support was given by the Technology Industries of Finland Centennial Foundation and Jane and Aatos Erkko Foundation for the project "Feed and food from carbon dioxide and electricity—research and piloting of the future protein production."

Conflicts of Interest: The authors declare no conflict of interest. The funders had no role in the design of the study; in the collection, analyses, or interpretation of data; in the writing of the manuscript, or in the decision to publish the results.

Appendix A. Materials and Methods

Appendix A.1. BES Cultivation

The HOB strain used in the BES cultivation was *Cupriavidus necator* H16 (DSM 428) supplied by the Leibniz-Institut DSMZ—Deutsche Sammlung von Mikroorganismen und Zellkulturen GmbH. The inoculum for the BES cultivation was grown in 20 mL liquid volume shake flasks under 12.5% H_2, 13.1% O_2, 25% CO_2, and 49.4% N_2 for nine days. The BES cultivation was performed in a small-scale (60 mL liquid volume) bioreactor with immersed rod electrodes (cathode: stainless steel, anode: iridium-oxide-coated titanium). The reactor was supplied with gaseous CO_2 and a constant electrolysis current of 18 mA. The bioreactor was jacketed, and the cultivation temperature was kept constant at 30 °C with external water circulation. Prior to the inoculation, reactors filled with a sterile growth medium were allowed to stabilize to the temperature, electrolysis, and CO_2 purge conditions for 2 h. The first data point was recorded at the end of the stabilizing period before inoculation. The BES reactor was inoculated with an appropriate volume of inoculum (2 mL) to get an initial optical density of 0.2 units for the cultivation broth. Subsequently, the optical density (OD) at 600 nm was measured daily by withdrawing samples of 1 mL from the reactor. The OD was correlated with the cell density by measuring the dry cell density at the end of the cultivation period from an aliquot of 2 mL. The biomass in the aliquot was separated by centrifugation, washed twice with pure water (Milli-Q Advantage A10 Water Purification system by Millipore), and finally, the biomass was dried at 105 °C. The correlation between the OD and the dry cell density was found to be 1 OD unit = 0.255 g/L biomass. During the BES cultivation, the hydrogen concentration at the reactor gas exhaust was measured with a Pfeiffer Vacuum Omnistar GDS 301 gas analysis system. Before cultivation, the Omnistar was calibrated against the known H_2 concentration of 10% in a reference gas supplied by AGA.

Appendix A.2. HOB Growth Rate Calculation from the Outlet Hydrogen Concentration Data

For the HOB biomass growth rate determination, the hydrogen concentration at the bioreactor outlet was transformed into a hydrogen utilization ratio:

$$\text{H}_2\text{ Utilization} = \frac{c_{H_2}^{\text{Out,Initial}} - c_{H_2}^{\text{Out}}}{c_{H_2}^{\text{Out,Initial}}}, \quad \text{(A1)}$$

where $c_{H_2}^{Out}$ is the hydrogen concentration at the reactor outlet, and $c_{H_2}^{Out,Initial}$ is the concentration at the beginning of cultivation. The use of H_2 was assumed to increase at the same rate as the biomass growth. A generic exponential function was fitted to the increasing range (between 0.5 h–12 h) of the H_2 utilization data:

$$H_2 \text{ Utilization} = Ae^{\mu t}, \tag{A2}$$

where A is a pre-exponential constant, and μ is the rate constant. The best fit was achieved with $A = 0.1675$ and $\mu = 0.1422$ h^{-1}. Because the biomass growth is dependent on the hydrogen consumption, the rate constant can be considered an approximation of the biomass growth rate. The H_2 utilization data and the fitted curve are shown in Figure A1.

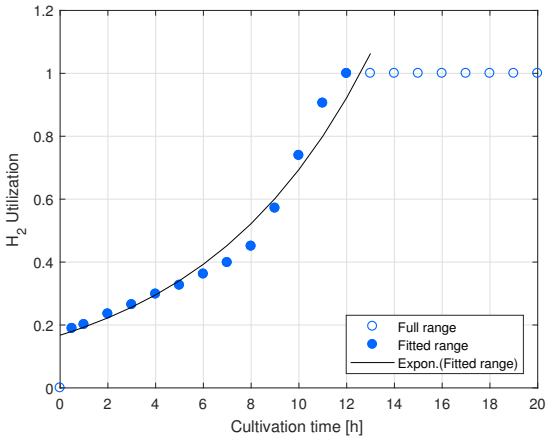

Figure A1. Development of hydrogen utilization in the small-scale BES. The exponential curve fitted to the part of the data range is associated with exponential biomass growth.

References

1. Brown, T.W.; Bischof-niemz, T.; Blok, K.; Breyer, C.; Lund, H.; Mathiesen, B.V. Response to 'Burden of proof: A comprehensive review of the feasibility of 100% renewable-electricity systems. *Renew. Sustain. Energy Rev.* **2018**, *92*, 834–847. [CrossRef]
2. Kousksou, T.; Bruel, P.; Jamil, A.; El Rhafiki, T.; Zeraouli, Y. Energy storage: Applications and challenges. *Sol. Energy Mater. Sol. Cells* **2014**, *120*, 59–80. [CrossRef]
3. Vidal, F.; Koponen, J.; Ruuskanen, V.; Bajamundi, C.; Kosonen, A.; Simell, P.; Ahola, J.; Frilund, C.; Elfving, J.; Reinikainen, M.; et al. Power-to-X technology using renewable electricity and carbon dioxide from ambient air: SOLETAIR proof-of-concept and improved process concept. *J. CO_2 Util.* **2018**, *28*, 235–246.
4. Pikaar, I.; Matassa, S.; Rabaey, K.; Bodirsky, B.L.; Popp, A.; Herrero, M.; Verstraete, W. Microbes and the Next Nitrogen Revolution. *Environ. Sci. Technol.* **2017**, *51*, 7297–7303. [CrossRef]
5. Kracke, F.; Wong, A.B.; Maegaard, K.; Deutzmann, J.S.; Hubert, M.A.; Hahn, C.; Jaramillo, T.F.; Spormann, A.M. Robust and biocompatible catalysts for efficient hydrogen-driven microbial electrosynthesis. *Commun. Chem.* **2019**, *2*, 45. [CrossRef]
6. Matassa, S.; Boon, N.; Verstraete, W. Resource recovery from used water: The manufacturing abilities of hydrogen-oxidizing bacteria. *Water Res.* **2015**, *68*, 467–478. [CrossRef] [PubMed]
7. Linder, T. Making the case for edible microorganisms as an integral part of a more sustainable and resilient food production system. *Food Secur.* **2019**. [CrossRef]
8. Pikaar, I.; Vrieze, J.D.; Rabaey, K.; Herrero, M.; Smith, P.; Verstraete, W. Science of the Total Environment Carbon emission avoidance and capture by producing in-reactor microbial biomass based food, feed and slow release fertilizer: Potentials and limitations. *Sci. Total. Environ.* **2018**, *644*, 1525–1530. [CrossRef] [PubMed]

9. Volova, T.G.; Barashkov, V.A. Characteristics of proteins synthesized by hydrogen-oxidizing microorganisms. *Appl. Biochem. Microbiol.* **2010**, *46*, 574–579. [CrossRef]
10. Oesterholt, F.; Matassa, S.; Palmen, L.; Roest, K.; Verstraete, W. Pilot scale production of single cell proteins using the power-to-protein concept Future global challenges. In Proceedings of the 2nd International Resource Recovery Conference, New York, NY, USA, 5–9 August 2018; pp. 1–16.
11. Matassa, S.; Verstraete, W.; Pikaar, I.; Boon, N. Autotrophic nitrogen assimilation and carbon capture for microbial protein production by a novel enrichment of hydrogen-oxidizing bacteria. *Water Res.* **2016**, *101*, 137–146. [CrossRef]
12. Yu, J. Bio-based products from solar energy and carbon dioxide. *Trends Biotechnol.* **2014**, *32*, 5–10. [CrossRef] [PubMed]
13. Torella, J.P.; Gagliardi, C.J.; Chen, J.S.; Bediako, D.K.; Colón, B.; Way, J.C.; Silver, P.A.; Nocera, D.G. Efficient solar-to-fuels production from a hybrid microbial–water-splitting catalyst system. *Proc. Natl. Acad. Sci. USA* **2015**, *112*, 2337–2342. [CrossRef] [PubMed]
14. Liu, C.; Ziesack, M.; Silver, P.A. Water splitting–biosynthetic system with CO_2 reduction efficiencies exceeding photosynthesis. *Science* **2016**, *352*, 1210–1213. [CrossRef] [PubMed]
15. Liu, C.; Sakimoto, K.K.; Colón, B.C.; Silver, P.A.; Nocera, D.G. Ambient nitrogen reduction cycle using a hybrid inorganic–biological system. *Proc. Natl. Acad. Sci. USA* **2017**, *114*, 6450–6455. [CrossRef]
16. Liu, C.; Colón, B.E.; Silver, P.A.; Nocera, D.G. Solar-powered CO_2 reduction by a hybrid biological|inorganic system. *J. Photochem. Photobiol. A Chem.* **2018**, *358*, 411–415. [CrossRef]
17. Nangle, S.N.; Sakimoto, K.K.; Silver, P.A.; Nocera, D.G. Biological-inorganic hybrid systems as a generalized platform for chemical production. *Curr. Opin. Chem. Biol.* **2017**, *41*, 107–113. [CrossRef]
18. Krieg, T.; Sydow, A.; Schro, U.; Schrader, J.; Holtmann, D. Reactor concepts for bioelectrochemical syntheses and energy conversion. *Trends Biotechnol.* **2014**, *32*, 645–655. [CrossRef] [PubMed]
19. Decourt, B.; Lajoie, B.; Debarre, R.; Soupa, O. *The Hydrogen-Based Energy Conversion FactBook*; The SBC Energy Institute: Melbourne, Australia, 2014.
20. Ursúa, A.; Gandía, L.; Sanchis, P. Hydrogen Production From Water Electrolysis: Current Status and Future Trends. *Proc. IEEE* **2012**, *100*, 410–426. [CrossRef]
21. Yu, J.; Munasinghe, P. Gas Fermentation Enhancement for Chemolithotrophic Growth of *Cupriavidus necator* on Carbon Dioxide. *Fermentation* **2018**, *4*, 63. [CrossRef]
22. Reilly, C.O.; Farrell, M.; Harvey, D.; Cassidy, J. Operation of an inexpensive bipolar alkaline electrolyser producing a mix of H_2/O_2 fuel. *Int. J. Hydrogen Energy* **2015**, *41*, 2197–2201. [CrossRef]
23. DSMZ GmbH. *81. Mineral Medium For Chemolithotrophic Growth (H-3)*; DSMZ: Braunschweig, Germany, 2011.
24. Pfennig, N. Rhodopseudomonas globiformis, sp. n., a new species of the Rhodospirillaceae. *Arch. Microbiol.* **1974**, *100*, 197–206. [CrossRef]
25. Roeßler, M.; Sewald, X.; Müller, V. Chloride dependence of growth in bacteria. *FEMS Microbiol. Lett.* **2006**, *225*, 161–165.
26. Givirovskiy, G.; Ruuskanen, V.; Ojala, L.; Lienemann, M.; Kokkonen, P.; Ahola, J. Electrode material studies and cell voltage characteristics of the in situ water electrolysis performed in a pH-neutral electrolyte in bioelectrochemical systems. *Heliyon* **2019**, *5*, e01690. [CrossRef]

Publication III

Givirovskiy, G., Ruuskanen, V., Väkiparta, T., and Ahola, J.

Electrocatalytic performance and cell voltage characteristics of 1st-row transition metal phosphate (TM-Pi) catalysts at neutral pH

Materials Today Energy,
vol. 17, Apr. 2020

Materials Today Energy 17 (2020) 100426

Contents lists available at ScienceDirect

Materials Today Energy

journal homepage: www.journals.elsevier.com/materials-today-energy/

Electrocatalytic performance and cell voltage characteristics of 1st-row transition metal phosphate (TM-Pi) catalysts at neutral pH

G. Givirovskiy*, V. Ruuskanen, T. Väkiparta, J. Ahola

LUT University, P.O. Box 20, FI-53851, Lappeenranta, Finland

ARTICLE INFO

Article history:
Received 7 January 2020
Received in revised form
21 April 2020
Accepted 23 April 2020
Available online xxx

Keywords:
In situ water electrolysis
Electrocatalyst
Transition metal phosphate
Oxygen evolution reaction
pH-neutral electrolyte

ABSTRACT

Water electrolysis represents a clean and sustainable route for large-scale hydrogen generation. However, efficient water splitting is hindered by the kinetically sluggish oxygen evolution reaction (OER), which requires significant energy inputs to drive the reaction at sufficiently fast rates. Recently, an increasing number of applications have emerged that require water electrolysis at neutral pH and under ambient conditions. This requirement creates additional challenges as the electrolysis of water is favorable in acidic and alkaline conditions. In order to tackle these challenges, considerable efforts have been devoted to the development of earth-abundant, highly effective, and robust electrocatalysts for the OER at pH = 7. Of these catalysts, amorphous transition-metal phosphates have attracted wide attention because of their unique electrocatalytic properties. In this paper, the OER performance of a series of amorphous first-row transition metal phosphate (TM-Pi) catalysts, namely Co-Pi, NiFe-Pi and Fe-Pi prepared with different deposition strategies onto various substrates, is comparatively studied in a neutral phosphate buffer solution (PBS). Additionally, a simplified cell model is applied to analyze the current-voltage characteristics and quantitatively evaluate and compare the reversible, ohmic, and activation overvoltage components of the studied TM-Pi. It is found that TM-Pi catalysts deposited onto a highly ordered nickel foam (NF) substrate are competitive with commercial Pt and IrO_2 catalysts in terms of OER activity and long-term stability.

1. Introduction

The intensive use of fossil and nuclear energy has exacted a considerable toll on the natural environment and has led to rapid depletion of many natural resources, adverse climate impacts from greenhouse gas emissions, as well as water, air and land pollution. Growing public awareness of climate change and other environmental issues have resulted in demands for clean and sustainable technologies based on renewable energy [1–3]. Hydrogen, which is the simplest and lightest element of the periodic table, has a high energy density and is considered an eco-friendly fuel to meet the world's increasing energy demand. Currently, the major part of hydrogen production is based on fossil fuel refining processes, such as steam reforming or partial oxidation of methane, which release significant amounts of carbon dioxide into the atmosphere. In contrast, electrochemical water splitting based on renewable electricity provides a sustainable carbon-neutral route for storing energy from intermittent sources using hydrogen as a carrier [4,5].

The water electrolysis process has formed the basis for a number of different energy storage or conversion devices, of which the most efficient and robust are electrolyzers [6,7], fuel cells [8], and metal-air batteries [9]. Bioelectrochemical systems (BES) [10] and hybrid biological-inorganic (HBI) systems [11] represent a fast-developing area of research and are interesting examples of integrating water electrolysis into the biological process to fix carbon dioxide into multicarbon organic compounds. Even though the module design of such systems varies, a common factor is that they are all two-electrode systems involving the hydrogen evolution reaction (HER) or oxygen reduction reaction (ORR) at the cathode and water oxidation or the oxygen evolution reaction (OER) at the anode [12]. The common constraint of these systems is the sluggish kinetics of the oxygen evolution reaction (OER) in which molecular oxygen is formed through a complex pathway involving the extraction of four electrons and four protons. The hydrogen evolution reaction (HER) however is exclusively a two-electron transfer reaction and,

* Corresponding author.
E-mail addresses: georgy.givirovskiy@lut.fi, georgy_givirovskiy@mail.ru (G. Givirovskiy).

https://doi.org/10.1016/j.mtener.2020.100426
2468-6069/

therefore, requires substantially less energy (overpotential) to overcome the kinetics of the reaction [12,13].

The oxygen evolution reaction (OER) is highly pH-dependent. In alkaline conditions, four hydroxyl groups (OH^-) are oxidized into two water molecules (H_2O) and one molecule of oxygen (O_2), while in acidic and neutral conditions, two water molecules (H_2O) are oxidized to be transformed into four protons (H^+) and one oxygen molecule (O_2) [13]. Electrochemical water splitting is hindered by the high stability of water, which requires 237 kJ mol^{-1} of Gibbs free energy change for the overall reaction [14]. According to the thermodynamics, the equilibrium or reversible cell voltage, which is the lowest potential required for the electrolysis to take place at 25°C and 1 atm, is equal to 1.23 V. In practice, however, commercial electrolyzers typically operate in the range of 1.8–2.1 V, indicating that water electrolysis proceeds far from its equilibrium potential [15]. Significant energy losses caused by the large overpotentials required to drive water splitting at sufficiently fast rates are mainly the result of the kinetically sluggish oxygen evolution reaction (OER) [12,13,16]. Therefore, highly efficient OER catalysts are required to lower the energy barrier and increase the overall efficiency of the water splitting process.

At the present time, noble metal-based catalysts made of ruthenium (Ru) and iridium (Ir) and especially their oxides exhibit superior performance for OER and are considered benchmark catalysts. A major drawback of these materials is their unsuitability for large-scale applications owing to their high cost and scarcity. In addition, in both acidic and alkaline electrolytes, IrO_2 and RuO_2 experience stability issues at high anodic potentials because of their oxidation into IrO_3 and RuO_4, respectively, and further dissolution in the electrolyte [12]. Considerable efforts have been therefore made to develop active, stable and low-cost catalysts made of earth-abundant materials capable of operating at low overpotentials at different pHs as substitutes for precious metal catalysts [12,13].

Various transition metal (TM) oxides [17–19], hydroxides [20], sulfides [21,22], nitrides [23,24], borides [25,26], carbides [27,28], selenides [29] and phosphides [23,30–33] have been extensively investigated as efficient catalysts for overall water splitting. Transition metal phosphates (TM-Pi) have attracted widespread scientific interest after the development of a cobalt phosphate (Co-Pi) catalyst by Matthew W. Kanan and Daniel G. Nocera in 2008 [34]. In subsequent studies, numerous other TM-Pi catalysts have been developed, and their electrocatalytic activity towards OER and HER has been shown. A common feature of all these catalysts is the doping of phosphate groups into a crystal lattice of transition metals, such as Ir [16,35], Fe [36,37], Co [34,35], Ni [38–41] and Mn [42] by different methods including electrodeposition, precipitation and hydrothermal synthesis. Phosphate groups facilitate the oxidation of metal atoms during the proton-coupled electron transfer process and distort the native atomic geometry favoring adsorption and oxidation of water molecules [43]. As a result of this unique feature, several reported catalysts, such as Ir-Pi and IrCo-Pi, exhibit an intrinsic performance superior to the benchmark IrO_2 [16,35]. However, even though the content of Ir in IrCo-Pi has been reduced by 50%, there is still a considerable capacity for optimization and reduction in expensive Ir usage.

In the present paper, a series of first-row transition metal phosphates (TM-Pi) are prepared and tested in a neutral phosphate buffer solution (PBS). It is well known that water electrolysis is kinetically difficult in pH-neutral conditions and more favorable in basic and acidic conditions because of the deprotonated molecules available for oxygen and hydrogen evolution reactions [14]. However, pH-neutral conditions exert a significantly less corrosive effect on the electrochemical devices and are vital for emerging biological processes with integrated water electrolysis. The materials analyzed included Co-Pi, Fe-Pi and NiFe-Pi. Co-Pi was selected as a benchmark catalyst from the TM-Pi family, which was exclusively developed to perform water splitting in artificial photosynthesis systems at neutral pH under ambient conditions [34]. Iron (Fe) is the cheapest and most abundant TM in the Earth's crust. Therefore, Fe-Pi prepared by a simple and cheap successive ionic layer deposition and reaction (SILAR) method [36,37] was selected as a candidate for analysis. Literature review suggests that Ni–Fe catalysts provide a promising alternative to catalysts based on precious metals. It is noteworthy that Ni–Fe catalysts are considerably more active for OER than pure Ni or Fe [39,41]. Consequently, bimetallic NiFe-Pi [39] was selected to quantify the synergistic effect of iron in NiFe-based structures. The performance of Fe-Pi and NiFe-Pi has been extensively studied in an alkaline medium, but to the authors' knowledge, it has not been studied in detail in neutral conditions. The main contribution of the present study is the comparative analysis of TM-Pi catalyst on different substrates under neutral conditions. A simplified mathematical electrolyzer cell model is used to deconvolute different overpotentials based on measured current–voltage characteristics.

2. Experimental section

2.1. Materials

Analytical grade reagents $NiSO_4 \cdot 6H_2O$, $FeSO_4 \cdot 7H_2O$, NaH_2PO_2, $NaOAc \cdot 3H_2O$, KH_2PO_4, K_2HPO_4, $Co(NO_3)_2 \cdot 6H_2O$, $FeCl_3 \cdot 6H_2O$, ethanol, and acetone were purchased from Sigma-Aldrich, USA. All chemicals were used as received without additional purification. Graphite electrodes were acquired from Gamry Instruments, USA. Titanium (Ti) coated with IrO_2, and Pt catalysts were purchased from PV3 Technologies, UK. Nickel foam (NF, thickness: 2 mm, porosity: 97%, purity: 99.8%, PPI: 110) was acquired from Tmax Battery Equipments Limited Company, China.

2.2. Catalyst fabrication (NiFe-Pi, Co-Pi, and Fe-Pi)

The procedure for catalyst fabrication was adopted from previous reports [34,37,39]. Electrodeposition and successive ionic layer deposition and reaction (SILAR) were the methods used for catalyst fabrication. The electrodeposition was carried out in the experimental setup depicted in Fig. 1. The setup consisted of: (i) a three-electrode electrolyzer cell with a cross-sectional area of 2.6cm^2; (ii) a WaveNow potentiostat to conduct electrochemical measurements; (iii) a constant flow pump to circulate the electrolyte through the external vessel equipped with the temperature measurement; and (iv) a water bath with an immersed Lauda heater to maintain constant temperature.

Graphite and nickel foam (NF) were used as substrates for deposition of the catalysts. Prior to deposition, a circular piece of NF (15.2cm^2) was cleaned in 2M HCL to remove the nickel oxide layer. Subsequently, ultrasonic cleaning was performed in ethanol, acetone and distilled deionized water to complete removal of surface contaminants. Pretreatment of the graphite substrates included polishing with sandpaper and rinsing with acetone and distilled deionized water. All samples were dried in ambient air prior to the deposition of the TM-Pi catalysts.

The NiFe-Pi catalyst was prepared with a cathodic electrodeposition strategy by cyclic voltammetry (CV) in the potential range from −1.2 to −0.7 V (vs.Ag/AgCl) at a scan rate of 5 mV/s for 8 cycles. The aqueous source solution contained 0.0125, 0.025, 0.0375 M $NiSO_4 \cdot 6H_2O$, 0.0125, 0.025, 0.0375 M $FeSO_4 \cdot 7H_2O$, 0.5 M NaH_2PO_2, and 0.1 M $NaOAc \cdot 3H_2O$ dissolved in distilled deionized water. The Co-Pi catalyst was prepared with an anodic electrodeposition strategy by CV at a scan rate of 5 mV/s for 100 cycles.

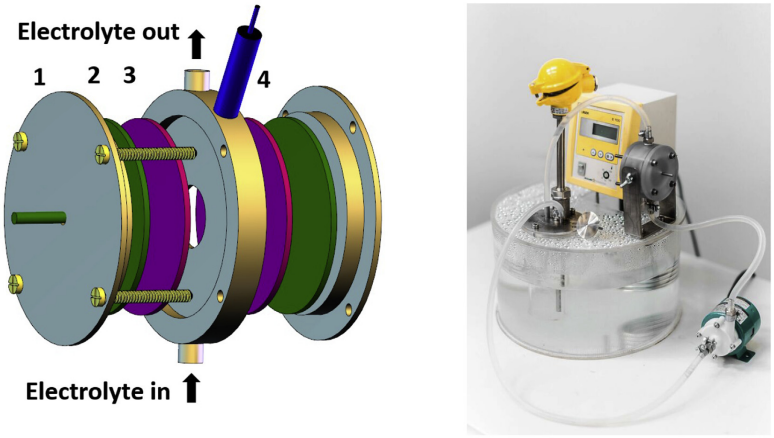

Fig. 1. Experimental setup used for the electrolysis tests. (a) 3D model of the electrolyzer cell; 1: teflon frame, 2: conductive stainless steel plates, 3: working and counter electrodes, 4: reference electrode (Ag/AgCl). (b) Photo of the experimental setup.

Potential ranges from 0.9 to 1.2 V (vs.Ag/AgCl) and from 0.8 to 1.1 V (vs.Ag/AgCl) were used when depositing onto graphite and NF, respectively. To obtain the solution for the electrodeposition, 0.5 mM of $Co(NO_3)_2 \cdot 6H_2O$ was added to the phosphate buffer solution (PBS), which was prepared by mixing 0.1 M KH_2PO_4 and 0.1 M K_2HPO_4. In both electrodeposition methods, graphite and NF were used as the working electrodes (WE), while a stainless steel plate was used as the counter electrode (CE). For the SILAR deposition method, 10 mM aqueous solutions of KH_2PO_4 and $FeCl_3 \cdot 6H_2O$ were prepared separately as the sources of cations and anions, respectively. To prepare the Fe-Pi coating, the cleaned substrates were successively immersed first in a KH_2PO_4 solution for 10 s and then immediately in a $FeCl_3 \cdot 6H_2O$ solution for 10 s. This procedure was repeated for 10 min. All solutions were prepared in ultrapure doubly distilled water obtained from a PURELAB flex system. After deposition, all samples were again gently rinsed with distilled deionized water and dried in ambient air before the electrochemical measurement tests.

2.3. Material characterization

A Hitachi S−3400N field-emission scanning electron microscope (SEM) equipped with energy dispersive X-ray spectroscopy (EDX) measurement was used to examine the surface morphologies and the compositional distribution of the elements of the fabricated catalysts. SEM images were obtained by operating the microscope at 10 kV and 20 mA using a UDV (secondary electron detector) and a BSE (backscatter electron detector). X-ray diffraction (XRD) analysis performed with a Bruker D8 Advance X-ray diffractometer was used to analyze the crystal structure of the studied TM-Pi catalysts. XRD patterns were obtained at 40 kV, 30 mA with Cu Kα-type radiation.

2.4. Electrochemical measurements

All the electrochemical measurements were conducted with a WaveNow Potentiostat from Pine Research Instrumentation, USA, in the three-electrode system shown in Fig. 1. As-prepared TM-Pi catalysts deposited on NF or graphite were directly used as the working electrodes (WE) without further treatment. A titanium (Ti) coated with a Pt circular electrode plate and an $Ag/AgCl,Cl^-$ (3M) electrode were used as the counter electrode (CE) and the reference electrode (RE), respectively. Polarization curves were obtained by linear sweep voltammetry (LSV) at a scan rate of 5 mV/s in a PBS solution, which was prepared by mixing 0.1 M KH_2PO_4 and 0.1 M K_2HPO_4. Long-term durability tests were carried out in the chronopotentiometry mode for 36 h in a PBS. All the potentials measured in this work were calibrated to a reversible hydrogen electrode (RHE) using the following equation:

$$E_{RHE} = E_{Ag/AgCl} + 0.1976\ V + 0.059pH \quad (1)$$

2.5. Cell model

Water electrolysis in neutral conditions (pH = 7) is described by the following electrochemical reactions [14].

The oxidation half-reaction at the anode−oxygen evolution reaction (OER):

$$2H_2O \rightarrow O_2 + 4H^+ + 4e^-,\ E_0 = 0.817\ V \quad (2)$$

The reduction half-reaction at the cathode−hydrogen evolution reaction (HER):

$$4H_2O + 4e^- \rightarrow 2H_2 + 4OH^-,\ E_0 = -0.413\ V \quad (3)$$

The overall reaction in the electrolytic cell:

$$2H_2O + \text{electrical energy} \rightarrow O_2 + 2H_2,\ E_0 = -1.23\ V \quad (4)$$

Virtually, higher voltages than equilibrium or reversible voltage (1.23 V) are required to initiate the dissociation of water. The high overvoltage and the subsequent energy loss are mainly caused by the additional overvoltages presented in the following equation [15]:

$$U_{cell} = U_{rev} + U_{ohm} + U_{act} + U_{con}, \quad (5)$$

where U_{cell} is the cell voltage, U_{rev} is the reversible open circuit voltage, U_{ohm} is the overvoltage caused by ohmic losses in the cell

elements, U_{act} is the activation overvoltage caused by electrode kinetics, and U_{con} is the concentration overvoltage caused by mass transport processes (usually, U_{con} is much lower than U_{ohm} and U_{act}, and it can thus be neglected).

A water electrolysis model developed and validated in our previous studies [44,45] was applied to analyze the collected current–voltage characteristics. The simplified cell model presented in the equation below allows quantitative evaluation and comparison of reversible, ohmic (the 2nd term in the equation after the equal sign) and activation overvoltages (the 3rd term in the equation after the equal sign) of different electrode sets.

$$U_{cell} = U_{rev} + \frac{\delta_m i_{cell}}{\sigma_m} + \alpha \operatorname{arcsinh}\left(\frac{i_{cell}}{2i_0}\right), \quad (6)$$

where δ_m is the distance between the electrodes (expressed in cm), i_{cell} is the current density (A cm^{-2}), σ_m is the conductivity of the electrolyte (S cm^{-1}), α is the charge transfer coefficient, and i_o is the exchange current density on the electrode surfaces. U_{rev}, σ_m, α, and i_0 are the parameters to be fitted by the experimental data.

3. Results and discussion

3.1. TM-Pi catalyst formation

Typical CV curves of the NiFe-Pi and Co-Pi electrodeposition process are presented in Fig. 2. The CV approach ensures fast deposition of TM ions in different potential ranges, and it is beneficial in comparison with traditional potentiostatic deposition of TM-Pi catalysts. It can be clearly seen from the curves that there is a steep increase in the voltammetric current observed over the first 20–30 cycles and a subsequent gradual increase during the electrodeposition of Co-Pi. A similar behavior can be observed in the potential region of the HER; the voltammetric current decreases fast at the beginning of the deposition of NiFe-Pi, and slows down at the end. It would appear that the increasing coverage of the substrate surface and the rising thickness of the TM-Pi coating accelerate the rate of the electrolysis reaction in both cases. After deposition of NiFe-Pi and Co-Pi, the central part of the NF substrate was evenly coated with a dark coating. When depositing NiFe-Pi onto graphite, the surface coating had a silver color as seen in Fig. 3.

The SILAR deposition method to prepare Fe-Pi is considered an inexpensive and facile strategy. Successive immersion of the substrate in the 10 mM cation solution of KH_2PO_4 and the 10 mM anion solution of $FeCl_3 \cdot 6H_2O$ for 10 min resulted in the formation of a white flocculent precipitate all over the surface which could be easily detected with the naked eye.

3.2. Physical characterization

XRD patterns were recorded for the substrate prior to and after the catalyst deposition. A typical XRD diagram of the TM-Pi catalysts deposited on NF is presented in Fig. 4. Diffraction peaks were

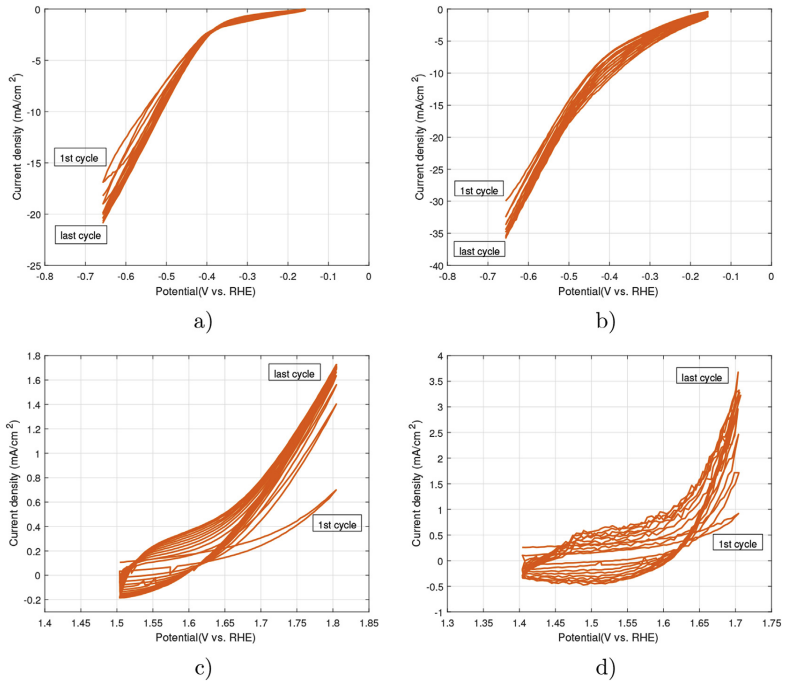

Fig. 2. Cyclic voltammograms of the deposition process of (a) NiFe-Pi onto graphite, (b) NiFe-Pi onto NF, (c) Co-Pi onto graphite and (d) Co-Pi onto NF.

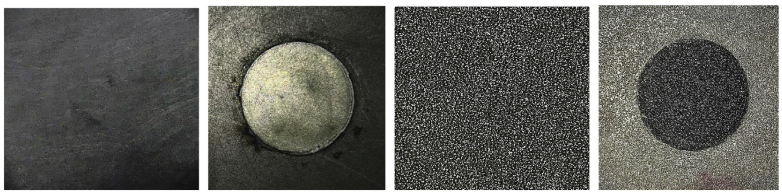

Fig. 3. Photos of electrode surfaces: (a) bare graphite, (b) graphite coated with NiFe-Pi, (c) NF, and (d) NF coated with Co-Pi.

observed at 44.5°, 55.8°, and 76.4° for the NF substrate. The peaks indicates that all the synthesized TM-Pi catalysts are amorphous in nature.

The morphology of the TM-Pi catalysts was studied using SEM. Fig. 5 shows SEM images of bare NF and as-deposited Fe-Pi and Co-Pi, while Fig. 6 depicts the surface morphology and elemental mapping of NiFe-Pi deposited on the NF substrate. The SEM analysis revealed that the surface of the NF was completely and uniformly coated with TM-Pi catalysts in all cases. The example of elemental mapping in Fig. 6d shows uniform distribution of Ni, Fe, and P in the film of NiFe-Pi catalysts. This observation applied also to other TM-Pi catalysts. According to SEM images at high magnification, all TM-Pi catalysts have different surface structures. In particular, the Fe-Pi coating demonstrates a highly rippled flake structure with numerous agglomerates. A Co-Pi layer is formed on the surface of the NF substrate with numerous 3D-porous micrometer-size particles on top of the film. Hierarchical NiFe-Pi mainly consists of nanobubbles with sizes ranging from approximately 200 nm−500 nm. Cracks observed in all the TM-Pi catalysts at higher magnifications probably result from loss of water when drying of samples in ambient air.

The EDXA spectra of bare NF and TM-Pi catalysts are depicted in Fig. 7. The presence of Ni, Fe, Co, and P can be verified from the corresponding peaks in the EDXA diagrams. The quantitative EDXA analysis showed that for Co-Pi catalyst a Co:P ratio varied from 2.5−3:1, while for Fe-Pi a typical Fe:P indicated a ratio of 1:2.2−2.5. The NiFe-Pi catalysts were prepared with different Ni/Fe wt.% compositions. The EDXA showed that the weight percent of Ni and Fe in the NiFe-Pi catalyst deposited onto graphite was close to the theoretical composition in all cases. For instance, for NiFe-Pi catalyst a Ni:Fe:P ratio was approximately 8:1:1.6. The amount of Ni was much higher when using the NF substrate, which can be explained by the EDXA spectrum probe, which reaches the NF substrate due to penetration through the thin catalyst layer.

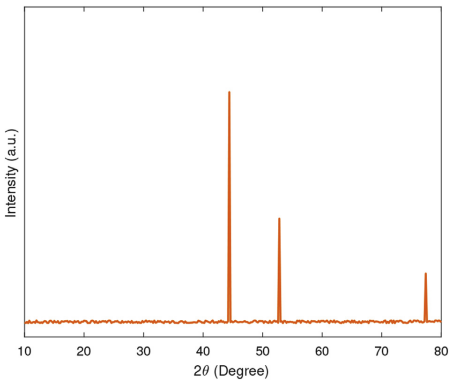

Fig. 4. Typical XRD diagram of the TM-Pi catalysts deposited on NF.

3.3. Catalytic activity

The electrochemical activity of all TM-Pi catalysts was evaluated using a three-electrode electrolyzer prototype in a neutral PBS electrolyte. In order to find the optimal Ni/Fe composition, NiFe-Pi catalyst deposited onto the graphite substrate with different compositional ratios of Ni and Fe were compared with each other. It was found that electrodes with 25 wt.% of Ni and 75 wt.% of Fe showed the worst electrochemical activity and the highest overpotential. Electrodes with a 50/50 wt.% composition of Ni/Fe had a slightly better OER performance than electrodes with 75/25 wt.%, and thus, the optimal 50/50 wt.% composition was used in subsequent tests.

One objective of the study was to investigate the role of the substrate material in the performance of TM-Pi catalysts. In the present study, graphite was selected as a flat, cheap, and commonly used electrode material, while NF was selected as a substrate with a high specific surface area and good OER activity. Fig. 8a and b shows the polarization curves of all TM-Pi catalysts deposited onto graphite and NF at a scan rate of 5 mV s^{-1} in a neutral PBS. The performance of the TM-Pi electrodes was compared with commercial noble materials, represented by Pt and IrO_2. It can be clearly seen that even though the composition of the catalyst layer is the most important parameter determining the OER activity, the nature of the substrate onto which the catalyst is deposited also plays a significant role. When studying TM-Pi catalysts deposited onto graphite, the LSV curves revealed that there was no current flow until the potential reached 1.5 V for all the studied electrodes. After 1.5 V, the current at noble Pt and IrO_2 started to rise steeply reaching a current density of 1 mA cm^{-2} at overpotentials of 450 mV and 430 mV, respectively. In the case of Co-Pi deposited onto graphite, after 1.5 V, the current increase was less steep, reaching 1 mA cm^{-2} at a significantly higher overpotential of 510 mV. The Fe-Pi and NiFe-Pi catalysts deposited onto graphite were approximately similar in performance, having the onset potential at 1.6 V and reaching current densities of 0.6 mA cm^{-2} and 0.88 mA cm^{-2} at 1.8 V, respectively.

The electrocatalytic OER activity of the series of TM-Pi was considerably enhanced when deposited onto the NF substrate. As shown in Fig. 8b, all the TM-Pi catalysts exhibited an onset overpotential comparable with the commercial Pt and IrO_2 electrodes. The reference current density of 1 mA cm^{-2} was reached at

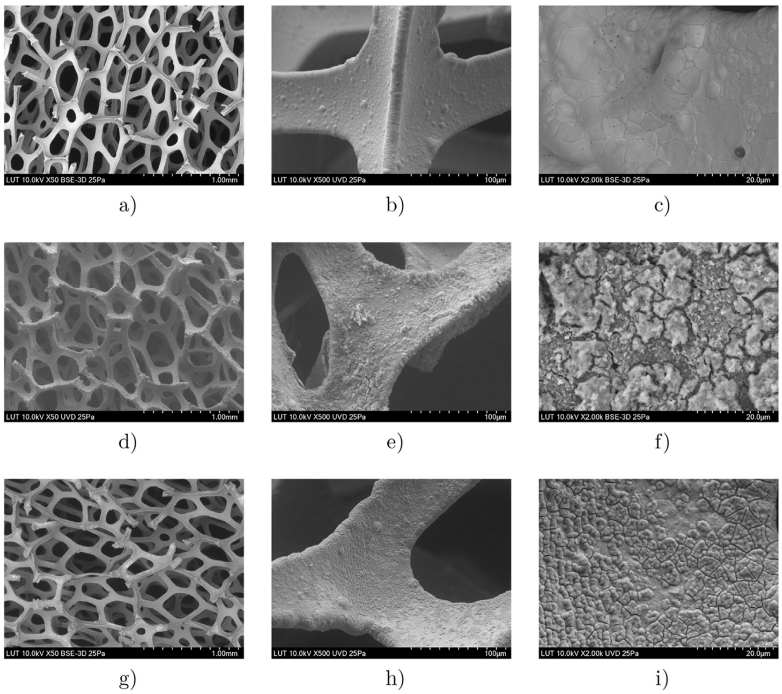

Fig. 5. SEM images of (a–c) bare nickel foam (NF), (d–f) Fe-Pi on NF and (g–i) Co-Pi on NF at different magnifications.

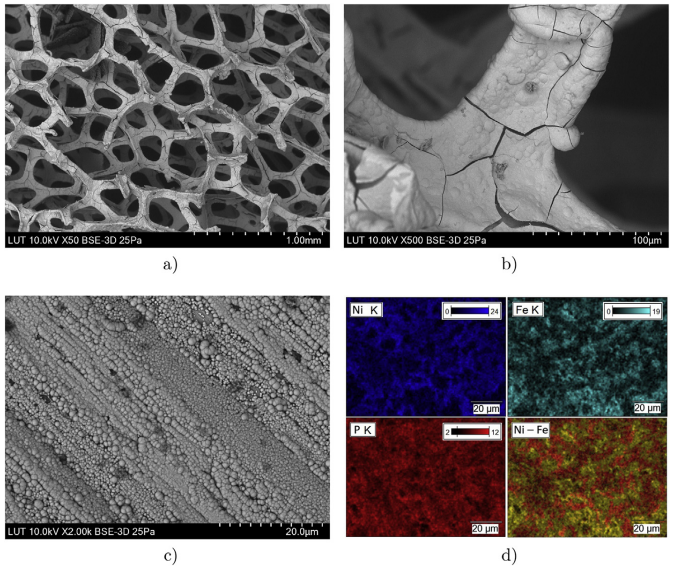

Fig. 6. SEM images of (a–c) NiFe-Pi on NF at different magnifications and (d) the corresponding EDS elemental mappings.

overpotentials of 420 mV, 495 mV, and 534 mV for Co-Pi, NiFe-Pi, and Fe-Pi, respectively. Notably, the OER performance of the Co-Pi catalyst deposited onto the NF surpassed that of the noble electrodes during the whole water splitting process. The superior OER activity of Co-Pi is due to both the high active surface area and the high intrinsic catalytic effect. NiFe-Pi and Fe-Pi were once again similar in performance; however, when the potential reached 1.7 V, the activity of NiFe-Pi increased significantly, and the current density reached 4.45 mA cm^{-2} at 1.8 V, exceeding that of the Pt and IrO_2 electrodes. The current density of Fe-Pi/NF was about 2.8 times as low as that of NiFe-Pi/NF and almost 3.4 times as low as that of Co-Pi/NF at the end of the electrolysis process.

In general, the performance of the TM-Pi-containing electrodes is far better than that of the bare substrates, especially for the NF series. Although the coating on all the studied electrodes has the same geometric surface area of 2.6cm^2, the real active area of the catalyst layer is much higher on the NF substrate because of its unique morphology (Fig. 5a–c). The greater active area explains the high electrocatalytic activity once the TM-Pi electrocatalysts are loaded on the NF. In light of the higher electrocatalytic activity, the TM-Pi catalysts prepared on NF were selected for further characterization and evaluation of the OER performance in the present study.

The Tafel slope is an essential representative parameter for evaluation of OER kinetics. Tafel slopes of TM-Pi/NF were determined from the data shown in Fig. 8c. Analysis revealed that IrO_2 and Co-Pi exhibited almost similar Tafel slopes of approximately 60 mV/dec. This value is representative for a chemical rate-determining step in which a fast OER occurs with the OH surface species rearrangement through a surface reaction [46]. Other tested catalysts showed exceptionally high Tafel slopes close to or higher than 120 mV/dec, which is consistent with the comparatively slow OER kinetics characterized by adsorption and discharge of OH- ions as a chemical rate-determining step. Detailed description of kinetic equations under different reaction conditions can be found in Ref. [47] while the mechanistic schemes are well-presented in Ref. [12]. In general, the mechanism for OER in neutral and alkaline conditions can be described by the following equations [16]:

$$S + OH^- \rightleftharpoons S - OH + e^- \quad (7)$$

$$S - OH + OH^- \rightleftharpoons S - O + H_2O + e^- \quad (8)$$

$$2S - O \rightleftharpoons 2S + O_2 \quad (9)$$

where S represents active sites on the catalyst while S—OH and S—O stand for adsorbed intermediates.

When the Tafel slope is close to 120 mV/dec, reaction described by equation (7) represents a rate-determining step. However, the rate-determining step for Tafel slope of 60 mV/dec is different. It is

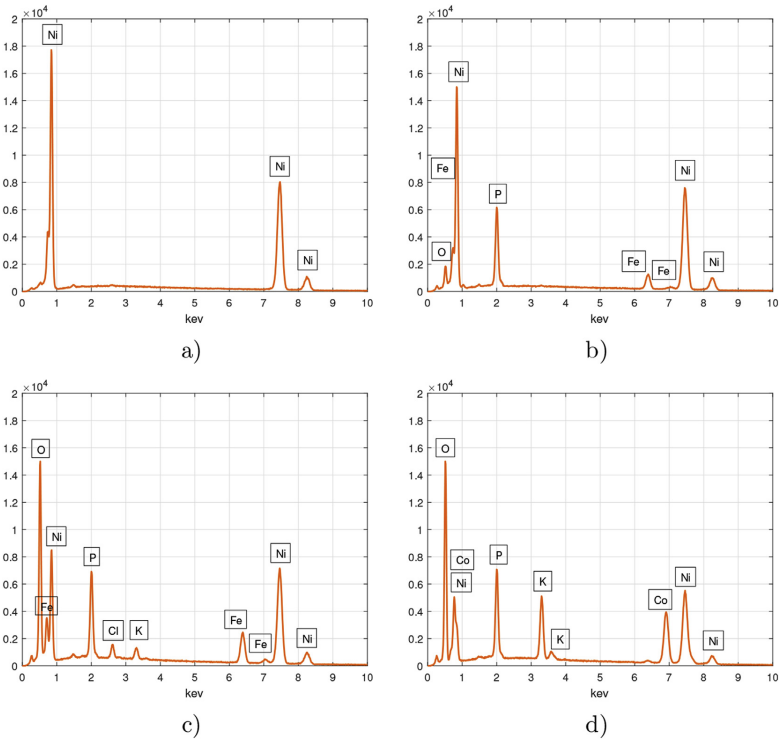

Fig. 7. EDXA spectra for (a) bare nickel foam (NF), (b) NiFe-Pi on NF, (c) Fe-Pi on NF and (d) Co-Pi on NF.

considered that reaction described by equation 7 is divided into the following steps and step described by equation (11) is the rate-determining step for 60 mV/dec:

$$S + OH^- \rightleftharpoons S - OH^* + e^- \quad (10)$$

$$S - OH^* \rightarrow S - OH \quad (11)$$

where S—OH* and S—OH stand for adsorbed intermediates with the same chemical structure, but different energy states.

Stability is an important parameter in evaluation of catalyst performance in practical applications. In this study, stability measurements for a series of TM-Pi/NF were performed successively at a constant current density of 1, 5, and 10 mA cm^{-2} for 36 h in the PBS solution (Fig. 8d). Fig. 9 shows SEM images of TM-Pi/NF after the 36 h durability test. It can be seen that the catalyst layer is partly detached from the substrate surface. Nevertheless, the catalysts continued to maintain a stable potential during the operation of water splitting. The stable operation indicates that an essential part of the TM-Pi catalysts remains on the surface, and its amount is sufficient to maintain the same level of activity. The formation of bubbles on the electrode surfaces under vigorous oxygen evolution and partial loss of effective catalyst may explain the minor increase in the overpotential over time for all the studied catalyst materials.

3.4. Overvoltage analysis

In the present study, a simplified cell model was used to describe the cell voltage components as a function of current density for various TM-Pi deposited onto NF in a pH-neutral PBS. To apply a developed model, the voltage and current were measured with the same electrolyzer prototype but using a two-electrode configuration to measure the whole cell. Cell voltage as a function of current density is presented in Fig. 10a. Again, NF coated with an appropriate TM-Pi catalyst was used as a working electrode, the Pt plate acting as a counter and reference electrode simultaneously. The parameters U_{rev}, σ_m, α, and i_0 in Eq. (6) were determined using experimental voltage and current data and the method of nonlinear least square regression, and presented in Table 1. Further, the reversible voltage, the ohmic voltage, and the activation voltage terms are presented separately in Fig. 10b—d.

Fig. 10 shows clearly that the measured data are in good agreement with the experiments with the three-electrode setup. The obtained Co-Pi/NF exhibited the lowest U_{rev} (Table 1) and outperformed NiFe-Pi/NF and Fe-Pi/NF throughout the water splitting process. The ohmic overpotential (σ_m), which is mainly caused by the voltage drop across the PBS electrolyte, was approximately similar for all the tested TM-Pi catalysts. The reversible voltage, ohmic overvoltage, and activation overvoltage at reference current density of 10 mA cm^{-2} for various TM-Pi catalysts deposited onto NF are summarized in Table 2. The obtained values match well with the experimentally measured conductivity of the

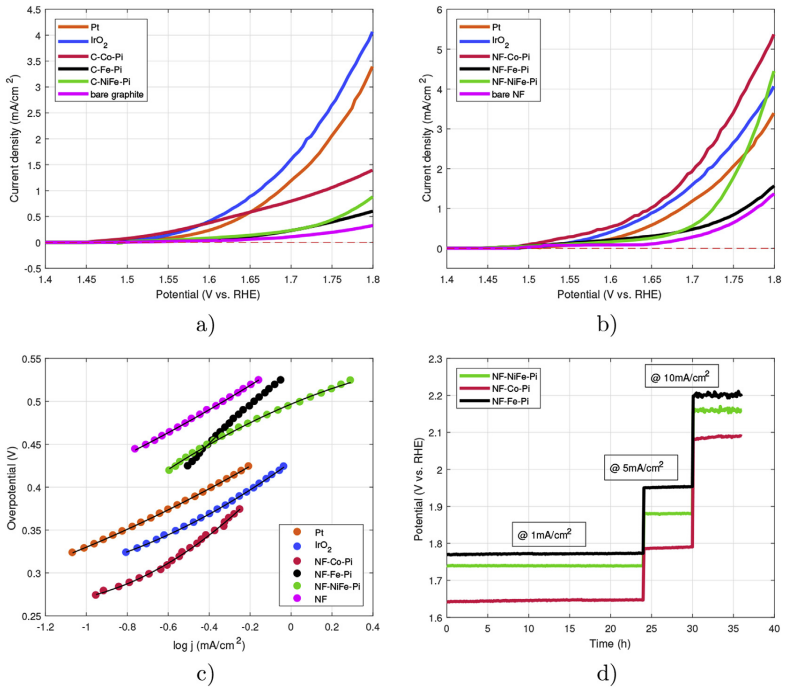

Fig. 8. OER catalytic properties of different catalysts in a PBS with pH = 7: (a) LSV curves of TM-Pi deposited onto graphite vs. noble catalysts, (b) LSV curves of TM-Pi deposited onto NF vs. noble catalysts, (c) corresponding Tafel plots and (d) long-term stability tests of TM-Pi.

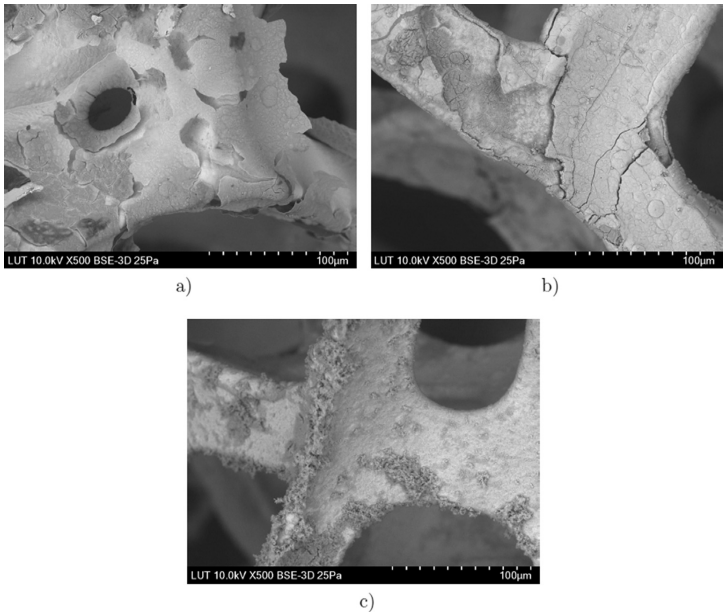

Fig. 9. SEM images recovered after the long-term durability tests for (a) Co-Pi/NF, (b) NiFe-Pi/NF and (c) Fe-Pi/NF.

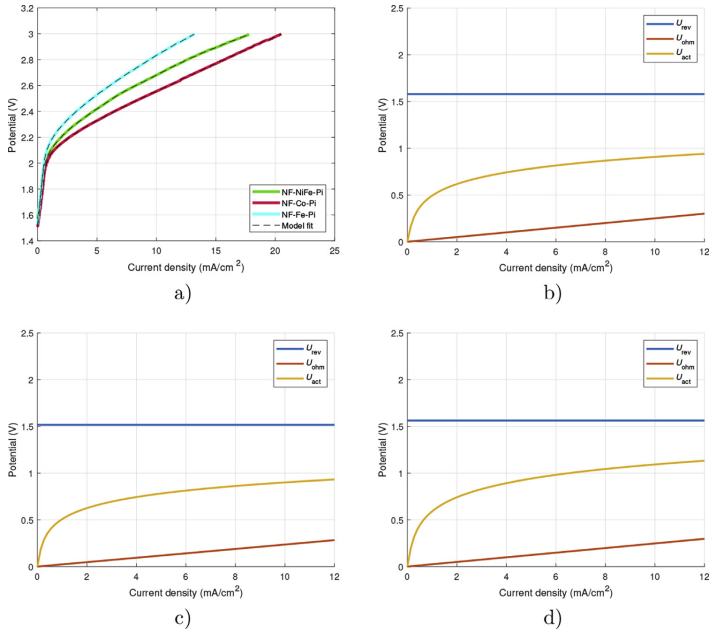

Fig. 10. Overvoltage analysis of the TM-Pi catalysts: (a) cell voltage as a function of current density and the fitted simplified mathematical model; reversible voltage, ohmic overvoltage, and activation overvoltage as a function of current density for (b) NiFe-Pi onto NF, (c) Co-Pi onto NF and (d) Fe-Pi onto NF.

Table 1
Experimentally fitted parameters of the simplified cell model with various TM-Pi catalysts deposited onto NF as anodes.

Anode material	U_{rev} (V)	σ_m (S cm^{-1})	α (−)	i_0 (mA cm^{-2})
NF−NiFe-Pi	1.5799	0.0220	0.1801	0.0001
NF−Co-Pi	1.5166	0.0223	0.1708	0.0001
NF−Fe-Pi	1.5627	0.0222	0.2180	0.0001

Table 2
Reversible voltage, ohmic overvoltage, and activation overvoltage at reference current density of 10 mA cm^{-2} for various TM-Pi catalysts deposited onto NF.

Anode material	U_{rev} (V)	U_{ohm} (V)	U_{act} (V)	U_{cell} (V)
NF−NiFe-Pi	1.5799	0.2500	0.8294	2.6593
NF−Co-Pi	1.5166	0.2466	0.7866	2.5498
NF−Fe-Pi	1.5627	0.2477	1.0039	2.8143

PBS of 22.5 mS cm^{-1} which supports the use of the simplified cell model.

4. Conclusions

A comparative study of the OER activity, stability and overvoltage components of amorphous TM-Pi catalysts deposited by different strategies onto different substrates was presented in this paper. The experimentally observed intrinsic OER activities for the studied catalysts in a neutral PBS decreased in the order of Co-Pi > NiFe-Pi > Fe-Pi. The catalysts exhibited activity comparable with or exceeding that of commercial precious Pt and IrO_2 when deposited onto a substrate with a high specific surface area such as NF. The reference current density of 1 mA cm^{-2} was reached at relatively small overpotentials of 420 mV, 495 mV, and 534 mV for Co-Pi, NiFe-Pi, and Fe-Pi, respectively. A simplified cell model was used to evaluate the current-voltage characteristics of the studied TM-Pi catalysts and to separate the reversible voltage, the ohmic voltage, and the activation voltage terms. All the studied TM-Pi catalysts exhibited sufficient stability for the OER during the 36 h durability tests in the electrolyzer prototype. The collected data and the proposed simplified cell model are valuable for further studies and evaluation of TM-Pi electrocatalyst performance.

Author contribution

Georgy Givirovskiy: Conceptualization, Methodology, Formal analysis, Investigation, Validation, Writing-Original Draft, Visualization; Vesa Ruuskanen: Software, Formal analysis, Writing - Review & Editing, Supervision, Funding acquisition, Resources; Toni Vakiparta: Formal analysis, Writing - Review & Editing, Resources; Jero Ahola: Writing - Review & Editing, Supervision, Project Administration, Funding acquisition, Resources.

Declaration of Competing Interest

The authors declare that they have no known competing financial interests or personal relationships that could have appeared to influence the work reported in this paper.

Acknowledgement

The authors are grateful for support from the Finnish Academy of Science, Finland as part of the “MOPED - Microbial Oil and Proteins from Air by Electricity-Driven Microbes” project funding under number 295866. Financial support was given by the Technology Industries of Finland Centennial Foundation and Jane and Aatos Erkko Foundation for the project “Feed and Food from Carbon dioxide and Electricity- Research and Piloting of Future Protein Production.”

References

[1] D.G. Nocera, M.P. Nash, Powering the planet: chemical challenges in solar energy utilization, PNAS 103 (43) (2006) 15729−15735, https://doi.org/10.1073/pnas.0603395103.
[2] T.W. Brown, T. Bischof-niemz, K. Blok, C. Breyer, H. Lund, B.V. Mathiesen, Response to Burden of proof : a comprehensive review of the feasibility of 100 % renewable-electricity systems ', Renew. Sustain. Energy Rev. 92 (2018) 834−847, https://doi.org/10.1016/j.rser.2018.04.113.
[3] F. Vidal, J. Koponen, V. Ruuskanen, C. Bajamundi, A. Kosonen, P. Simell, J. Ahola, C. Frilund, J. Elfving, M. Reinikainen, N. Heikkinen, J. Kauppinen, P. Piermartini, Power-to-X technology using renewable electricity and carbon dioxide from ambient air : SOLETAIR proof-of-concept and improved process concept, J. CO2 Util. 28 (2018) 235−246, https://doi.org/10.1016/j.jcou.2018.09.026.
[4] M.S. Dresselhaus, I.L. Thomas, Alternative energy technologies, Nature 414 (2001) 332−337, https://doi.org/10.1038/35104599.
[5] N.Z. Muradov, T.N. Vezirog, Green path from fossil-based to hydrogen economy : an overview of carbon-neutral technologies 33 (2008) 6804−6839, https://doi.org/10.1016/j.ijhydene.2008.08.054.
[6] K. Zeng, D. Zhang, Recent progress in alkaline water electrolysis for hydrogen production and applications, Prog. Energy Combust. Sci. 36 (3) (2010) 307−326, https://doi.org/10.1016/j.pecs.2009.11.002.
[7] S. Marini, P. Salvi, P. Nelli, R. Pesenti, M. Villa, M. Berrettoni, G. Zangari, Y. Kiros, Advanced alkaline water electrolysis, Electrochim. Acta 82 (2012) 384−391, https://doi.org/10.1016/j.electacta.2012.05.011.
[8] L. Carrette, K.A. Friedrich, U. Stimming, Fuel Cells − Fundamentals and Applications, Fuel Cells (1) (2001) 5−39, https://doi.org/10.1002/1615-6854(200105)1:1<5::AID-FUCE5>3.0.CO;2-G.
[9] Y. Li, J. Lu, Metal−air batteries : will they be the future electrochemical energy storage device of choice? ACS Energy Lett. 2 (2017) 1370−1377, https://doi.org/10.1021/acsenergylett.7b00119.
[10] G. Kumar, R.G. Saratale, A. Kadier, P. Sivagurunathan, G. Zhen, S.H. Kim, G.D. Saratale, A review on bio-electrochemical systems (BESs) for the syngas and value added biochemicals production, Chemosphere 177 (2017) 84−92, https://doi.org/10.1016/j.chemosphere.2017.02.135.
[11] S.N. Nangle, K.K. Sakimoto, P.A. Silver, D.G. Nocera, Biological-inorganic hybrid systems as a generalized platform for chemical production, Curr. Opin. Chem. Biol. 41 (2017) 107−113, https://doi.org/10.1016/j.cbpa.2017.10.023.
[12] S. Nian-Tzu, H. Sung-Fu, Q. Quan, Z. Nan, X. Yi-Jun, C. Hao Ming, Electrocatalysis for the oxygen evolution reaction : recent development and future perspectives, Chem. Soc. Rev. 46 (2017) 337−365, https://doi.org/10.1039/C6CS00328A.
[13] M. Tahir, L. Pan, F. Idrees, X. Zhang, L. Wang, J.J. Zou, Z.L. Wang, Electrocatalytic oxygen evolution reaction for energy conversion and storage: a comprehensive review, Nanomater. Energy 37 (2017) 136−157, https://doi.org/10.1016/j.nanoen.2017.05.022.
[14] Y. Cheng, S. Ping, Advances in Electrocatalysts for Oxygen Evolution Reaction of Water Electrolysis-From Metal Oxides to Carbon Nanotubes, Progress in Natural Science: Materials International 25 (2015) 545−553, https://doi.org/10.1016/j.pnsc.2015.11.008.
[15] A. Ursúa, L. Gandía, P. Sanchis, Hydrogen production from water electrolysis: current status and future trends, Proc. IEEE 100 (2) (2012) 410−426, https://doi.org/10.1109/JPROC.2011.2156750.
[16] A. Irshad, N. Munichandraiah, High catalytic activity of amorphous Ir-Pi for oxygen evolution reaction, ACS Appl. Mater. Interfaces 7 (2015) 15765−15776, https://doi.org/10.1021/acsami.5b02601.
[17] Q. Liu, Z. Chen, Z. Yan, Y. Wang, S. Wang, S. Wang, G. Sun, Crystal-plane-dependent activity of spinel Co3O4 towards water splitting and oxygen reduction reaction, ChemElectroChem 5 (2018) 1080−1086, https://doi.org/10.1002/celc.201701302.
[18] J. Zaffran, M.C. Toroker, A deep understanding of oxygen evolution reaction on two- dimensional NiO2 catalyst, ChemElectroChem 4 (2017) 2764−2770, https://doi.org/10.1002/celc.201700445.
[19] J. Huang, Y. Su, Y. Zhang, W. Wu, C. Wu, Y. Sun, Y. Li, X. Jie, FeOx/FeP hybrid nanorods neutral hydrogen evolution electrocatalysis: insight into interface, J. Mater. Chem. A 6 (2018) 9467−9472, https://doi.org/10.1039/C8TA02204F.
[20] C.G. Morales-guio, L. Liardet, X. Hu, Oxidatively electrodeposited thin-film transition metal (Oxy)hydroxides as oxygen evolution catalysts, J. Am. Chem. Soc. 138 (2016) 8946−8957, https://doi.org/10.1021/jacs.6b05196.
[21] X. Long, G. Li, Z. Wang, H. Zhu, T. Zhang, S. Xiao, W. Guo, S. Yang, X. Long, G. Li, Z. Wang, H. Zhu, T. Zhang, S. Xiao, W. Guo, Metallic iron-nickel sulfide ultrathin nanosheets as a highly active electrocatalyst for hydrogen evolution reaction in acidic media metallic iron-nickel sulfide ultrathin nanosheets as a highly active electrocatalyst for hydrogen evolution reaction in Ac, J. Am. Chem. Soc. 137 (2015) 11900−11903, https://doi.org/10.1021/jacs.5b07728.
[22] Z. Ma, H. Meng, M. Wang, B. Tang, J. Li, Porous Ni-Mo-S nanowire network film electrode as high- efficiency bifunctional electrocatalyst for overall water splitting, ChemElectroChem 5 (2017) 335−342, https://doi.org/10.1002/celc.201700965.

[23] X. Wang, W. Li, D. Xiong, D.Y. Petrovykh, L. Liu, Bifunctional nickel phosphide nanocatalysts supported on carbon fiber paper for highly efficient and stable overall water splitting, Adv. Funct. Mater. 26 (2016) 4067–4077, https://doi.org/10.1002/adfm.201505509.
[24] K. Xu, P. Chen, X. Li, Y. Tong, H. Ding, X. Wu, K. Xu, P. Chen, X. Li, Y. Tong, H. Ding, X. Wu, W. Chu, Metallic nickel nitride nanosheets realizing enhanced electrochemical water oxidation, J. Am. Chem. Soc. 137 (2015) 4119–4125, https://doi.org/10.1021/ja5119495.
[25] X. Chen, Z. Yu, L. Wei, Z. Zhou, S. Zhai, J. Chen, Ultrathin nickel boride nanosheets anchored on functionalized carbon nanotubes as bifunctional electrocatalysts for overall water splitting, J. Mater. Chem. A 7 (2019) 764–774, https://doi.org/10.1039/c8ta09130g.
[26] J. Masa, P. Weide, D. Peeters, I. Sinev, W. Xia, Z. Sun, C. Somsen, M. Muhler, W. Schuhmann, Amorphous cobalt boride (Co2B) as a highly efficient nonprecious catalyst for electrochemical water splitting : oxygen and hydrogen evolution, Adv. Energy Mater. 6 (2016) 1502313, https://doi.org/10.1002/aenm.201502313.
[27] L. Liao, S. Wang, J. Xiao, X. Bian, Y. Zhang, A nanoporous molybdenum carbide nanowire as an electrocatalyst for hydrogen evolution reaction, Energy Environ. Sci. 7 (2014) 387–392, https://doi.org/10.1039/c3ee42441c.
[28] H. Lin, Z. Shi, S. He, X. Yu, S. Wang, Q. Gao, Y. Tang, Heteronanowires of MoC–Mo2C as efficient electrocatalysts for hydrogen evolution reaction, Chem. Sci. 7 (2016) 3399–3405, https://doi.org/10.1039/C6SC00077K.
[29] C. Tang, N. Cheng, Z. Pu, W. Xing, X. Sun, NiSe nanowire film supported on nickel foam : an efficient and stable 3D bifunctional electrode for full water splitting, Angew. Chem. Int. Ed. 54 (2015) 9351–9355, https://doi.org/10.1002/anie.201503407.
[30] J. Tian, Q. Liu, N. Cheng, A.M. Asiri, X. Sun, Self-Supported Cu3P nanowire arrays as an integrated high-performance three-dimensional cathode for generating hydrogen from water, Angew. Chem. Int. Ed. 53 (2014) 9577–9581, https://doi.org/10.1002/anie.201403842.
[31] J. Huang, Y. Li, Y. Xia, J. Zhu, Q. Yi, H. Wang, J. Xiong, Flexible cobalt phosphide network electrocatalyst for hydrogen evolution at all pH values 10 (2017) 1010–1020, https://doi.org/10.1007/s12274-016-1360-y.
[32] B. Zhang, Y.H. Lui, H. Ni, S. Hu, Bimetallic (FexNi1-x)2P nanoarrays as exceptionally efficient electrocatalysts for oxygen evolution in alkaline and neutral media, Nanomater. Energy 38 (2017) 553–560, https://doi.org/10.1016/j.nanoen.2017.06.032.
[33] B. Zhang, Y.H. Lui, L. Zhou, X. Tang, S. Hu, An alkaline electro-activated Fe-Ni phosphide nanoparticle-stack array for high-performance oxygen evolution under alkaline and neutral conditions, J. Mater. Chem. 5 (26) (2017) 13329–13335, https://doi.org/10.1039/c7ta03163g.
[34] M.W. Kanan, D.G. Nocera, In situ formation of an oxygen-evolving catalyst in neutral water containing phosphate and Co2+, Science 321 (2008) 1072–1075, https://doi.org/10.1126/science.1162018.
[35] Z. Wang, Z. Lin, P. Diao, Hybrids of iridium-cobalt phosphates as a highly efficient electrocatalyst for the oxygen evolution reaction in neutral solution, Chem. Commun. 55 (2019) 3000–3003, https://doi.org/10.1039/C8CC10278C.
[36] P.T. Babar, A.C. Lokhande, H.J. Shim, M.G. Gang, B.S. Pawar, S.M. Pawar, J. Hyeok, SILAR deposited iron phosphate as a bifunctional electrocatalyst for efficient water splitting, J. Colloid Interface Sci. 534 (2018) 350–356, https://doi.org/10.1016/j.jcis.2018.09.015.
[37] D. Zhong, L. Liu, D. Li, C. Wei, Q. Wang, G. Hao, Q. Zhao, J. Li, Facile and fast fabrication of iron-phosphate supported on nickel foam as a highly efficient and stable oxygen evolution catalyst, J. Mater. Chem. A 5 (2017) 18627–18633, https://doi.org/10.1039/C7TA05580C.
[38] Q. Zhang, T. Li, J. Liang, N. Wang, X. Kong, J. Wang, H. Qian, Y. Zhou, F. Liu, C. Wei, Y. Zhao, X. Zhang, High wettable and metallic NiFe-Phosphate/Phosphide catalyst synthesized by plasma for high efficient oxygen evolution reaction, J. Mater. Chem. A 6 (2018) 7509–7516, https://doi.org/10.1039/C8TA01334A.
[39] J. Xing, H. Li, M.M.-c. Cheng, S.M. Geyer, K.Y.S. Ng, Electro-synthesis of 3D porous hierarchical Ni-Fe phosphate film/Ni foam as a high-efficiency bifunctional electrocatalyst for overall water splitting, J. Mater. Chem. A 4 (2016) 13866–13873, https://doi.org/10.1039/c6ta05952j.
[40] Q. Liang, L. Zhong, C. Du, Y. Luo, Y. Zheng, S. Li, Achieving highly efficient electrocatalytic oxygen evolution with ultrathin 2D Fe-doped nickel thiophosphate nanosheets, Nanomater. Energy 47 (2018) 257–265, https://doi.org/10.1016/j.nanoen.2018.02.048.
[41] Y. Li, C. Zhao, Iron-Doped nickel phosphate as synergistic electrocatalyst for water oxidation, Chem. Mater. 28 (2016) 5659–5666, https://doi.org/10.1021/acs.chemmater.6b01522.
[42] K. Jin, J. Park, J. Lee, K.D. Yang, G.K. Pradhan, S.H. Kim, S. Han, K.T. Nam, Hydrated manganese(II) phosphate (Mn3(PO4)2 · 3H2O) as a water oxidation catalyst, J. Am. Chem. Soc. 136 (2014) 7435–7443, https://doi.org/10.1021/ja5026529.
[43] R. Guo, X. Lai, J. Huang, X. Du, Y. Yan, Y. Sun, G. Zou, J. Xiong, Phosphate-based electrocatalysts for water splitting: a review on recent progress, ChemElectroChem 5 (2018) 3822–3834, https://doi.org/10.1002/celc.201800996.
[44] G. Givirovskiy, V. Ruuskanen, L.S. Ojala, M. Lienemann, P. Kokkonen, J. Ahola, Electrode material studies and cell voltage characteristics of the in situ water electrolysis performed in a pH-neutral electrolyte in bioelectrochemical systems, Heliyon 5 (2019) e01690, https://doi.org/10.1016/j.heliyon.2019.e01690.
[45] G. Givirovskiy, V. Ruuskanen, L.S. Ojala, P. Kokkonen, J. Ahola, In situ water electrolyzer stack for an electrobioreactor, Energies 12 (1904) (2019) 1–13, https://doi.org/10.3390/en12101904.
[46] T. Reier, M. Oezaslan, P. Strasser, Electrocatalytic oxygen evolution reaction (OER) on Ru , Ir , and Pt catalysts : a comparative study of nanoparticles and bulk materials, ACS Catal. 2 (2012) 1765–1772, https://doi.org/10.1021/cs3003098.
[47] J.O. Bockris, Kinetics of activation controlled consecutive electrochemical reactions: anodic evolution of oxygen, J. Chem. Phys. 24 (4) (1956) 817–827, https://doi.org/10.1063/1.1742616.

Publication IV

Ruuskanen, V., Givirovskiy, G., Elfving, J., Kokkonen, P., Karvinen, A., Järvinen, L., Sillman, J., Vainikka, M., and Ahola, J.

Neo-Carbon Food concept: A pilot-scale hybrid biological-inorganic system with direct air capture of carbon dioxide

Journal of Cleaner Production,
vol. 278, Jul. 2020

Journal of Cleaner Production 278 (2021) 123423

Contents lists available at ScienceDirect

Journal of Cleaner Production

journal homepage: www.elsevier.com/locate/jclepro

Neo-Carbon Food concept: A pilot-scale hybrid biological–inorganic system with direct air capture of carbon dioxide

Vesa Ruuskanen [a, *], Georgy Givirovskiy [a], Jere Elfving [b], Petteri Kokkonen [b], Aku Karvinen [b], Lauri Järvinen [a], Jani Sillman [a], Miika Vainikka [a], Jero Ahola [a]

[a] LUT University, P.O. Box 20, FI-53851, Lappeenranta, Finland
[b] VTT Technical Research Centre of Finland Ltd., P.O. Box 1000, 02044 VTT, Finland

ARTICLE INFO

Article history:
Received 17 June 2020
Received in revised form
14 July 2020
Accepted 24 July 2020
Available online 22 August 2020

Handling editor. Cecilia Maria Villas Bôas de Almeida

Keywords:
Hybrid biological-inorganic system
In situ water electrolysis
Direct air capture
Carbon dioxide
Microbial protein

ABSTRACT

The pace at which the human population is growing raises serious concerns related to food security while at the same time conventional agriculture-based food production is becoming a major cause of environmental pollution and greenhouse gas emissions. Numerous solutions have been proposed to boost food production among which edible microbial biomass is considered a promising alternative to conventional sources of food and feed with lower environmental footprint. This work introduces the Neo-Carbon Food concept that is a pilot-scale hybrid biological–inorganic process suitable for the production of microbial biomass. The concept includes integrated hydrogen production by water electrolysis, direct air capture (DAC) of carbon dioxide, and its subsequent assimilation by autotrophic hydrogen-oxidizing bacteria (HOB). The hydrogen production with in situ electrolysis achieved specific energy consumption just below 100 kWh/kgH_2 while the specific energy consumption of DAC was around 20 kWh/kg$_{CO_2}$.

1. Introduction

To achieve the climate mitigation goal of the Paris Agreement, 4–5 Gigatonnes of CO_2 must be stored annually (Dowell et al., 2017). According to IPCC, 23% of total anthropogenic greenhouse gas emissions (2007–2016) derive from Agriculture, Forestry and Other Land Use (AFOLU) (IPCC, 2019). Further, maintaining food security is becoming more challenging due to the growing population, lack of additional arable land and freshwater resources, overfishing, and climate change (FAO, 2017). Additionally, unwanted environmental impacts of the conventional agricultural practices such as loss of biodiversity, eutrophication, and salinization of groundwater resulting from fertilizer runoff, inefficient irrigation, and overuse of pesticides harm the sustainability of food production (Mateo-Sagasta et al., 2017). Because of agriculture, six out of nine planetary boundaries have exceeded safe operational spaces (Campbell et al., 2017). Therefore, net-zero carbon emission society requires net CO_2-free food production, which is less dependent on arable land, weather conditions, etc.

1.1. Microbial protein as an emerging technology

One emerging strategy that might significantly contribute to the decoupling of food production from the conventional agricultural production routes is microbial assimilation of carbon. Diverse microbes, such as bacteria, yeast, algae, and fungi, have been known for years for their ability to produce a microbial protein (MP) also known as single-cell protein (Pikaar et al., 2018). The idea of generating an essential protein for human and animal nutrition using microbes, anywhere renewable energy is available, is astonishing.

Indeed, the production of MP as a meat substitute is regaining attention in recent years (Pikaar et al., 2018; Sillman et al., 2019). An attractive feature of microbial protein-based systems is that the production can be performed in fully controlled, enclosed, and automated fermentation bioreactors showing minimal environmental impact (Sillman et al., 2020). Reactor-based MP production is not dependent on using organic substrates, such as starch or cellulose, does not require the utilization of toxic pesticides to control pests and weeds, emits no phosphorous, and requires a

* Corresponding author.
E-mail address: vesa.ruuskanen@lut.fi (V. Ruuskanen).

https://doi.org/10.1016/j.jclepro.2020.123423

limited amount of freshwater inputs. Moreover, the main nutrient ammonia, which is conventionally produced by Haber–Bosch method using fossil fuels, is fully utilized in the closed system (Pikaar et al., 2017). Taking into account that globally the major part of the arable land is currently dedicated to agricultural production of food and feed, the transition towards reactor-based protein production might considerably decrease the environmental pressure. As a consequence, a net positive greenhouse gas emissions from agricultural land use can be diminished drastically while at the same time problems related to deforestation, biodiversity loss, and land-use change would be tackled.

The main carbon source in the process is captured CO_2 which is accessible from anywhere in the world while the main energy source for bacterial growth is H_2 which can be produced through water electrolysis powered by renewable energy. These unique features of the reactor-based process open up the opportunity to launch the production of MP in any geographical location making it almost independent of weather conditions. Furthermore, direct use of captured CO_2 as a feedstock in the process has the potential to make the MP production carbon-neutral (Pikaar et al., 2017; Linder, 2019).

It is worth noting that scaling up the MP production process requires consideration of the important aspects related to assurance of stability of the growing culture, processing of cells to the final product, guaranty of the process safety, and product quality (Pikaar et al., 2017; Linder, 2019). All these requirements have been already successfully achieved and several commercial companies producing food and feed from microbial biomass exist at the market. One of such success stories is the Finnish start-up Solar Foods which uses microbes and CO_2 as a carbon source for the manufacturing of high-protein ingredient branded Solein which will be available in the market in 2021 (Solein, 2019).

1.2. CO_2 assimilation by hydrogen-oxidizing bacteria

Among various microorganisms, autotrophic hydrogen-oxidizing bacteria (HOB) has been pointed as one of the most powerful microbial actuators of the transition towards sustainable food production. The unique feature of HOB enables it to use the chemical energy embedded in hydrogen gas H_2 to assimilate CO_2 and to build new carbonaceous compounds and energy carriers (Yu, 2014). This feature is advantageous as the efficiency of autotrophic growth of HOB is not hindered by the utilization of expensive plant-derived carbon sources, such as sugars or carbohydrates, required for heterotrophic growth (Nangle et al., 2017). The intrinsic premier product of CO_2 assimilation by HOB is biomass which is high in total protein content, has valuable amino acid content, and availability for proteolytic enzymes, and therefore can be considered as a potential protein source and a meat substitute (Volova and Barashkov, 2010).

The concept of CO_2 assimilation by HOB has been successfully proven by different research groups. For instance, Matassa et al. (2016) evaluated the potential of HOB to upgrade NH_3 and CO_2 under autotrophic conditions into biomass with a protein content of approximately 71%. The research group managed to achieve maximum volumetric productivity of 0.41 g of cell dry weight per liter per hour under the continuous operation of the fermentation process. Studies of Yu et al. (2013) revealed the trends affecting the energy efficiency of CO_2 fixation in accordance with the limitation of essential gas substrates required for HOB growth. It was found out that the efficiency of biomass production is substantially affected by the CO_2 concentration. Biomass was produced with a high energy efficiency of up to 50% with moderate O_2 concentrations signifying the possible overall solar-to-biomass conversion efficiency of 5%. Under H_2 limitation, the CO_2 fixation efficiency declined with time. Obviously, the overall process efficiency of CO_2 fixation by HOB is to a great extent dependent on the mass transfer of the main reactant gasses (CO_2, H_2, and O_2) to bacterial cells suspended in the cultivation medium (Yu, 2014). To the best of the authors' knowledge, the maximum value of H_2 conversion efficiency up to 80% in the continuous operation of the fermentation process is reported in (Matassa et al., 2016).

1.3. CO_2 fixation with hybrid biological–inorganic systems

In order to overcome the inherent constraints related to the low solubility of the main reactant gasses, a scalable electricity-driven CO_2 fixation process in the so-called hybrid biological–inorganic (HBI) systems have been developed by Torella et al. (2015). Overall, HBI systems couple biocompatible catalysts to produce H_2 by in situ water splitting and specific microorganisms that use the derived reducing equivalent as an energy source for CO_2 fixation (Nangle et al., 2017). A combination of water electrolysis and CO_2 fixation by HOB in the HBI system may potentially overcome many of the challenges intrinsic to the traditional gas fermentation process relying on the external supply of the reactants. Besides improved gas transfer to the liquid medium HBI process does not experience selectivity problems between organic compounds over a narrow thermodynamic range, does not suffer from difficulties of performing multi-electron reductions for C–C bond formation and its efficiency is not significantly diminished when utilizing air instead of concentrated CO_2 source (Nangle et al., 2017; Liu et al., 2016). Moreover, the HBI process is presumably beneficial over gas fermentation because it allows avoiding the utilization of separate electrolyzer unit and hence decreases the CAPEX while at the same time increasing the safety of the process as the handling of the explosive H_2 and O_2 mixture is not required.

The HBI process has been first tested on a laboratory scale by Torella et al. (2015). They reported the development of an integrated bioelectrochemical system in which water splitting is performed using earth-abundant biocompatible catalysts and HOB to fix CO_2 into biomass and isopropanol with substantial yields of 17.8% and 3.9% of thermodynamic maximum over 24 h, respectively. In the subsequent studies, Liu et al. (2016) managed to improve the HBI process and achieved CO_2 reduction efficiency of approximately 50% when producing bacterial biomass. It is interesting to note, that the CO_2 reduction efficiency decreased only by a factor of 2.7 and reached 20% when using air instead of pure CO_2. However, utilization of concentrated CO_2 might play an important role in the overall HBI process efficiency as it brings practical advantages such as smaller required flow-rate, leading to e.g. less effect on the temperature balance in the bioreactor than by using air as the CO_2 source. Other chemicals, such as polyhydroxybutyrate (PHB) and isopropanol, were produced with the 24-h maximum efficiencies of 42% and 39%, correspondingly. Finally, the calculated solar-to-chemical efficiencies were 9.7% for biomass, 7.6% for bioplastic, and 7.1% for fusel alcohols.

One notable constraint of the HBI process is the incidental formation of reactive oxygen species (ROS), such as hydrogen peroxide (H_2O_2) or hydroxyl radicals, at the cathode side. At pH = 7 ROS formation is thermodynamically more favorable than H_2 production at and below potentials of hydrogen evolution reaction (HER). ROS are toxic to HOB and hinder its biological growth affecting overall process energy efficiency. To overcome this constraint, huge efforts have been made to develop catalysts selective for H_2 production instead of ROS production (Nangle et al., 2017). Substantial increase in performance has been achieved when using cobalt-phosphorous (Co-P) as a HER catalyst in studies of Liu et al. (2016). Sluggish kinetics of oxygen evolution reaction (OER) in neutral pH represents another challenge for HBI processes.

However, the problem is once again tackled by using efficient earth-abundant catalysts such as cobalt−phosphate (Co−Pi) alloy developed by Kanan et al. (Kanan and Nocera, 2008) and successfully applied as anode coating for HOB cultivation in (Torella et al., 2015; Liu et al., 2016). After phenomenological and proof-of-concept discovery of the HBI process, the scientific focus has shifted towards the objectives of enhanced energy efficiency, product selectivity, process robustness, and scaling up. Up to date the research in the field has mostly concentrated on single electrolytic cells immersed in the cultivation medium, and multiple cell stack structures suitable for industrial-scale production have not been widely studied (Givirovskiy et al., 2019a).

Herein, the Neo-Carbon Food demonstration setup for the pilot-scale HBI process is introduced (LUT University VTT Technical Research Centre of Finland, 2019). So far the production of value-added commodities with the HBI system has been proven on a laboratory scale. Thus, the main objective of this paper is to discuss topics related to scaling up the HBI system. In situ water electrolysis stack is introduced to enable hydrogen production directly in the cultivation medium to overcome relatively low hydrogen utilization rates reported for traditional fermentation. Laboratory scale cultivations show a very high hydrogen utilization rate for the HBI system (Givirovskiy et al., 2019a). Aspects related to the specific energy consumption of in situ electrolysis are studied and discussed in detail including the practical aspects related to combining hydrogen production into the HBI system with biomass. Further, the integration of the direct CO_2 capture from the air to the HBI system is studied. Finally, the specific energy consumption of the in situ water electrolysis and CO_2 capture are reported.

2. Materials and methods

2.1. Medium

The mineral medium used for the bioelectrochemical cultivation of HOB is based on a Leibniz-Institut DSMZ growth medium number 81 (DSMZ, 2011) with the following changes: (i) The major chloride compounds have been replaced with the corresponding sulfates, to minimize the production of chlorine gas by the electrolysis current. The trace element solution SL-6 of Pfennig (1974), used in the medium preparation was left unchanged both for convenience, and because some bacteria might require chloride as a micronutrient especially at high salt concentrations (Roeβler et al., 2006). (ii) The ferric ammonium citrate concentration was lowered to 5 mg/L from the 50 mg/L recommended by DSMZ, to prevent iron precipitation from the medium during even a few days storage. (iii) Na_2SO_4 was added to increase the electrical conductivity of the medium and lower the required electrolysis voltage. The final mineral medium composition is given in Table 1.

The medium has a pH of 7 and a conductivity of 12 mS/cm^2.

Table 1
Composition of the cultivation medium.

Compound	Amount
KH_2PO_4	2.3 g/L
$Na_2HPO_4*2H_2O$	2.9 g/L
Na_2SO_4	5.45 g/L
$(NH_4)_2SO_4$	1.19 g/L
$MgSO_4*7H_2O$	0.5 g/L
$CaSO_4*2H_2O$	11.7 mg/L
$MnSO_4*H_2O$	4.4 mg/L
$NaVO_3$	5 mg/L
$NaHCO_3$	0.5 mg/L
$C_6H_8FeNO_7$	5 mg/L
$ZnSO_4*7H_2O$	0.5 mg/L
H_3BO_3	1.5 mg/L
$CoCl_2*6H_2O$	1 mg/L
$CuCl_2*2H_2O$	0.05 mg/L
$NiCl_2*6H_2O$	0.1 mg/L
$Na_2MoO_4*2H_2O$	0.15 mg/L

2.2. Pilot plant description and operation

The main parts of the studied HBI pilot are: the bioreactor tank, the direct air capture unit of CO_2, and the in situ water electrolyzer as shown in Fig. 1. The image of the pilot unit is depicted in Fig. 2 while the piping and instrument schematic of HBI system with equipment labels and key specification is given in the Appendix. The equivalent information of the direct air capture setup is given in (Bajamundi et al., 2019).

A stainless steel bioreactor tank is one of the core elements of the system used for biomass growth, accumulation, sampling, and process monitoring. The tank is equipped with the 2-blade stirrer (E-6) operated at 900 rpm to ensure completely mixed conditions. Water jacket and Lauda RP855 circulation thermostat were used to maintain the optimal for HOB cultivation temperature of 30°C. A centrifugal vertical multistage pump (P-1) EBARA model EVMSUL with maximum flow rate of 3 m^3/h, controlled by a frequency converter (ABB ACS355), was used to guarantee constant liquid circulation in the system.

At the beginning of the process, the system was flushed with ethanol for sterilization. Subsequently, the fresh medium with the total volume of 20 L and enriched HOB culture was supplied to the bioreactor tank successively using the Flowrox dosing pump (P-5) through the sterile filtering system (E-5). The semi-continuous operation of the system was set by extracting a predefined amount and supplying the same amount of fresh medium to the reactor with an interval defined by the measured optical density. The 1M NH_4OH and 1M H_3PO_4 solutions were used to maintain the pH neutral conditions during the process.

In order to enhance the hydrogen production rate and energy efficiency, compared with simply immersed electrodes, an in situ water electrolysis stack (E-1), shown in Fig. 2 (c) was designed and implemented. The cultivation medium with microbes was pumped through the electrolyzer stack to maximize the H_2 gas utilization. Electrolyzer stack current was supplied and measured in case of serial connection with a Sorensen DLM (40V/15A) laboratory power source and in case of parallel connection with an Aim-TTi QPX1200SP (60V/50A) laboratory power source while the stack cell voltages were measured with a Keithley 2701 data acquisition system.

Flammability of H_2 represents a concern for the safety of any hydrogen containing process. Furthermore, the energy efficiency of the HBI process is dependent on the value of applied current in the electrolyzer stack by means of hydrogen utilization and voltage−current characteristics of the electrolyzer stack. Thus, it is critical to supply current at values satisfying the condition when the amount of H_2 produced is equal to the amount of H_2 consumed by HOB and no excess H_2 is accumulated in the headspace of the bioreactor. To make sure that explosive gas mixture accumulation doesn't happen even when the production of H_2 exceeds the consumption, air purging was implemented to the bioreactor.

The H_2 concentration in the exhaust gas was analyzed using BCP-H_2 (BlueSens) thermal conductivity detector (TCD) equipped with a two-stage drying solution based on a condensing dryer (E-3) followed by silica gel tank (E-4) to prevent moisture ingress from the gas flow into TCD. Electrolyzer stack current had been shifting in accordance with the collected data of H_2 concentration in the exhaust. The H_2 concentration was maintained under the lower explosion limit of 4% during the whole pilot operation. The ambient hydrogen level is monitored with Honeywell Sensepoint XCL gas

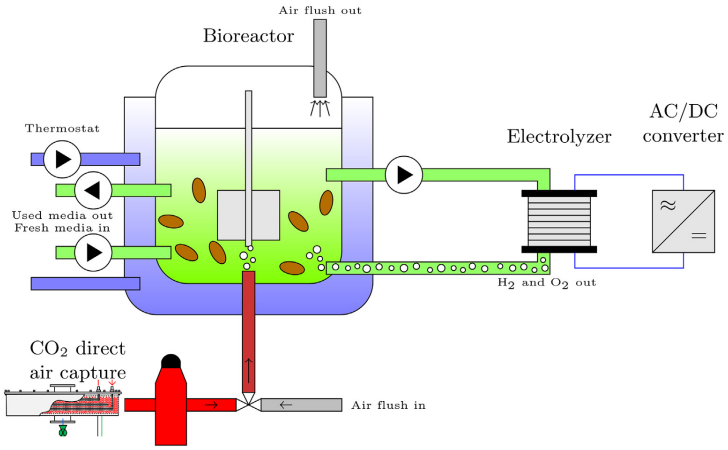

Fig. 1. Schematic diagram of the HBI system with in situ water electrolysis and direct air capture of CO_2.

detector to trigger an alarm and stop operation automatically in case of hydrogen leaks.

The pressure (Tragaf FTP 6.0 A) and temperature (Pt100 RTD + IPAQ C201) transmitters apply 20 mA signal. The pressure and temperature input signals are logged with the EL3058 Beckhoff automation Ethercat module connected to Beckhoff EK9000 Modbus TCP/UDP Bus Coupler. The pH balancing pumps (P-2 and P-3) are controlled over RS-485 (EL6022) and mass flow controllers (MFC-1 and MFC-2) over RS-232 (EL6002) with Beckhoff CX8190 embedded PC communicating with the main automation system over Modbus TCP.

The measurement system control automation of the pilot setup is implemented in a LabVIEW environment. All data is stored online with a 100 ms interval to the LUT measurement database, which can be accessed with the Grafana data observation platform. All the analyses are performed and illustrations plotted with MATLAB software.

2.3. In situ water electrolysis stack

The electrolyzer device was designed as a stack of 2 mm thick electrode plates with zig-zag flow arrangement, shown in Fig. 2(c). The active area of a single electrode is 380 cm^2, and there are ten cells connected in series. So far the electrodes are plain AISI 316L stainless steel, although it has been shown that energy efficiency could be further improved by suitable catalyst coating (Givirovskiy et al., 2019b, 2020). The slit orifices in electrode plates pass the fluid flow between the electrolyzer stages. The orifice locations were chosen based on computational fluid dynamics (CFD) calculations with OpenFOAM software of a few varied cases, so that sufficiently uniform flow velocity distribution over the electrode plates was achieved. The fluid flow velocity distribution is shown in Fig. 3.

Compared with the initial in situ electrolysis stack prototype, described in (Givirovskiy et al., 2019a), the distance between electrodes is decreased to 2.8 mm to minimize conduction losses. The distance is set by using machined spacer rings between the electrode plates. The spacer rings machined of polyacetal (POM) plastic provide also the electrical insulation, carry the preload of the stack assembly, locate the elements in the stack, and electrically isolate the bolts from the electrodes. The electrodes are sealed by planar elastomer seal rings.

Attachment points for electrical connections were laser cut to the electrode plates for electrical connections and monitoring of the individual electrolyzer cell voltages during the test runs. The stainless steel AISI 316L endplates of 10 mm thickness carry the pressure. The design pressure is 8 bar. Welded hose connections are used for the inlet and outlet. The stack is assembled using eight M8 bolts, and the bolt preload is distributed evenly to the stack by the thick washer rings.

The stack arrangement of the electrolyzer device enables reconfigurable arrangement for testing and development of the process, and scalability of the process to industrial scale. In addition, the well-defined alignment of electrode plates allows minimal variation of distance between the electrodes, and thus even electrical current density to the electrolysis process. The measured flow rate in the electrolyzer device was in the range of 0.8 m^3/h-1.3 m^3/h. The flow between the electrode plates is turbulent but close to the laminar condition. Slight turbulence was intended as a design objective to keep the electrode surfaces clean from accumulating biomass and to provide local mixing and slight agitation to the microbes.

2.4. Direct air capture of CO_2

The CO_2 is the carbon source and the main building material for HOB growth. In the present study, CO_2 was captured from air using a DAC unit based on temperature–vacuum swing adsorption. The solid adsorbent in the DAC is a proprietary aminoresin adsorbent. The operation of the DAC unit and the physicochemical characteristics of the adsorbent have been reported earlier in Bajamundi et al. (2019) and Elfving et al., 2017a, 2017b, respectively.

The unit was operated by adsorbing at night taking advantage of lower night temperatures enhancing the adsorption and producing CO_2 during the daytime, such as in the SOLETAIR-project (Vidal et al., 2018). The desorption phase was carried out by using the automated sequence reported earlier (Bajamundi et al., 2019). Typically a 60 min CO_2 desorption time was used for each bed pair, which means the time when the bed pair is subjected to both

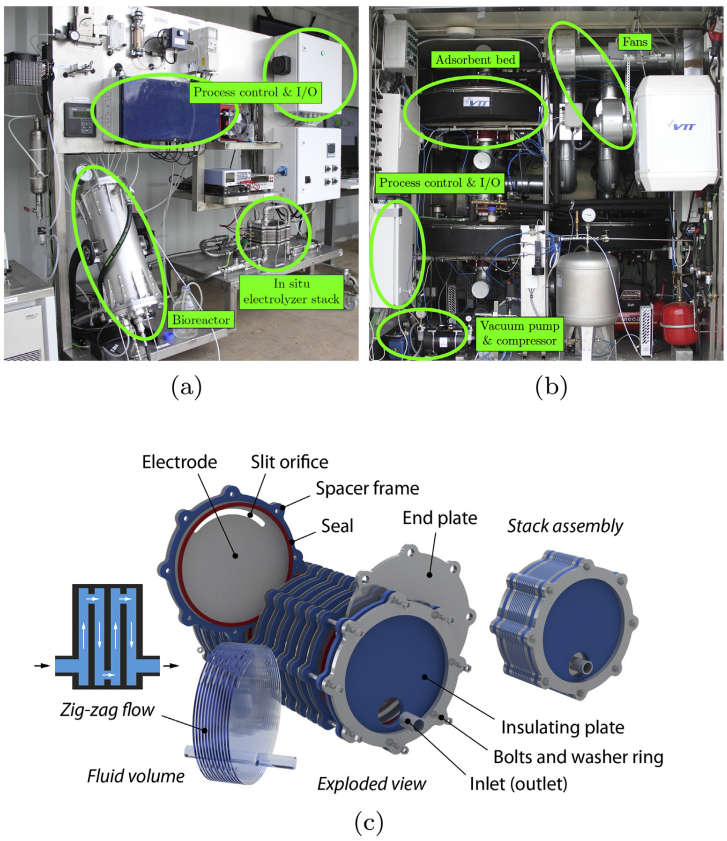

Fig. 2. Neo-Carbon Food setup: (a) Pilot-scale setup for MP production with in situ water electrolysis; (b) Direct air capture unit of CO_2; (c) In situ water electrolysis stack with ten cells in series.

heating at a maximum of 80°C and vacuum. The produced CO_2 gas was stored into an initially empty buffer with volume of 650 L, consisting of one 50 L buffer tank and a 600 L bundle. CO_2 from the buffer was continuously supplied to the bioreactor at a flow rate of 250 mL_n/min and sparged at the bottom of the bioreactor mixed with an airflow of 1 L_n/min.

3. Results and discussion

3.1. Hydrogen production with in situ water electrolysis

The performance of the in situ electrolysis is verified without hydrogen-consuming biomass by measuring the exhaust gas hydrogen content with thermal conductivity detector (TCD) under air flush controlled by a mass flow controller. The test was performed with both serial and parallel connection of the electrolyzer stack cells to compare the performance and especially to detect the amount of stray currents. Measured stack voltages as a function of current are shown in Fig. 4.

Cell voltages are typicaly well above the thermoneutral voltage 1.48 V. Voltage efficiency can be defined by the stack voltage and thermoneutral voltage

$$\eta_U = \frac{U_{tn}\, N_{cell}}{U}, \tag{1}$$

where U_{tn} is the thermoneutral voltage, N_{cell} is the number of cells in series, and U is the stack voltage. The lack of catalyst and the low conductivity of the cultivation medium cause that cell voltages even reach the level of 3 V indicating voltage efficiency to be below 50%. In case of parallel connection all the cells have same voltage, but in case of serial connection the outermost cells have significantly higher voltage than the other cells. This indicates high leakage currents in the serial connected stack. The hydrogen production rate (mol/s) of an electrolyzer stack is linearly proportional to the stack current

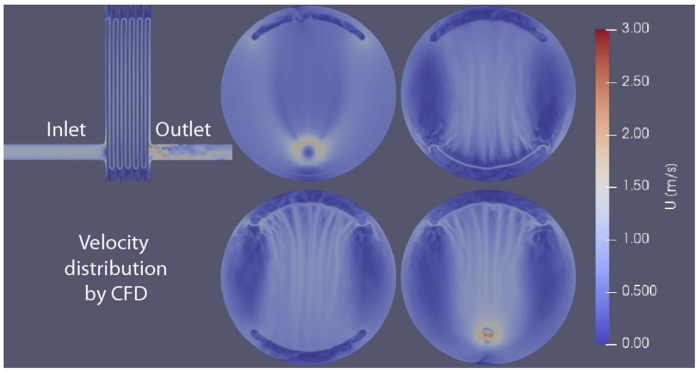

Fig. 3. Fluid flow distribution of the in situ electrolyzer stack analyzed by computational fluid dynamics.

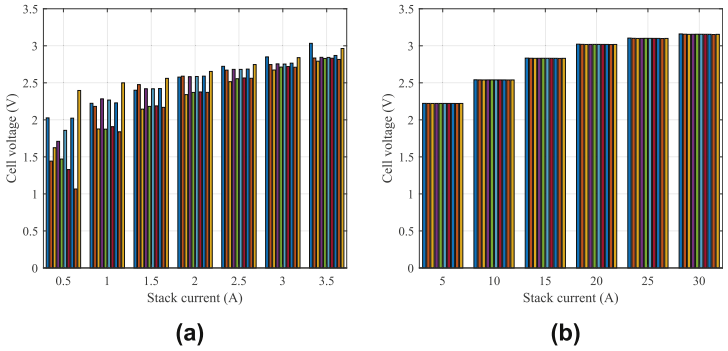

Fig. 4. Individual cell voltages of the in situ water electrolyzer stack as a function of stack current without microbes: (a) Serial connection; (b) Parallel connection.

$$\dot{n}_{H_2} = \eta_F N_{cell} \frac{i}{zF}, \tag{2}$$

where z is the number of moles of electrons transferred in the reaction (for hydrogen, $z = 2$), F is the Faraday constant (9.6485×10^4C/mol), i is the stack current (A), and η_F is the Faraday efficiency, also known as the current efficiency, and N_{cell} is the number of electrolytic cells in series. Faraday efficiency calculated by measured hydrogen flow rate at the exhaust air and stack current is presented in Fig. 5.

In the case of serial connection, the Faraday efficiency is low throughout the current range supporting the assumption of high leakage currents through the flow channels. With a parallel connection, the Faraday efficiency gets values above 80% at currents higher than 15 A. However, the low efficiency at the lowest current levels remains unexplained, but the hydrogen and oxygen gas recombination, other possible side reactions, and measurement inaccuracy are the most probable explanations. As no catalyst is present recombination should be moderate and is not considered as a safety issue in the water solution.

The specific energy consumption E_s of an electrolysis process can be obtained based on the stack voltage, current, and hydrogen production rate

$$E_s = \frac{\int_0^T i(t)\, u(t)\, dt}{\int_0^T \dot{m}_{H_2}\, dt}, \tag{3}$$

where T is the time interval under study. The higher heating value (HHV) is the minimum energy required to produce hydrogen gas with a thermoneutral process. The per mass unit HHV of hydrogen gas is 39.4 kWh/kg, which can be assumed to represent the energy consumption of the process with a 100% efficiency. The specific energy consumption of the in situ electrolyzer is given in Fig. 6.

The SEC of the in situ electrolyzer is significantly higher compared with traditional alkaline or PEM electrolyzers, which typically reach values around 50 kWh/kgH_2. The main factors leading to high specific energy consumption even under Faraday efficiencies exceeding 80% are low conductivity of the cultivation medium and the lack of catalyst coating of the electrodes. However, the efficiency of the in situ electrolyzer can be significantly improved by redesigning the stack to avoid stray currents and applying catalytic coatings. On the other hand, even the studied

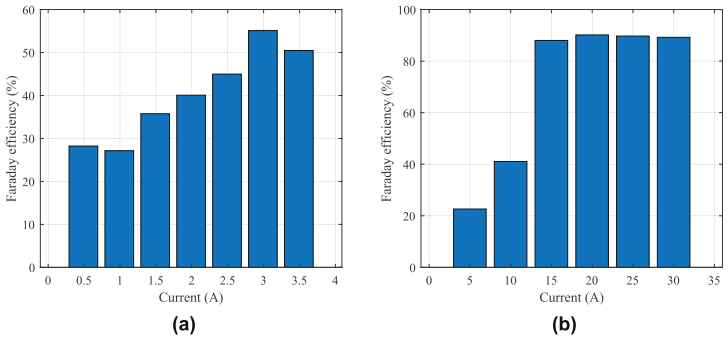

Fig. 5. Faraday efficiencies as a function of current without microbes: (a) Serial connection; (b) Parallel connection.

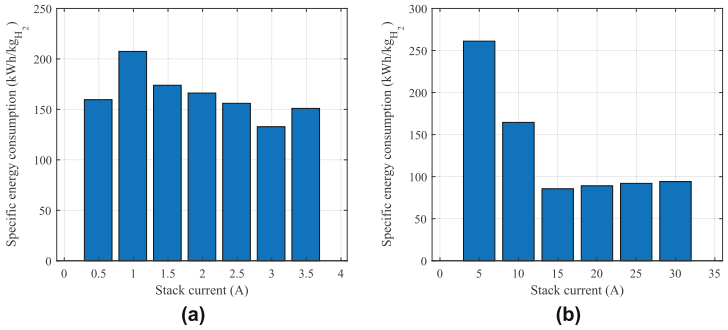

Fig. 6. Specific energy consumption as a function of current without microbes: (a) Serial connection; (b) Parallel connection.

prototype of in situ electrolysis with relatively simple structure and low-cost materials offers a high hydrogen utilization ratio as shown later on. For biomass cultivation campaigns the parallel connection is selected based on the higher efficiency. As scaled up to industrial-scale the parallel connection would require high current with a very low voltage level that is unfavorable for the power supply electronics. Therefore, the stack should be redesigned to minimize the stray currents in case of serial connection.

3.2. Carbon dioxide production

Direct air capture (DAC) is a carbon-negative technology that was first introduced as a process utilizing hydroxide-solutions for chemisorption of CO_2 from air (Jonge et al., 2019; Sanz-Perez et al., 2016). DAC has been reported to be an option for CO_2 enrichment in greenhouses (Rodríguez-Mosqueda et al., 2018), however to the best of authors' knowledge its use in microbial cultivation has not been reported yet. In the present study solid-adsorbent, DAC is used for the HBI cultivation of protein-rich biomass because this type of DAC offers advantages such as small unit size, scalability, and low-temperature demand, often less than 100°C (Sanz-Perez et al., 2016; Bajamundi et al., 2019). The CO_2 production of the direct air capture unit of 2 kg–3 kg per day (Bajamundi et al., 2019) is well over the approximately 0.49 kg per day (using gas correction factor of 0.74 for CO_2) that was supplied to the bioreactor. Therefore, after the initial filing of the CO_2 buffer, the DAC unit was not operated every day. The specific energy requirements of the DAC were calculated in six typical days of operation and the results are shown in Fig. 7. As it can be clearly seen from Fig. 7 higher produced CO_2 amounts usually also resulted in lower specific energy

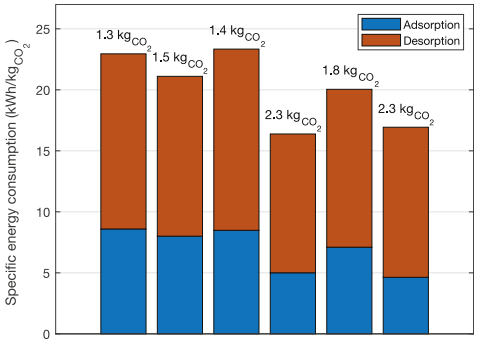

Fig. 7. The specific energy consumption of the DAC unit of six experiments. The produced daily CO_2 amounts are also shown on top of each bar.

consumption (SEC). It is also evident that the contribution of the desorption phase is much higher than the adsorption phase, ranging from 62% up to 73% of the total SEC. The lower amounts of produced CO_2 and higher SEC than reported earlier in (Bajamundi et al., 2019) are partly the result of a shorter desorption phase (60 min vs. 75 min). However, most of the variation can probably be explained with changes in atmospheric conditions.

3.3. Biomass production

The biomass cultivation was tested with several test campaigns. The pilot setup was operated in a semi-continuous mode with periodic extraction of the biomass-rich medium and simultaneous addition of the same amount of approximately 4 L of fresh cultivation medium to the system. The CO_2 captured from the air was continuously sparged from the bottom of the bioreactor through the mineral medium with the experimentally defined flow of 250 mL_n/min while mixed with airflow of 1L_n/min. In order to saturate the culture with H_2 and O_2, the medium with biomass was pumped through the in situ electrolyzer stack with a constant flow rate of approximately 1 m^3/h over the first test campaign.

The visual comparison of the electrolyzer device opened after several weeks of test runs and the CFD velocity distributions are presented in Fig. 8. The comparison shows a good correlation between the amount of accumulated biomass on the surfaces and the flow velocity distribution determined by CFD.

Further, the electrodeposition of metals from the medium solution onto the surfaces of electrodes and corrosion of the electrode plates at the regions near the edges of the slit orifices was found. The indications of corrosion may be due to the high local flow velocity and abrupt geometry at the slit orifices together with gas mixed or diluted into the fluid, that would favor cavitation. The cavitation induced erosion together with oxygen present in the process may then have been caused the corrosion. A Hitachi S-3400N field-emission scanning electron microscope (SEM) equipped with an energy-dispersive X-ray spectroscopy (EDX) measurements was used to examine the surface of the electrolyzer stack electrodes. It can be clearly seen from Fig. 9 that the surfaces of stainless steel (SS) electrodes after the first run were fully coated. The EDS analysis revealed that most of the attached compounds were metals from the medium solution, such as Mg, Zn, Ni, Fe, Co, and carbon referring to the bacterial biomass. In addition to more powerful pumping with flow rate approximately 1.5 m^3/h, the problem was tackled by switching the polarity every 15 min in the electrolyzer stack with a pair of relays. Electrode material with higher resistance against pitting corrosion should be selected.

The biomass analysis showed heavy contamination proposing most of the biomass to be contaminants instead of the desired HOB. However, most of the hydrogen produced is consumed in the process as the exhaust hydrogen content is much smaller than in the test without microbes with the same current proposing that at least some hydrogen consuming organism is produced. The actual CO_2 fixation cannot be estimated as the CO_2 content of the exhaust gas was not monitored. The most probable reason for contamination is the unsuccessful sterilization of the system despite the sanitation with 2% NaOH and flushing with 70% ethanol at a temperature of 55 °C before the autoclaved cultivation medium was added through a sterile filter.

Because of contamination, it is impossible to conduct any analysis of the specific energy consumption of the MP production. In the previous laboratory tests, the hydrogen utilization rate was with in situ electrolysis close to 100%, which is considerably higher than the gaseous hydrogen utilization rate of 80% reported for external hydrogen production (Matassa et al., 2016).

The in situ electrolysis increases the system complexity compared with traditional fermentors making system sterilization more challenging. Furthermore, with in situ electrolysis the proportion of produced hydrogen and oxygen cannot be controlled, which may lead to unfavorable growth conditions. Therefore, the key challenge in the future, in addition to maximizing the hydrogen production energy efficiency, is to avoid contamination.

The production of edible microbial biomass using the HBI process with integrated water electrolysis and biological catalysis is still in the early and developing stage (Nangle et al., 2017). Despite outlined technical challenges and optimization prerequisites, when scaling up a panoptic economical evaluation and life-cycle analysis is required to give a final decision on the viability of the investigating process. Various aspects must be taken into consideration among which are the costs required for renewable electricity for water electrolysis, CO_2 capture costs, expenditures for nutrients and chemicals used for cultivation medium, capital investments, and others. Applied marketing research is of crucial importance to

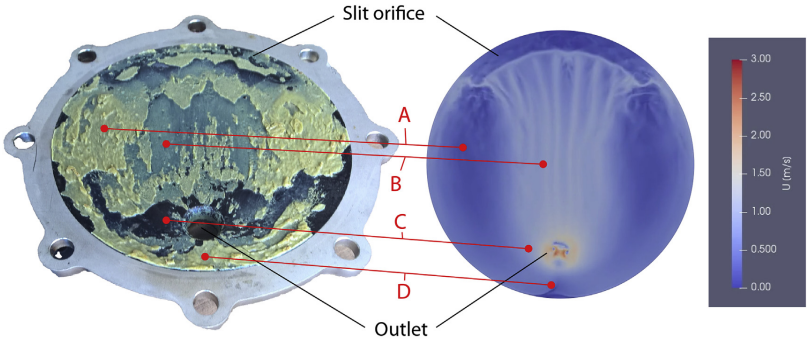

Fig. 8. The amount of accumulated biomass on the electrode plate of the end chamber after first test runs is shown on the left. The visual comparison to the flow velocity distribution by CFD shows thick layer of biomass at areas at low flow velocity (locations A and D), thin layer of biomass at intermediate flow velocity (location B), and clean surface at higher velocity (location C).

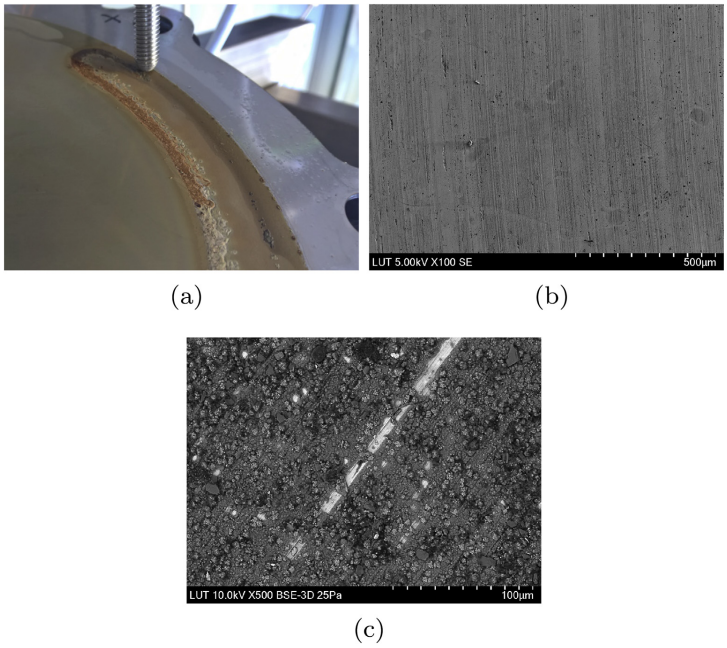

Fig. 9. Stack coating during the first test campaign: (a) Electrode plate coating and corrosion; (b) SEM image of electrode surface (SS) in the beginning of the campaign; (c) SEM image of the coated electrode surface in the end of the campaign.

understand the overall acceptability from regulators and consumers. Regardless, it is already ponderable that the process has significant potential in terms of competing with the purely chemical approaches from CO_2 and provides a viable source of sustainable manufacturing.

4. Conclusions

In the present study, a pilot-scale hybrid biological-inorganic (HBI) process has been introduced to enable sustainable production of microbial protein. The specific energy consumption of in situ water electrolysis and direct air capture of CO_2 have been reported. The major advantage of in situ electrolysis is high hydrogen utilization and no need to handle hydrogen gas in concentrations above lower explosion limit. On the other hand, the efficiency of the hydrogen production is limited and in situ electrolysis also increases the system complexity making the sterilization more challenging compared with external electrolysis.

The key directions of future research will be focused on the: (i) development of microbial culture capable to increase the rate of CO_2 conversion into bacterial biomass; (ii) optimization of electrolyzer stack design in order to mitigate the effect of leakage currents and increase the energy efficiency of in situ water electrolysis; (iii) application of biocompatible earth-abundant electrode coatings and high-surface materials to improve the electrocatalytic efficiency of water splitting and avoid leaching of compounds toxic for bacterial growth; (iv) an extensive economic analysis is essential to evaluate the industrial viability of the HBI production of the protein; (v) assessing whether tailoring the direct air capture process for microbial cultivation can lower the specific energy requirement of produced CO_2, and to support this objective; (vi) studying which is the optimal CO_2 concentration level for maximum growth of the microbial biomass; (vii) studying the optimal current density to maximize the growth. As the test cultivations showed high contamination, the next goal is to achieve a sterile environment for microbial protein growth to further report biomass yield and specific energy consumption of microbial protein production with pilot-scale HBI system. Nevertheless, even now it is possible to conclude that the developed process represents the potential to revolutionize the food and feed production industries, drastically changing their effect on the planet's environment.

CRediT authorship contribution statement

Vesa Ruuskanen: Conceptualization, Methodology, Software, Investigation, Writing - original draft, Project administration, Funding acquisition. **Georgy Givirovskiy:** Conceptualization, Methodology, Investigation, Writing - original draft. **Jere Elfving:** Conceptualization, Methodology, Investigation, Writing - original draft. **Petteri Kokkonen:** Conceptualization, Methodology, Investigation, Writing - original draft. **Aku Karvinen:** Conceptualization, Methodology, Investigation, Writing - original draft. **Lauri Järvinen:** Investigation, Writing - review & editing, Software, Visualization. **Jani Sillman:** Conceptualization, Writing - review & editing. **Miika Vainikka:** Investigation, Writing - review & editing, Visualization. **Jero Ahola:** Conceptualization, Methodology, Writing - review & editing, Funding acquisition, Supervision.

Declaration of competing interest

The authors declare that they have no known competing financial interests or personal relationships that could have appeared to influence the work reported in this paper.

Acknowledgement

This work was supported by the Academy of Finland [grant numbers 295883, 295866]; the Technology Industries of Finland Centennial Foundation with Jane and Aatos Erkko Foundation [grant "Feed and food from carbon dioxide and electricity—research and piloting of the future protein production."]

Appendix. Piping and instrument diagram with list of equipment

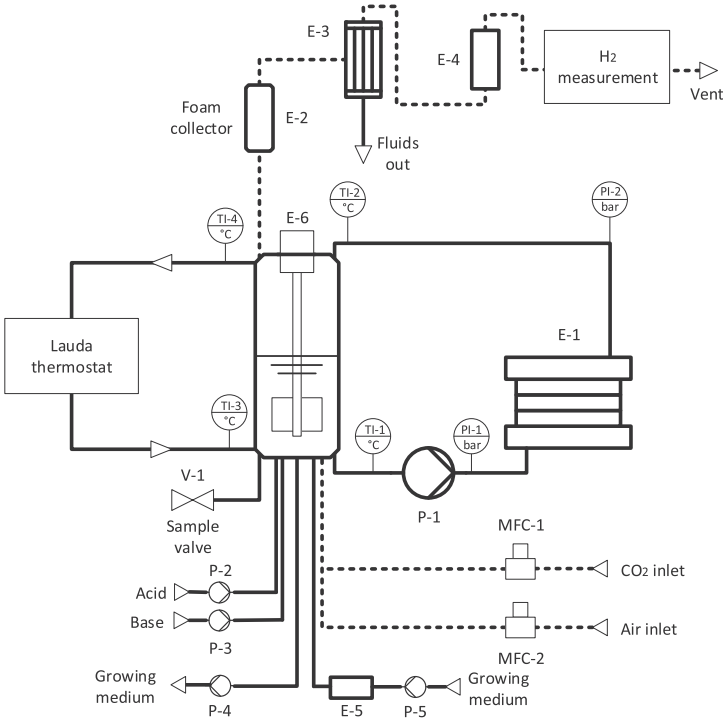

Fig. 10. Piping and instrument diagram of the Neo-Carbon Food setup. Labeled as follows: valves (V), equipment (E), pumps (P) and mass flow controllers (MFC). Gas piping is indicated by dashed lines.

Table 2
List of main equipment with their key specifications. For most equipment the accuracy is given related to reading (RD) and full scale (FS).

Device	Type	Range	Accuracy
Pump P-1	EBARA EVMSUL	0–3 m^3/h	–
Pump P-3	Watson Marlow 400/A	0–30 mL/min	–
Pump P-4	Watson Marlow 400/A	0–30 mL/min	–
Pump P-5	Flowrox LPP-M2-S	0–2.1 L/min	–
Current supply	Aim-TTi QPX1200SP	0–50 A	±0.3% RD ±20 mA
Voltage meas.	Keithley 2701	0–1000 V	±4ppm FS ±10ppm RD
MFC-1 (CO_2)	Bronkhorst MCL-016F	6-300 mL_n/min	±0.1% FS ±0.5% RD
MFC-2 (Air)	Bronkhorst F-201CI	0–5 L/min	±0.1% FS ±0.5% RD
H_2 TCD	BCP-H_2	010$\%_{Vol.}$	±0.2% FS ±3% RD
TI-1 … 4	Pt100 RTD + IPAQ C201	0100°C	±0.1°C
PI-1 … 2	Tragaf FTP 6.0	0–6 bar(g)	±0.4% FS
Analog input	Beckhoff EL3058	4–20 mA	±0.3% FS

References

Bajamundi, C.J.E., Koponen, J., Ruuskanen, V., Elfving, J., Kosonen, A., Kauppinen, J., Ahola, J., 2019. Capturing CO_2 from air : technical performance and process control improvement. J. CO_2 Util. 30, 232–239. https://doi.org/10.1016/j.jcou.2019.02.002.

Campbell, B., Beare, D., Bennett, E., Hall-Spencer, J., Ingram, J., Jaramillo, F., Ortiz, R., Ramankutty, N., Sayer, J., Shindell, D., 2017. Agriculture production as a major driver of the Earth system exceeding planetary boundaries. Ecol. Soc. 22 https://doi.org/10.5751/ES-09595-220408.

Dowell, N.M., Fennell, P.S., Shah, N., Maitland, G.C., 2017. The role of CO_2 capture and utilization in mitigating climate change. Nat. Clim. Change 7 (4), 243–249. https://doi.org/10.1038/nclimate3231.

Elfving, J., Bajamundi, C., Kauppinen, J., 2017a. Characterization and performance of direct air capture sorbent. Energy Proc 114, 6087–6101. https://doi.org/10.1016/j.egypro.2017.03.1746.

Elfving, J., Bajamundi, C., Kauppinen, J., Sainio, T., 2017b. Modelling of equilibrium working capacity of PSA , TSA and TVSA processes for CO_2 adsorption under direct air capture conditions. J. CO_2 Util. 22, 270–277. https://doi.org/10.1016/j.jcou.2017.10.010.

Food and Agriculture Organization of the United Nations (FAO), 2017. The Future of Food and Agriculture: Trends and Challenges, Rome, Italy. URL. http://www.fao.org/3/a-i6583e.pdf.

Givirovskiy, G., Ruuskanen, V., Ojala, L.S., Kokkonen, P., Ahola, J., 2019a. In situ water electrolyzer stack for an electrobioreactor. Energies 12 (10), 1–13. https://doi.org/10.3390/en12101904.

Givirovskiy, G., Ruuskanen, V., Ojala, L.S., Lienemann, M., Kokkonen, P., Ahola, J., 2019b. Electrode material studies and cell voltage characteristics of the in situ water electrolysis performed in a pH-neutral electrolyte in bioelectrochemical systems. Heliyon 5 (5), e01690. https://doi.org/10.1016/j.heliyon.2019.e01690.

Givirovskiy, G., Ruuskanen, V., Väkiparta, T., Ahola, J., 2020. Electrocatalytic performance and cell voltage characteristics of 1st- row transition metal phosphate (TM-Pi) catalysts at neutral pH, Mater. Today Energy 17, 1–11. https://doi.org/10.1016/j.mtener.2020.100426, 100426.

DSMZ GmbH, 2011. 81. Mineral Medium for Chemolithotrophic Growth (H - 3). https://www.dsmz.de/microorganisms/medium/pdf/DSMZ_Medium81.pdf.

Jonge, M.M.J.D., Daemen, J., Loriaux, J.M., Steinmann, Z.J.N., Huijbregts, M.A.J., 2019. Life cycle carbon efficiency of Direct Air Capture systems with strong hydroxide sorbents. Int. J. Greenh. Gas Control 80, 25–31. https://doi.org/10.1016/j.ijggc.2018.11.011.

Kanan, M.W., Nocera, D.G., 2008. In situ formation of an oxygen-evolving catalyst in neutral water containing phosphate and Co^{2+}. Science 321 (5892), 1072–1075. https://doi.org/10.1126/science.1162018.

Linder, T., 2019. Making the case for edible microorganisms as an integral part of a more sustainable and resilient food production system. Food Secur 11 (2), 265–278. https://doi.org/10.1007/s12571-019-00912-3.

Liu, C., Colón, B.C., Ziesack, M., Silver, P.A., Nocera, D.G., 2016. Water splitting–biosynthetic system with CO_2 reduction efficiencies exceeding photosynthesis. Science 352 (6290), 1210–1213. https://doi.org/10.1126/science.aaf5039. http://science.sciencemag.org/content/352/6290/1210.

Matassa, S., Verstraete, W., Pikaar, I., Boon, N., 2016. Autotrophic nitrogen assimilation and carbon capture for microbial protein production by a novel enrichment of hydrogen-oxidizing bacteria. Water Res. 101, 137–146. https://doi.org/10.1016/j.watres.2016.05.077.

Mateo-Sagasta, J., Zadeh, S.M., Turral, H., Burke, J., 2017. Water pollution from agriculture: a global review: executive summary. In: Food and Agriculture Organization of the United Nations (FAO), International Water Management Institute on Behalf of the Water Land and Ecosystems Research Program, Rome, Italy, Colombo, Sri Lanka. URL. http://www.fao.org/3/a-i7754e.pdf.

Nangle, S.N., Sakimoto, K.K., Silver, P.A., Nocera, D.G., 2017. Biological-inorganic hybrid systems as a generalized platform for chemical production. Curr. Opin. Chem. Biol. 41, 107–113. https://doi.org/10.1016/j.cbpa.2017.10.023.

LUT University, VTT Technical Research Centre of Finland, 2019. Neo-carbon food project. URL. www.neocarbonfood.fi.

Pfennig, N., 1974. Rhodopseudomonas globiformis, sp. n., a new species of the Rhodospirillaceae. Arch. Microbiol. 100 (1), 197–206. https://doi.org/10.1007/BF00446317.

Pikaar, I., Matassa, S., Rabaey, K., Bodirsky, B.L., Popp, A., Herrero, M., Verstraete, W., 2017. Microbes and the next nitrogen revolution. Environ. Sci. Technol. 51 (13), 7297–7303. https://doi.org/10.1021/acs.est.7b00916.

Pikaar, I., Vrieze, J.D., Rabaey, K., Herrero, M., Smith, P., Verstraete, W., 2018. Carbon emission avoidance and capture by producing in-reactor microbial biomass based food , feed and slow release fertilizer : potentials and limitations. Sci. Total Environ. 644, 1525–1530. https://doi.org/10.1016/j.scitotenv.2018.07.089.

Rodríguez-Mosqueda, R., Bramer, E.A., Brem, G., 2018. CO_2 capture from ambient air using hydrated Na_2CO_3 supported on activated carbon honeycombs with application to CO_2 enrichment in greenhouses. Chem. Eng. Sci. 189, 114–122. https://doi.org/10.1016/j.ces.2018.05.043.

Roeßler, M., Sewald, X., Müller, V., 2006. Chloride dependence of growth in bacteria. FEMS Microbiol. Lett. 225 (1), 161–165. https://doi.org/10.1016/S0378-1097(03)00509-3.

Sanz-Perez, E.S., Murdock, C.R., Didas, S.A., Jones, C.W., 2016. Direct capture of CO_2 from ambient air. Chem. Rev. 116 (19), 11840–11876. https://doi.org/10.1021/acs.chemrev.6b00173.

Sillman, J., Nygren, L., Kahiluoto, H., Ruuskanen, V., Tamminen, A., Bajamundi, C., Nappa, M., Wuokko, M., Lindh, T., Vainikka, P., Pitkänen, J.-P., Ahola, J., 2019. Bacterial protein for food and feed generated via renewable energy and direct air capture of CO_2: can it reduce land and water use? Glob. Food Secur. 22, 25–32. https://doi.org/10.1016/j.gfs.2019.09.007. http://www.sciencedirect.com/science/article/pii/S221191241830141X.

Sillman, J., Uusitalo, V., Ruuskanen, V., Ojala, L., Kahiluoto, H., Soukka, R., Ahola, J., 2020. A life cycle environmental sustainability analysis of microbial protein production via power-to-food approaches. Int. J. Life Cycle Assess.

Solein, 2019. Solar Foods. URL. www.solarfoods.fi.

IPCC, 2019. Special Report on Climate Change and Land. Geneva, Switzerland. https://www.ipcc.ch/report/srccl/.

Torella, J.P., Gagliardi, C.J., Chen, J.S., Bediako, D.K., Colón, B., Way, J.C., Silver, P.A., Nocera, D.G., 2015. Efficient solar-to-fuels production from a hybrid microbial-water-splitting catalyst system. Proc. Natl. Acad. Sci. Unit. States Am. 112 (8), 2337–2342. https://doi.org/10.1073/pnas.1424872112. http://www.pnas.org/content/112/8/2337.abstract.

Vidal, F., Koponen, J., Ruuskanen, V., Bajamundi, C., Kosonen, A., Simell, P., Ahola, J., Frilund, C., Elfving, J., Reinikainen, M., Heikkinen, N., Kauppinen, J., Piermartini, P., 2018. Power-to-X technology using renewable electricity and carbon dioxide from ambient air : SOLETAIR proof-of-concept and improved process concept. J. CO_2 Util. 28, 235–246. https://doi.org/10.1016/j.jcou.2018.09.026.

Volova, T.G., Barashkov, V.A., 2010. Characteristics of proteins synthesized by hydrogen-oxidizing microorganisms. Appl. Biochem. Microbiol. 46 (6), 574–579. https://doi.org/10.1134/S0003683810060037.

Yu, J., 2014. Bio-based products from solar energy and carbon dioxide. Trends Biotechnol. 32 (1), 5–10. https://doi.org/10.1016/j.tibtech.2013.11.001.

Yu, J., Dow, A., Pingali, S., 2013. The energy efficiency of carbon dioxide fixation by a hydrogen-oxidizing bacterium. Int. J. Hydrogen Energy 38 (21), 8683–8690. https://doi.org/10.1016/j.ijhydene.2013.04.153.

Publication V

Givirovskiy, G., Ruuskanen, V., Kokkonen, P., Karvinen, A., Givirovskaia, D., Repo, E., and Ahola, J.

Pilot-scale in situ water electrolyzer with an improved fluid flow and modified electrodes for upscaling hybrid biologicalâ“inorganic systems

Journal of Cleaner Production,
vol. 314, Jun. 2021

Journal of Cleaner Production 314 (2021) 128001

Contents lists available at ScienceDirect

Journal of Cleaner Production

journal homepage: www.elsevier.com/locate/jclepro

Pilot-scale in situ water electrolyzer with an improved fluid flow and modified electrodes for upscaling hybrid biological–inorganic systems

Georgy Givirovskiy [a,*], Vesa Ruuskanen [a], Petteri Kokkonen [b], Aku Karvinen [b], Daria Givirovskaia [a], Eveliina Repo [a], Jero Ahola [a]

[a] LUT University, P.O. Box 20, FI-53851, Lappeenranta, Finland
[b] VTT Technical Research Centre of Finland Ltd, P.O. Box 1000, 02044, VTT, Finland

ARTICLE INFO

Handling editor: Cecilia Maria Villas Bôas de Almeida

Keywords:
In situ water electrolysis
Electrolyzer stack design
Hybrid biological–inorganic system
Electrocatalyst
pH-neutral conditions
Environmental sustainability

ABSTRACT

Anthropogenic emissions of CO_2 and other greenhouse gases have increased since the pre-industrial era, driven largely by economic and population growth, and are now higher than ever. In this scope, hybrid biological–inorganic systems represent a sustainable and versatile chemical synthesis platform using CO_2 as a feedstock which realizes the idea of 'Cleaner Production'. Practical implementation of hybrid biological–inorganic systems for the production of value-added chemical products requires development of scalable and robust electrobioreactors with a high energy efficiency and an adequate size. This work reports an in situ water electrolyzer stack design as part of an electrobioreactor system required for the pilot-scale operation of the hybrid biological–inorganic process approaching the aforementioned requirements. The electrolyzer is designed by applying fluid dynamics simulation tools to model the electrolyte flow. The design takes into consideration the problem of leakage currents, reported in the previous works, which is tackled by applying an electrically insulating coating. Different electrode surface modification approaches, such as coating with electrocatalysts and etching, are used to further enhance the performance and energy efficiency of the electrolyzer. The performance of the electrolyzer stack was evaluated in a pH-neutral solution required for the hybrid biological–inorganic processes. The in situ water electrolyzer developed in this study showed a high Faraday efficiency close to 90% and acceptable specific energy consumption below 90 kWh kg_{H2}^{-1}. The obtained energy-efficiency values are the highest reported for similar applications with a similar scale which emphasizes the successful design of the in situ water electrolyzer stack. All data collected during experimental work might be applied to further investigation, simulation, and optimization of electrobioreactors operating at neutral pH. Overall, the results achieved in this study are promising and represent a crucial step toward the industrial implementation of hybrid biological–inorganic systems.

1. Introduction

Technologies capable of combining sustainable energy generation and production of valuable products are needed to adjust the focus from a fossil-based economy to a renewable and circular economy and to tackle environmental pollution (Nocera and Nash, 2006; Geissdoerfer et al., 2017). In this context, hybrid biological–inorganic (HBI) systems coupling the advantages of biological components and electrochemical techniques provide a sustainable and efficient chemical synthesis platform. A variety of high-value products, such as biomass, polymers, and alcohols, can be synthesized by using hybrid technology. The operating principle of HBI systems is based on the utilization of specific autotrophic microorganisms interfaced to biocompatible electrodes in systems with integrated water electrolysis. These biocompatible electrodes or catalysts are, in turn, used for the conversion of electrical energy into H_2 or energetic reducing equivalents, subsequently used by microbes as an energy source for assimilation of CO_2 and building of new carbonaceous compounds. In this regard, HBI systems might potentially play a significant role in storing energy from intermittent energy sources and also provide a reliable mechanism for fixing CO_2 – the annual anthropogenic emissions reaching 32 billion metric tons (Nangle et al., 2017).

The HBI processes circumvent many of the challenges inherent to purely chemical conversion of CO_2 (Szczygieł and Kułażyński, 2020;

* Corresponding author.
E-mail addresses: georgy.givirovskiy@lut.fi, georgy_givirovskiy@mail.ru (G. Givirovskiy).

https://doi.org/10.1016/j.jclepro.2021.128001
Received 26 February 2021; Received in revised form 7 June 2021; Accepted 16 June 2021
Available online 22 June 2021

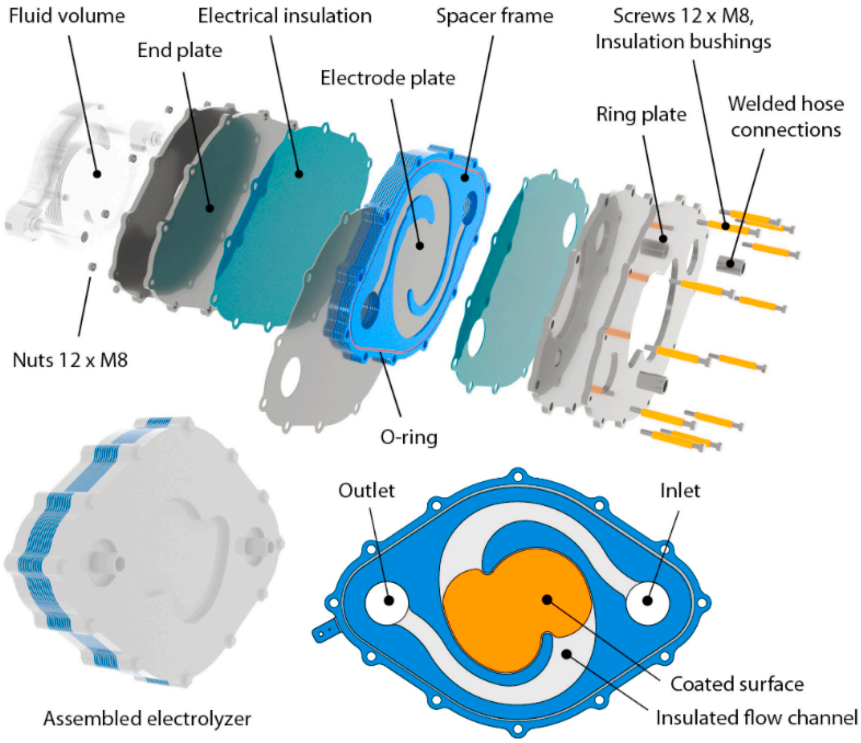

Fig. 1. In situ water electrolysis stack with ten cells in series. An exploded view, assembly, and the coated surfaces of the electrode plate. The spacer frame acts as the flow guide and separates the electrode plates at the desired distance. The flow channels, bolts, and end plates are insulated to reduce the leakage currents. The coated active surface area in the electrolysis process is shown with orange color.

Nieminen et al., 2018), among which are selectivity problems between organic products of a similar thermodynamic potential, difficulties of performing multielectron reductions for C–C bond formation, slow CO_2 reduction rates, and gas transfer limitations caused by the low solubility of the main reactant gases. After the phenomenological and proof-of-concept discovery of the HBI process, the scientific focus has shifted toward the objectives of enhanced energy efficiency, product selectivity, process robustness, and upscaling (Nangle et al., 2017).

Practical implementation and upscaling of the HBI technology is, to a great extent, dependent on the successful solution of the challenges identified in the initial phase. Important scientific tasks, revealed in the first stage, include promotion of the intimate association of electrotrophs and high surface area electrodes, study of mechanism of electron transfer from electrode to bacterium and avoidance of toxic byproducts synthesis (Nangle et al., 2017). The attempts to solve the later problem included the development of selective electrocatalysts that kinetically favor H_2 production instead of reactive oxygen species (ROS) generation (Liu et al., 2016). In this regard, the key research directions cover, but are not limited to, the following aspects: development of stable microbial cultures or microbiomes enabling fast CO_2 conversion rates under aerobic growth conditions, successful implementation of advances in bioreactor and process designs, as well as integration of innovative material structures (Osadolor et al., 2014; Alattar and Bazhin, 2020).

The upscaling of an HBI system is closely associated with the development of a robust, efficient, and ergonomic reactor design with in-situ electrolysis of the cultivation medium (De Francesco and Costamagna, 2004; Wrana et al., 2010). For this purpose, stackable reactor structures, widely used in industrial electrolysis (Bhandari et al., 2014) and dialysis applications, represent a viable technological option capable of achieving targeted volumes by simply increasing the number of stacked units (Krieg et al., 2014). Furthermore, using a stacked reactor for in situ electrolysis has multiple advantages, among which are, for instance, the improved power output and current generation, avoidance of ohmic losses and edge effects, homogeneous current distribution over the reaction volume, and ease of characterization of the overall performance by analyzing the performance of individual cells (Givirovskiy et al., 2019).

There are a few applications of stacks for HBI processes available in the literature, with most of the research concentrating on single electrolytic cells immersed in the cultivation medium (Torella et al., 2015; Liu et al., 2018). Nevertheless, this technology could presumably mitigate many of the existing problems attributed to HBI systems, such as the low conductivity of the cultivation medium, an increase in the ohmic losses, current density limitations set by the microorganisms (Zhang et al., 2020), and the requirements for a design with an acceptable electrode surface-to-volume ratio. Moreover, a substantial improvement in performance can be reached by using coatings of electrode surfaces (Givirovskiy et al., 2020), which, at the same time, tackle biocompatibility issues (Liu et al., 2016).

In this paper, our research group proposes a novel stack structure

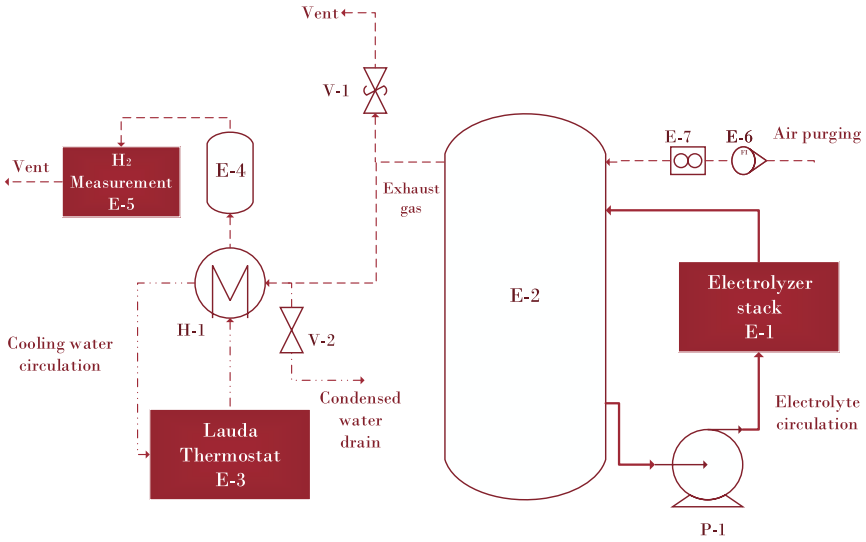

Fig. 2. Process flow diagram of the experimental setup.

design for in situ water electrolysis in HBI systems. The stack is anticipated to increase the hydrogen production rate and the energy efficiency in comparison with the previous versions (Givirovskiy et al., 2019; Ruuskanen et al., 2021). The performance of the stack is experimentally studied, and fluid dynamics simulations are used to design and evaluate the fluid flow.

2. Materials and methods

The following section provides insight into the materials and methods used in this study. First, the in situ water electrolyzer stack design is described in detail followed by the description of the experimental setup used for water electrolysis tests. Thereafter, details related to the preparation of electrocatalysts are presented complemented with the surface characterization techniques used in this study. Eventually, electrochemical methods and fundamental equations describing water electrolysis are given for the readers.

2.1. Materials

Commercially available analytical grade chemicals were used as received without further purification. The stack plates were manufactured from duplex stainless steel 1.4462, purchased from Karose Oy. The following compositional summary of the selected steel material can be found from the material data sheet: Fe 64–72% / Cr 21–23% / Ni 4.5–6.5% / Mo 2.5–3.5% / N 0.08–0.2% (impurities: Mn < 2%, Si < 1%, C < 0.03%, P < 0.03%, S < 0.02%). The insulating Teflon coating for the stack plates was acquired from ATV-Pintakäsittely Oy.

2.2. Description of the in situ water electrolyzer stack design

An improved stacked electrolyzer device was designed based on experiences gained from the test runs with the electrolyzer devices presented in (Givirovskiy et al., 2019; Ruuskanen et al., 2021). Different sources of uncertainty related to the functionality of the electrolyzer device were identified, and countermeasures were devised in the electrolyzer design. The main uncertainties were (i) signs of local erosion or corrosion; (ii) occurrence of leakage currents; (iii) variation in the contact conditions between the spacers and the electrode plates; and (iv) variation in the distance between the electrode plates, which may cause concentration of the electrical current density. The main design changes compared with the previous electrolyzer devices (Givirovskiy et al., 2019; Ruuskanen et al., 2021) were (i) arrangement of the fluid flow through electrically insulated flow channels to decrease the stray currents; (ii) the use of a parallel flow arrangement for even flow velocity distribution; and (iii) a decrease in the pressure drop. The electrolyzer device, shown in Fig. 1, comprises a stack of electrode plates separated by spacer frames and sealed by o-rings. The spacer frames also act as flow guides. The stainless steel end plates carry the pressure load. The stack is assembled with 12 M8 bolts. The ring plate under the bolts provides even distribution of the bolt preload to the spacer frames and seals to avoid leaking. The electrical connections were laser cut to the electrode plates to monitor the electrical current and potential separately at each electrode.

The corrosion resistance of the electrode plates was improved by using duplex stainless steel 1.4462 with the pitting resistance equivalent (PRE) number of 35.1 in comparison with the stainless steel AISI 316L with the PRE number of 24.4 used in the previous electrolyzer (Ruuskanen et al., 2021). In addition, the risk of cavitation was decreased by avoiding abrupt changes in the flow direction by using a parallel flow arrangement. The conditions favoring cavitation were considered to increase the risk of corrosion by local erosion and oxygen present in the process. The rolled surfaces of the duplex steel electrode plates were ground at grit 600 by a roll grinder to provide a roughened surface for the basis of the coating.

To minimize the leakage currents that reduce the Faraday efficiency of the electrolyzer stack, 100 μm Teflon coating was applied. The resistance of the leakage current path through the electrolyte flow channels was maximized by completely coating the electrode plate, only excluding the active areas indicated by orange color in Fig. 1. Special attention was paid to the coating quality in the axial inlet and outlet flow channel areas. Further, the length of the insulated flow channels

between the electrode plates was maximized despite the increased need for electrode plate material.

In the improved electrolyzer device, the fluid is fed by a centrifugal pump to the inlet manifold, from which the fluid flows parallel between the electrodes, and further to the outlet manifold. The distance between the electrode plates is set to 2 mm, compared with the previous 3 mm, to increase the efficiency of the electrochemical process by decreasing the ohmic losses caused by the resistivity of the pH-neutral electrolyte. The active cell area is 239 cm^2. The distance is defined by the thickness of the spacer frame. The relatively small distance between the electrodes tends to keep the flow laminar, and therefore, mixing by turbulence was not applicable in the current design. The electrolyzer device was designed for lab-scale test runs, but the scalability to the industrial scale was considered in the choices throughout the design process. The stack arrangement enables linear scaling of the process by varying the number of electrode pairs. The laminar flow condition and the low-pressure drop at the parallel flow arrangement allow a rather linear scalability also by variation of the diameter, as the small distance between the electrodes tends to keep the flow laminar despite the change in the electrode plate diameter. To ensure the flatness of the electrode plates on the industrial scale, intermediate spacers can be used to support the electrode plates from bending. Further, intermediate spacers can also be used as flow guides.

2.3. Experimental setup

Fig. 2 illustrates the flow diagram of the experimental setup used for the electrolysis tests, consisting of (i) an electrolyzer stack (E-1); (ii) a constant-flow water circulation pump (P-1); (iii) a plastic vessel for the electrolyte input and output (E-2); (iv) an exhaust gas analysis equipment (E-5); and (v) control automation.

A Grundfos Alpha2 25–60 household hot water circulation pump (P-1) with an integrated frequency converter was used for pumping of the electrolyte. In order to avoid H_2 accumulation in the headspace of the plastic vessel (E-2), flushing with air was applied. The flush air flow was controlled with a manual pressure regulator (E-7) and a needle valve and measured with a MASS-VIEW MV-104 mass flow meter (E-6). The H_2 concentration in the exhaust gas was analyzed using an SRS BGA244 binary gas analyzer (E-5) equipped with a two-stage drying solution based on a water-condensing plate heat exchanger (H-1) followed by a silica gel tank (E-4) to prevent moisture ingress from the gas flow into the gas analyzer. Water for the plate heat exchanger was cooled down to 1 °C by a Lauda circulation thermostat (E-3). The electrolyzer stack current was supplied and measured by a GAMRY reference 3000 potentiostat and a Reference 30k booster. A Hioki PW6001 power analyzer with a Hioki CT6862-05 current probe was used for the verification of the measurements. The measurement system control automation of the pilot setup was implemented in a LabVIEW environment. All the data were stored online with a 100 ms interval to the LUT measurement database, which can be accessed with the Grafana data observation platform.

2.4. Modification of the electrolyzer stack plates

The procedure for catalyst fabrication was adopted from previous reports (Kanan and Nocera, 2008; Xing et al., 2016). Electrodeposition was the main method used for the coating preparation of the catalysts. Prior to deposition, the active area of each electrolyzer stack plate was polished with sandpaper, cleaned in 2M HCL to remove the oxide layer, and rinsed with acetone and distilled deionized water to remove possible surface contaminants. Then, the plates were dried in ambient air before further use.

To obtain the solution for the electrodeposition of Co–Pi, 0.5 mM of $Co(NO_3)_2{\cdot}6H_2O$ was added to the phosphate buffer solution (PBS), which was prepared by mixing 0.1 M KH_2PO_4 and 0.1 M K_2HPO_4. The solution for CoFe–P was prepared by dissolving 0.0375 M $CoSO_4 \cdot 7H_2O$, 0.0125 M $FeSO_4 \cdot 7H_2O$, 0.5 M $NaH_2PO_2 \cdot H_2O$, and 0.1 M NaOAc · $3H_2O$.

The Co–Pi catalyst coating was prepared in situ by cyclic voltammetry using the anodic electrodeposition strategy at a scan rate of 5 mV/s in a potential range from 1.7 V to 2.2 V for 4 h. For the deposition of the CoFe–P coating, the cathodic electrodeposition strategy using the chronoamperometry mode was applied at a constant voltage of −2.6 V for 45 min.

The etching solution contained approximately two portions of 30% H_2O_2 solution and one portion of 35% HCl solution. The etchant was poured onto the active surface of each electrolyzer plate with a syringe and left for 30 min. Subsequently, the etchant was gently removed by using a paper towel, and the surfaces were rinsed with deionized water. Teflon was protected by applying adhesive tape.

All solutions were prepared in ultrapure doubly distilled water obtained from a PURELAB flex system. After deposition, all plates were again gently rinsed with distilled deionized water and dried in ambient air before the electrochemical measurement tests.

2.5. SEM and XRD characterization

A Hitachi S–3400N field-emission scanning electron microscope (SEM) equipped with energy-dispersive X-ray spectroscopy (EDX) measurement was used to examine the surface morphologies and the compositional distribution of the elements of the fabricated catalysts. SEM images were obtained by operating the microscope at 10 kV and 20 mA using a UDV (secondary electron detector) and a BSE (backscatter electron detector). X-ray diffraction (XRD) analysis performed with a Bruker D8 Advance X-ray diffractometer was used to analyze the crystal structure of the studied electrocatalysts. XRD patterns were obtained at 40 kV, 30 mA with Cu Kα-type radiation.

2.6. Electrochemical measurements

All the electrochemical measurements were conducted with a potentiostat and booster by Gamry Instruments, the USA. The electrolyzer was connected by using a two-electrode configuration to measure the voltage drop across the whole device. A PBS solution, which was prepared by mixing 0.1 M KH_2PO_4 and 0.1 M K_2HPO_4, was used as an electrolyte for all the electrochemical measurements. Polarization curves were obtained by linear sweep voltammetry (LSV) at a scan rate of 20 mV s^{-1}.

2.7. Performance evaluation

There are several crucial parameters describing the water electrolysis process. The minimum thermodynamic potential required for water electrolysis, called reversible voltage, is 1.23 V in standard ambient conditions. Without auxiliary heat, the required minimum voltage is higher and dependent on the electrolysis conditions (e.g., 1.48 V in standard ambient conditions). From the perspective of energy efficiency, the voltage driving the electrolysis should thus be kept as low as possible. The actual voltage required to drive the electrolysis is higher because of overvoltages (i.e. voltage losses) caused by the impedance between the electrodes and the activation reactions. Hence, the overall cell voltage is the sum of different overvoltages (overpotentials) presented in the following equation

$$U_{cell} = U_{rev} + U_{ohm} + U_{act} + U_{con}, \quad (1)$$

where U_{cell} is the cell voltage, U_{rev} is the reversible open circuit voltage, U_{ohm} is the overvoltage caused by ohmic losses in the cell elements, U_{act} is the activation overvoltage caused by electrode kinetics, and U_{con} is the concentration overvoltage caused by the mass transport processes (Ursúa et al., 2012).

Cell voltages are typically well above the thermoneutral voltage

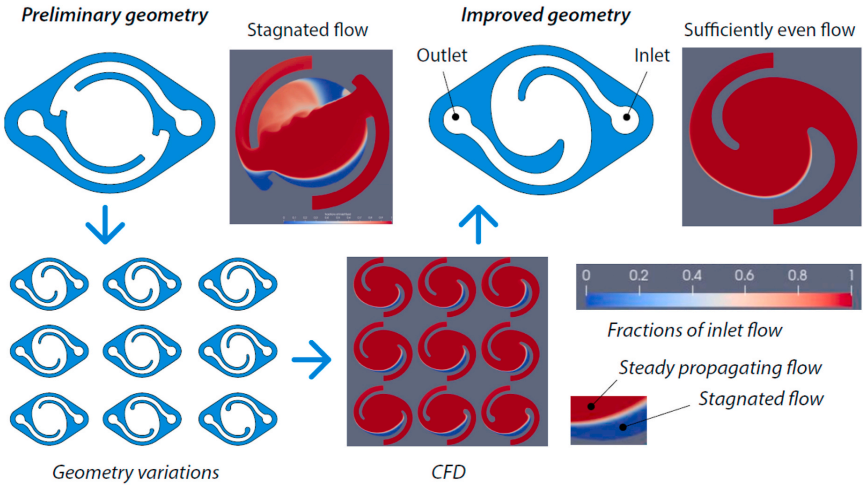

Fig. 3. CFD-based design of the flow guide.

1.48 V. Voltage efficiency can be defined by the stack voltage and the thermoneutral voltage

$$\eta_U = \frac{U_{tn} N_{cell}}{U}, \tag{2}$$

where U_{tn} is the thermoneutral voltage, N_{cell} is the number of cells in series, and U is the stack voltage.

The hydrogen production rate (mol s^{-1}) of an electrolyzer stack is linearly proportional to the stack current

$$\dot{n}_{H_2} = \eta_F N_{cell} \frac{i}{z F}, \tag{3}$$

where z is the number of moles of electrons transferred in the reaction (for hydrogen, $z = 2$), F is the Faraday constant (9.6485×10^4 C mol^{-1}), i is the stack current (A), and η_F is the Faraday efficiency, also known as the current efficiency, and N_{cell} is the number of electrolytic cells in series.

The specific energy consumption E_s of an electrolysis process can be obtained based on the stack voltage, current, and hydrogen production rate

$$E_s = \frac{\int_0^T i(t)\, u(t)\, dt}{\int_0^T \dot{m}_{H_2}\, dt}, \tag{4}$$

where T is the time interval under study. The higher heating value (HHV) is the minimum energy required to produce hydrogen gas with a thermoneutral process. The per mass unit HHV of hydrogen gas is 39.4 kWh kg^{-1}, which can be assumed to represent the energy consumption of the process with a 100% energy efficiency.

3. Results and discussion

The following section presents the main results of in situ water electrolyzer stack performance. First, an improvement of the electrolyte flow with computational fluid dynamics tools is mentioned. Subsequently, values of Faraday efficiency and specific energy consumption are calculated based on hydrogen production rates. Finally, substantial performance enhancement by electrode surface modification is described in detail.

3.1. Improvement of the electrolyte flow

The geometry of the electrolyzer stack was designed by using computational fluid dynamics (CFD) to avoid a stagnated flow and to achieve a revolving flow in laminar flow conditions. A widely used and extensively validated OpenFOAM (openfoam.org) library was used as the CFD software. Even though the desired flow situation was a laminar flow, a detached eddy simulation (DES) turbulence modeling procedure was applied. The k-ω SSTDES (Menter et al., 2003) model (Shear Stress Transport DES) was used as a turbulence model for the simulation. In the DES procedure, the core region of the flow is simulated using large eddy simulation (LES), and in the vicinity of the wall, the traditional RANS (Reynolds Averaged Navier Stokes) turbulence model is used. By this method, excessive computational resources are not needed unlike in the case of a real LES simulation because of the dense grid resolution requirement in the boundary layer region. When the flow velocity is slow enough and the flow approaches the laminar case, excessive dissipation produced by the subgrid model of the DES ceases, and the simulation is a laminar simulation in effect. The computational grids used in the simulation consist of about 1 million cells. Because of the large number of geometries tested and the time-dependent nature of the DES simulation, relatively coarse meshes were used.

Design exploration was used to find a suitable geometry; some of the designs investigated are presented in Fig. 3. The preliminary geometry produced stagnation flow, and therefore, several geometry variations were tested and simulated further. The final geometry was visualized by CFD simulation to produce uniform flow velocity distribution. The resulting flow geometry is asymmetric and enables uniform flow in laminar flow conditions. It should be noted that a mathematical optimization algorithm was not used, and it was left for a future study.

3.2. In situ hydrogen production

First, the performance of the electrolyzer stack was verified by measuring the exhaust gas hydrogen content with a binary gas analyzer under air flush with a constant flow of 5 L min^{-1}. The performance was compared for both a serial and a parallel connection of 5 electrolyzer stack cells. In case of serial connection the stack voltage is the sum of cell voltages as in parallel connection the stack current is the sum of cell

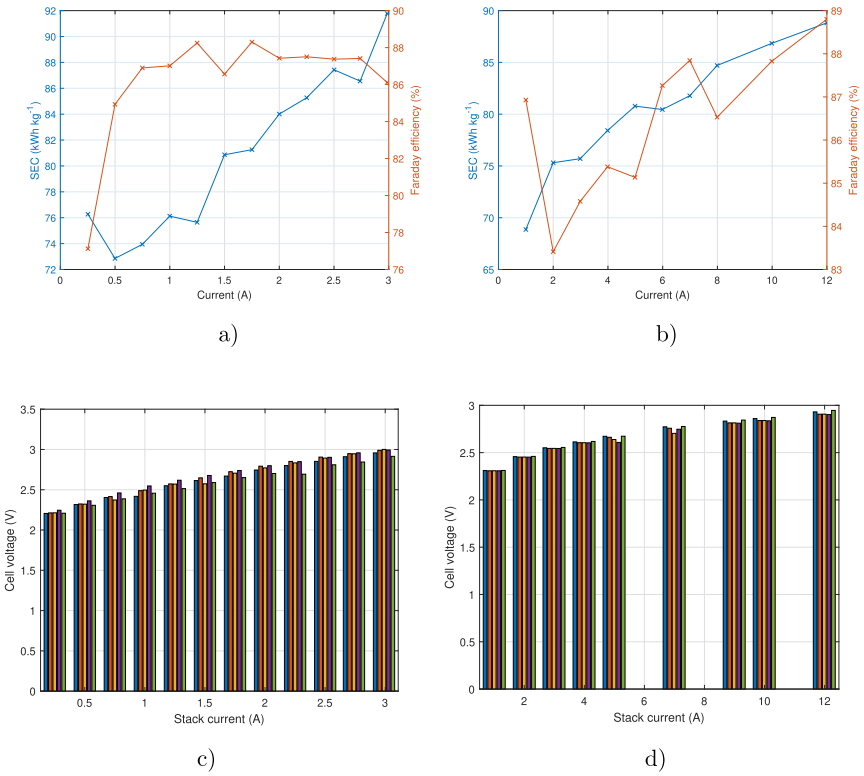

Fig. 4. Specific energy consumption (SEC) and Faraday efficiency as a function of stack current for (a) serial connection and (b) parallel connection of 5 electrolyzer stack cells; Example of individual cell voltages distribution of the in situ water electrolyzer stack as a function of stack current for (c) serial connection and (d) parallel connection.

currents. The specific energy consumption (SEC) and Faraday efficiency of the stack were calculated based on the collected current–voltage relationships and the measured hydrogen production and presented in Fig. 4.

The previous stack prototype (Ruuskanen et al., 2021) suffered from high leakage currents as maximum Faraday efficiency with serial connection was around 50%. In the newer version leakage currents were decreased by applying an insulating Teflon coating throughout the surface of the electrolyzer stack plates except the active electrode area located in the middle. The performance of the solution was verified by the evenly distributed cell voltages in the stack for both the parallel and serial connections as it is depicted in Fig. 4c and in Fig. 4d. In both cases, the Faraday efficiency was close to 90% at cell currents of 1.5 A–2.5 A indicating that leakage currents are relatively small. The hydrogen production rate was almost similar for both serial and parallel connection of the stack cells. For instance, at stack current of 2 A and stack voltage of 15.17 V the hydrogen production rate was 3.66 NL h^{-1} and at 10 A and 2.89 V it was 3.68 NL h^{-1}, correspondingly for serial and parallel connection.

Furthermore, the specific energy consumption was significantly reduced in contrast with the earlier study despite the use of the PBS with a lower conductivity (Ruuskanen et al., 2021). As the cell voltages are at the same range compared with the previous stack prototype the performance improvement is mainly because of the reduced leakage currents. For the current range of 1.5 A–2.5 A per cell, the specific energy consumption did not exceed 90 kWh kg_{H2}^{-1}, which, once again, indicates successful redesign of the electrolyzer stack with the application of proper insulation. The obtained values of SEC are almost 1.8 times as high as that of the traditional alkaline and PEM electrolyzers, which are typically around 50 kWh kg_{H2}^{-1} at 47% – 82% efficiency (Ursúa et al., 2012). One of the factors leading to higher SEC even under Faraday efficiencies of 90% is lower conductivity of PBS solution in comparison to, for instance, KOH used in alkaline water electrolysis. However, it is evident that despite certain similarities between pH-neutral in situ water electrolysis and conventional water electrolysis, the application of these technologies varies significantly. Thus, it is not fair to give any negative conclusions regarding the viability of the studied process based only on efficiency and SEC differences (Rieth and Nocera, 2020).

3.3. Modification of the electrolyzer stack surface and performance evaluation

In order to further enhance the performance of the electrolyzer stack, different surface modification options were examined. First, coating with the benchmark Co–Pi catalysts deposited onto a polished stainless steel electrode plate was tested. Amid deposition of Co–Pi, a gradual

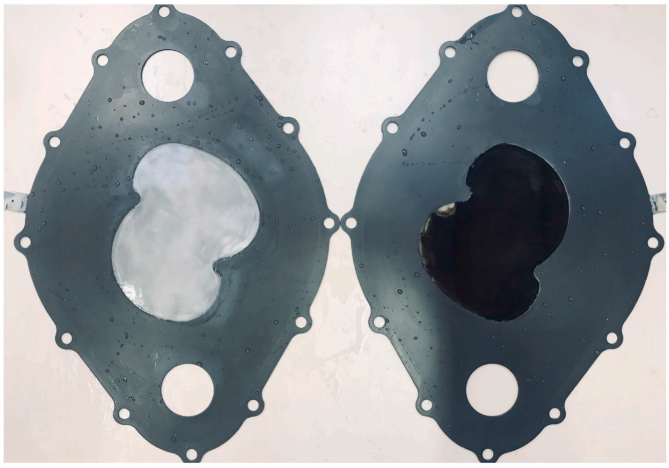

Fig. 5. Photo of the electrolyzer stack plates before and after coating with the CoPi catalyst.

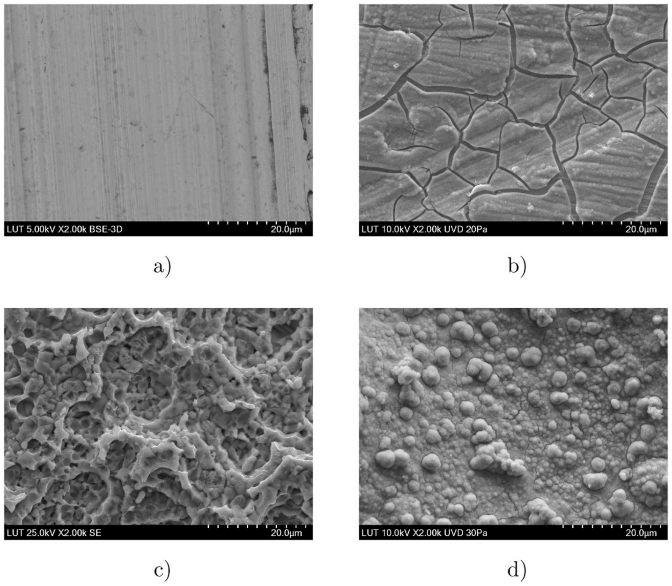

Fig. 6. SEM images of (a) bare SS, (b) Co-Pi on SS, (c) etched SS, and (d) CoFe–P on the etched SS at the same magnification.

increase in the voltammetric current was observed, indicating a higher coverage of the substrate surface and an increasing thickness of the coating. After deposition of Co–Pi, the active area of all the anode plates was evenly coated with a dark coating as shown in Fig. 5. As expected, all the cathode plates remained uncoated.

After deposition and visual inspection, the selected anode plate was analyzed with SEM equipped with EDS. According to Fig. 6b, the flat SS surface (Fig. 6a) was coated with numerous 3D-porous micrometer-size particles. Based on the EDXA diagram depicted in Fig. 7b, the presence of the desired Co and P was evident. The cracks observed on the surface of Co–Pi are a result of the moisture loss during the drying process.

The performance of the electrolyzer stack was analyzed with LSV before and after coating with Co–Pi in a neutral PBS. For all the LSV measurements, the electrolyzer stack was connected in parallel. As it can be seen in Fig. 7d, before coating there was absolutely no current flow in the electrolyzer stack until the potential reached 2.15 V. After 2.15 V,

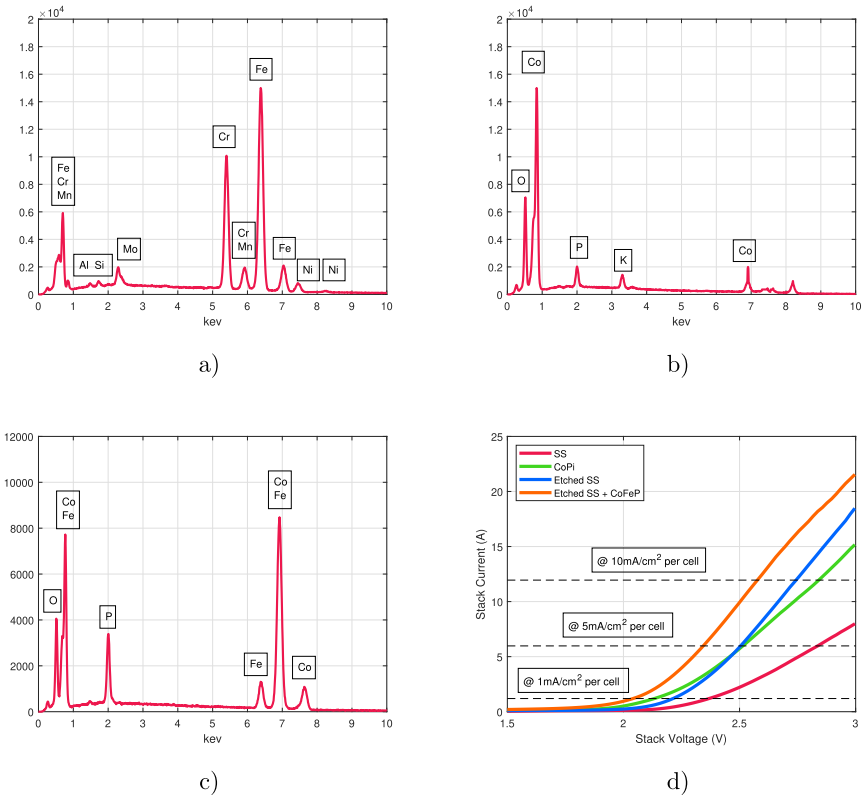

Fig. 7. EDXA spectra for (a) etched SS, (b) CoPi on SS, (c) CoFe–P on SS, and (d) corresponding LSV curves of the electrolyzer stack with different surface morphologies.

the gradual increase in current started to reach the reference current densities of 1 mA cm^{-2} and 5 mA cm^{-2} per electrolyzer cell at the overpotentials of 1.14 V and 1.6 V, respectively. The reference current density of 10 mA cm^{-2} was not reached at 3 V. After coating of the anode plates with Co–Pi, a considerable increase in the electrolyzer stack performance was observed. The current started to rise steeply already after 1.85 V. The same reference current densities of 1 mA cm^{-2} and 5 mA cm^{-2} were reached at significantly lower overpotentials of 0.9 V and 1.28 V in comparison with the bare SS anodes.

In the present study, etching with a mixture of H_2O_2 and HCl was used to roughen the substrate surface and to bare the grains of stainless steel. One can see in Fig. 6c that by that means, the active surface area of the electrolyzer stack plates has been significantly increased. The effect of etching on the electrolyzer stack performance was studied with the LSV, and it is illustrated in Fig. 7d. After 2 V, the current in the etched electrolyzer stack started to rise steeply, reaching a current density of 5 mA cm^{-2} per electrolyzer cell at a similar overpotential of 1.28 V as in the case of the anodes coated with Co–Pi. Although before 2.5 V the performance of the stack was slightly worse compared with the previous test with the Co–Pi coating, after 2.5 V the current rise in the etched stack was faster. The maximum current achieved at 3 V in the etched stack was close to 18 A, which is approximately 3 A higher than that of the electrolyzer stack coated with Co–Pi.

After experiments with etched SS surfaces, another CoFe–P-based coating was tested for the electrolyzer stack because of the high catalytic activity reported in the previous studies (Li et al., 2019; Yoon et al., 2018). During deposition of the CoFe–P catalyst, a gradual decrease in the potential region of the HER was observed. At the end of the deposition procedure, the selected plate was checked once again with SEM equipped with EDS, which revealed a clear change in the surface morphology (Fig. 6d) and the presence of the desired Co, Fe, and P peaks in the diagram (Fig. 7c). The CoFe–P morphology is presented with nodular grains covered with nanoparticles, which explains the large specific surface area and the high catalytic activity of this coating. Similar to the previous reports (Kanan and Nocera, 2008; Yoon et al., 2018), the XRD diffraction peaks of both the tested Co-based coatings revealed the amorphous nature of the synthesized catalysts.

It appeared that with the CoFe–P coating deposited onto the etched SS anodes, the onset overpotential was the lowest, and all the reference current densities were reached at lower overpotentials among all the previously tested options. The current started to increase rapidly before the potential in the stack reached 1.75 V, indicating the start of water splitting. Subsequently, the reference current densities of 1 mA cm^{-2}, 5 mA cm^{-2}, and 10 mA cm^{-2} per electrolyzer cell were reached at the overpotentials of 0.8 V, 1.07 V, and 1.34 V, respectively. At 3 V, the current in the electrolyzer etched and coated with CoFe–P was 2.7 times

as high as in the configuration with flat and uncoated SS electrodes. The superior performance is due to both the increased active surface area achieved by etching and the high intrinsic catalytic effect of the CoFe–P coating in neutral pH.

4. Conclusions

In the present study, a novel pilot-scale in situ water electrolyzer stack for HBI systems was designed and tested. The specific energy consumption and Faraday efficiency of the developed electrolyzer were reported. Compared with the previous research, the performance of the in situ water electrolyzer was considerably enhanced. Above all, leakage currents were prevented by the successful implementation of the insulating Teflon coating. Secondly, the use of modern fluid dynamics tools enabled the improvement of the electrolyte flow. Finally, modification of the active electrode surface area by applying a combination of etching and deposition of in situ Co–Fe–P-based electrocatalysts allowed to reach enhanced current densities at similar voltages in the stack. The results achieved in the study could be considered another crucial step in the development and upscaling of the HBI process.

CRediT authorship contribution statement

Georgy Givirovskiy: Conceptualization, Methodology, Investigation, Validation, Writing – original draft. **Vesa Ruuskanen:** Conceptualization, Methodology, Software, Investigation, Writing – original draft, Project administration, Funding acquisition. **Petteri Kokkonen:** Conceptualization, Methodology, Investigation, Writing – original draft. **Aku Karvinen:** Conceptualization, Methodology, Investigation, Writing – original draft. **Daria Givirovskaia:** Investigation, Writing – review & editing. **Eveliina Repo:** Resources, Writing – review & editing. **Jero Ahola:** Conceptualization, Methodology, Resources, Writing – review & editing, Funding acquisition, Supervision.

Declaration of competing interest

The authors declare that they have no known competing financial interests or personal relationships that could have appeared to influence the work reported in this paper.

Acknowledgment

This work was supported by the Academy of Finland [grant numbers 295883, 295866]; the Technology Industries of Finland Centennial Foundation with Jane and Aatos Erkko Foundation [grant "Feed and food from carbon dioxide and electricity–research and piloting of the future protein production."]

References

Alattar, A.L., Bazhin, V.Y., 2020. Al–Cu–B_4C composite materials for the production of high-strength billets. Metallurgist 64, 566–573. https://doi.org/10.1007/s11015-020-01028-2.

Bhandari, R., Trudewind, C.A., Zapp, P., 2014. Life cycle assessment of hydrogen production via electrolysis - a review. J. Clean. Prod. 85, 151–163. https://doi.org/10.1016/j.jclepro.2013.07.048.

De Francesco, M., Costamagna, P., 2004. On the design of electrochemical reactors for the treatment of polluted water. J. Clean. Prod. 12, 159–163. https://doi.org/10.1016/S0959-6526(02)00191-9.

Geissdoerfer, M., Savaget, P., Bocken, N.M., Hultink, E.J., 2017. The Circular Economy – a new sustainability paradigm? J. Clean. Prod. 143, 757–768. https://doi.org/10.1016/j.jclepro.2016.12.048.

Givirovskiy, G., Ruuskanen, V., Ojala, L.S., Kokkonen, P., Ahola, J., 2019. In situ water electrolyzer stack for an electrobioreactor. Energies 12, 1–13. https://doi.org/10.3390/en12101904.

Givirovskiy, G., Ruuskanen, V., Väkiparta, T., Ahola, J., 2020. Electrocatalytic performance and cell voltage characteristics of 1st- row transition metal phosphate (TM-Pi) catalysts at neutral pH. Mater. Today Energy 17, 1–11. https://doi.org/10.1016/j.mtener.2020.100426.

Kanan, M.W., Nocera, D.G., 2008. In situ formation of an oxygen-evolving catalyst in neutral water containing phosphate and Co^{2+}. Sci 321, 1072–1075. https://doi.org/10.1126/science.1162018.

Krieg, T., Sydow, A., Schro, U., Schrader, J., Holtmann, D., 2014. Reactor concepts for bioelectrochemical syntheses and energy conversion. Trends Biotechnol. 32, 645–655. https://doi.org/10.1016/j.tibtech.2014.10.004.

Li, K., Li, Y., Peng, W., Zhang, G., Zhang, F., Fan, X., 2019. Bimetallic Iron–Cobalt catalysts and their applications in energy-related electrochemical reactions. Catalysts 9. https://doi.org/10.3390/catal9090762.

Liu, C., Colón, B.C., Ziesack, M., Silver, P.A., Nocera, D.G., 2016. Water splitting–biosynthetic system with CO_2 reduction efficiencies exceeding photosynthesis. Sci 352, 1210–1213. https://doi.org/10.1126/science.aaf5039.

Liu, C., Colón, B.E., Silver, P.A., Nocera, D.G., 2018. Solar-powered CO_2 reduction by a hybrid biological | inorganic system. J. Photochem. Photobiol. Chem. 358, 411–415. https://doi.org/10.1016/j.jphotochem.2017.10.001.

Menter, F.R., Kuntz, M., Langtry, R., 2003. Ten years of industrial experience with the SST turbulence model turbulence heat and mass transfer. Cfd.Spbstu.Ru 4, 625–632.

Nangle, S.N., Sakimoto, K.K., Silver, P.A., Nocera, D.G., 2017. Biological-inorganic hybrid systems as a generalized platform for chemical production. Curr. Opin. Chem. Biol. 41, 107–113. https://doi.org/10.1016/j.cbpa.2017.10.023.

Nieminen, H., Givirovskiy, G., Laari, A., Koiranen, T., 2018. Alcohol promoted methanol synthesis enhanced by adsorption of water and dual catalysts. J. CO_2 Util. 24, 180–189. https://doi.org/10.1016/j.jcou.2018.01.002.

Nocera, D.G., Nash, M.P., 2006. Powering the planet: chemical challenges in solar energy utilization. PNAS 103, 15729–15735. https://doi.org/10.1073/pnas.0603395103.

Osadolor, O.A., Lennartsson, P.R., Taherzadeh, M.J., 2014. Introducing textiles as material of construction of ethanol bioreactors. Energies 7, 7555–7567. https://doi.org/10.3390/en7117555.

Rieth, A.J., Nocera, D.G., 2020. Hybrid inorganic-biological systems: faradaic and quantum efficiency, necessary but not sufficient. Joule 4, 2051–2055. https://doi.org/10.1016/j.joule.2020.08.012.

Ruuskanen, V., Givirovskiy, G., Elfving, J., Kokkonen, P., Karvinen, A., Järvinen, L., Sillman, J., Vainikka, M., Ahola, J., 2021. Neo-Carbon Food concept : a pilot-scale hybrid biological inorganic system with direct air capture of carbon dioxide. J. Clean. Prod. 278, 1–11. https://doi.org/10.1016/j.jclepro.2020.123423.

Szczygiel, J., Kułażyński, M., 2020. Thermodynamic limitations of synthetic fuel production using carbon dioxide: a cleaner methanol-to-gasoline process. J. Clean. Prod. 276 https://doi.org/10.1016/j.jclepro.2020.122790.

Torella, J.P., Gagliardi, C.J., Chen, J.S., Bediako, D.K., Colón, B., Way, J.C., Silver, P.A., Nocera, D.G., 2015. Efficient solar-to-fuels production from a hybrid microbial-water-splitting catalyst system. Proc. Natl. Acad. Sci. Unit. States Am. 112, 2337–2342. https://doi.org/10.1073/pnas.1424872112.

Ursúa, A., Gandía, L., Sanchis, P., 2012. Hydrogen production from water electrolysis: current status and future trends. Proc. IEEE 100, 410–426. https://doi.org/10.1109/JPROC.2011.2156750.

Wrana, N., Sparling, R., Cicek, N., Levin, D.B., 2010. Hydrogen gas production in a microbial electrolysis cell by electrohydrogenesis. J. Clean. Prod. 18, S105–S111. https://doi.org/10.1016/j.jclepro.2010.06.018.

Xing, J., Li, H., Cheng, M.M.c., Geyer, S.M., Ng, K.Y.S., 2016. Electro-synthesis of 3D porous hierarchical Ni – Fe phosphate film/Ni foam as a high-efficiency bifunctional electrocatalyst for overall water splitting. J. Mater. Chem. 4, 13866–13873. https://doi.org/10.1039/c6ta05952j.

Yoon, S., Kim, J., Lim, J.H., Yoo, B., 2018. Cobalt iron-phosphorus synthesized by electrodeposition as highly active and stable bifunctional catalyst for full water splitting. J. Electrochem. Soc. 165, H271–H276. https://doi.org/10.1149/2.1221805jes.

Zhang, W., Zhang, F., Niu, Y., Li, Y.X., Jiang, Y., Bai, Y.N., Dai, K., Zeng, R.J., 2020. Power to hydrogen-oxidizing bacteria: effect of current density on bacterial activity and community spectra. J. Clean. Prod. 263, 121596. https://doi.org/10.1016/j.jclepro.2020.121596.

ACTA UNIVERSITATIS LAPPEENRANTAENSIS

977. EL WALI, MOHAMMAD. Sustainability of phosphorus supply chain – circular economy approach. 2021. Diss.

978. PEÑALBA-AGUIRREZABALAGA, CARMELA. Marketing-specific intellectual capital: Conceptualisation, measurement and performance. 2021. Diss.

979. TOTH, ILONA. Thriving in modern knowledge work: Personal resources and challenging job demands as drivers for engagement at work. 2021. Diss.

980. UZHEGOVA, MARIA. Responsible business practices in internationalized SMEs. 2021. Diss.

981. JAISWAL, SURAJ. Coupling multibody dynamics and hydraulic actuators for indirect Kalman filtering and real-time simulation. 2021. Diss.

982. CLAUDELIN, ANNA. Climate change mitigation potential of Finnish households through consumption changes. 2021. Diss.

983. BOZORGMEHRI, BABAK. Finite element formulations for nonlinear beam problems based on the absolute nodal coordinate formulation. 2021. Diss.

984. BOGDANOV, DMITRII. Transition towards optimal renewable energy systems for sustainable development. 2021. Diss.

985. SALTAN, ANDREY. Revealing the state of software-as-a-service pricing. 2021. Diss.

986. FÖHR, JARNO. Raw material supply and its influence on profitability and life-cycle assessment of torrefied pellet production in Finland – Experiences from pilot-scale production. 2021. Diss.

987. MORTAZAVI, SINA. Mechanisms for fostering inclusive innovation at the base of the pyramid for community empowerment - Empirical evidence from the public and private sector. 2021. Diss.

988. CAMPOSANO, JOSÉ CARLOS. Integrating information systems across organizations in the construction industry. 2021. Diss.

989. LAUKALA, TEIJA. Controlling particle morphology in the in-situ formation of precipitated calcium carbonate-fiber composites. 2021. Diss.

990. SILLMAN, JANI. Decoupling protein production from agricultural land use. 2021. Diss.

991. KHADIM, QASIM. Multibody system dynamics driven product processes. 2021. Diss.

992. ABDULKAREEM, MARIAM. Environmental sustainability of geopolymer composites. 2021. Diss.

993. FAROQUE, ANISUR. Prior experience, entrepreneurial outcomes and decision making in internationalization. 2021. Diss.

994. URBANI, MICHELE. Maintenance policies optimization in the Industry 4.0 paradigm. 2021. Diss.

995. LAITINEN, VILLE. Laser powder bed fusion for the manufacture of Ni-Mn-Ga magnetic shape memory alloy actuators. 2021. Diss.

996. PITKÄOJA, ANTTI. Analysis of sorption-enhanced gasification for production of synthetic biofuels from solid biomass. 2021. Diss.

997. MASHLAKOV, ALEKSEI. Flexibility aggregation of local energy systems—interconnecting, forecasting, and scheduling. 2021. Diss.

998. NIKITIN, ALEKSEI. Microwave processes in thin-film multiferroic heterostructures and magnonic crystals. 2021. Diss.

999. VIITALA, MIRKA. The heterogeneous nature of microplastics and the subsequent impacts on reported microplastic concentrations. 2021. Diss.

1000. ASEMOKHA, AGNES. Understanding business model change in international entrepreneurial firms. 2021. Diss.

1001. MUSTO, JIRI. Improving the quality of user-generated content. 2021. Diss.

1002. INKERI, EERO. Modelling of component dynamics and system integration in power-to-gas process. 2021. Diss.

1003. GARIFULLIN, AZAT. Deep Bayesian approach to eye fundus image segmentation. 2021. Diss.

1004. ELFVING, JERE. Direct capture of CO2 from air using amine-functionalized resin - Effect of humidity in modelling and evaluation of process concepts. 2021. Diss.

1005. KOMLEV, ANTON. Magnetism of metal-free graphene-based materials. 2021. Diss.

1006. RISSANEN, MATTI. EcoGame and Ecosystem Profiler: solutions for business ecosystem management. 2021. Diss.

1007. VANHAMÄKI, SUSANNA. Implementation of circular economy in regional strategies. 2021. Diss.

1008. LEHTINEN, VESA. Organisaation emergentti itseohjautuvuus, case sinfoniaorkesteri: ”Miksi orkesteri soittaa hyvin, vaikka sitä johdettaisiin huonosti?”. 2022. Diss.

1009. KÄHKÖNEN, TIINA. Employee trust repair in the context of organizational change – identification and measurement of active trust repair practices. 2022. Diss.

1010. AHONEN, AILA. Challenges in sport entrepreneurship: cases in team sport business. 2022. Diss.

1011. LEVIKARI, SAKU. Acoustic emission testing of multilayer ceramic capacitors. 2022. Diss.

1012. ZAHEER, MINHAJ. Evaluation of open-source FEM software performance in analysing converter-fed induction machine losses. 2022. Diss.

1013. HAAPANIEMI, JOUNI. Power-based electricity distribution tariffs providing an incentive to enhance the capacity effectiveness of electricity distribution grids. 2022. Diss.

1014. BUAH, ERIC. Artificial intelligence technology acceptance framework for energy systems analysis. 2022. Diss.

LUT University

ISBN 978-952-335-789-1
ISBN 978-952-335-790-7 (PDF)
ISSN-L 1456-4491
ISSN 1456-4491
Lappeenranta 2022